AROMATIC AND QUINOIDAL CONJUGATION OF LADDER-TYPE MACROMOLECULES

A Dissertation

by

XIAOZHOU JI

Submitted to the Office of Graduate and Professional Studies of
Texas A&M University
in partial fulfillment of the requirements for the degree of

DOCTOR OF PHILOSOPHY

Chair of Committee,	Lei Fang
Committee Members,	Micah J. Green
	Daniel A. Singleton
	Karen L. Wooley
Head of Department,	Simon W. North

December 2020

Major Subject: Chemistry

ABSTRACT

Ladder-type conjugated molecules and macromolecules are attractive organic materials with optical and electronic properties suitable for various applications, as a result of their extended π-delocalization and strong intermolecular coupling facilitated by rigid coplanar structures. This dissertation focuses on incorporation of ladder-type constitution in aromatic and quinoidal conjugated oligomers and polymers, in order to address the fundamental challenges associated with conjugated organic materials, such as stability and limited delocalization ranges of states or quasi-particles.

This dissertation begins with an introduction of ladder-type conjugated structures and quinoidal resonance (Chapter I). Important concepts involved in the following chapters are introduced and related challenges are discussed.

Chapter II describes an example of conjugated ladder polymer featuring rigid coplanar backbone and self-complementary intermolecular hydrogen-bonding interactions. To address the low-solubility challenge of ladder polymers, a reversible protection and cleavage strategy is employed, realizing solution-phase characterization and processing. The rigid backbone with strong intermolecular interactions leads to compact aggregation and this ladder polymer demonstrates excellent thermal and chemical stability, showing promising potential as coating materials for harsh environment applications.

In Chapter III, ladder-type constitution is incorporated in a pernigraniline salt-derived system containing quinoidal building blocks. As the fully-oxidized and acid-

doped derivative of polyanilines, pernigraniline salt is not well-understood due to their poor stability and configurational uncertainty. Ladder-type constitution is imparted into oligomers to address these issues, demonstrating well-defined configuration and excellent chemical stability, rendering it possible to reveal the intrinsic electronic and magnetic properties. A dominant Pauli paramagnetism was observed, indicating the delocalization nature of polarons in ladder oligomers as a result of extended intramolecular and intermolecular interactions.

In Chapter IV, this design principle is expanded into a macromolecular system as ladder-type polyaniline derivatives. Chemical stability the ladder polymer ensures an unprecedented electrochemical stability under highly oxidative conditions. This material is applied in an electrochromic device, showing distinct switches between UV- and near-infrared-absorbing states with a remarkable cyclability and high tolerance to operation voltages.

Overall, this dissertation is to demonstrate the strategy of incorporating ladder-type constitution in aromatic and quinoidal conjugated macromolecules to address challenges in the field of organic electronic materials in both fundamental and application research. Enhanced stability and extended delocalization ranges of states are investigated in ladder-type conjugated macromolecules, showing their great potential as next-generation electronic active materials.

DEDICATION

To my mother and father

ACKNOWLEDGEMENTS

First and foremost, I would like to thank my Ph.D. advisor Professor Lei Fang, for his invaluable guidance, encouragement, and trust throughout my graduate study at Texas A&M University. It is my distinct honor to be his student, and I have learned so many lessons from him, in both science and life, that have furthered my growth as a scientist and a person. I am very grateful for his unreserved advice and support for my research and career development, and for introducing me to academic research. His professionalism, enthusiasm and kindness will have a long-term influence throughout my life.

I would also like to thank Professor Daniel A. Singleton for serving on my committee and for teaching me valuable physical organic chemistry knowledge during CHEM 646 class. I also appreciate Professor Karen L. Wooley for giving her precious advice as my committee member that greatly improved the way I present science, and for providing her kind support during my postdoc application. I also thank Professor Micah J. Green for his inspirational suggestions and discussions while serving on my committee.

I am also very grateful to have worked with Fang's group members throughout five years. I would like to give special thanks to Dr. Yang Zou for his great mentorship and guidance, and to Dr. Congzhi Zhu for his continuous help and encouragement throughout my graduate study. I also thank Dr. Zi-Hao Guo, Dr. Jongbok Lee, Dr. Tianyu Yuan, Dr. Alex J. Kalin, Dr. Chenxu Wang, Dr. Sai Che, Mariela Vazquez, Anthony U. Mu, Bailey K. Phillips, Che-Hsuan Chang, Yirui Cao, Bo-Ji Peng, Chenxuan Li, Octavio Miranda, and Mingwan Leng. I also appreciate the visiting scholars I have worked with.

They are Dr. Wan Zhang and Dr. Ruixia Niu. I appreciate the creative and friendly environment they created and their generous help and support. I would also thank the undergraduate student Yun Zhu who worked with me.

I would like to thank my collaborators, including Professor Mohammed Al-Hashimi and Professor Mohammad Naraghi. Special acknowledgement goes to Professor Kim R. Dunbar and her student Dr. Haomiao Xie. Their expertise in magnetic materials is essential to my graduate research. I am also grateful to all the staff in the Department of Chemistry, Materials Characterization Facility, and High Performance Computing facilities at Texas A&M University for their kind support.

I gratefully acknowledge the financial support from Texas A&M University including F. A. Cotton Endowed Memorial Graduate Travel Award and Graduate Student Research and Presentation Travel Award.

Finally, I would like to thank my family for their unconditional love, understanding, and support for my career and life. I am also truly grateful to my friends Dr. Mei Dong and Dr. Yue Song for their treasured company and all the fun we have had together throughout our Ph.D. life.

CONTRIBUTORS AND FUNDING SOURCES

Contributors

This work was supervised by a dissertation committee consisting of Professor Lei Fang (chair of committee), Professor Daniel A. Singleton, and Professor Karen L. Wooley of the Department of Chemistry and Professor Micah J. Green of the Department of Chemical Engineering.

Synthesis and characterization work in Chapter II was completed collaboratively by Dr. Yang Zou and the graduate student together. The AFM and GIXRD data in Chapter II were acquired and analyzed by Dr. Tianyu Yuan. With help from Dr. Joseph Strzalka, this test used resources of the Advanced Photon Source, a US Department of Energy (DOE) Office of Science User Facility operated for the DOE Office of Science by Argonne National Laboratory under contract no. DE-AC02-06CH11357. These data were published in 2017. The GIWAXS data were provided by Dr. Alex J. Kalin at Lawrence Berkeley National Laboratory. The magnetic susceptibility data in Chapter III was acquired by Dr. Haomiao Xie. The AC impedance data in Chapter III was acquired by Dr. Shaoyang Wang. The crystal structures were determined and provided by Dr. Nattamai Bhuvanesh. The TGA data were acquired by Dr. Chenxu Wang. These data were published in 2020.

All other work conducted for the dissertation was completed by the student independently.

Funding Sources

This work was supported in part by Texas A&M University, Texas A&M Energy Institute, the donors of the American Chemical Society Petroleum Research Fund (grant no. 54249-DNI7), Robert A. Welsh Foundation (A-1898), Qatar National Priority Research Program (NPRP9-160-2-088, NPRP10-0111-170152, and NPRP11S-1204-170062), and the President's Excellence Fund (Texas A&M University X-grant).

NOMENCLATURE

AFM	Atomic Force Microscopy
BINAP	2,2'-Bis(diphenylphosphino)-1,1'-binaphthalene
BLA	Bond Length Alternation
Boc	*t*-Butyloxylcarbonyl
CV	Cyclic Voltammetry
DFT	Density Functional Theory
DMAP	4-Dimethylaminopyridine
DMF	*N*,*N*-dimethylformamide
DMSO	Dimethyl Sulfoxide
DMSS	Dimethyl Succinyl Succinate
DPV	Differential Pulse Voltammetry
EPR	Electron Paramagnetic Resonance
ESI	Electron Spray Ionization
Fc/Fc^+	Ferrocene/Ferrocenium
FT-IR	Fourier Transform Infrared Spectroscopy
GIXRD	Grazing Incidence X-Ray Diffraction
GIWAXS	Grazing Incidence Wide-Angle X-Ray Scattering
^1H-^1H COSY	^1H-^1H Correlation Spectroscopy
HMBC	Heteronuclear Multiple Bond Correlation Spectroscopy
HOMO	Highest Occupied Molecular Orbital

HRMS	High Resolution Mass Spectrometry
MALDI-TOF	Matrix-Assisted Laser Desorption Ionization-Time of Flight
HSQC	Heteronuclear Single Quantum Coherence Spectroscopy
ITO	Indium Tin Oxide
LUMO	Lowest Unoccupied Molecular Orbital
mCPBA	meta-Chloroperoxybenzoic Acid
M_n	Number Average Molecular Weight
MSA	Methanesulfonic Acid
NIR	Near-Infrared
NMR	Nuclear Magnetic Resonance
NOSY	Nuclear Overhauser Effect Spectroscopy
PTSA	*para*-Toluenesulfonic acid
RMS	Root-Mean-Square
SEC	Size Exclusion Chromatography
SQUID	Superconducting Quantum Interference Device
STD	Standard Deviation
$TBAPF_6$	Tetrabutylammonium Hexafluorophosphate
TFA	Trifluoroacetic Acid
TGA	Thermogravimetric Analysis
THF	Tetrahydrofuran
UV-vis	Ultraviolet-Visible Spectroscopy
$Đ$	Dispersity

TABLE OF CONTENTS

Page

LIST OF FIGURES

Page

LIST OF TABLES

Page

CHAPTER I

INTRODUCTION

1.1 Ladder-Type Conjugated Molecules

A π-conjugated system is a molecular entity whose structure may be represented as a system of alternating single and multiple bonds.[1] In conjugated molecules and polymers, the relatively narrow energy bandgap [the energy difference between highest occupied molecular orbital (HOMO) and lowest unoccupied molecular orbital (LUMO)] resulted from π-electron delocalization leads to semiconducting or conducting properties. Starting from the early 1960s, organic conjugated molecules and polymers have been one of the most important modern materials in diverse optical and electronic applications. In recent decades, research interest has never waned in development of organic conjugated molecules and polymers as next-generation materials.

In a conventional conjugated structure, the torsional rotation of sigma bond connections results into a non-coplanar conformation, which renders them good solubility, while limits the π-conjugation scale and intermolecular interactions (**Figure 1a**). In contrast, the torsional rotation is prohibited in a ladder-type conjugated structure. A ladder-type molecule is defined as a multiple-strand molecule consisting of an uninterrupted sequence of rings with adjacent rings sharing two or more atoms (**Figure 1b**).[2] Ladder molecules feature high backbone rigidity and coplanarity, and lack configurational or conformational disorders.[3, 4] The high coplanarity promotes both intramolecular π-conjugation[5] and intermolecular interactions.[6] As a result, π-electron delocalization scale is extended efficiently in ladder polymers. In the condensed phases,

the reorganization energy of ladder polymer is much decreased and intrinsic charge mobility is enhanced. Although the first ladder polymer was synthesized in 1960s, not until recent decades have people achieved efficient synthesis of soluble ladder-type conjugated polymers and studied their electronic properties systematically (**Figure 1c**). Their unique optical and electronic properties are suitable for diverse applications in organic light-emitting diodes,[7] organic field-effect transistors,[8, 9] organic photovoltaics,[10-12] thermoelectrics,[13] molecular wire,[10] *etc.* For example, in an organic field-effect transistor device, the representative ladder poly(benzimidazole benzophenanthroline) possesses an electron mobility 10^5 times higher than that of the non-ladder analogue.[14] Ladder molecules and polymers also acquire advanced stability from the structure with multi-strand of bonds, promising their great potential in various demanding applications.

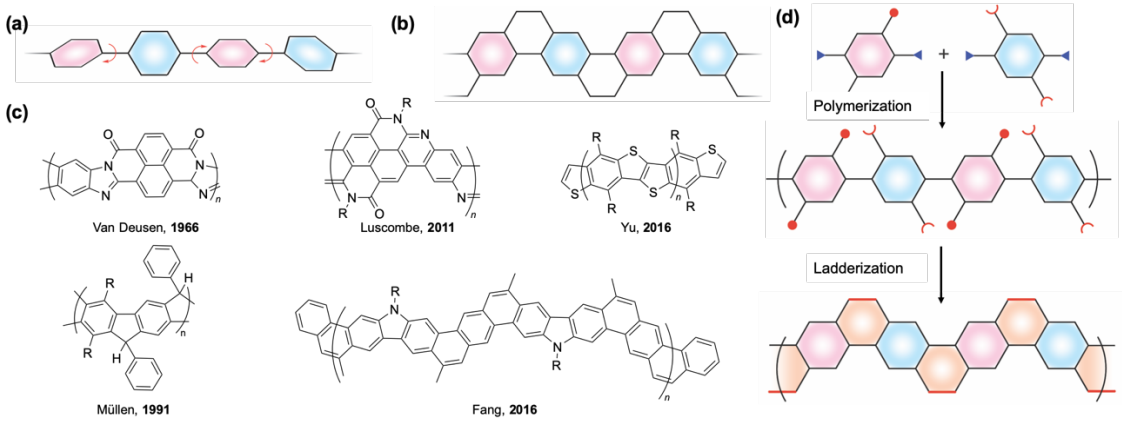

Figure 1. Graphic representations of (a) a π-conjugated molecule connected with a single strand of bonds, (b) a ladder-type π-conjugated molecule, and (d) stepwise synthesis approach of ladder-type conjugated polymers. (c) Representative examples of ladder-type conjugated macromolecules.

Despite the intriguing properties, challenges still remained in the field of ladder molecules and polymers. The rigid backbones and strong intermolecular interactions lead to intrinsically low solubility of ladder systems, which renders synthesis, characterization and processing difficult. Sufficient solubilizing substituents are required to be incorporated. Additionally, high demands are also present in controlling a low defect level in the ladder-type backbone through efficient synthesis route to achieve desired structures and properties.[15] In recent decades, a stepwise approach is commonly employed to construct ladder polymers (**Figure 1c**). Based on the polymerized non-ladder-precursors, efficient ring-annulation reactions are required to complete the intramolecular "ladderization" step. A broad library of reactions, including electrophilic aromatic substitution, Schiff base formation, olefin metathesis, Scholl coupling, *etc.*, have been explored.[16, 17] In these reactions, bulky side-chains can be used to prevent the undesired intermolecular reactions, while too much bulkiness would decrease the reactivity and lead to high defect levels. Therefore, a delicate balance is required to maintain a high reactivity meanwhile avoid intermolecular side reactions. Regioselectivity is another important factor which controls the configuration of the final ladder products. Highly regioselective ring-annulation reactions are required to obtain isometrically pure ladder structures. Defects can occur in ladder polymers in multiple ways, including incomplete ladderization reactions, loss of solubility en route to the products, undesired end groups, or degradation side reactions. Although many structurally perfect ladder-type conjugated macromolecules have been synthesized, further efforts are still needed to develop wider

scope of this material and achieve defect-free ladder polymers with superior electronic properties and chemical, thermal, and photostability.[18]

Overall, novel ladder conjugated polymers with synthetic/processing feasibility, structural versatility and controlled functionality are expected to deliver breakthrough performance in potential optical, electronic, and magnetic applications.

1.2 Quinoidal Structure in Conjugated Molecules and Polymers

1.2.1 Quinoidal Resonance

Most conjugated polymers contain cyclic π-units in the mainchain. These building blocks can adopt either a Hückle aromatic form or a quinoidal form. The aromatic building blocks are typically connected with one another by single bonds. In contrast, in the quinoidal form, a π-conjugated unit exerts no local ring aromaticity and is typically connected with others by double bonds. These polymers often exhibit drastically different structural features, such as bond lengths, conformation, and open-shell character, *etc.*, compared to their counterparts composed of non-quinoidal aromatic units. As a result, quinoidal conjugated polymers can exhibit distinctive electronic, optical, and magnetic properties that are often not accessible in aromatic conjugated polymers, promising for a wide range of applications.

A quinoidal π-system differs from its aromatic counterpart drastically in terms of the bond length alternation (BLA), which is defined as the average of the differences in bond lengths between the alternating single and double bonds.[19] As an important structural parameter, BLA governs the electronic properties of a conjugated polymer, such as the

energy bandgap and Peierls distortion. In one of the simplest examples, polyacetylene (**Figure 2a**), the resonance hybrid with BLA = 0 should be metallic in an ideal situation. However, such metallic state is unstable and Peierls distortion takes place to generate a more stable form with |BLA| > 0. As a result, one of the resonance forms is favored and the distorted structure possesses an energy bandgap, leading to the non-metallic nature of polyacetylene in reality. For an infinite chain of conjugated polymers with cyclic π-units, the quinoidal and aromatic forms can be viewed as resonance forms with respect to each other (**Figure 2b**). The aromatic form, however, often dominates the contribution due to the added stability by Hückle aromaticity.

Despite the fact that aromatic conjugated polymers dominate the research field due to their favorable stability and ease of synthesis, research attentions have been paid on the quinoidal conjugated polymers since the early days of conductive polymers.[20-22] It was hypothesized and confirmed that a conjugated polymer in its quinoidal form is more electrically conductive than the corresponding aromatic form.[23, 24] On an infinite chain, theoretically, the maximum π-conjugation scale is obtained where all bond lengths are equal (BLA = 0), although it is an unstable form in between the quinoidal and the aromatic forms.[25] In reality, a polymer containing quinoidal building blocks often also exhibits contribution from its aromatic resonance form, resulting a smaller |BLA| value compared to a "pure" aromatic polymer. The resonance transformation in between quinoidal and aromatic forms of building blocks also leads to the generation of open-shell radical character. Combining these features, polymers containing quinoidal building blocks often

possess larger degree of π-conjugation and higher conductivity compared to "pure" aromatic polymers.[26]

Apart from BLA, the backbone conformations of conjugated polymers are also drastically different between quinoidal and aromatic resonance forms. On account of the all-double-bond connections, a quinoidal structure often possesses higher coplanarity and rigidity, while its aromatic counterpart has a higher degree of freedom for torsional rotation about the single bond linkages (**Figure 2c**).[27] The coplanarity of quinoidal structure further facilitates electron delocalization throughout the π-system, contributing to a larger π-conjugation scale.

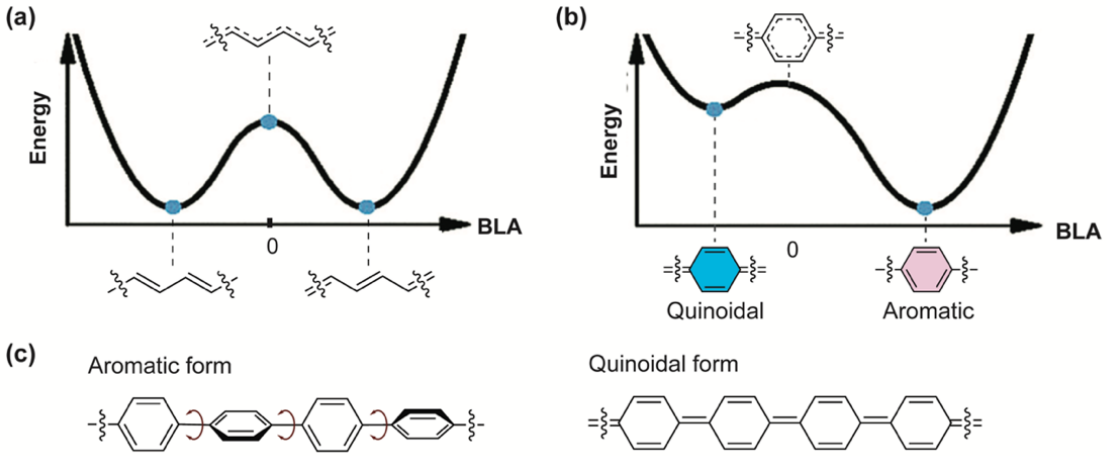

Figure 2. Energy diagrams of the ground state of (a) polyacetylene and (b) conjugated polymers with infinite chain length. Reproduced (adapted) from ref [23] with permission from John Wiley and Sons. (c) Aromatic and quinoidal form showing constitutional and conformational differences.

Although the importance of quinoidal structure has been revealed for a long time, polymeric π-systems with intrinsic quinoidal character (defined as quinoidal conjugated

polymers in this article) are less reported due to challenges associated with the synthesis and stability.[28] Despite these challenges, a number of important advances have been made to further our knowledge on the design and synthesis of quinoidal conjugated polymers and to deepen our understanding of the quinoidal properties for a wide range of diverse applications.

1.2.2 Open-Shell Diradical Character

In quinoidal structures featuring small BLA, the small energy bandgap can enable admixing of HOMO and LUMO in the ground state, leading to open-shell diradical character and spin-active states.[29, 30] From the perspective of resonance forms, such open-shell diradical character can be considered as a result of increased resonance contribution of the diradical form due to the stabilization effect of the central ring gaining Hückle aromaticity (**Figure 3**).[31, 32] In a diradical system, with the increasing of one-electron overlap integral S_{AB} of two odd electrons, the singlet state is stabilized and triplet state is destabilized, leading to increasing of singlet-triplet gap.[33]

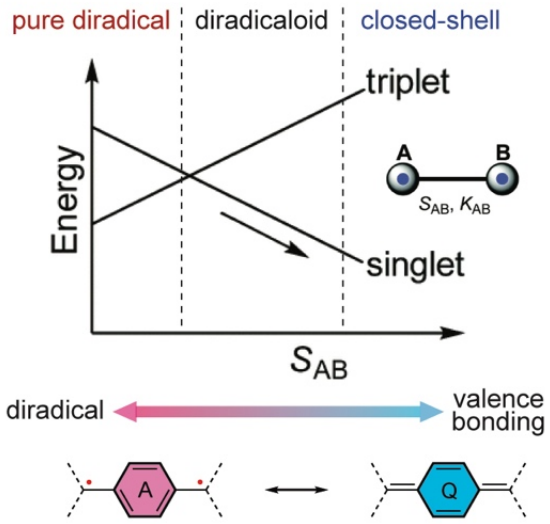

Figure 3. Change of energies of triplet/singlet pair with increased of one-electron overlap integral SAB and resonances between open-shell diradical and closed-shell quinoidal structures. Reproduced (adapted) from ref. [29] with permission from the Royal Society of Chemistry.

For quinoidal conjugated molecules, open-shell character and singlet-triplet gap is critically dependent on the molecular structures. The diradical open-shell resonance is favored when a significant aromaticity is obtained in this form compared to the closed-shell quinoidal form. High torsional rotation is also usually employed to reduce the overlap between two spins and increase the diradical character. In recent literatures, coplanar quinoidal molecules with polycyclic skeletons have been investigated extensively, displaying intriguing diradical and polyradical properties (**Figure 4a**).[34-37] Conjugated polymers with quinoidal building blocks have also been investigated. For example, a high-spin ground state and small singlet-triplet energy gap was achieved in a copolymer composed of cyclopentadithiophenyl and thiadiazoloquinoxaline units[38] (**Figure 4b**) as a result of the open-shell character of the thiadiazole-based quinoidal moieties.

The unpaired electrons and their corresponding magnetic moments render intriguing behaviors of quinoidal conjugated polymer that are not observable on their closed-shell counterparts. Therefore, the investigation of quinoidal polymers with isolable stability of high-spin states has emerged in diverse research fields, including spin manipulation, organic magnetism, quantum functionalities, and interrelated optoelectronic properties.[39] It is believed that there is a close correlation between diradical and polyradical character and two-photon absorption, magnetic properties, singlet fission phenomenon, *etc.*, indicating great potential of quinoidal conjugated molecules as materials for various applications including organic photonics, electronics, spintronics, energy storage, and so on.

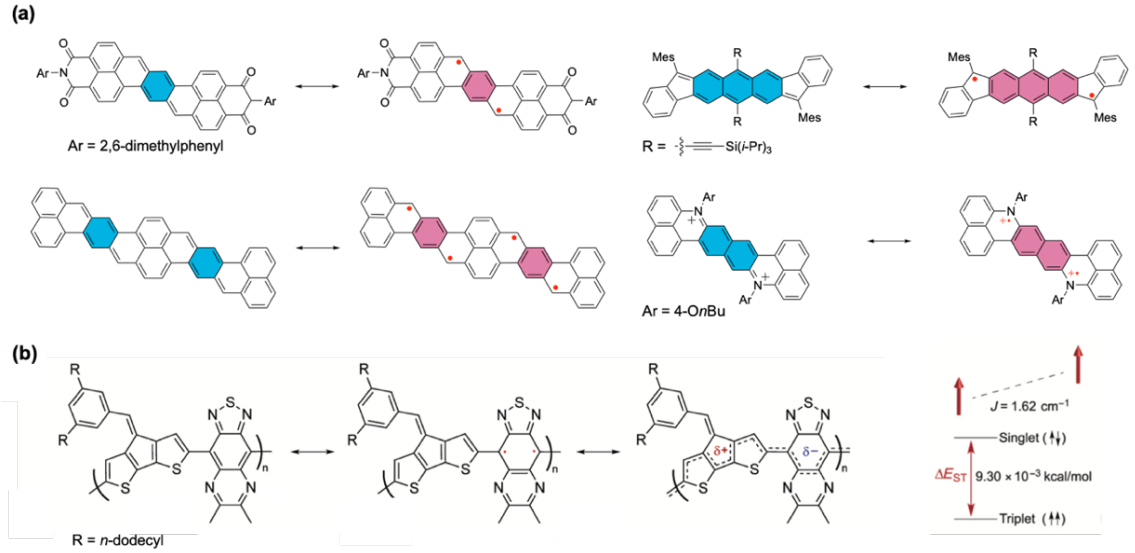

Figure 4. (a) Structures of some recently reported quinoidal molecules and their open-shell diradical resonance form. (b) Structure of a quinoidal conjugated polymer with high-spin ground state. Reproduced from Ref. [38] with permission from the American Association for the Advancement of Science.

1.2.3 Extended Delocalization of Polarons/Bipolarons

Quinoidal forms are important in the doping process of π-conjugated polymers. In fact, in early studies, most of the quinoidal characters of conjugated polymers were investigated in the doped states[20] or in the transient states[40] of their aromatic precursors, such as polypyrrole, polythiophene, and polyaniline (PANI), *etc.* Upon doping, the aromatic building blocks in conjugated polymer are partially converted into their quinoidal form, therefore affording drastically changed chemical, electronic, and magnetic properties (**Figure 5a**). For example, without doping, polypyrrole and polythiophene possess a dominant aromatic form. The relatively small energy gap between the overall π-bonding and π*-antibonding orbitals, corresponding to valence and conductance bands, respectively, renders semiconducting properties.[41] Upon oxidative doping, positive charges are created and local reorganization leads to an ionized quinoidal form. In the solid state, the lattice deformation with radical cation is termed as a "polaron", whose energy levels are localized in the forbidden band (**Figure 5b**), leading to the shift of the Fermi level simultaneously and electrical conductivity. At a higher doping level, radical cations in close proximity can combine so that the two neighboring positive charges are coupled in the quinoidal unit.[42] Such a doubly-charged quinoidal section can be considered as a "bipolaron" that delocalizes over several rings. In this case, two localized states form in the original bandgap and evolve into two bipolaron bands with increased doping levels. In doped polymers, both high-spin polarons and spinless bipolarons are charge carriers. The low effective mass of polarons and bipolarons and high carrier mobility give rise to the ultrahigh conductivity of polymers with quinoidal segments,[43] while polarons are

believed to possess higher mobility than bipolarons.[44] Overall, the quinoidal form is ubiquitous in the doping process of conjugated polymers, and is critical to the generation of polarons and bipolarons for electrical conductivity.

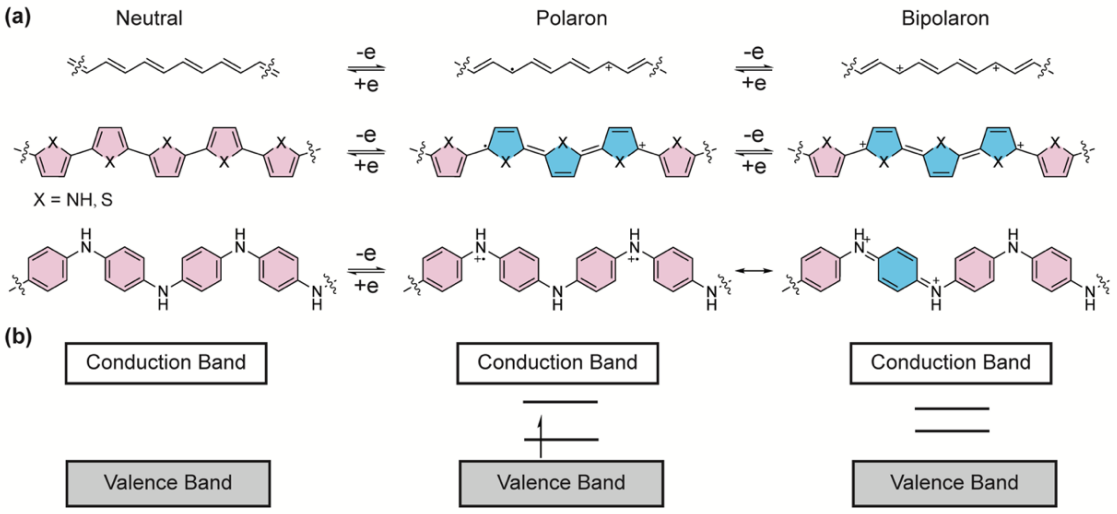

Figure 5. (a) Structural formulas of polyacetylene, polypyrrole, polythiophene and PANI in their undoped aromatic form and partially quinoidal form after doping; (b) Energy diagrams of the neutral, polaron, and bipolaron states.

Recently, direct observation of quinoidal units as charge carriers was reported in poly(*para*-phenylene) (PPP) chains.[45] The aromatic (benzenoid) and quinoidal forms can be distinctively visualized under scanning tunneling microscopy (STM) and noncontact atomic force microscopy. Under STM with a voltage bias, both *intrachain* and *interchain* transports of quinoidal segments were observed (**Figure 6**), showing high mobility character of the quinoidal polarons or bipolarons. High-spin polarons and bipolarons can also be generated in conjugated copolymers with quinoidal building blocks. In recent research, the high conductivity rendered by hopping of the quinoidal segment has been

applied in organic conducting and thermoelectric devices.[38, 46-49] In a recent study, DFT calculation was also used to reveal the formation of stable triplet bipolarons which is believed to be the reason of the large Seebeck coefficient for thermoelectric application despite the high electrical conductivity.

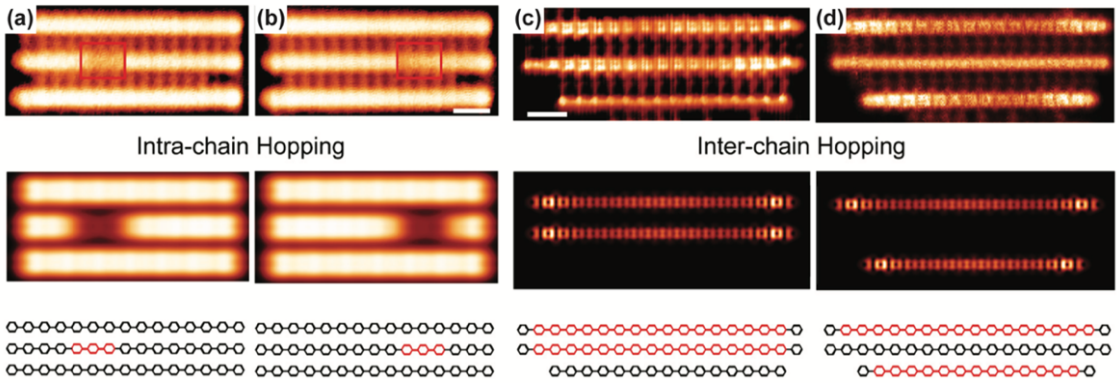

Figure 6. (a, b) (top) experimental STM images of PPP chains showing the transport of quinoidal segment in one of the chains; (middle) simulated STM images; (bottom) structural representation of the three chains shown above. (c, d) (top) Constant-height STM images of PPP chains showing the hopping of quinoidal segment from the middle chain to the bottom chain; (middle) simulated current images; (bottom) structural representation of the three chains shown above. Reproduced from ref. [45] with permission from the American Chemical Society.

1.2.4 Conclusion and Perspectives

Quinoidal characters impart a number of intriguing properties — including but not limited to open-shell character, polaron/bipolaron delocalization and narrowed energy bandgap — into conjugated systems. A wide range of small molecules and polymers with diverse structural constitutions have been investigated and demonstrated great potential as novel materials. However, various challenges still remain in this research topic. First, the

scope of structures and syntheses of quinoidal monomeric building blocks is relatively narrow compared to traditional aromatic conjugated polymers. Second, it is still challenging to precisely predict and control energy levels of quinoidal building blocks due to the complex contribution from BLA, *intrachain* charge transfer, and Peierls distortion.[50] Last but not least, the open-shell character of quinoidal structure could bring in stability issues for practical applications.

In future research, the discovery and development of novel quinoidal building blocks and synthetic methodologies are desired in order to achieve precision control of the unique properties of quinoidal conjugated polymers. Further fundamental investigations on the open-shell high-spin character and polaron and/or bipolaron delocalization properties are critical to understand the nature of quinoidal structures and to render high stability in these materials.[47]

In this context, integration of quinoidal units and ladder-type constitution can be a viable strategy to achieve robust organic materials with metallic ground states for applications including thermoelectricity, spintronics, and nonlinear optics, *etc.*

CHAPTER II

AROMATIC LADDER POLYMER FEATURING INTERMOLECULAR HYDROGEN-BONDS*

2.1 Introduction

In conjugated polymers, in addition to the constitutional and conformational features of individual chains, *interchain* interactions also play a key role in governing a wide range of properties/functions of polymers, particularly for those closely related to solid-state packing.[51-54] This concept applies to ladder polymers as well. It is crucial to manipulate the intermolecular interactions (non-covalent bonds), as well as the macromolecular characteristics (rigid ladder-type backbone), to precisely control the properties and functions of ladder polymers.[55] In the context of addressing this grand challenge, hydrogen bonds (H-bonds) represent a class of ideal non-covalent interactions because they are highly selective and directional. Furthermore, the important role of H-bonding in shaping the properties of conjugated systems has been recognized in the literature,[56-63] demonstrating profound impacts in the charge transport, mechanical strength and film-forming properties of these materials. Therefore, the incorporation of well-defined H-bonds into ladder polymer backbones represents an important advance in terms of both fundamental investigation of structure-property relationship and practical exploration for electronic or mechanical performances.

---

*Reprinted (adapted) with permission from "Synthesis and Solution Processing of A Hydrogen-Bonded Ladder Polymer" Zou, Y.; Ji, X.; Cai, J.; Yuan, T.; Stanton, D. J.; Lin, Y. H.; Naraghi, M.; Fang, L. *Chem* **2017**, *2*, 139. Copyright 2017 Elsevier.

Despite the numerous examples of ladder polymers, only a handful with intermolecular H-bonds were proposed or reported in the literature.[64-66] Precise structural characterization of these examples, however, has not been well-established because of their insoluble nature. The formidable challenges associated with this class of polymer are twofold: difficulties in constructing ladder-type backbones with H-bond donors and acceptors, and the solubility issues in the synthesis, characterization and processing.

2.2 Molecular Design

Molecular design of the H-bonded ladder polymer was developed on the basis of a quinacridone unit,[67] which features 5 linearly fused rings (**Figure 7a**). As an inexpensive, non-toxic and environmentally friendly pigment with a pentacene-like backbone, quinacridone is a promising building block of high performance optoelectronics materials.[60, 68-71] Two sets of self-complementary H-bonds can be formed intermolecularly between the carbonyl and N−H functional groups on the quinacridone unit.[72-74] These H-bonding interactions promote strong intermolecular electronic coupling[60] of quinacridone molecules and guide their self-assembly to give compact packing mode, leading to good charge carrier mobility,[60] as well as high thermal, chemical and photochemical stability.[75-77] We envisioned that the incorporation of quinacridone into a ladder polymer backbone could create a rigid ladder-type polymer chain with fixed conformation and multiple H-bonding interactions, addressing the aforementioned grand challenge. In this context, ladder-type poly(indenoquinacridone) (**PIQA**) was designed for this study (**Figure 7b**).

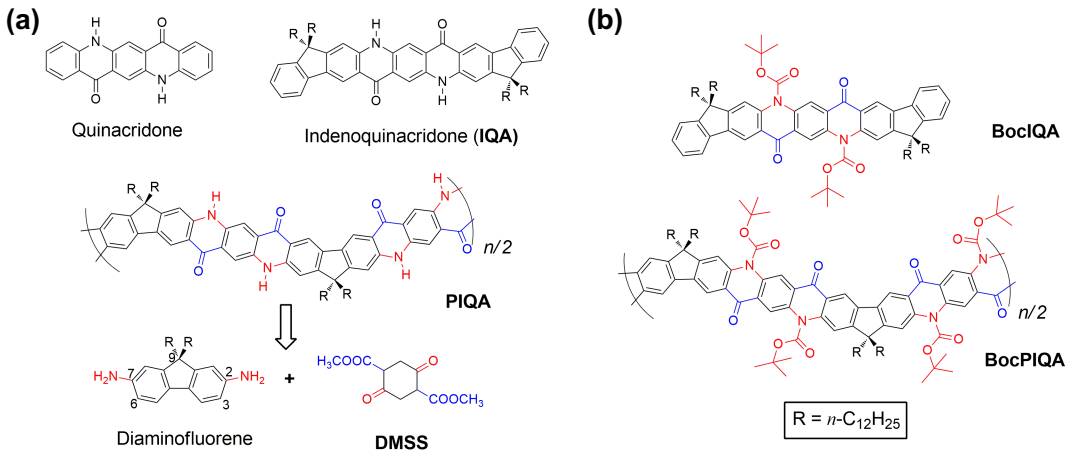

Figure 7. (a) Structural formula of quinacridone, IQA, and PIQA. The two starting materials for PIQA are diaminofluorene and DMSS; (b) Structural formula of Boc functionalized IQA and PIQA: BocIQA and BocPIQA. Reprinted with permission from [78].

2.3 Synthesis and Characterization

The synthetic strategy of **PIQA** was devised based on our previously reported "condensation-followed-by-cyclization" method[79] which afforded indenoquinacridone (**IQA**) small molecules in high efficiency. Building upon this strategy, **PIQA** can be constructed in a similar manner through a polycondensation-followed-by-cyclization strategy.

Based on the aforementioned design principles, a highly efficient 3-step-synthesis was developed and optimized (**Figure 8**) to give **PIQA** in gram-scale without using noble metal catalysts. The synthesis started with the step-growth imine condensation polymerization between 9,9-didodecyl-2,7-diaminofluorene and dimethyl succinyl succinate (DMSS). A subsequent tautomerization[80, 81] to the enamine form afforded the intermediate cyclohexadiene-fluorene polymer — **P1**.[82] The polymerization conditions

were optimized as using *p*-toluenesulfonic acid (PTSA) as the catalyst in $CHCl_3$ at 95 °C for 72 hr. End-capping of the polymer was attempted with monofunctional aniline and carbonyl compounds. However, due to the dynamic nature of imine condensation, the polymer degraded into oligomers as a result of loss of the stoichiometric balance of functional groups. Therefore, **P1** was not treated with an end-capping reagent. The linear *n*-dodecyl chains on diaminofluorene monomer were essential for achieving a reasonable degree of polymerization. Shorter alkyl chains such as ethyl or 2-ethylhexyl were insufficient in maintaining the solubility, hence led to precipitation of oligomers during the reaction. In contrast, long branched alkyl chains (*i.e.*2-octyldodecyl) led to lower reactivity and resulted in a low degree of polymerization. **P1** was readily oxidized[79, 83] into the conjugated fluorene-aniline polymer—**P2** in air in the presence of catalytic amount of trifluoroacetic acid (TFA), leading to a color change from light orange to red. After purification by acetone extraction, size exclusion chromatography (SEC) of **P2** revealed a number-average molecular weight (M_n) of 24.0 kg/mol and a dispersity ($Đ$) of 2.3. The structure of **P2** was further characterized by using Fourier-transform infrared spectroscopy (FT-IR) (**Figure 20**) and ^{1}H NMR, ^{13}C NMR, ^{1}H-^{1}H COSY, NOESY NMR spectroscopy (**Figure 23**, **27**, **28**).

To complete the construction of the ladder backbone, an electrophilic aromatic cyclization reaction was employed to form the second strand of covalent bonds between the fluorene units and the carbonyl groups. The only remaining reactive sites on the fluorene unit for electrophilic cyclization are C3 and C6 positions while the C1 and C8 positions are too steric hindered to react.[84-88] The regiospecific reactivity of the fluorene

unit avoids the possibility of isomer formation during the cyclization step. Reaction optimization demonstrated that a carboxylic acid was a better substrate, affording quantitative conversion, compared to the less efficient methyl ester substrate. In this context, the pendant methyl ester groups in **P2** were hydrolyzed by potassium hydroxide into carboxylic acid groups quantitatively. The resulting polymer — **P3** was subjected to the electrophilic aromatic cyclization. The regiospecificity of the fluorene unit guaranteed a regio-regular product.[88-90] The optimized conditions involved heating in methanesulfonic acid (MSA), an inexpensive and environmentally friendly reagent,[91] and resulted in a near-quantitative yield. During this process, the acidic MSA promoted[79] the electrophilic cyclization at high temperature and maintained the intermediate and product well solubilized, ensuring the completion of the reaction. In fact, MSA is the only known solvent capable of dissolving the ladder polymer product **PIQA**. Overall, the gram-scale, transition-metal-free synthesis of **PIQA** was achieved in only 3 steps from diaminofluorene, with a 66% overall yield.

Despite the solubilizing dodecyl side-chains, with a rigid ladder-type backbone and strong intermolecular H-bonds, the solubility of **PIQA** was extremely low in common organic solvents, preventing any meaningful solution-phase characterization. To overcome this issue, we designed a unique post-functionalization method to reversibly convert **PIQA** into a highly soluble material. This strategy involved the attachment of Boc onto the N–H functional groups by treating **PIQA** suspension in THF with di-*tert*-butyl dicarbonate at 60 ºC. Once attached to the polymer backbone, the bulky Boc moieties not only diminished the intermolecular H-bonds, but also prohibited the *interchain* π-π

interaction by steric effects. Therefore, the resulting product **BocPIQA** was highly soluble in chloroform (over 100 mg/mL), THF, toluene, *etc*. It is noteworthy that the conversion of **PIQA** into **BocPIQA** was not 100% because the higher molecular weight fraction of **PIQA** was extremely insoluble hence not reacted during the reaction time scale. As a result, the SEC measured molecular weight of **BocPIQA** (M_n = 14.0 kg/mol) was lower than the measured M_n of precursor **P2** (24.0 kg/mol). The Boc units in **BocPIQA**, however, could be easily cleaved to regenerate **PIQA** quantitatively.

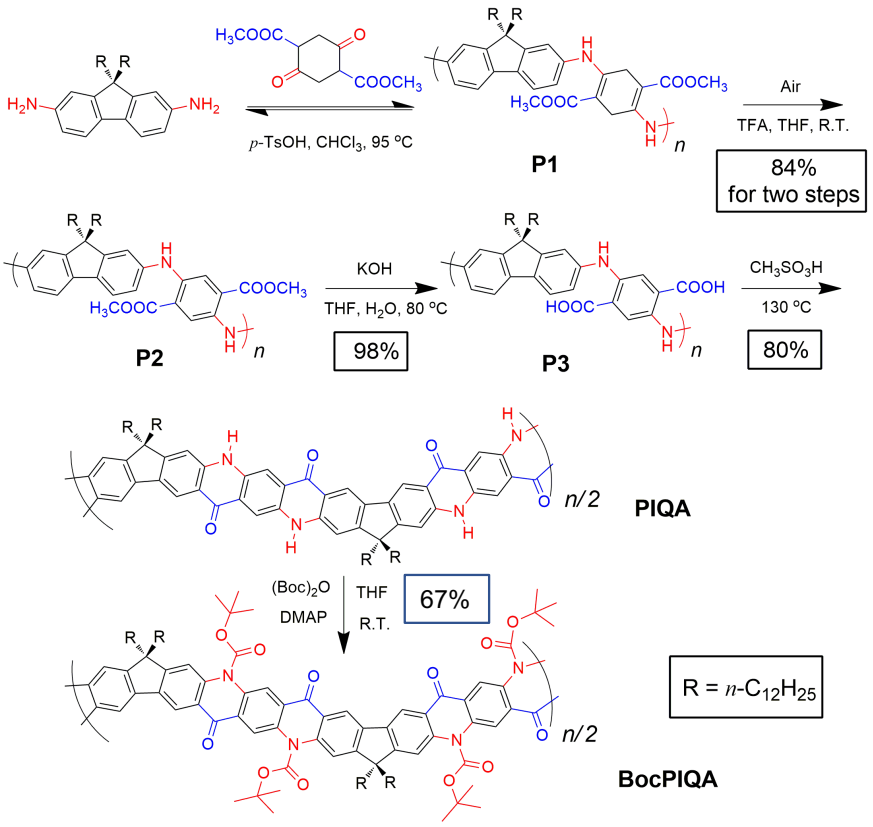

Figure 8. Synthetic route of the quinacridone derived ladder polymer PIQA and its Boc protected derivative BocPIQA. Reprinted with permission from [78].

Characterization of **BocPIQA** confirmed the structure of its precursor — insoluble **PIQA**— unambiguously. ^{1}H NMR spectrum of **BocPIQA** showed broad[15, 89, 92, 93] yet well-defined peaks (**Figure 28**), corresponding to the highly symmetrical protons on the ladder-type backbone. ^{1}H-^{1}H COSY NMR spectrum of **BocPIQA** (**Figure 29**) demonstrated no coupling between any of the aromatic proton signals, ruling out the possibility of regioisomers formed by the C1/C8 electrophilic cyclization. More importantly, the excellent solubility of **BocPIQA** allowed for the acquirement of a concentration-demanding ^{13}C NMR spectrum with a high signal/noise ratio (**Figure 9c, 25**). Sharp and characteristic ^{13}C resonance peaks were observed and all were assigned to specific carbons on the polymer. This assignment was rigorously performed using the small molecular model compound **BocIQA** as a reference (**Figure 22**, **26**). All the ^{13}C resonance peaks of **BocIQA** were assigned based on its HSQC and HMBC spectra (**Figure 9a**). Sharing a similar constitutional structure, **BocPIQA** showed ^{13}C resonance patterns matching that of **BocIQA** (**Figure 9b, c**), with less signals due to the more symmetrical nature of its repeating units. The clean and well-defined ^{13}C NMR spectrum of **BocPIQA** confirmed its unique regio-regular ladder-type structure and a low defect level along the backbone.[15]

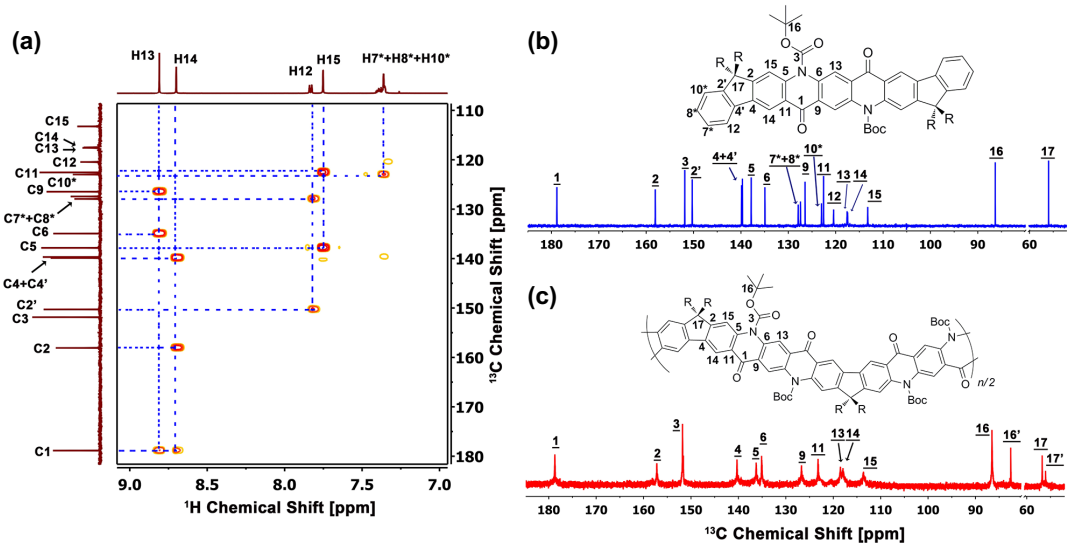

Figure 9. (a) ^{1}H-^{13}C HMBC spectrum of BocIQA. ^{13}C NMR (125 MHz) spectra and ^{13}C signal assignment of (b) BocIQA and (c) BocPIQA. ($CDCl_3$, 298 K). Reprinted with permission from [78].

In addition, **PIQA** and **BocPIQA** shared similar photophysical properties with their small molecular analogues, **IQA** and **BocIQA** respectively, as revealed by UV-vis absorption spectroscopy (**Figure 10**, **11**). Compared to **IQA** and **BocIQA**, the bathochromic shift of **PIQA** and **BocPIQA** indicates the extended conjugation of the polymeric chains.

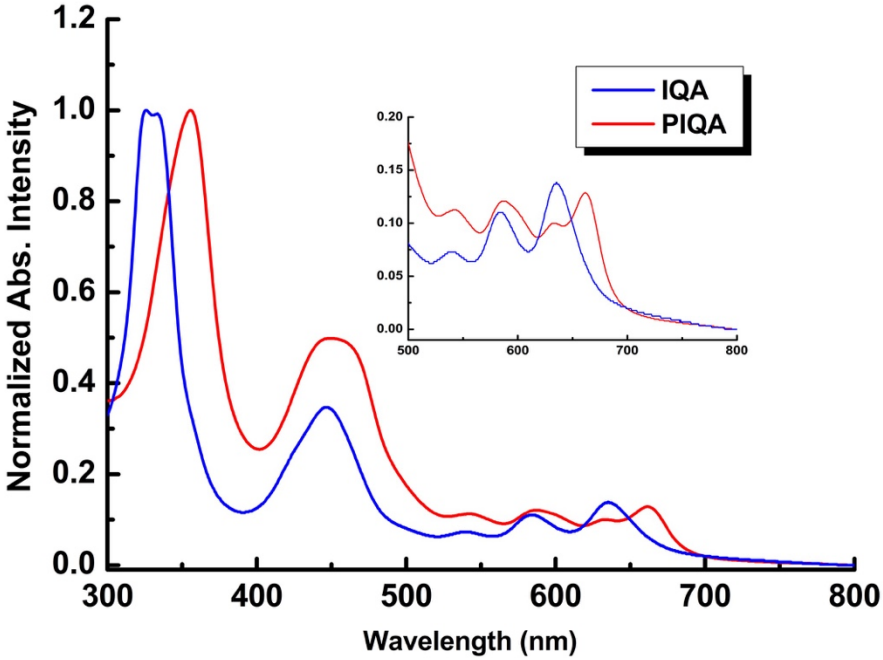

Figure 10. UV-vis spectra of IQA and PIQA in MSA. Reprinted with permission from [78].

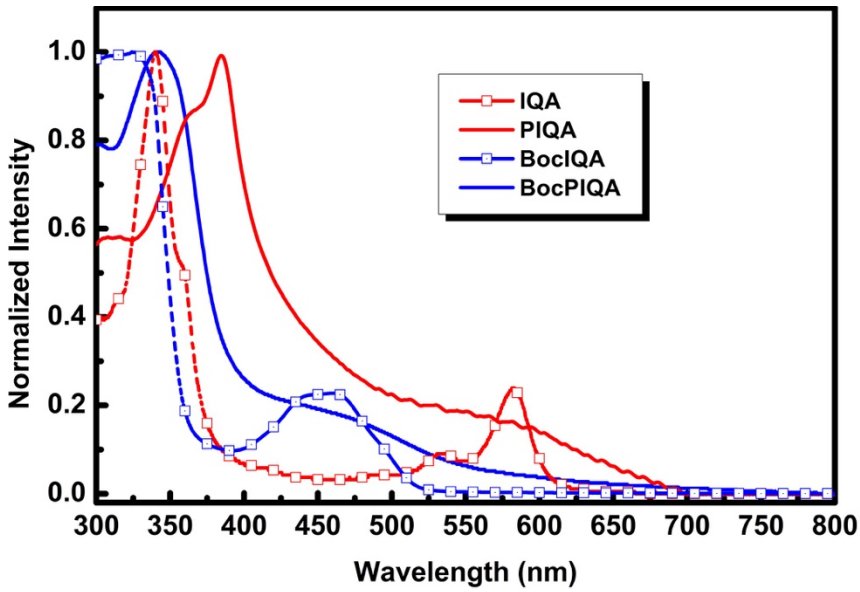

Figure 11. UV-vis spectra of IQA, BocIQA, PIQA, and BocPIQA in thin film. Reprinted with permission from [78].

In order to further correlate the characterization data of **BocPIQA** with **PIQA**, it was also essential to demonstrate that **BocPIQA** could be converted back to **PIQA** completely after the anticipated thermal treatment (**Figure 12a**). We first performed thermogravimetric analysis (TGA) of **BocPIQA** to demonstrate a weight loss at 160−200 °C (**Figure 12b**), representing the Boc cleavage process.[94] This phenomenon was similar to that of **BocIQA**, and the 22% weight loss agreed well with the theoretical weight percentage of Boc groups in **BocPIQA** (23%). One of the anticipated properties of sp^2 ladder polymers was high thermal stability, considering the thermodynamically stable nature of carbon materials like graphene and carbon nanotubes.[95] TGA of **PIQA** (**Figure 12b**) demonstrated the remarkably higher thermal stability of ladder polymer over conventional polymers in terms of both decomposition temperature (T_d) and carbonization yield. For example, before ring-cyclization, **P2** showed a T_d at 315 °C with carbonization yield of 32% at 800 °C. In contrast, **PIQA** showed an elevated T_d at 370 °C. The weight loss at 370 °C was attributed to the decomposition of the sp^3 dodecyl side-chains. The conjugated, fused-ring sp^2 backbone, however, remained the weight at temperatures as high as 800 °C. The carbonization yield of 50% at this temperature was much higher than that of **P2**, and agreed well with the theoretical sp^2 backbone weight (49%). The results clearly demonstrated that **BocPIQA** possesses both thermal-cleavable side chains and a backbone with good thermal stability, allowing for further applications under harsh thermal treatment conditions.

Furthermore, FT-IR was employed to characterize the chemical structure before and after the thermal cleavage. Compared to that of **PIQA**, the FT-IR spectrum of

BocPIQA showed (**Figure 12c**) additional C=O stretching at 1758 cm^{-1} corresponding to the Boc group, and absence of N–H stretching at 3100~3500 cm^{-1}. After thermal annealing of **BocPIQA**, the FT-IR spectrum became identical to the original spectrum of **PIQA**, clearly demonstrating the fully recovered structure of **PIQA** from **BocPIQA**.

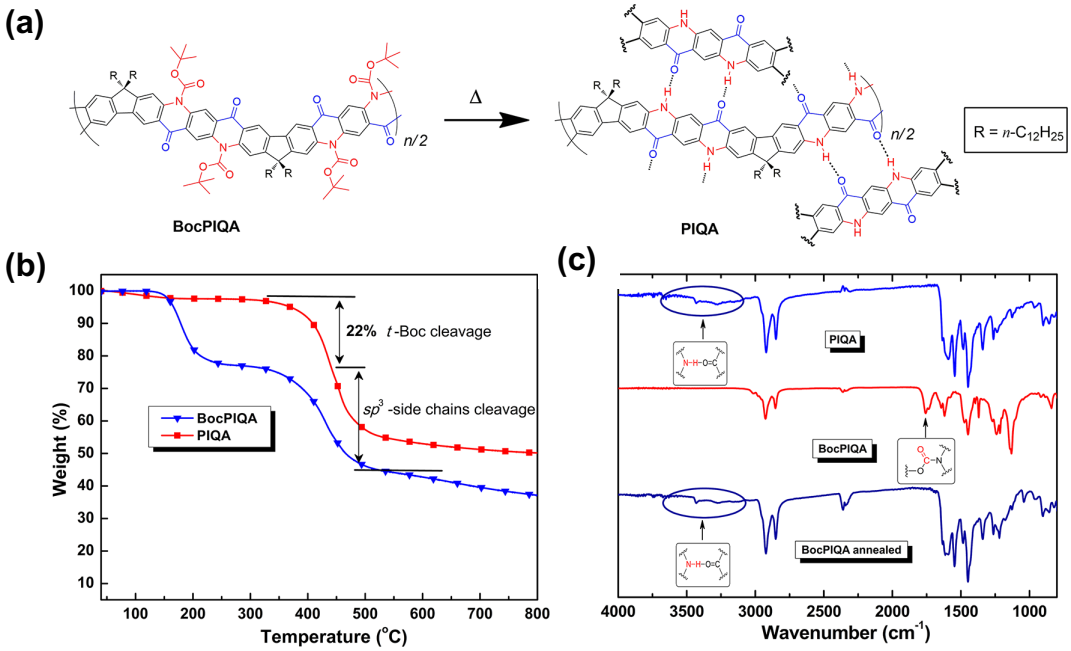

Figure 12. (a) Schematic representation of Boc cleavage of BocPIQA by thermal annealing in the solid state, regenerating PIQA with intermolecular H-bonds; (b) TGA curves of PIQA and BocPIQA showing key weight losses and carbonizations yields at 800°C; (c) FT-IR spectra of PIQA, and BocPIQA before and after thermal annealing. Reprinted with permission from [78].

Cleavage of the Boc groups was also observed by UV-vis absorption and fluorescence emission spectroscopy. The solid-state UV-vis spectrum of **BocPIQA**, after annealing at 200 °C for 30 min showed an identical absorption spectrum as that of **PIQA** (**Figure 13**), while its strong fluorescence was quenched due to aggregation (**Figure 14**).

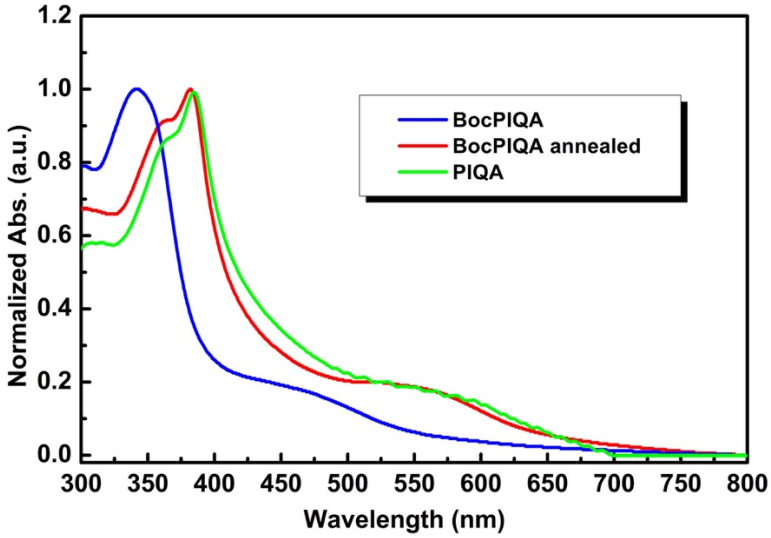

Figure 13. UV-vis absorption spectra of BocPIQA thin film before and after thermal annealing at 200 ˚C for 30 min. Reprinted with permission from [78].

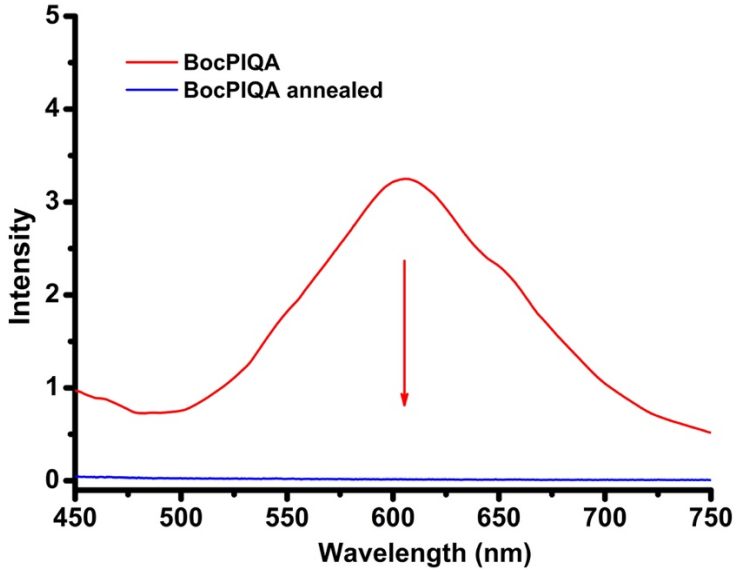

Figure 14. Fluorescence emission spectra of BocPIQA before and after thermal annealing at 200 ˚C for 30 min. Excitation wavelength was 440 nm. Reprinted with permission from [78].

2.4 Thin Film Processing and Solvent Resistance Test

Processability is vital for almost all the applications of polymers. Thanks to the excellent solubility of **BocPIQA** and its efficient regeneration back to **PIQA**, thin films of this H-bonded ladder polymer can be easily processed through spin-coating **BocPIQA,** followed by thermal Boc cleavage (**Figure 15a**). To the best of our knowledge, this approach represents the first example of solution processed thin films of an insoluble, rigid ladder polymer in common organic solvents. Uniform films of **BocPIQA** with thickness of 83 and 125 nm on silicon wafer substrates were prepared by spin-casting from chlorobenzene solution, at spin speeds of 1000 and 600 rpm, respectively. Under atomic force microscopy (AFM), both films showed smooth surface morphology with root-mean-square (RMS) roughness of around 0.35 nm. To regenerate the H-bonded **PIQA** thin films, they were annealed at 180 °C for 30 min. Both films were found to remain smooth and uniform (RMS ~ 0.41 nm), with a moderate decrease in the thickness to 62 nm and 90 nm, respectively (**Figure 15a, 21**). This thickness decrease was attributed to the loss of Boc groups and a resulting tighter solid-state packing promoted by the regenerated H-bonds. Grazing incidence X-ray diffraction (GIXRD) was employed to examine the nanostructure of the polymer thin films of **BocPIQA** before and after thermal annealing (**Figure 15c, 19**). Two characteristic peaks were observed for both as-cast and annealed samples. The peak at q~ 0.30 A^{-1}corresponded to the scattering of dodecyl chains on fluorene moieties and did not shift before and after thermal annealing. The $\pi-\pi$ stacking scattering of the backbone, however, shifted significantly from 1.35 A^{-1} to 1.47A^{-1} after converting **BocPIQA** into **PIQA**, corresponding to a decrease of the $\pi-\pi$ distance from 4.65Å for

BocPIQA to 4.27Å of **PIQA**. This change agreed with the thickness decrease, as a result of the removal of bulky Boc groups.[96]

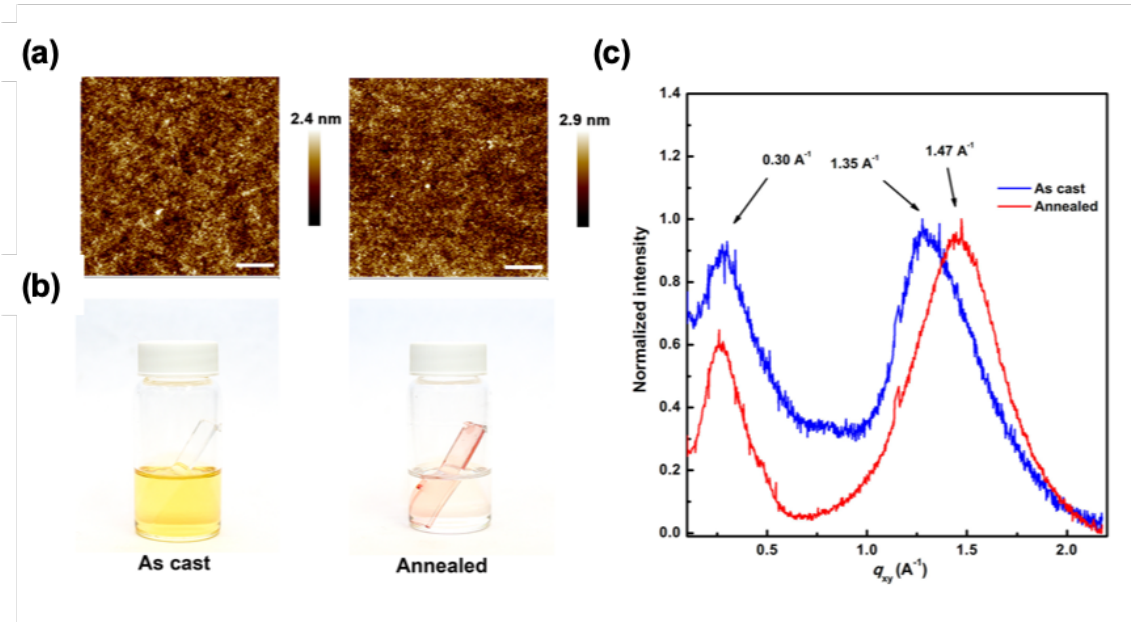

Figure 15. (a) AFM height profile images of a BocPIQA thin film on silicon wafer (left) before and (right) after (right) thermal annealing; (b) Photographic image of the result after soaking the (left) as cast and the (right) annealed thin films on glass slide into chlorobenzene; (c) GIXRD of the as cast and annealed thin films. Reprinted with permission from [78].

Because of the stability and low solubility of **PIQA**, its thin films were expected to be solvent and heat resistant. The annealed films, indeed, remained intact against a wide variety of aggressive solvents at a high temperature, except for concentrated H_2SO_4 and MSA (**Figure 16**). Solvent resistance tests were performed by soaking annealed **PIQA** thin films (with thickness of ~ 105 nm) on glass substrates into varies solvents for 30 min. UV-vis absorption spectroscopy and AFM measurements were performed after solvent treatments to evaluate the integrity of these thin films. It was found that they remained

intact in most of the hot organic solvents and acid solutions, including boiling THF, chloroform, chlorobenzene, 13 M HCl aqueous solution, ethyl acetate, and hexane. No significant change was found in the UV-vis spectra either after soaking (**Figure 17**). Moreover, as revealed by AFM, the film thickness and morphology remained the same, with thickness of 105 ± 5 nm and RMS ~ 0.5 nm (**Figure 16**, **Table 1**). No solvent swelling induced thickness increase was observed, indicating an extremely tight intermolecular interaction between **PIQA** chains in the thin film state. The only exceptions were observed when soaking the thin films into very aggressive boiling DMSO, room temperature H_2SO_4, or MSA. A partial degradation/dissolvation took place in boiling DMSO or in room temperature H_2SO_4. MSA was the only solvent that can fully dissolve the thin film at room temperature. Overall, the H-bonded ladder polymer **PIQA** demonstrated excellent resistance to aggressive solvents in the thin film state.

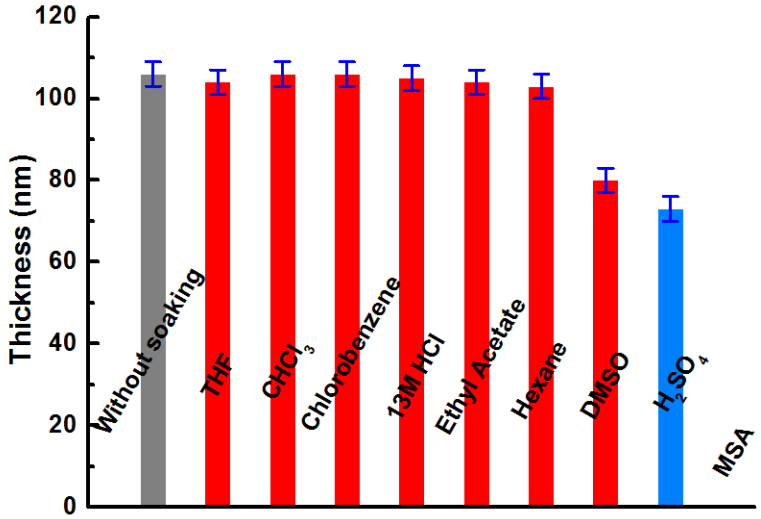

Figure 16. Thickness of annealed BocPIQA film after soaking in different solvents for 30 minutes. The red bars represent boiling solvents/solutions, while the blue bars represent treatment at room temperature. Reprinted with permission from [78].

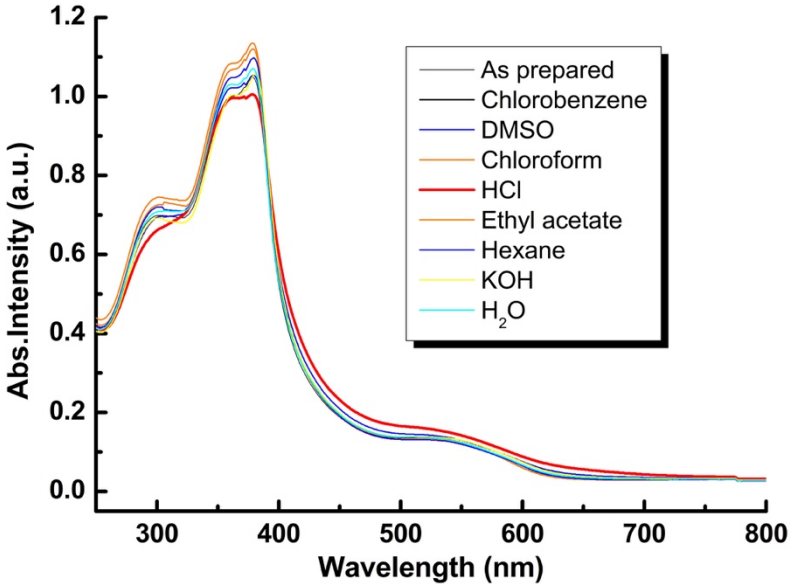

Figure 17. UV-vis absorption spectra of annealed BocPIQA film after soaked in different solvents. Reprinted with permission from [78].

In addition, **BocPIQA** was anticipated to be a precursor for carbon-based materials since all the soluble side chains can be cleaved at high temperature as demonstrated by TGA, leaving the graphitic *sp2*-carbon backbone, which may be further aligned by multiple intermolecular H-bonds. Temperature-dependent conductivity measurement was performed to investigate the effect of heat treatment on **BocPIQA**'s electrical conductivity. **BocPIQA** was found to be an insulator at room temperature, while the DC conductivity was slightly increased after annealing at 200 °C (cleaving Boc) and 500 °C (cleaving the alkyl chains). After further annealing 700 °C, **BocPIQA** was found to became conductive with conductivity of 5.45×10^{-4} S/cm. Raman spectra was selected to explore the origin of the conductivity enhancement, the sample carbonized at 700 °C showed an enhancement characteristic peak at 1754 cm^{-1} known as G band, indicating a regulated graphitic sp^2 structure after heating (**Figure 18**). This result clearly demonstrated

the ladder polymer's future application as a processable, fused ring precursor for high performance, graphitic carbon-based materials.[97, 98]

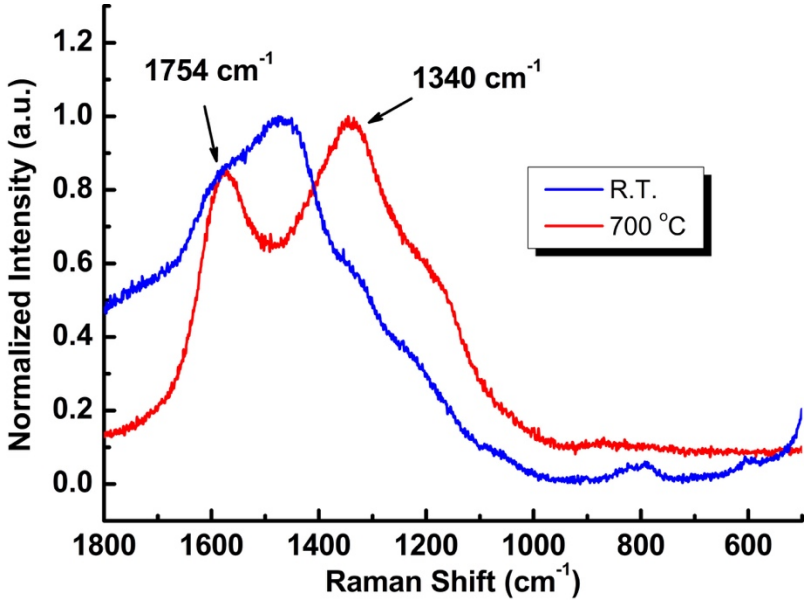

Figure 18. Raman spectra of as cast and annealed (700 ˚C) BocPIQA films. Reprinted with permission from [78].

2.5 Conclusion

In summary, we present here **PIQA –** a unique class of polymeric material with self-complementary H-bonds incorporated into ladder-type repeating units. The synthetic approach to **PIQA** requires only 3 steps with a high overall yield of 66%. Feasible gram-scale preparation has been demonstrated. No noble metal reagent or catalyst is involved in the synthesis. Clear solution-phase characterization and solution-processing of this polymer were achieved through a reversible post-functionalization strategy. This approach enabled concentration-demanding methods such as ^{13}C NMR spectroscopy for structure elucidation. Furthermore, it imparts solution processability to such a highly challenging

material through a processing-followed-by-annealing approach, enabling not only thin film casting that is demonstrated here, but also potential solution processing techniques such as printing and electrospinning, *etc*.

PIQA features of backbone rigidity and strong intermolecular H-bonds are integrated to render its excellent thermal stability and chemical/solvent resistance in the solid state. In particular, the stability against aggressive solvents at high temperature allows the polymer film to be used as protective coating materials for harsh environments, or employed in applications involving extreme operation conditions or multiple steps of solution-processing/etching/development. Moreover, with the thermal labile side-chain and thermal stable all-fused aromatic backbone, after annealing at 700 ºC, a characteristic G-band was observed in Raman spectra. The insulate **BocPIQA** becomes conductive, demonstrating its potential to be a precursor for carbon materials. Our synthetic approach opens up the possibility of design and large-scale production of highly rigid, strongly self-associated macromolecules possessing unprecedented properties. Its unique properties allow for the possibility of functional ladder polymers for various applications.

2.6 Experimental Details

2.6.1 General Methods

All starting materials were obtained from commercial suppliers and were used without further purification. DMSS was recrystallized from toluene before polymerization. Reaction solvents were purified by solvent purification system prior to use. 2,7-Diamino-9,9-didodecylfluorene[99] and compound **IQA**[79]were prepared according

to the literature. ^{1}H, ^{13}C, ^{1}H-^{1}H COSY, NOESY, HSQC, and HMBC NMR spectra were obtained on a Varian Inova 500 MHz spectrometer at room temperature. Chemical shifts were reported in ppm relative to the signals corresponding to the residual non-deuterated solvents ($CDCl_3$: δ = 7.26 ppm, d_8-THF: δ = 3.58 ppm for ^{1}H, and $CDCl_3$: δ = 77.16 ppm, d_8-THF: δ = 67.67 ppm for ^{13}C at 298 K). SEC was performed on a TOSOH EcoSEC (HLC-8320GPC) chromatograph at 40° C with THF as the eluent. The molecular weights were calculated using a calibration curve based on polystyrene standards. The SEC columns were TSK gel SuperHM-M and TSK gel SuperH-RC. TGA was taken with a TAQ500 thermogravimetric analyzer. UV-vis absorption spectra were recorded using a Shimadzu UV-2600 UV-vis spectrophotometer, while the fluorescent spectra were measured on Horiba Fluoromax-4. FT-IR spectra were recorded with ZnSe ATR using Shimadzu IRAffinity-1S.

2.6.2 Synthesis

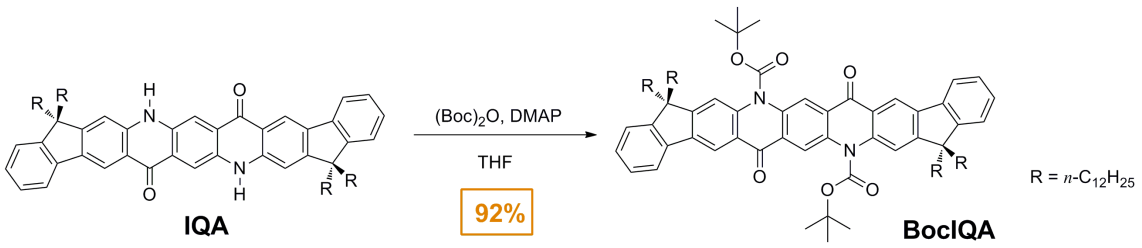

Synthesis of BocIQA: To a solution of **IQA** (1.00 g, 0.86 mmol) and DMAP (0.21 g, 1.72 mmol) in 20 mL anhydrous THF at room temperature under N_2 protection, di-*tert*-butyl dicarbonate (0.47 g, 2.15 mmol) in 10 mL anhydrous THF was added slowly. The reaction was carried out at room temperature for overnight. The yellow solution was then poured into water, extracted with dichloromethane (3 × 15 mL). The organic layers were

combined and dried with anhydrous $MgSO_4$. After removing the solvent under reduced pressure, the residue was purified by column chromatography (SiO_2, CH_2Cl_2/hexane: v/v = 1/4) to obtain a yellow powder (0.94 g, 80%).^{1}H NMR (500 MHz, $CDCl_3$, 298 K, ppm) δ = 8.81 (s, 2H), 8.70 (s, 2H), 7.84-7.82 (m, 2H), 7.75 (s, 2H), 7.40-7.35 (m, 6H), 2.05-2.01 (m, 8H), 1.78 (s, 18H),1.23-1.04 (m, 72H), 0.85-0.82 (m, 12H), 0.67 (br, 8H). ^{13}C NMR (125 MHz, $CDCl_3$, 298 K, ppm) δ = 178.86, 158.08, 151.86, 150.29, 139.88, 139.69, 137.83, 134.94, 127.92, 127.43, 126.47, 122.99, 122.56, 120.45, 117.59, 117.49, 113.25, 86.33, 55.96, 40.93, 31.98, 30.10, 29.68, 29.63, 29.41, 29.35, 28.00, 27.96, 23.98, 22.76, 14.17.

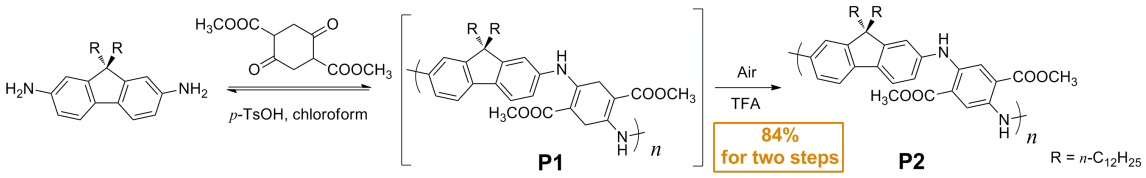

Synthesis of P2: 2,7- Diamino-9,9-didodecylfluorene (1.17g, 2.20 mmol), DMSS (502 mg, 2.20 mmol) and PTSA·H_2O (76 mg, 0.44 mmol) were dissolved in 14 mL of dry chloroform in a 100 mL Schlenk tube and degassed with freeze-pump-thaw for 3 times. The tube was then sealed and heated to 95 ºC for 72 h to form a viscous orange mixture. The reaction mixture was then cooled to room temperature. After quenching the reaction with 20 mL solution of triethylamine/THF (v/v = 1/10), the solvent was removed under reduced pressure. The resulting orange solid was dissolved in 100 mL THF, and 0.1 mL of TFA was added. The orange solution was stirred in air at 50 ºC for 24 h and the color changed to deep-red. After removing the solvent under reduced pressure, the resulting solid was transferred to a Soxhlet extractor and extracted with acetone for 24 h to obtain

the product as a deep-red solid (1.37 g, 86%). ^{1}H NMR (500 MHz, $CDCl_3$, 298 K, ppm) δ = 8.96 (s, 2H), 8.09 (s, 2H), 7.60-7.59 (m, 2H), 7.19-7.17 (m, 4H), 3.89 (s, 6H), 1.97-1.67 (m, 4H), 1.20-1.11 (m, 36H), 0.84-0.77 (m, 10H). ^{13}C NMR (125 MHz, $CDCl_3$, 298 K, ppm) δ = 168.28, 152.16, 140.41, 138.19, 135.84, 119.83, 118.97, 118.58, 118.24, 114.87, 55.22, 52.41, 40.81, 32.04, 30.52, 29.89, 29.76, 29.62, 29.46, 24.14, 22.82, 14.25. SEC analysis: M_n = 24.0 kg/mol, $Đ$ = 2.3.

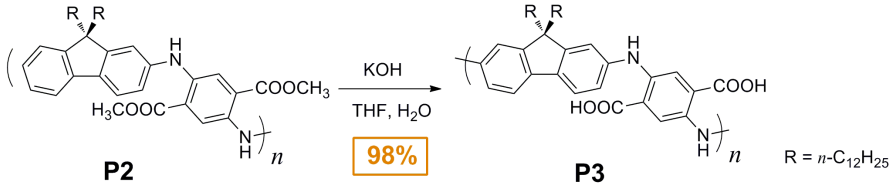

Synthesis of P3: **P2** (1.50 g), KOH (2.00 g, 36 mmol), THF (40 mL), methanol (20 mL) and H_2O (20 mL) were mixed in a 250 mL flask and degassed with N_2. The mixture was heated to 80 ºC for 24 h. After cooling to room temperature, the deep-green solution was transferred to a beaker in ice water bath and acidified drop-wise with 2 M HCl. The resulting purple solid was collected by filtration, and washed with acetone and chloroform (3 × 10 mL). The product was obtained as a deep-violet solid after drying (1.41 g, 98%). ^{1}H NMR (500 MHz, d_8-THF, 298 K, ppm) δ = 9.32 (s, 2H), 8.20 (s, 2H), 7.59-7.57 (m, 2H), 7.28 (s, 2H), 7.14-7.13 (m, 2H), 2.00 (br, 4H), 1.22-1.13 (m, 36H), 0.86-0.79 (m, 10H). ^{13}C NMR (125 MHz, d_8-THF, 298 K, ppm) δ = 169.12, 151.68, 140.50, 137.97, 135.60, 119.47, 118.44, 118.32, 118.07, 113.72, 54.94, 40.58, 31.88, 29.63, 29.61, 29.43, 29.31, 22.57, 13.50.

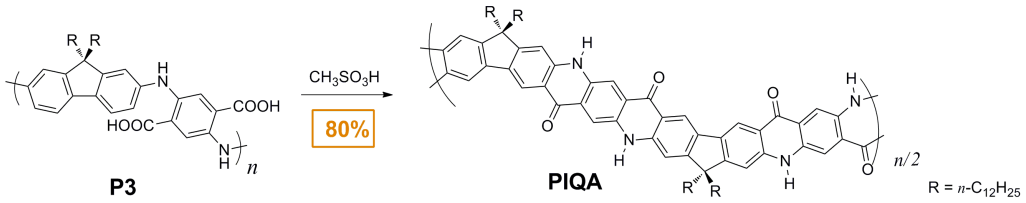

Synthesis of PIQA: **P3** (1.00 g) was mixed with fresh MSA (20 mL) and degassed with N_2. Then the mixture was heated to 130 ºC for 48 h. After cooling to room temperature, the reaction mixture was poured into ice water and the solid was collected by filtration. The solid was transferred to Soxhlet extractor and extracted with THF for 24 h to obtain **PIQA** as a black solid (0.76 g, 80%). NMR spectra were not obtained due to extreme poor solubility. FT-IR (KBr, cm^{-1}) ν = 3423, 2913, 2852, 1593, 1545, 1447, 1341, 1254, 889.

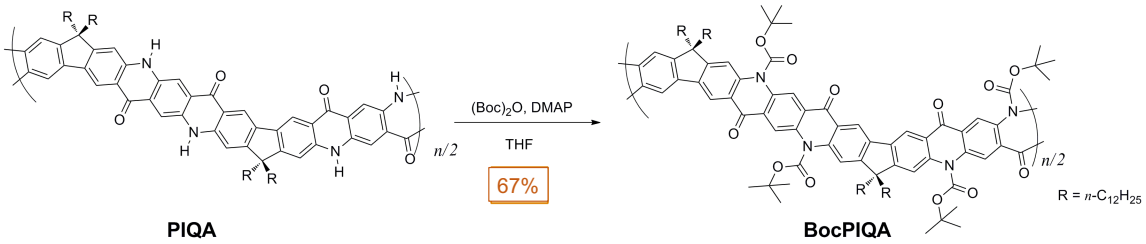

Synthesis of BocPIQA: **PIQA** (0.50 g), di-*tert*-butyl dicarbonate (1 mL), DMAP (100 mg) were mixed in 20 mL dry THF and stirred at room temperature for 72 h. The reaction mixture was then filtered. After removing the solvent of the filtrates under reduced pressure, the resulting solid was washed with acetone and dried under vacuum. Product was obtained as a brown solid (0.36 g, 67%). ^{1}H NMR (500 MHz, d_8-THF, 298 K, ppm) δ = 8.89-8.86 (br, 8H), 8.02-7.92 (br, 4H), 2.23-2.13 (br, 8H), 1.77 (s, 36H), 1,17-1.15 (br, 72H), 0.81-0.80 (br, 20H). ^{13}C NMR (125 MHz, $CDCl_3$, 298 K, ppm) δ = 178.69, 157.24, 151.78, 140.30, 136.26, 135.12, 126.70, 123.21, 118.49, 117.94, 113.62, 86.52, 82.56,

56.72, 56.05, 41.34, 31.96, 30.06, 29.69, 29.66, 29.63, 29.39, 28.01, 24.12, 22.75, 14.18. SEC analysis: M_n = 14.0 kg/mol, $Đ$ = 2.3.

2.6.3 Thin Film Processing and Characterization

BocPIQA solutions in chlorobenzene (20 mg/mL) were added to a UV-Ozone cleaned silicon wafer. **BocPIQA** thin films were formed by spin-coating with the condition of 600 or 1000 rpm for 7s then 2000 rpm for 13 s. After casting, the films were thermally annealed at 180 ºC for 0.5 h inside a glovebox to remove the Boc groups. The film morphology before and after thermal annealing was examined by optical microscope and AFM. AFM images were recorded with Bruker Dimension S4 Icon AFM in a tapping mode and processed using NanoScope Analysis. GIXRD measurements were carried out on Sector 8-ID-E at the Advanced Photon Source, Argonne National Laboratory. Beamline 8-ID-E operates at an energy of 7.35 keV and images were collected from a Pilatus 1MF camera (Dectris), with two exposures for different vertical positions of the detector. Using the GIXSGUI package2 for Matlab (Mathworks), data were corrected for X-ray polarization, detector sensitivity and geometrical solid-angle. The beam size was 200 μm (h) × 20 μm (v). Sample detector distance was 204 mm. Sample measurement and thermal annealing were carried out under vacuum which was in the range of $2 \sim 3 \times 10^{-6}$ bar, with the sample stage interfaced with a Lakeshore 340 unit.

2.7 Appendix

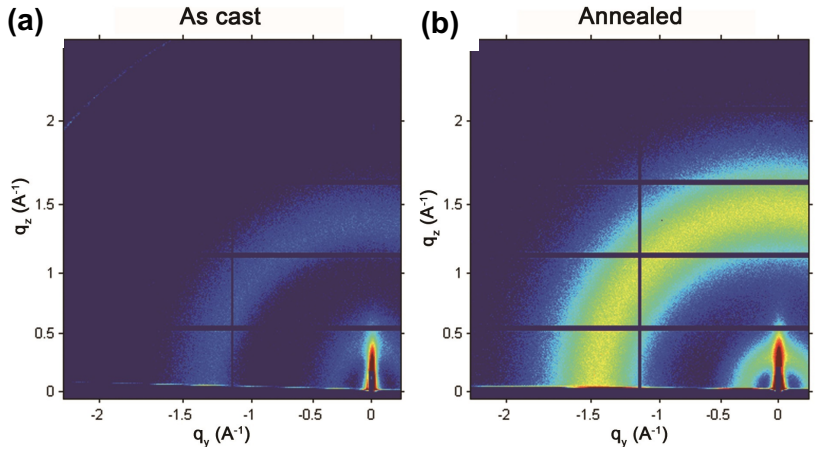

Figure 19. 2D-GIXRD patterns of a BocPIQA film before and after thermal annealing. Reprinted with permission from [78].

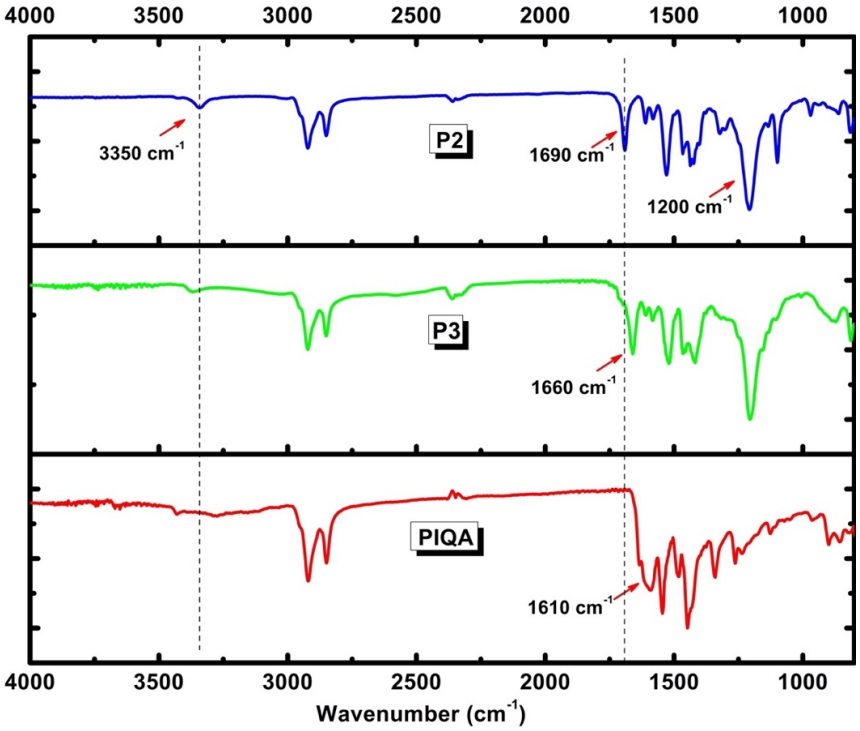

Figure 20. FT-IR Spectra of P2, P3, and as-synthesized PIQA. Reprinted with permission from [78].

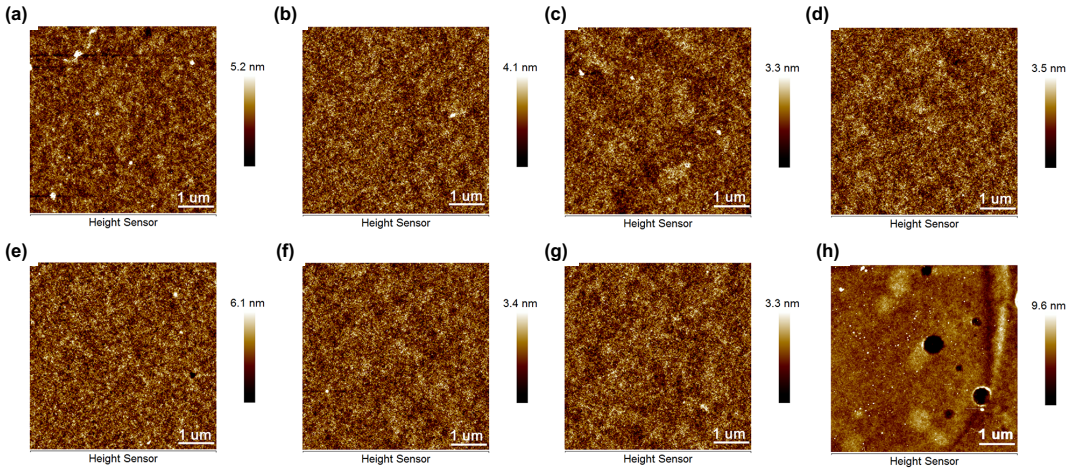

Figure 21. AFM high profile images of annealed BocPIQA film after being soaked in boiling solvent. (a) THF, (b) $CHCl_3$, (c) 13 M HCl, (d) chlorobenzene, (e) DMSO, (f) hexane, (g) ethyl acetate, (h) H_2SO_4. Reprinted with permission from [78].

Table 1. Thickness and RMS data of as cast and annealed BocPIQA films after soaked in boiling solvents. Reprinted with permission from [78].

	As cast	THF	$CHCl_3$	13 M HCl	Chlorobenzene	Hexane	Ethyl acetate	H_2SO_4
Thickness (nm)	106±3	104±3	106±3	106±3	105±3	104±3	104±3	73±3
RMS (nm)	0.466	0.798	0.593	0.485	0.499	0.500	0.489	1.270

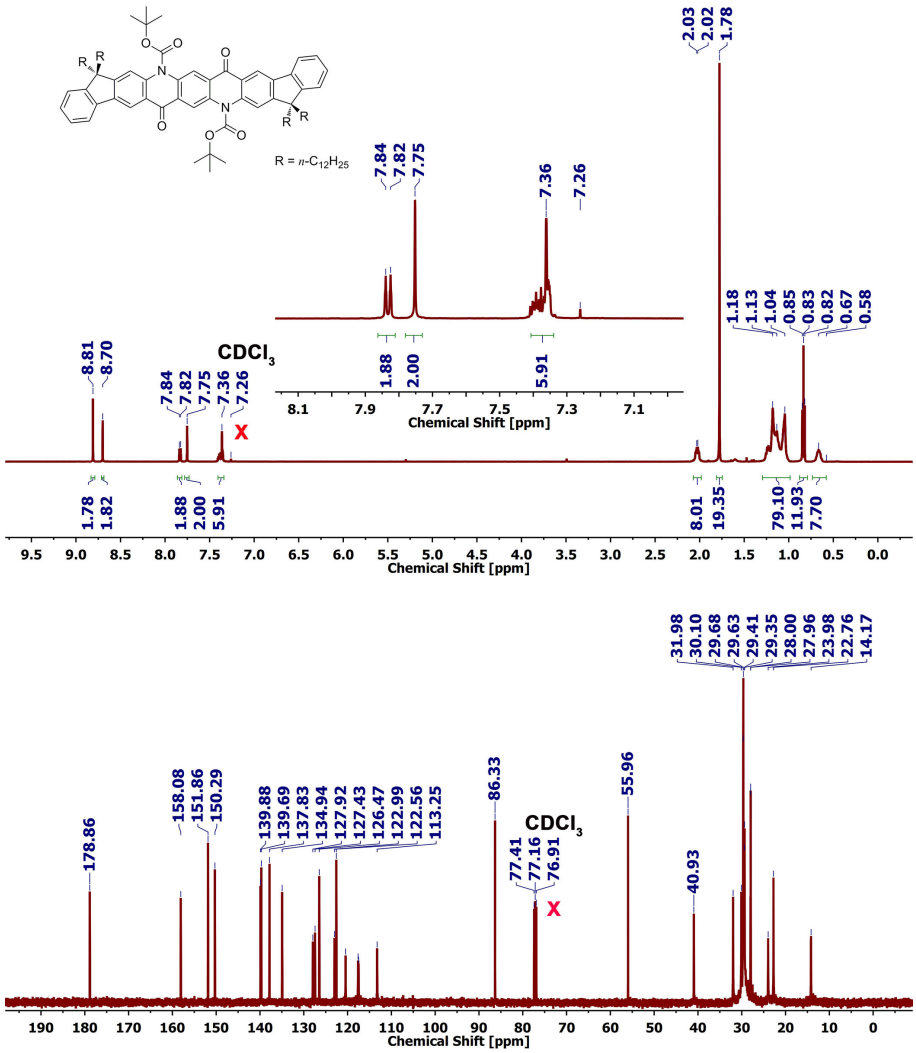

Figure 22. ^{1}H (500 MHz) and ^{13}C (125 MHz) NMR of BocIQA in $CDCl_3$ at 298 K. Reprinted with permission from [78].

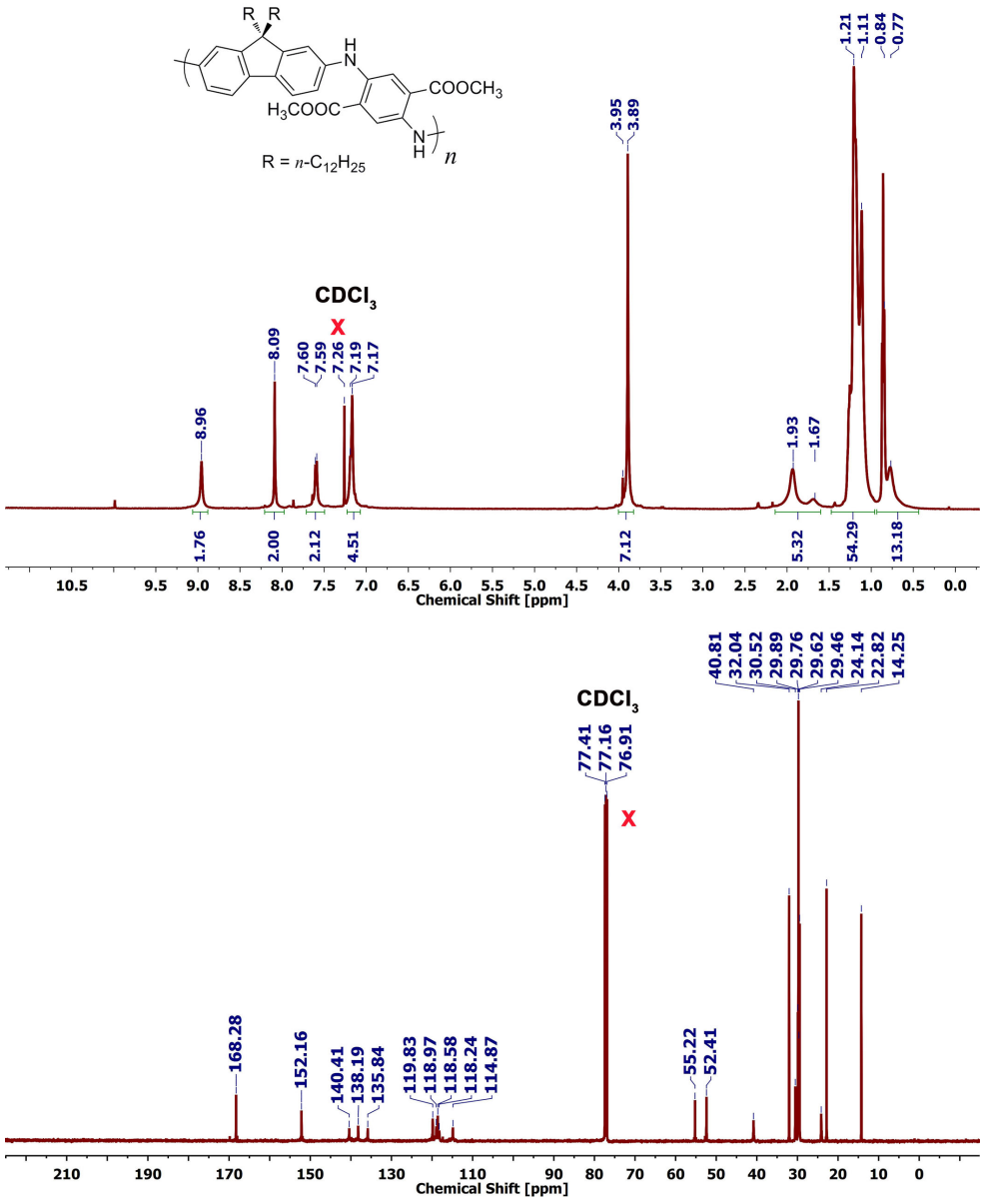

Figure 23. ^{1}H (500 MHz) and ^{13}C (125 MHz) NMR of P2 in $CDCl_3$ at 298 K. Reprinted with permission from [78].

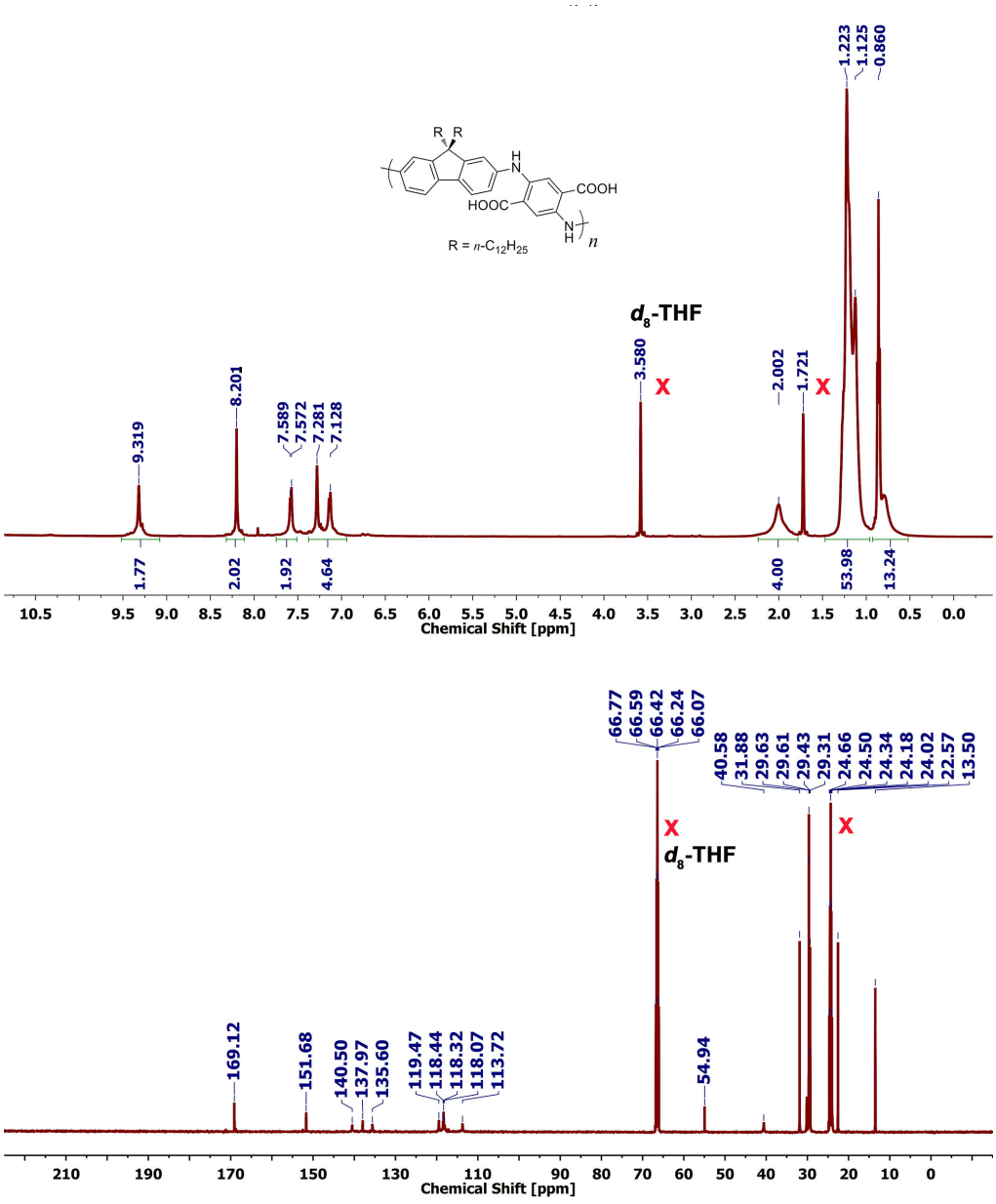

Figure 24. ^{1}H (500 MHz) and ^{13}C (125 MHz) NMR of P3 in d_8-THF at 298 K. Reprinted with permission from [78].

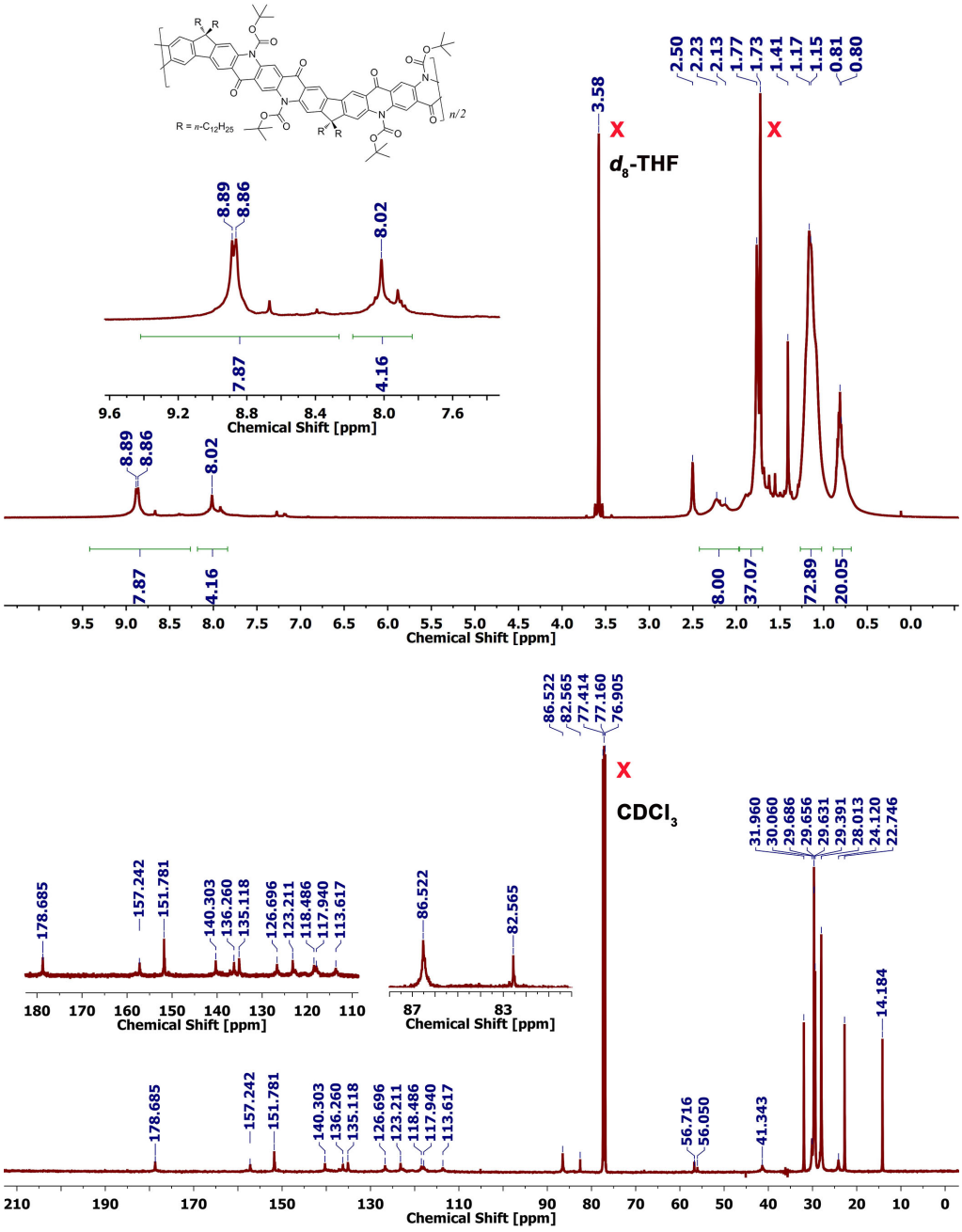

Figure 25. ^{1}H NMR (500 MHz) of BocPIQA in d_8-THF and ^{13}C NMR (125 MHz) of BocPIQA in $CDCl_3$ at 298 K. Reprinted with permission from [78].

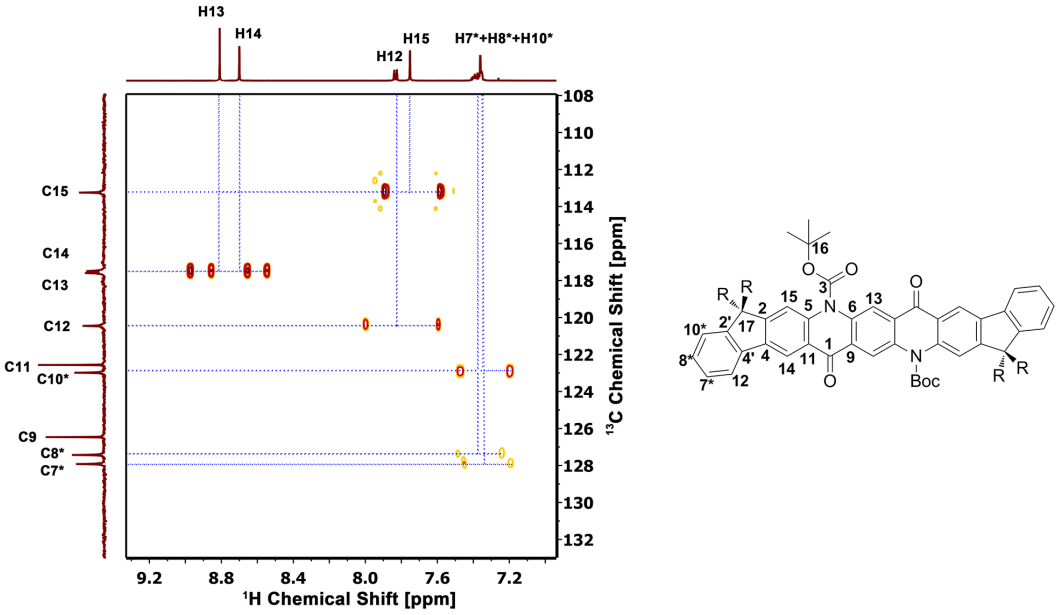

Figure 26. ^{1}H-^{13}C HSQC spectrum (without decoupling) of BocIQA in $CDCl_3$ at 298 K. Reprinted with permission from [78].

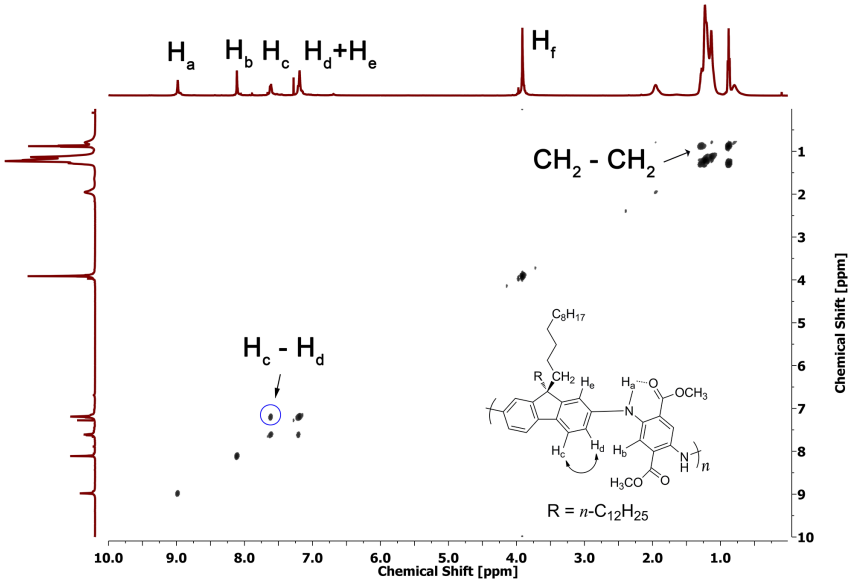

Figure 27. ^{1}H -^{1}H COSY NMR spectrum of P2 in $CDCl_3$ at 298 K. Reprinted with permission from [78].

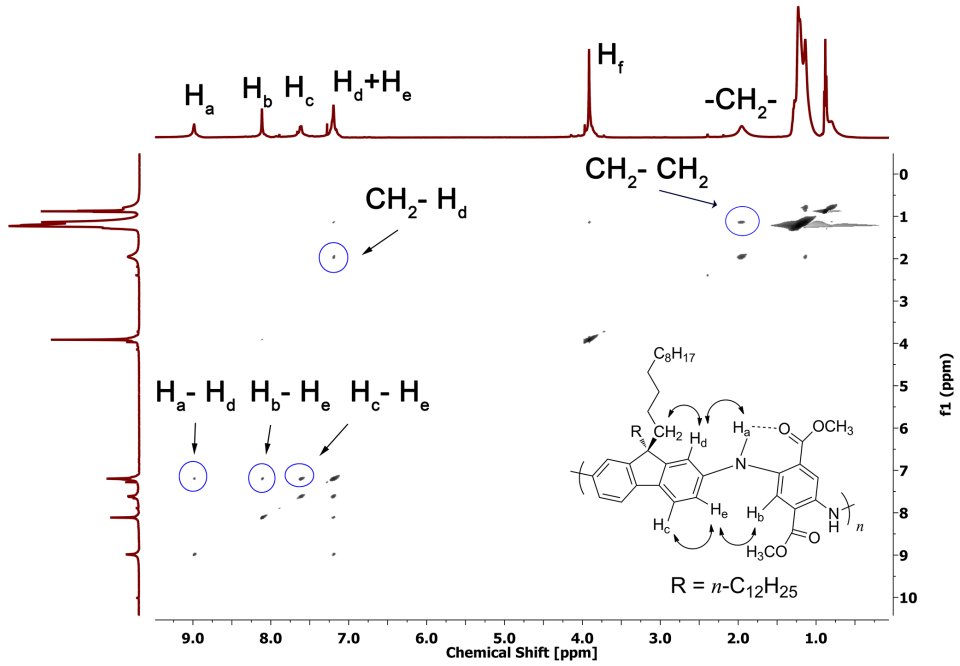

Figure 28. ^{1}H -^{1}H NOESY NMR spectrum of P2 in $CDCl_3$ at 298 K. Reprinted with permission from [78].

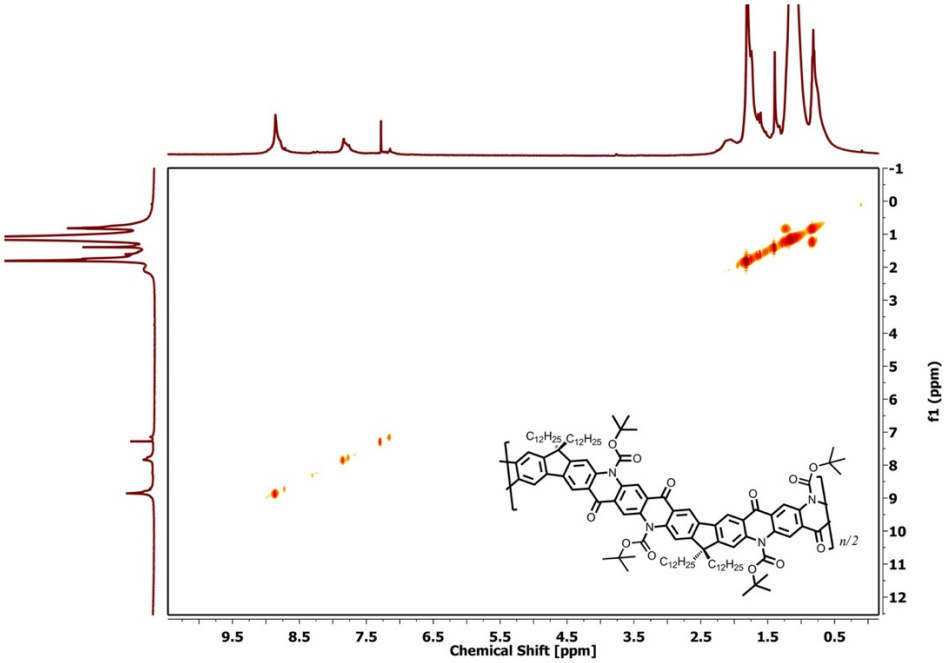

Figure 29. ^{1}H -^{1}H COSY spectrum of BocPIQA in $CDCl_3$ at 298 K. Reprinted with permission from [78].

CHAPTER III

QUINOIDAL LADDER-TYPE PERNIGRANILINE OLIGOMERS*

3.1 Introduction

Polyaniline (PANI) derivatives represent one of the most widely used classes of conductive polymers, applied in a great variety of fields, such as anticorrosive coatings,[100] energy storage systems,[101-103] and electrochromic devices,[104, 105] among others. In addition, their intriguing multi-stage redox chemistry, doping processes, and magnetic properties have been the subject of fundamental research for decades.[106-112] PANI properties are determined by the oxidation and protonation levels (**Figure 30**). The fully-reduced leucoemeraldine base, half-oxidized emeraldine base, and fully-oxidized pernigraniline base states are all insulating materials. High conductivity is achieved by oxidative-doping of leucoemeraldine base, or acid-doping of emeraldine base, affording emeraldine salt which possesses both aromatic resonance with polarons and the quinoidal resonance with bipolarons.[106] Both forms can serve as charge carriers while polaron species are believed to possess higher mobility. In previous reports, emeraldine salt exhibits both Curie paramagnetism and Pauli paramagnetism.[113] While the fully-oxidized and protonated counterpart, the pernigraniline salt, was hypothesized to possess dominant bipolaron resonance due to a strong Coulombic repulsion,[114, 115] and to act as insulators because of

---

*Reprinted (adapted) with permission from "Pauli Paramagnetism of Stable Analogues of Pernigraniline Salt Featuring Ladder-Type Constitution" Ji, X.; Xie, H.; Zhu, C.; Zou, Y.; Mu, A. U.; Al-Hashimi, M.; Dunbar, K. R.; Fang, L. *J. Am. Chem. Soc.* **2020**, *142*(1), 641. Copyright 2020 American Chemical Society.

the strong localization of the bipolarons.[116] Recently *in situ* electrochemical conductivity measurements on stabilized pernigraniline salt, however, indicated[117] that it may be intrinsically conductive. Unfortunately, in-depth and rigorous investigation of pernigraniline salt is severely limited to date.[118-121] Firstly, pernigraniline salt suffers from poor stability as they readily degrade through hydrolysis[119], reduction[118, 122-124], and conjugated addition[125] under ambient conditions. Efforts have been made in stabilizing them by chemical modification[116] or protection, which have met with limited success.[117, 126, 127] Secondly, the uncontrollable *cis*/*trans* isomerization of the iminium bonds[128] and the torsional rotation of the backbone give rise to structural complexity of pernigraniline salt and discrepant results of their reported properties.[111, 116, 117, 119]

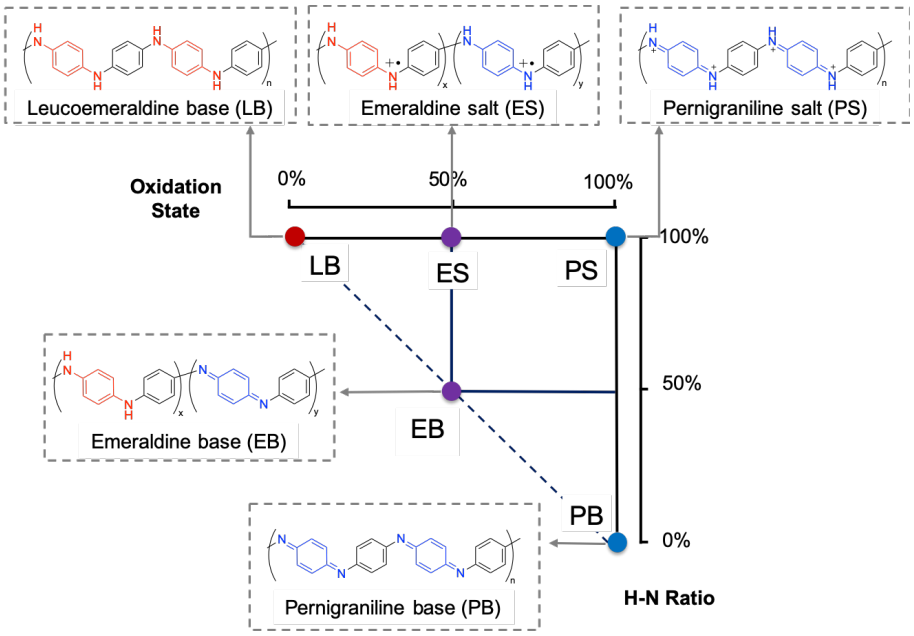

Figure 30. Formulas and names of PANI at various oxidation and protonation (H-N ratio) levels.

In this context, there is an urgent demand to solve the stability and isomerization issues before further fundamental investigations and practical applications of pernigraniline salt derivatives can be conducted rigorously and extensively. Herein, we report a strategy to address these issues simultaneously by implementing a ladder-type constitution in analogues of pernigraniline salts. A series of oligomeric, ladder-type analogues were synthesized, comprehensively investigated, and compared to a non-ladder-type control compound, the results of which revealed enhanced stability and unexpected Pauli paramagnetism produced by the ladder-type constitution.

3.2 Molecular Design

In this work, a series of ladder-type pernigraniline oligomers – **Q1** ~ **Q4** (**Figure 31**) rather than polymers, were selected as the subjects of investigation in order to circumvent issues associated with ladder polymers, such as polydispersity, structural defects, and limited solubility.[16, 32, 129-133] In addition, the series of ladder oligomers with well-defined structures and variable sizes allow for the study of precise property evolution from a small molecule to a polymer. **Q1** ~ **Q4** were designed based on the structure of quinonediimine, wherein **Qn** contains *n* quinonediimine units. Bridging dimethylmethene units were installed to fuse the neighboring units into a rigid coplanar ladder-type constitution while fixing the imine bond into a *trans*-configuration. In order to ensure good solubility, fluorene units with two hexyl groups installed at the 9-position were incorporated into the backbone as the aromatic unit to prohibit overly strong intermolecular π-π stacking. A control compound **NLQ** was designed as a non-ladder-type

analogue which resembles the constitutional structure of **Q1** except for the lack of the dimethylmethene bridge.

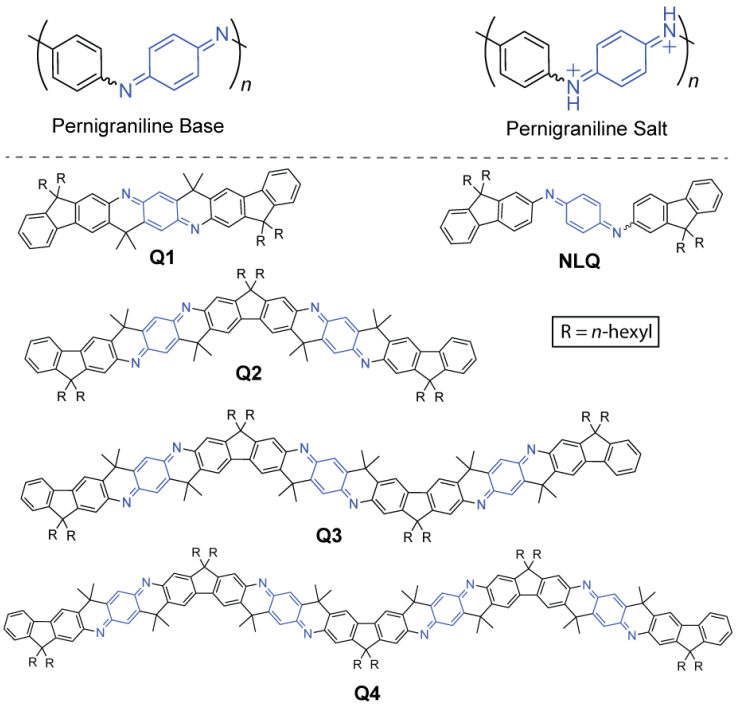

Figure 31. Structural formulas of pernigraniline base, pernigraniline salt, NLQ, and ladder-type oligomeric analogues of pernigraniline base Q1 ~ Q4. Reprinted with permission from [134].

3.3 Synthesis and Characterization

The synthesis of **Q1** started with the preparation of an aniline-like intermediate **A1** through imine condensation between 9,9-dihexyl-2-aminofluorene and DMSS, followed by *in situ* oxidative aromatization under ambient conditions (**Figure 32a**).[79] The ester groups on **A1**, which are *para* to each other, were used in the subsequent cyclization. The methyl Grignard reagent was first used to convert the ester group into a tertiary alcohol,

followed by a regioselective Friedel-Crafts cyclization at the 3-position of the fluorene units promoted by boron trifluoride as a Lewis acid catalyst.[135] The resulting fused-ring product **1** was then further oxidized with Ag_2O to afford the quinoidal molecule **Q1** (**Figure 32a**), in which the *trans*-configuration is predetermined by the *para* position of the ester groups and locked by the covalent dimethylmethene bridge. This procedure was highly efficient and produced **Q1** on a gram scale. **Q1** exhibited moderate solubility in organic solvents (e.g., 0.4 mg/mL in THF). The structure of **Q1** was characterized unambiguously by NMR, HRMS, and single crystal X-ray diffraction (**Figure 52**). Synthesis of the control compound **NLQ** was achieved using a similar strategy. Solution phase ^{1}H and COSY NMR spectra of **NLQ** revealed the presence of both *cis* and *trans* isomers at room temperature in a ratio of 0.42/0.58 (**Figure 57**), in agreement with a previously reported example of pernigraniline base.[128] These configurational isomers dynamically interconvert at room temperature in solution, making it impractical to isolate a pure isomer.

A modified strategy was employed for the synthesis of the longer oligomers **Q2** ~ **Q4**. First the linear precursors **B2**, **B3**, and **B4** were synthesized by sequential Buchwald-Hartwig coupling reactions[136, 137] of varied combinations of diamino- and dibromo-functionalized intermediates (**Figure 32b**). In these reactions, the formation of byproducts with higher degrees of oligomerization were suppressed by adjusting the stoichiometric ratio of the starting materials and optimizing the reaction conditions, leading to good yields ranging from 56% to 87% (**Table 3**). Compounds **B2**, **B3**, and **B4** were then end-capped by 9,9-dihexyl-2-aminofluorene through another Buchwald-Hartwig coupling,

affording the oligomeric intermediates **A2**, **A3**, and **A4**, respectively in excellent yields (85 ~ 96%) (**Figure 32c, 59 ~ 61**). Subsequently, ring-annulation and oxidation procedures similar to the synthesis of **Q1** were applied to produce the quinoidal oligomer series **Q2**, **Q3**, and **Q4** in which all of the quinonediimine units are locked into the *trans*-configuration. Through this route, the longest oligomer **Q4**, which consists of 27 fused rings, was synthesized in five steps with a 34% overall yield. **Q2**, **Q3**, and **Q4** were isolated as intensely colored powders (ranging from purple to blue) with increased solubility in organic solvents compared to that of **Q1**. All products were characterized by ^{1}H, ^{13}C NMR, and HRMS. ^{1}H NMR spectra of **Q1** ~ **Q4** demonstrated that they exclusively adopt the designed *trans*-configuration, in contrast to the undefined and isomerizing configuration of **NLQ**. Based on the NOESY NMR spectrum of **Q1** (**Figure 58**), the ^{1}H NMR signals in the sp^2 region were assigned to the bay region hydrogens (orange and pink), the K-region hydrogens (green), terminal phenyl hydrogens (purple), and the quinoid hydrogens (blue), from downfield to upfield (**Figure 32d**). The extension of the molecular size did not impact the patterns and chemical shifts of the NMR signals significantly. The numbers of the sharp signals (blue) of quinoid hydrogens corresponded well with the numbers of distinct repeating units in different chemical environments.

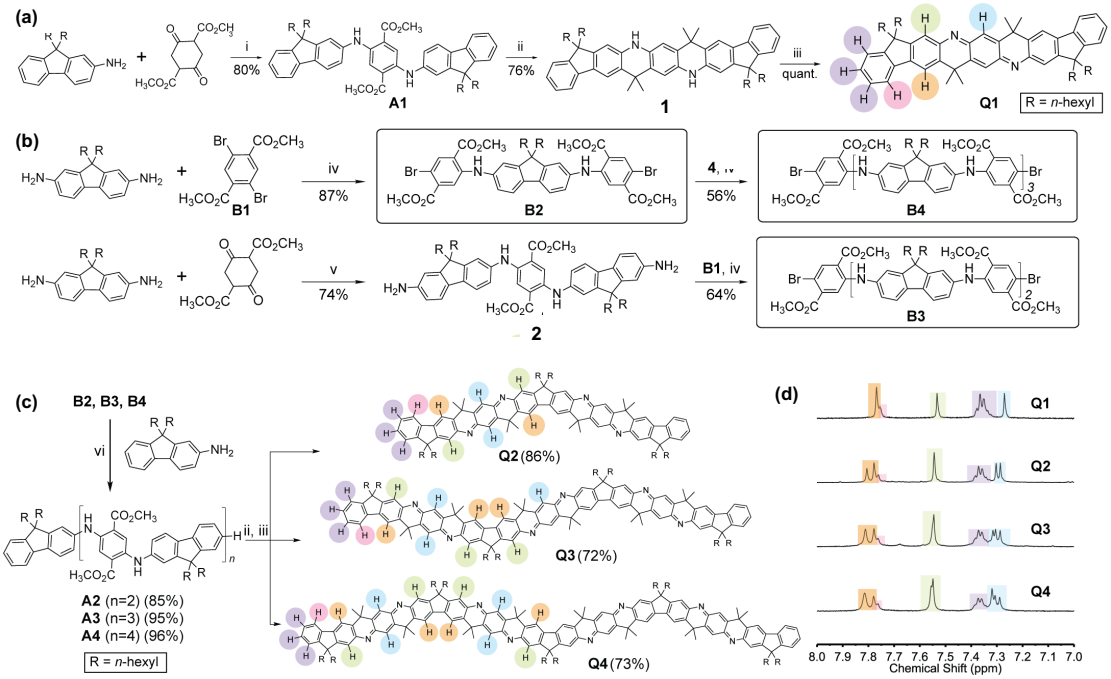

Figure 32. (a) Synthesis of Q1. Reaction conditions: i) PTSA (0.2 equiv.), ethanol, 80 ˚C, in air; ii) CH_3MgBr (10 equiv.), THF, 40 ˚C; then $BF_3{\cdot}Et_2O$, dichloromethane, rt; iii) Ag_2O, THF, rt. (b) Synthesis of dibromo-functionalized intermediates B2, B3, and B4. Reaction conditions: (iv) $Pd(OAc)_2$ (10 mol%), Xantphos (15 mol%), Cs_2CO_3 (4 equiv.), toluene, 110~120˚C; molar ratio between starting materials [NH_2] : [Br] = 1 : 2; (v) PTSA (0.2 equiv.), DMF, 110 ˚C, in air. (c) Synthesis of Q2, Q3, and Q4. Reaction conditions: (vi) $Pd_2(dba)_3$ (10 mol%), BINAP (30 mol%), Cs_2CO_3 (4 equiv.), toluene, 120 ˚C; molar ratio between starting materials [NH_2] : [Br] = 1.5 : 1. (d) Downfield regions (7.0 ~ 8.0 ppm) of the ^1H NMR spectra of Q1, Q2, Q3, and Q4 with color coded labels (500 MHz, $C_2D_2Cl_4$, 298 K). Reprinted with permission from [134].

Based on the CV and DPV results, all of these ladder oligomers demonstrated quasi-reversible multi-electron electrochemical reduction processes, while that of the control compound **NLQ** was irreversible. This observation indicated that the ladder constitution better stabilized the anionic species upon reduction (**Figure 33**).

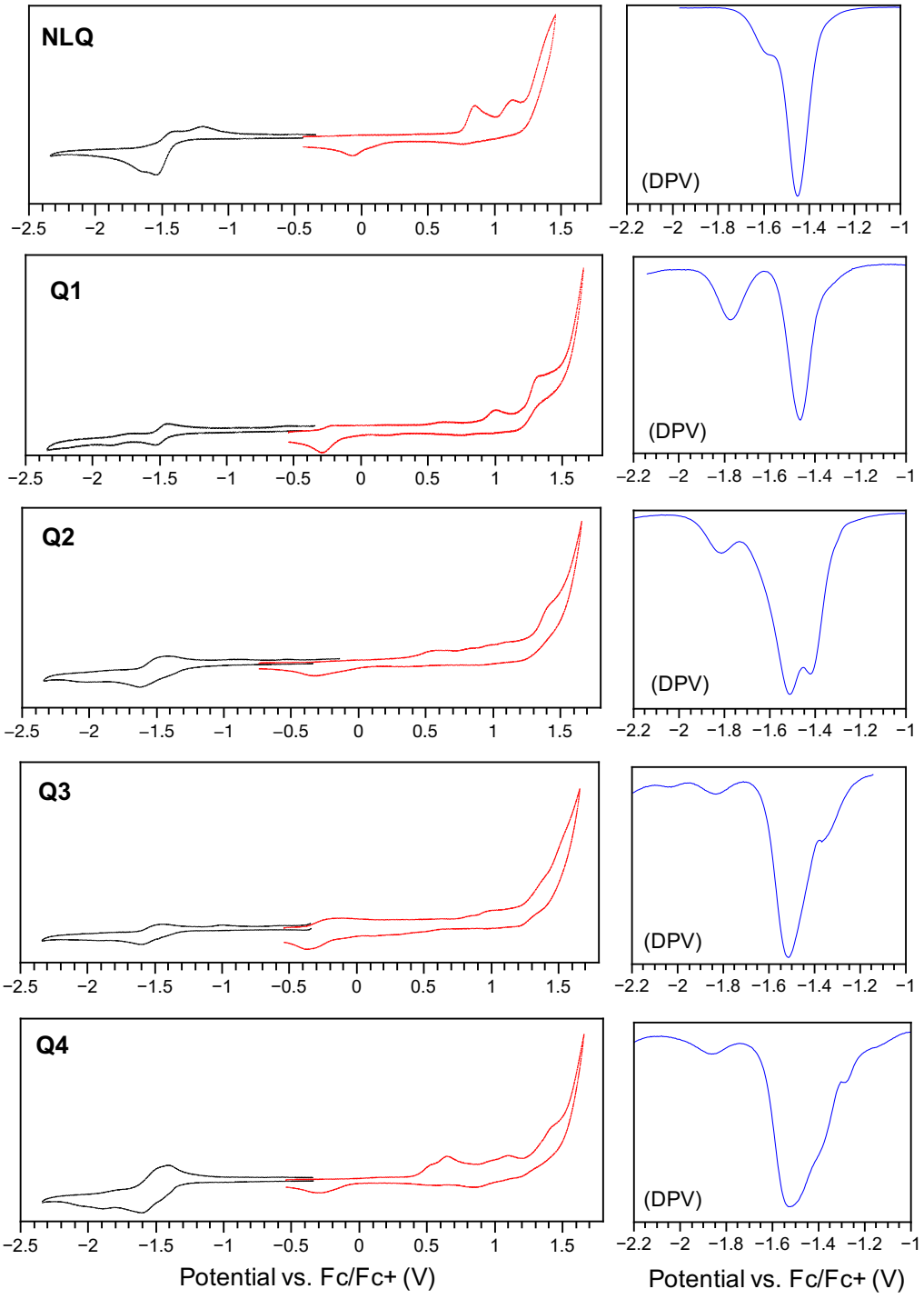

Figure 33. Cyclic voltammograms and differential pulse voltammograms of Q1 ~ Q4 and NLQ in dichloromethane. Reprinted with permission from [134].

The ladder-type backbone rigidity was expected to impact the optical properties of **Q1** ~ **Q4** significantly. All the absorption spectra of **Q1** ~ **Q4** demonstrated distinctive vibrational progressions owing to their conformational rigidity. In a sharp contrast, the control compound **NLQ**, with a flexible backbone, exhibited a broad absorption peak at around 500 nm, similar to that of pernigraniline base, indicative of its flexible conformation and isomerizing configuration. The maximum absorption wavelengths of **Q1** to **Q4** red-shifted from 553 nm to 680 nm with the increase of the oligomer sizes due to the increased extension of π-conjugation and the consequent decreased energy bandgaps. A linear relationship with $R^2 = 0.99$ was found when plotting the optical energy bandgap ($E_{g,\ optical}$) *versus* the reciprocal of repeating unit numbers (n^{-1}), similar to other reported rigid polycyclic aromatic systems (**Figure 34**, **53**).

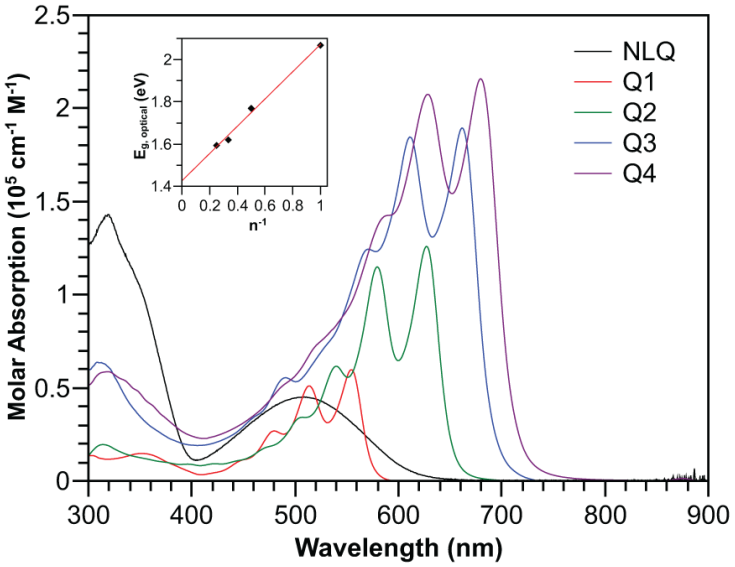

Figure 34. UV-vis absorption spectra of NLQ and Qn (n=1 ~ 4) in toluene (10^{-5} M). Inset: the plot of optical band gap *versus* n^{-1} (n = 1 ~ 4). Reprinted with permission from [134].

In solid-state thin films, despite the rigid backbone, no feature of close π-π interaction was observed in **Qn** by grazing incidence wide-angle X-ray scattering (GIWAXS) experiment (**Figure 35**).

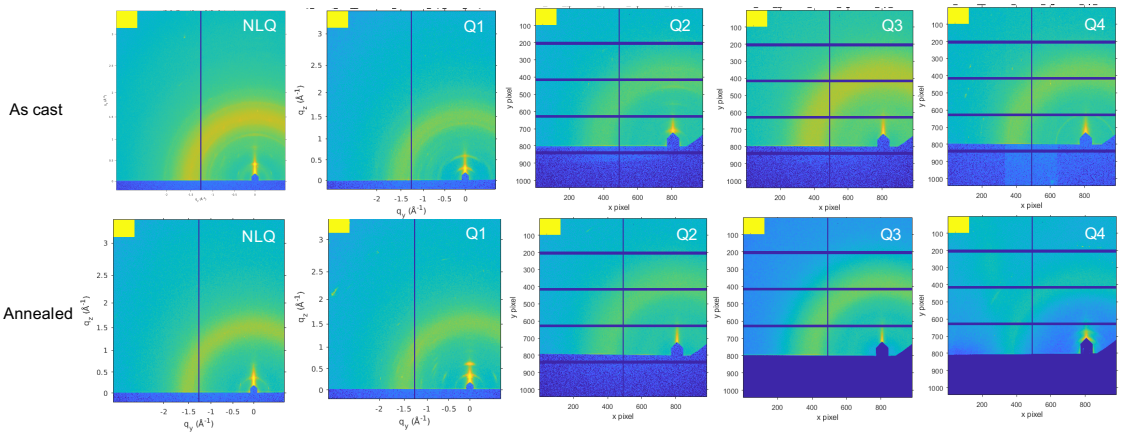

Figure 35. GIWAXS patterns of NLQ and Qn (n = 1 ~ 4) spin-coated films on silicon wafer before and after annealing. Reprinted with permission from [134].

3.4 Protonation Study

The ladder-type constitution of **Q1** ~ **Q4** was expected to promote the stability of the corresponding protonated species, leading to unprecedented stable pernigraniline salt derivatives. Upon protonation by Brønsted acids, the absorption bands of these oligomers dramatically red-shifted into the near-infrared (NIR) region, as a result of lowered LUMO levels and smaller BLA of the conjugated core. For example, with the increasing addition of MSA, **Q1** showed a well-defined two-stage protonation process in THF solution (**Figure 36a**). The first stage took place with up to 9 mM of MSA, resulting in the mono-protonated **H-Q1**$^{+}$ with a broad lower-energy absorption band (λ_{max} = 640 nm). In the second stage when the MSA concentration was further increased to 1.5 M, **H-Q1**$^{+}$ was converted into the fully-protonated salt **H$_2$-Q1**$^{2+}$, leading to a strong NIR absorption band

(λ_{max} = 798 nm). The well-defined isosbestic points in both stages indicated the clean transformations of **Q1** to **H-Q1**$^{+}$ and **H-Q1**$^{+}$ to **H$_2$-Q1**$^{2+}$ without notable side reactions. In contrast, the protonation of **NLQ** did not give a clear isosbestic point, likely attributed to the *cis-/trans-* isomerization and decomposition (**Figure 36b**).

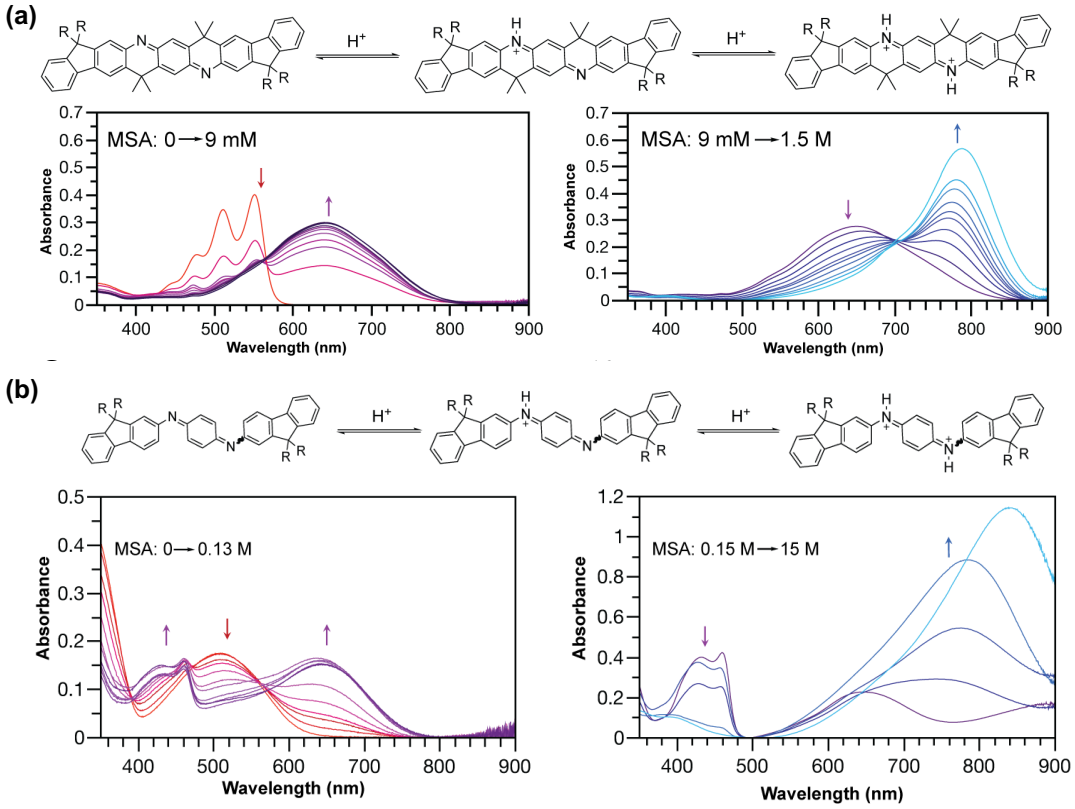

Figure 36. Structural formulas and UV-vis absorption spectra corresponding to the protonation stages of Q1 and NLQ in THF solution (10^{-5} M) with increasing amount of MSA. Reprinted with permission from [134].

Similar to **Q1**, oligomers **Q2** ~ **Q4** also displayed well-defined conversion into the protonated species **H$_{2n}$-Qn**$^{2n+}$ in acidic conditions, with absorption bands further red-shifted to 1020 ~ 1190 nm (**Figure 37a, 37b**). In a drastic contrast with conventional pernigraniline salt and protonated **NLQ**, protonated **Qn** were all stable in highly acidic

conditions at room temperature. It has been reported that acid-doped pernigraniline salts readily decompose through redox pathway,[118, 124] hydrolysis,[121] and conjugated addition.[125]

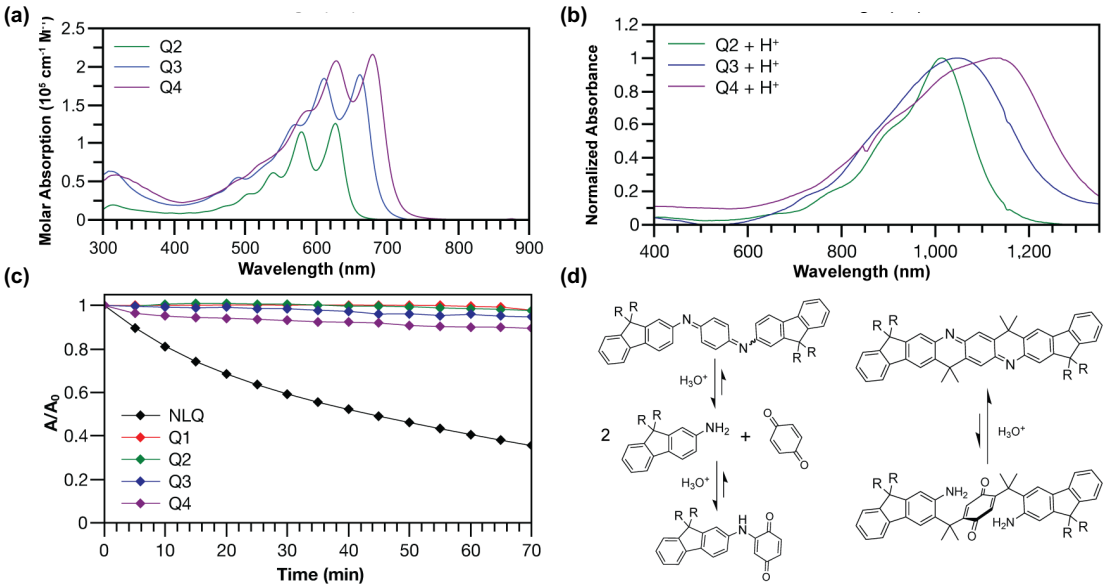

Figure 37. UV-vis absorption spectra of (a) Qn (n = 2 ~ 4) in toluene and (b) protonated Qn in TFA/THF (0.44 M) at room temperature. (c) Time-dependent UV-vis absorbance intensity at λ_{max} of NLQ and Qn. (d) Scheme of possible degradation of NLQ and Q1 in acidic conditions. Reprinted with permission from [134].

Such degradation was indeed observed for the control compound **NLQ** in our study. In an MSA/THF solution (0.8 M) under ambient conditions, the intensity of the main absorption peak of protonated **NLQ** (840 nm) decreased significantly over the course of one hour (**Figure 38**). Mass spectrometry data of the resulting solution indicated the presence of decomposed products *via* hydrolysis and further Michael addition (**Figure 39**).[125] The reduced product (Peak 1), the hydrolyzed amino product (Peak 2), and the

rearranged product (Peak 4 and 5) were observed. After 1 day, only low molecular weight species were present.

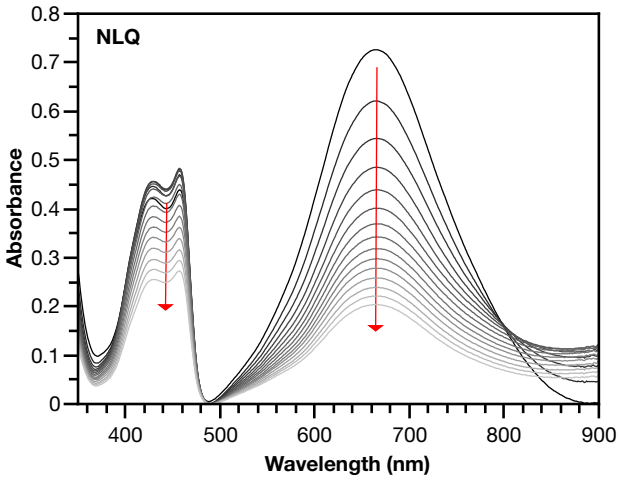

Figure 38. Time-dependent UV-vis spectra of NLQ in MSA/THF (0 ~ 70 min). Reprinted with permission from [134].

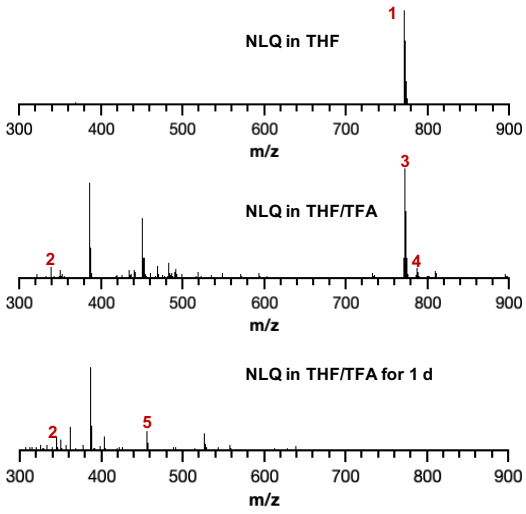

Peak	Structure	m/z (calcd. / found)
1	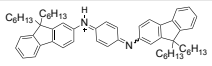	771.5612 / 771.5550
2	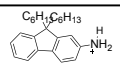	350.2842 / 350.2832
3	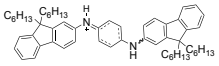	772.5690 / 772.5669
4	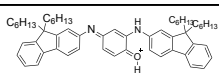	787.5561 / 787.5545
5	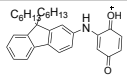	456.2897 / 456.2756

Figure 39. Mass spectra of NLQ in TFA/THF (v/v = 1/10) and peak assignments. Reprinted with permission from [134].

The ladder-type **Qn** products exhibited good stability under the same condition with little change in the absorption (**Figure 37c**) and ^{1}H NMR spectra (**Figure 51**). The significantly higher chemical stability of the ladder-type molecules can be attributed to the additional strand of bonds, which decreases the entropy gain of the potential hydrolysis of the iminium bonds, rendering the decomposition process less thermodynamically favorable (**Figure 37d**).

It is also noteworthy that, under thermogravimetric analysis (**Figure 40**), the ladder-type oligomers all showed carbonization yields over 40% compared to 0% residue weight of **NLQ** at 900 °C, indicating the much higher thermodynamic stability of the sp^2 ladder-type backbones.

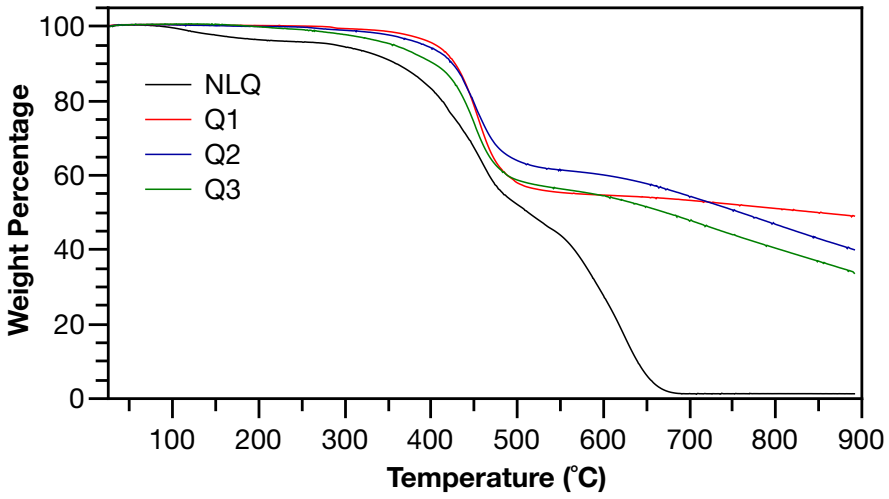

Figure 40. TGA plots of NLQ and Qn (n = 1 ~ 3) in nitrogen with a heating rate of 10.00 °C/min). Reprinted with permission from [134].

3.5 Spin and Paramagnetism Characterization

The superior stability of the ladder-type pernigraniline salt analogues sets the stage to perform extensive fundamental investigations with ensured structural integrity. In the

past, investigation of the magnetic property of conventional pernigraniline salts have been challenging due to the aforementioned poor stability and isomerization issues.[138] In comparison, emeraldine salts have been extensively studied,[113, 139] revealing the presence of both Curie and Pauli paramagnetism and providing important insights regarding their remarkable electronic conductivity. Herein, the excellent chemical robustness of protonated **Qn** allowed for the examination of the radical characters in pernigraniline salts by electron paramagnetic resonance spectroscopy (EPR).[140] It was hypothesized that after protonation, the resonance contribution of the open-shell diradical cations increased. Indeed, solution-phase EPR spectra of neutral **Q1** ~ **Q4** all exhibit weak signals at room temperature with spin densities less than 10^{-3} spins per molecule (**Figure 41**), a confirmation of their dominant closed-shell resonance of the quinoidal building blocks.

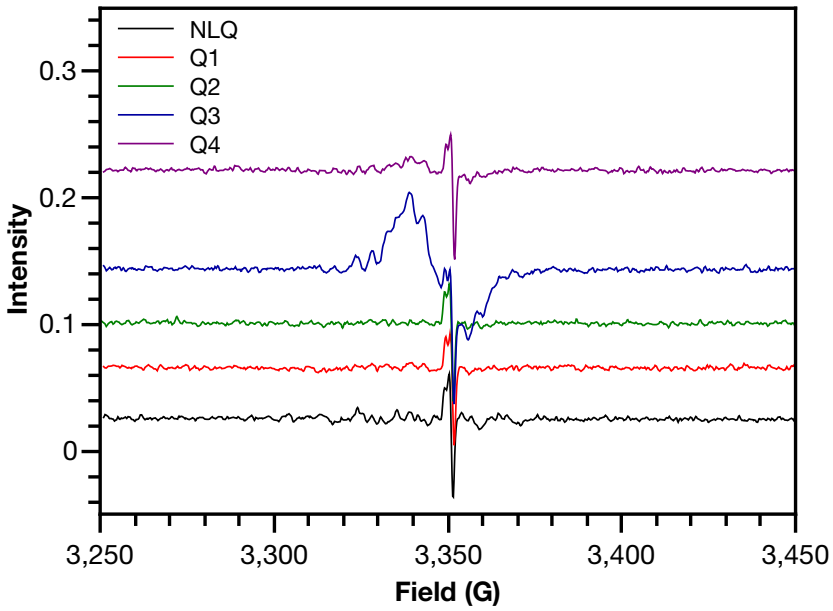

Figure 41. EPR spectra of NLQ and Qn in triethylamine/dichloromethane (v/v = 1/10). Reprinted with permission from [134].

In the presence of TFA (0.1 M), strong EPR signals (*g* factors = 2.0029 ~ 2.0040) with spin densities ranging from 0.3 to 0.8 spins per molecule were observed (**Figure 42**), indicating significantly increased open-shell characters upon protonation in solution. The well-split EPR signal of $\mathbf{H_2\text{-}Q1^{2+}}$ was attributed to the hyperfine coupling of the spins with the nitrogen atoms.[141] In sharp contrast, the non-ladder-type analogue **NLQ** exhibited no well-resolved splitting,[138] likely a result of the configurational isomerization and torsional rotation of the backbone. Broad EPR signals were also observed for the higher oligomers $\mathbf{H_{2n}\text{-}Q_n^{2n+}}$ (n = 2 ~ 4). The lack of resolved splitting in these cases is attributed to overlapping signals of multiple radical pairs and the complex hyperfine spin coupling with multiple nitrogen atoms in these larger molecules. The open-shell character of protonated **Q1** and **NLQ** was also compared using DFT calculation, showing a slightly lower diradical character in $\mathbf{H_2\text{-}Q1^{2+}}$ (0.65) than that in trans-$\mathbf{H_2\text{-}NLQ^{2+}}$ (0.70) because the locked coplanar conformation of $\mathbf{H_2\text{-}Q1^{2+}}$ favors the closed-shell resonance contribution (**Table 2**).

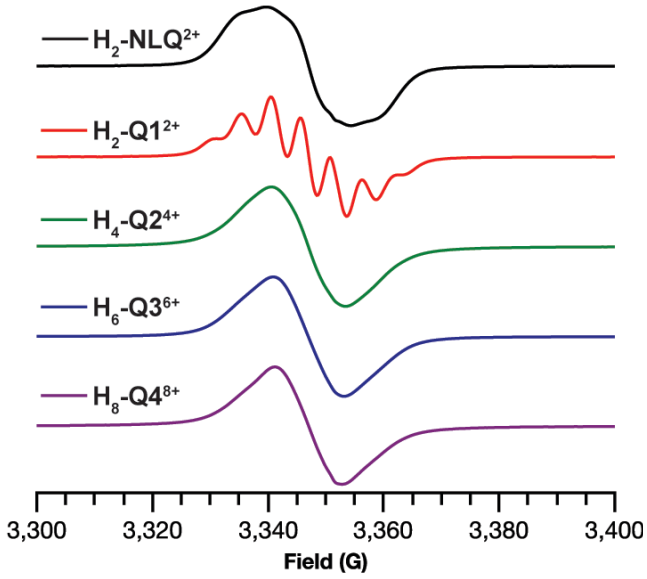

Figure 42. Normalized EPR spectra of protonated NLQ and Q1 ~ Q4 solution (10 mM) in TFA/dichloromethane (0.1 M) at room temperature. Reprinted with permission from [134].

Table 2. Calculated diradical character of Q1, H_2-Q1^{2+}, H_2-NLQ^{2+}, Me-Q1^{2+} and PS-dimer. Reprinted with permission from [134].

Compound	σ_{HONO}	σ_{LUNO}	y
Q1	1.3759	0.6241	0.34
H_2-Q1^{2+}	1.1830	0.8169	0.65
H_2-NLQ^{2+}	1.1554	0.8446	0.70
Me-Q1^{2+}	1.2618	0.7382	0.51
PS-dimer	1.3195	0.6805	0.42

In order to further understand the magnetic and electronic properties of protonated **Qn** in the condensed phase, their spin characters were also investigated in the solid state. Complete protonation of **Q1** was achieved in the solid state by mixing with 5 equivants of PTSA which was confirmed by the fact that a thin-film absorption spectrum is similar to that of **H_2-Q1^{2+}** in solution (**Figure 43a**).

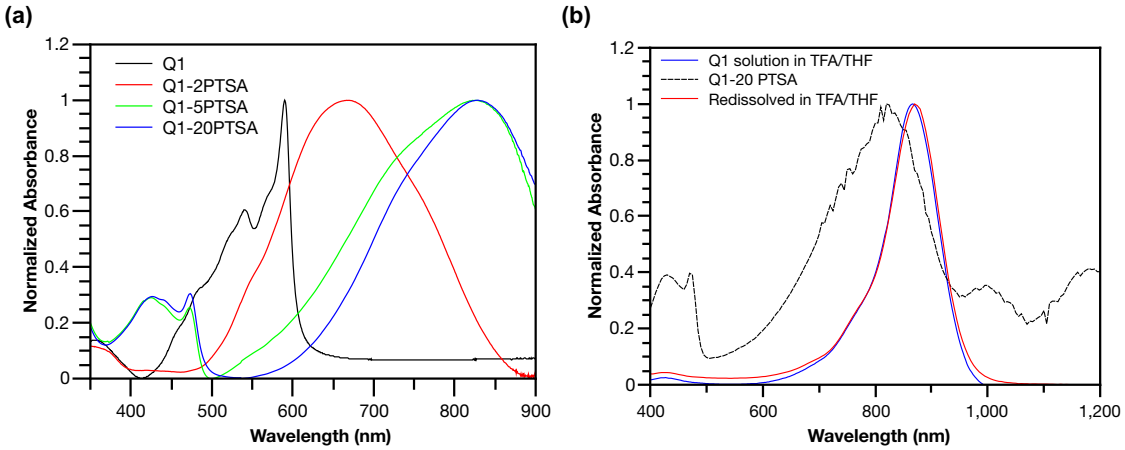

Figure 43. (a) Solid-state UV-vis-NIR absorption spectra of Q1 with varied equivalents of PTSA as thin films; (b) Normalized UV-vis-NIR absorption spectra of Q1 solution (10^{-5} M) in TFA/THF (0.44 M) (red), Q1 with 20 equivalents of PTSA thin film (black), and the solution prepared by redissolving the film in TFA/THF (0.44 M) (blue). Reprinted with permission from [134].

Using this same approach, solid-state $\mathbf{H_{2n}\text{-}Qn^{2n+}}$ samples were prepared by treatment with 5*n* equivalents of PTSA. To confirm the structural integrity of these solids after exposure to ambient conditions, they were redissolved and subjected to solution-phase absorption spectroscopy, the results of which were identical to the measurements made before the solid state protonation treatment (**Figure 43b**, **44**).

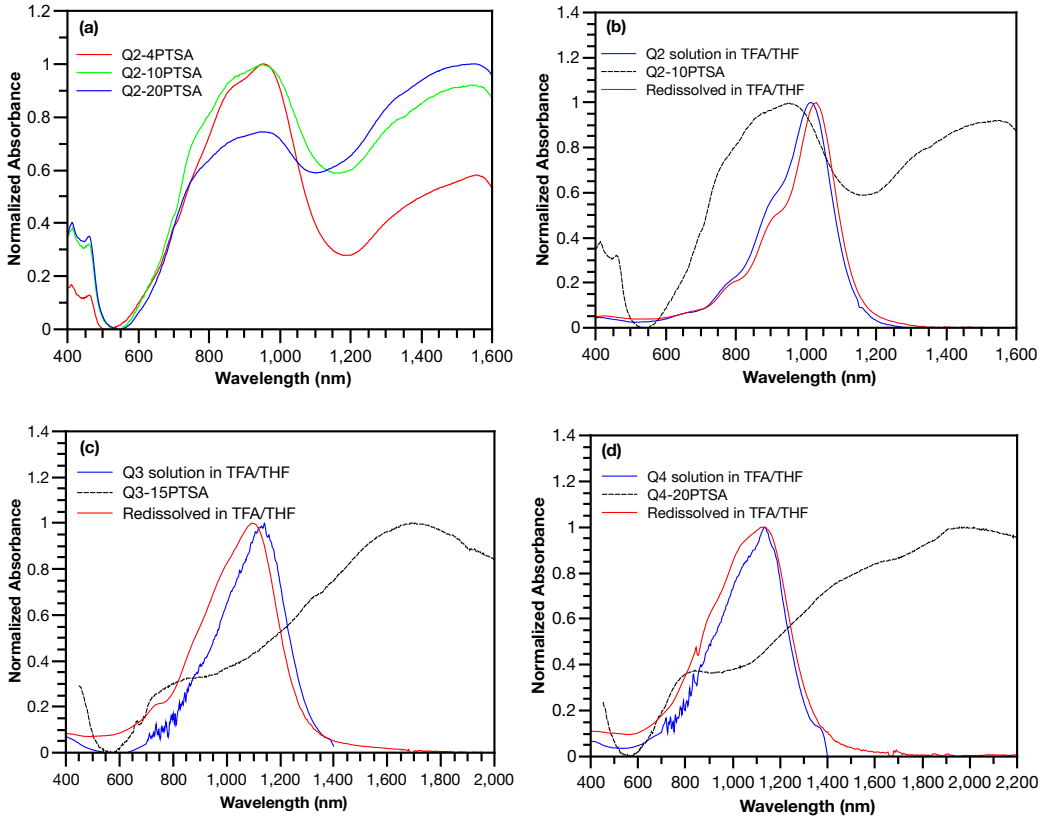

Figure 44. UV-vis-NIR absorption spectra of (a) Q2 with varies equivalents of PTSA in thin films, (b)(c)(d) Qn (n = 2 ~ 4) solutions (10^{-5} M) in TFA/THF (0.44 M) (blue), and Qn with 5n equivalents of PTSA thin film (black), and the solution prepared by redissolving the film in TFA/THF (0.44 M) (red). Reprinted with permission from [134].

Superconducting quantum interference device (SQUID) magnetic measurements were used to further characterize the spin character in the solid state. Surprisingly, all of the protonated ladder-type oligomers exhibit dominant temperature-independent paramagnetism (**Figure 45**). Magnetic susceptibility data obtained from 2 to 300 K revealed constant values. The product of molar magnetic susceptibility and temperature ($\chi_{total}T$) was plotted against temperature, revealing a linear relationship with $R^2 > 0.99$ [See equation (1)]. This temperature-independent paramagnetism behavior is attributed to Pauli

paramagnetism, given that van Vleck temperature-independent paramagnetism is only significant in cases of transition metal paramagnets of heavier elements wherein ground states mix with excited states.[142, 143] Among $\mathbf{H_{2n}\text{-}Qn^{2n+}}$, the χ_{Pauli} per mol of quinoediiminium unit increases steadily from 4×10^{-3} emu/mol for $\mathbf{H_2\text{-}Q1^{2+}}$ to 1.2×10^{-2} emu/mol for $\mathbf{H_8\text{-}Q4^{8+}}$, indicating that the temperature-independent paramagnetism is correlated to the size of the extended backbones. The densities of states at the Fermi level $\rho(E_F)$ were calculated to be in the range of 7×10^{25} to 2.2×10^{26} eV^{-1} mol^{-1}. It is also noteworthy that the $\chi_{total}T$ *vs* T plot exhibited only a very small contribution from Curie paramagnetism (vertical intercepts on the plot), indicating the dominant delocalized nature of spins in the solid states of protonated **Qn**.

$\chi_{total}\,T = C + \chi_{Pauli}T$ (*C*: Curie paramagnetism; *T*: temperature) (1)

Pauli paramagnetism in organic materials (*e.g.*, doped polyacetylene[144] and polythiophene[145]) is commonly indicative of the presence of a metallic polaron lattice, and can serve as a measurement of the density of states near the Fermi level.[146] Among PANI derivatives, a combination of Pauli and Curie paramagnetism was observed in emeraldine salts as a result of the presence of both delocalized and localized paramagnetic centers.[109, 113, 114] The magnetic susceptibility of conventional pernigraniline salts, however, has not been well-established due to the stability and isomerization issues. In the present case, such measurements are rendered possible by the ladder-type constitution, which not only enhances the stability but also locks the configuration and conformation of these pernigraniline salt analogues. The dominant Pauli paramagnetism observed for protonated **Qn** revealed the delocalized nature of the polarons in the solids, in agreement with the

recent discovery of high conductivity of a pernigraniline salt film measured *in situ* by electrochemical methods.[117]

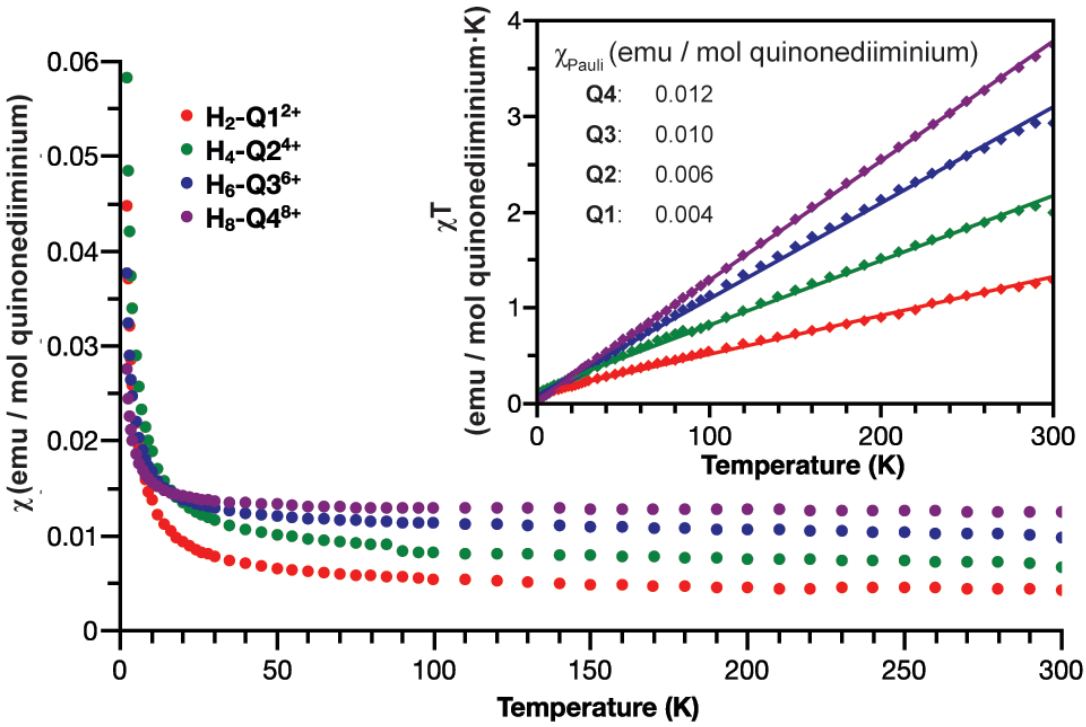

Figure 45. Solid-state magnetic susceptibility (χ) of PTSA doped Qn measured over the temperature range of 2 ~ 300 K in the powder form; (inset) χT-T plots (dots: experimental data points; lines: linear fitting). Reprinted with permission from [134].

Magnetic saturation plots were obtained at 2 K to investigate the spin ground states of these pernigraniline salt analogues (**Figure 46**). The data spots of **NLQ** data fit well with theoretical doublet plot, showing no spin-spin coupling (**Figure 46a**). While the data spots of **Q1** and **Q2** are fit based on a singlet ground state and a triplet excited state. The magnetization data for **H₂-Q1**$^{2+}$ are in accord with a singlet ground state (S = 0) with a small negative coupling constant (–0.49 K), suggesting a weak antiferromagnetic coupling

between the radical pair (**Figure 46b**).[147] Such coupling is likely facilitated by the rigidity and coplanarity of the conjugated ladder-type backbone. For **H$_6$-Q3^{6+}**, the ground state changes from singlet to triplet with a small positive *J* value (**Figure 46d**). More interestingly, the fitting for **H$_8$-Q4^{8+}** could not be achieved using a singlet-triplet model as the M/M$_{sat}$ curve of **H$_8$-Q4^{8+}** is above the theoretical M/M$_{sat}$ curve for a triplet (*S* = 1), which indicates higher spin ground state could be involved (**Figure 46e**). The *J* values shift from small negative to positive as the conjugation systems are enlarged from **H$_2$-Q1^{2+}** to **H$_8$-Q4^{8+}**. The antiferromagnetically coupled nature of radical pair(s) in **H$_2$-Q1^{2+}** and **H$_4$-Q2^{4+}** is consistent with behaviors of benzene bridged diradicals with 1,4-connection.[148] The ferromagnetic coupling in **H$_6$-Q3^{6+}** and **H$_8$-Q4^{8+}** is likely caused by the nearly degenerated nature of radical molecular orbitals in solid-state local enviroments.[147, 149]

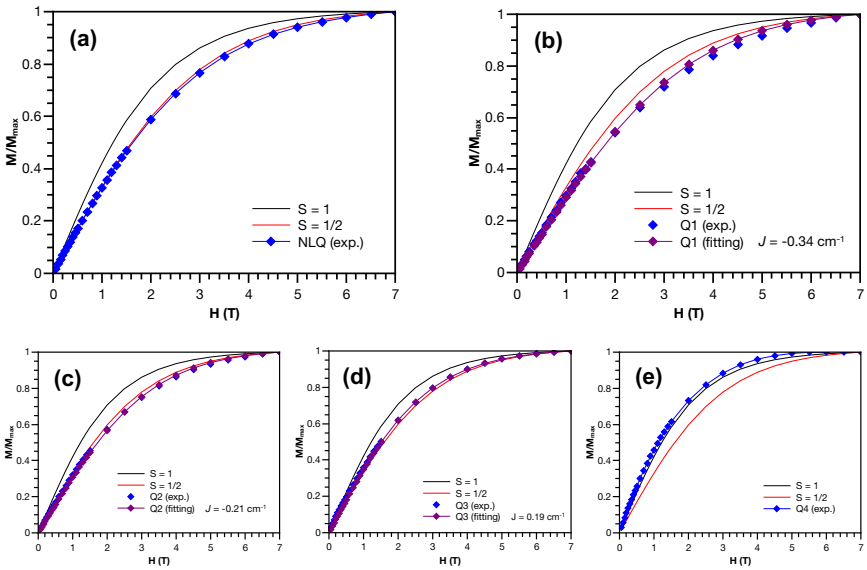

Figure 46. Magnetization saturation plots of (a) NLQ and (b ~ e) Qn with 5n equiv. PTSA at 2 K (dots: experimental data points; lines: fitting curves). Reprinted with permission from [134].

To further corroborate the magnetism data, solid-state conductivity measurements were performed on compressed pellets of **Q1** and protonated **Q1** and **Q2** using a four-probe method (**Figure 47a**, **47b**, **47c**); the conductivity of protonated **NLQ** could not be properly measured due to the rapid decomposition. Although limited by insulating hexyl chains and PTSA, as well as significant grain boundaries and disorder in the polycrystalline state (**Figure 56**), the protonated solids of **Q1** nevertheless showed electrical conductivity up to 10^{-5} S/cm, in a sharp contrast to the insulating nature of pristine **Q1** (conductivity less than 10^{-10} S/cm). Obvious DC conductivity was also observed for protonated **Q1** and **Q2** in as drop-casted thin films (**Figure 47e**, **47f**).

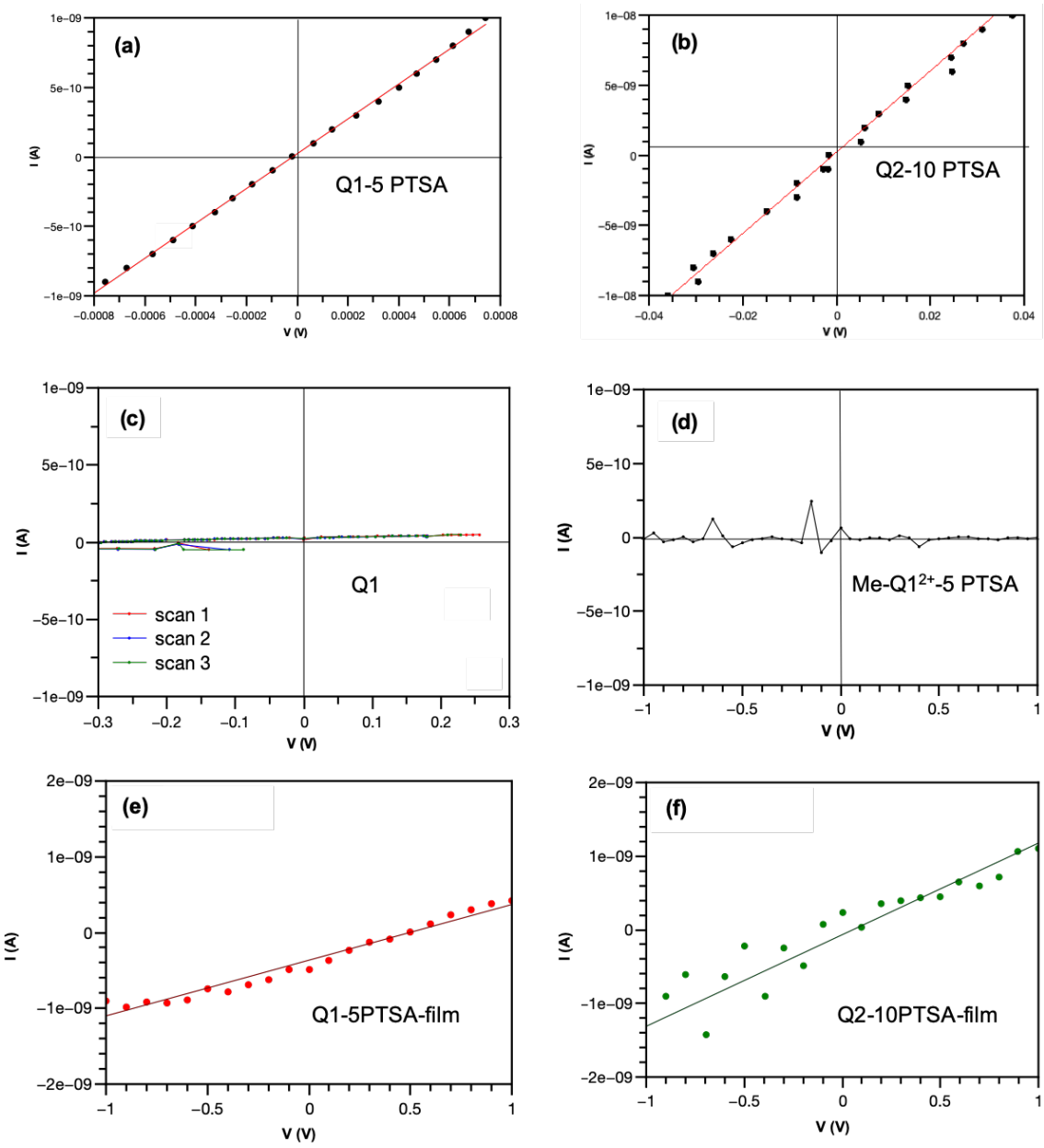

Figure 47. I-V plots from four-probe conductivity measurement of (a) Q1-5PTSA, (b) Q2-10PTSA, (c) pristine Q1, (d) Me-Q1^{2+} mixed with 5 equiv. PTSA as pellet samples, (e) Q1-PTSA and (f) Q2-10PTSA as drop-casted films. Reprinted with permission from [134].

In addition, AC impedance measurement of the $\mathbf{H_2\text{-}Q1^{2+}}$ pellet sample showed only one semicircle Nyquist plot[150], which should be attributed to the electronic conductive component as charge transport occurs through hopping. The real part of the impedance is attributed to the hopping process and the imaginary contribution comes from the atomic polarizability.[151, 152] The AC impedance results indicate that the conductivity was mainly electronic with no observable ionic contribution (**Figure 48**).

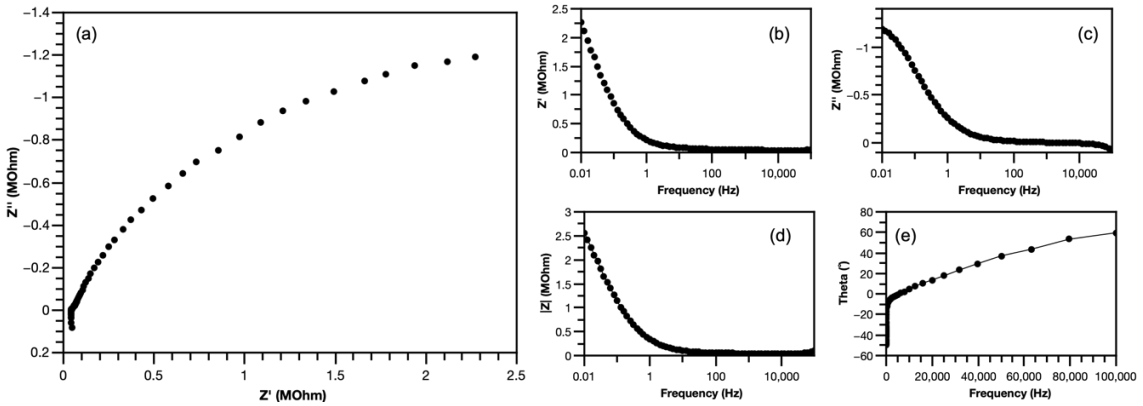

Figure 48. (a) Impedance plot and frequency dependence of (b)(c)(d) impedance and (e) phase shift of Q1-5PTSA pellet. Frequency was swept from 0.01 Hz to 100 kHz. Reprinted with permission from [134].

We attributed the delocalization nature of polarons to the intermolecular interaction[153] through the protonated N–H units, which has also been a key factor contributing to the conductivity of emeraldine salts.[154] To confirm this hypothesis, a control compound $\mathbf{Me\text{-}Q1^{2+}}$ was synthesized and characterized by single crystal X-ray diffraction and UV-vis absorption spectroscopy (**Figure 49**, **54**). The only difference between $\mathbf{Me\text{-}Q1^{2+}}$ and $\mathbf{H_2\text{-}Q1^{2+}}$ was the N–CH_3 unit that inhibits the potential intermolecular interaction between N–H groups. DFT calculation on $\mathbf{Me\text{-}Q1^{2+}}$ revealed

similar delocalized spin density and a smaller diradical character (0.51) compared to that of **H_2-Q1^{2+}** (0.65) (**Figure 55**, **Table 2**).

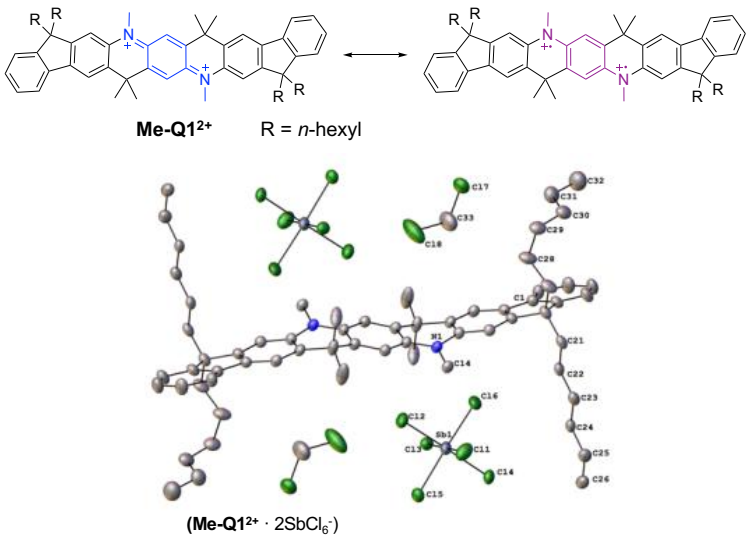

Figure 49. Formula and single crystal structure of Me-Q1^{2+}. Reprinted with permission from [134].

Interestingly, SQUID magnetometer measurements of **Me-Q1^{2+}** showed a typical paramagnetic behavior of a localized diradical system (**Figure 50**),[37, 155-157] dramatically different from that of **H_2-Q1^{2+}**. The decrease of χT value at low temperature indicates the antiferromagnetically coupled nature of the diradical. A fitting with the Bleaney-Bowers equation yields a coupling constant $J = -0.96$ cm^{-1}. The small and negative sign of the coupling constant reveals that **Me-Q1^{2+}** possesses singlet ground state while its singlet and triplet states are almost degenerated. Conductivity of a mixture of **Me-Q1^{2+}** with 5 equivalents of PTSA was measured by the same four-probe method described above, showing no observable conductivity (**Figure 47d**).

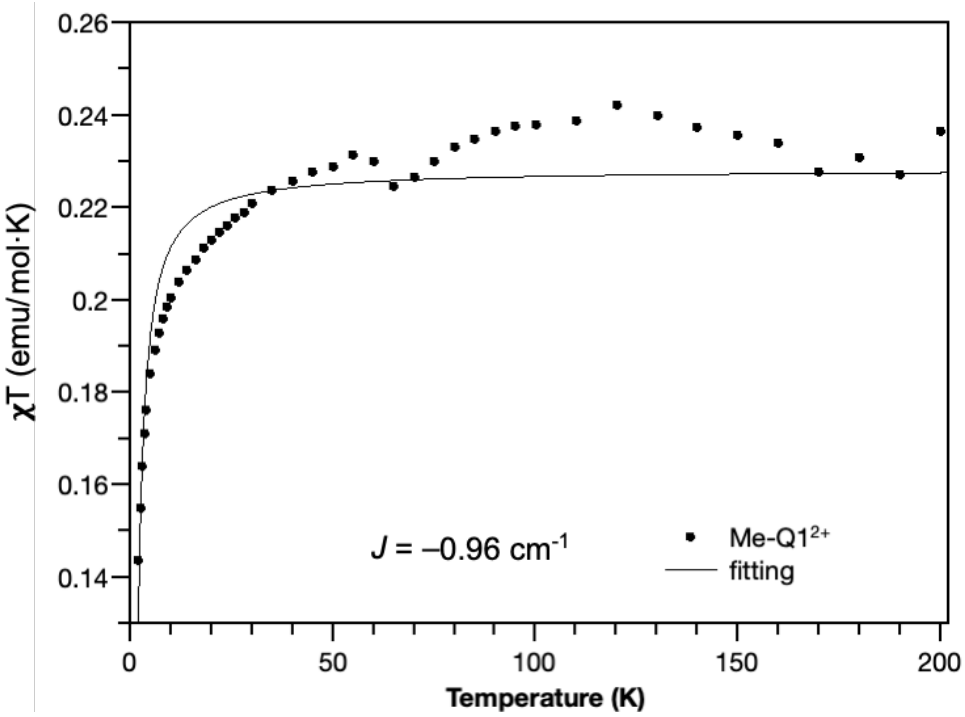

Figure 50. χT-T plot of Me-Q1^{2+}· 2 $SbCl_6^-$ (dots: experimental data points; line: Bleaney-Bowers fitting). Reprinted with permission from [134].

Comparing the different paramagnetic behavior and bulk conductivity of **Me-Q1**$^{2+}$ and **H$_2$-Q1**$^{2+}$, we confirmed that intermolecular interaction through N–H units is an important factor to facilitate the polaron delocalization in the solid of PTSA protonated ladder-type compound **H$_2$-Q1**$^{2+}$. Taken together, the observed Pauli paramagnetism and conductivity of these stable ladder-type analogues of pernigraniline salt are incontrovertible evidence for the delocalized nature of fully-oxidized PANI derivatives and findings that address the long-standing challenge in understanding their intrinsic electronic characters.

3.6 Conclusion

In this work, a series of ladder-type oligomers resembling the structure of pernigraniline base/salt have been designed and synthesized. With the additional strand of covalent bonds, the conjugated backbones are pre-determined to be in an all-*trans* configuration and are locked into a rigid coplanar conformation, allowing for the establishment of a structure-property correlation of pernigraniline salt-analogues excluding the influence of decomposition, isomerization and torsional disorder. Protonation of these pernigraniline base-analogues leads to pronounced open-shell resonance contribution with high spin density. Compared with conventional pernigraniline salts and the non-ladder type control compound, these ladder-type oligomers exhibit much higher stability in acidic conditions, enabling fundamental investigations and practical applications of this unique class of organic materials with reliable structural integrity. Interestingly, in the solid state, these pernigraniline salt-like oligomers exhibit a dominant temperature-independent Pauli paramagnetism, indicative of the delocalized status of the polarons. A methylated control compound, in contrast, did not show Pauli paramagnetism, confirming the key role of intermolecular interaction for the solid-state polaron delocalization. This observation agrees with their moderate conductivity properties measured in the solid state. Simply put, the ladder-type constitutional design imparts the desired chemical stability and structural certainty into acid-doped PANI materials in high oxidation states, such that their unexpected metallic magnetic and electronic properties can be revealed.

3.7 Experimental Details

3.7.1 General Methods

All reaction solvents were dried and purified by an Inert Technology pure solvent system (PureSolv-MD-5a). All starting materials were obtained from commercial suppliers and were used without further purification unless otherwise specified. ^{1}H, ^{13}C, ^{1}H-^{1}H COSY and ^{1}H-^{1}H NOESY NMR spectra were recorded on a Varian Inova 500 MHz spectrometer at room temperature and processed by MestReNova 10.0.2. Chemical shifts are reported in ppm relative to the signals corresponding to the residual non-deuterated solvents (for ^{1}H NMR: $CDCl_3$ δ = 7.26 ppm; 1,1,2,2-$C_2D_2Cl_4$ δ = 6.00 ppm; CD_2Cl_2 δ = 5.32 ppm; for ^{13}C NMR: $CDCl_3$ δ = 77.16 ppm). Flash column chromatography purifications were carried out using a Biotage® Isolera™ Prime with various sizes of SiO_2 Biotage SNAP® cartridges. Preparative SEC purifications were performed at room temperature using a JAI recycling preparative HPLC (LC-92XXII NEXT SERIES) equipped with a reciprocating double plunger pump (model P-9104B), a UV-vis 4ch NEXT detector (254 nm, 280 nm, 300 nm, 3300 nm), and a two-column set including a JAIGEL-H 40P Gard column and a JAIGEL-2H-40 HPLC column. Chloroform was used as the eluent at a flow rate of 14 mL/min. UV-vis-NIR absorption spectra were recorded on a Hitachi U-4100 UV-Vis-NIR spectrophotometer. ESI-MS experiments were performed using a Thermo Scientific Q-Exactive Focus operated in full MS in positive mode. High resolution Matrix-assisted laser desorption ionization-time of flight mass spectrometry (MALDI-TOF MS) was performed on a microflex™ LRF mass spectrometer (Bruker Corporation) in positive linear mode with 2,4,6-

trihydroxyacetophenone monohydrate (THAP) as the matrix. EPR spectroscopy was conducted on a Bruker ELEXSYS II E500 with microwave frequency of *ca.* 9.38 GHz at 288 K. 1 mm ID sample tubes were used for solutions and 4 mm ID sample tubes were used for solids. The spectra were acquired at 1 G modulation and 100 kHz modulation frequency with various powers. Magnetic measurements were conducted on a Quantum Design MPMS XL SQUID magnetometer from 2 to 300 K. The magnetization measurements were performed at 2 K over the magnetic field range of 250 - 70000 Oe. The diamagnetic contributions of the sample holders and the atoms were corrected with blank holders and the Pascal's constants**.** Conductivity of **Q1** and PTSA treated **Q1** and **Q2** was evaluated by a four-point probe method under vacuum. Pellet samples were prepared by compressing the powder materials (*ca.* 0.1 g) in a mold with inner diameter of 25 mm at pressure of 20 kPa in air. The electrical resistance was measured with a Keithley 2450 SourceMeter. The thickness of the pellet was measured using scanning electron microscopy as *ca.* 10^{-2} cm. The electrical conductivity was calculated based on the slope of the I-V plots. AC impedance experiment was performed with a Solartron SI 1287 electrochemical interface and a Solartron SI 1260 impedance/gain-phase analyzer. The AC amplitude was set as 10 mV versus open circuit. The frequency sweep range was 0.01 Hz to 100 kHz. Gold paste was applied on both sides of a Q1-5PTSA pellet. The measured values of cross-sectional area and thickness were 0.35 cm^2 and 0.08 cm. For diradical character calculation, $\mathbf{H_2\text{-}Q1^{2+}}$ and $\mathbf{H_2\text{-}NLQ^{2+}}$ was optimized at the DFT UB3LYP/6-311+G(d,p) level of theory with broken-symmetry. **Q1** and $\mathbf{Me\text{-}Q1^{2+}}$ was calculated based on the single crystal structure without optimization. The occupancy

number of highest occupied natural orbital (HONO) (σ_{HONO}) and lowest unoccupied natural orbital (LUNO) (σ_{LUNO}), and corresponding diradical character *y* were calculated for **Q1**, **H₂-Q1²⁺**, **H₂-NLQ²⁺** and **Me-Q1²⁺** at UHF/6-31+G(d,p) level of theory.[158] Pernigraniline salt dimer (**PS-dimer**) was also calculated at the same level of theory.

3.7.2 Synthesis

Condition screening was conducted on the Buchwald-Hartwig cross-coupling reactions between diamino fluorene and ester functionalized aryl dibromide **B1**, by varying the molar ratio between starting materials, catalyst and ligand loading, and temperature. The optimized condition is highlighted in **Table 3**.

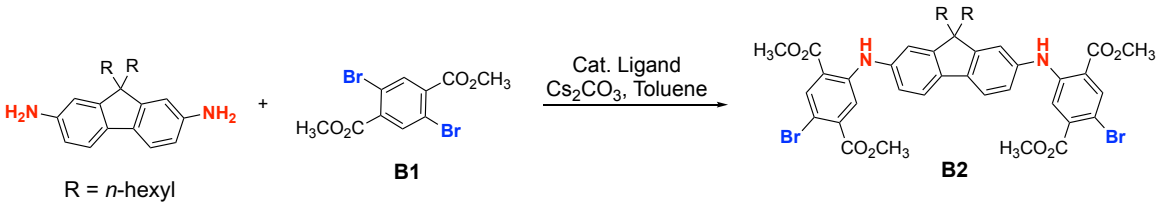

Table 3. Screened conditions and results of Buchwald-Hartwig reaction for synthesis of B2. Reprinted with permission from [134].

Equiv. (NH_2 / Br)	Catalyst (mol %)	Ligand (mol %)	T (˚C)	Yield (%)[a]
1 / 3.0	$Pd_2(dba)_3$ (10 %)	*t*Bu_3P (40 %)	120	--[b]
1 / 3.0	$Pd_2(dba)_3$ (10 %)	Xphos (40 %)	120	--[b]
1 / 3.0	$Pd_2(dba)_3$ (10 %)	BINAP (30 %)	120	55
1 / 3.0	$Pd(OAc)_2$ (20 %)	BINAP (30 %)	120	44
1 / 3.5	$Pd(OAc)_2$ (20 %)	BINAP (15 %)	110	--[b]
1 / 3.5	$Pd_2(dba)_3$ (10 %)	BINAP (30 %)	110	28
1 / 3.0	$Pd(OAc)_2$ (10 %)	Xantphos (15 %)	110	56
1 / 4.0	**$Pd(OAc)_2$ (10 %)**	**Xantphos (15 %)**	**120**	**87**

[a] Isolated yield; [b] Oligomeric byproducts were observed.

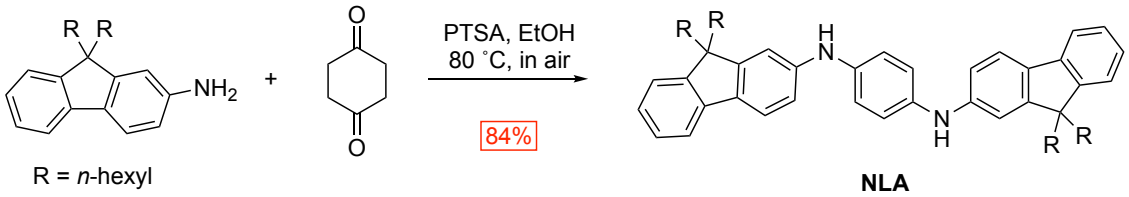

NLA: 9,9-Dihexyl-2-amino fluorene (0.51g, 1.46 mmol), 1,4-cyclohexanone (0.065 g, 0.58 mmol), PTSA·H_2O (22 mg, 0.12 mmol), and ethanol (15 mL) were charged in a 50 mL-round-bottom flask with a condenser. The mixture was stirred open to the air at 80 ˚C for 12 h. After cooled to room temperature, the precipitate was filtered and washed with methanol to give the product as a grey powder (0.47 g, 84%). ^{1}H NMR (500 MHz, CD_2Cl_2, 298 K, ppm) δ = 7.63 – 7.57 (m, 4H), 7.34 – 7.28 (m, 4H), 7.23 (td, J_1 = 7.4 Hz, J_2 = 1.1 Hz, 2H), 7.14 (s, 4H), 7.05 (d, J = 2.1 Hz, 2H), 7.00 (dd, J_1 = 8.2, J_2 = 2.2 Hz, 2H), 5.84 (s, 2H), 2.01 – 1.88 (m, 8H), 1.21 – 1.03 (m, 24H), 0.80 (t, J = 7.2 Hz, 12H), 0.76 – 0.59 (m, 8H). ^{13}C NMR (125 MHz, $CDCl_3$, 298 K, ppm) δ = 152.62, 150.21, 143.65, 141.44, 137.62, 134.14, 126.78, 125.79, 122.79, 120.56, 120.38, 118.72, 115.82, 111.72, 55.06, 40.67, 31.69, 29.90, 23.91, 22.76, 14.18. HRMS (+ESI): $C_{56}H_{72}N_2$ $[M+H]^+$ calcd. *m/z* = 773.5768, found *m/z* = 773.5725.

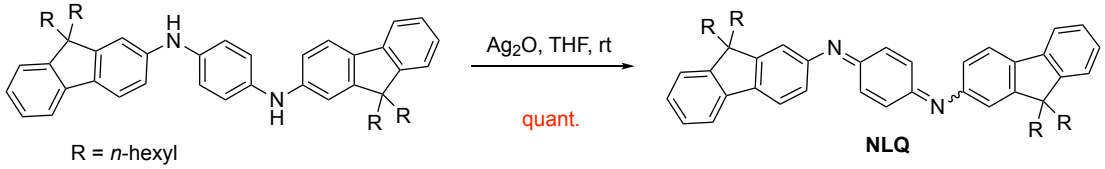

NLQ: Ag_2O (60 mg) was added into a solution of **NLA** (0.1 g, 0.13 mmol) in THF (10 mL). The mixture was stirred at room temperature in ambient condition for 12 h. The precipitate was filtered out and the filtrate was concentrated with a rotatory evaporator, affording the product a purple oil (0.1 g, quant.). ^{1}H NMR (500 MHz, CD_2Cl_2, 298 K,

ppm) δ = 7.80 – 7.69 (m, 4H), 7.43 – 7.30 (m, 6H), 7.19 – 7.15 (s, 0.84H), 7.05 – 7.01 (s, 2.32H), 6.98 – 6.92 (s, 3.16H), 6.91 – 6.85 (m, 1.68H), 2.01 (m, 8H), 1.22 – 1.01 (m, 27.36H), 0.82 (t, J = 7.3 Hz, 5.04H), 0.79 – 0.58 (m, 11.6H). ^{13}C NMR (125 MHz, $CDCl_3$, 298 K, ppm) δ = 158.45, 158.30, 152.00, 151.93, 150.74, 150.70, 149.28, 140.56, 140.52, 138.94, 138.92, 137.62, 136.53, 126.99, 126.97, 126.87, 126.84, 125.08, 124.49, 122.81, 120.09, 119.94, 119.70, 119.51, 119.46, 116.22, 116.03, 55.20, 55.17, 40.46, 40.41, 31.52, 31.49, 29.69, 29.65, 23.79, 23.74, 22.56, 22.53, 14.00, 13.96. HRMS (+ESI): $C_{56}H_{70}N_2$ $[M+H]^+$ calcd. m/z = 771.5612, found m/z = 771.5550.

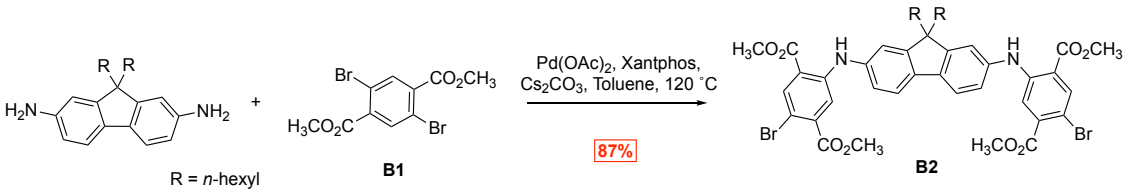

B2: 2,7-Diamino-9,9-dihexylfluorene (0.19 g, 0.54 mmol), dimethyl 2,5-dibromoterephthalate **B1** (0.75 g, 2.14 mmol), $Pd(OAc)_2$ (12 mg, 0.054 mmol), Xantphos (47 mg, 0.081 mmol), and Cs_2CO_3 (1.05 g, 3.24 mmol) were mixed in 10 mL of dry toluene in a 50 mL-Schlenk tube. After freeze-pump-thaw for 3 times, the mixture was heated at 120 ˚C and stirred for 12 h. After cooling down, the mixture was diluted in dichloromethane and filtered through a Celite pack and concentrated by the rotatory evaporator. It was further purified by flash column chromatography (SiO_2, hexane/ethyl acetate: v/v = 7/1). The product was isolated as a yellow powder (0.42 g, 87%). ^{1}H NMR (500 MHz, $CDCl_3$, 298 K, ppm): δ = 0.68 (qd, 4H, J_1 = 3.2 Hz, J_2 = 2.5 Hz, 4H), 0.77 (t, J = 7.1 Hz, 6H), 1.07-1.16 (m, 12H), 1.92 (m, 4H), 3.86 (s, 6H), 3.95 (s, 6H), 7.16 (d, J = 1.9 Hz, 2H,), 7.20 (dd, J = 8.0 Hz, 2H), 7.64 (d, J = 8.0 Hz, 2H), 8.21 (s, 2H), 9.54 (s, 2H).

^{13}C NMR (125 Hz, $CDCl_3$, 298 K, ppm): δ = 167.61, 166.62, 152.61, 147.23, 138.50, 137.61, 137.49, 136.71, 121.96, 120.50, 117.79, 116.51, 114.62, 105.85, 55.48, 52.84, 52.52, 40.71, 31.78, 30.04, 24.14, 22.87, 14.19. HRMS (+ESI): $C_{45}H_{50}Br_2N_2O_8$ $[M+H]^+$ calcd. *m/z* = 907.1987, found *m/z* = 907.1954.

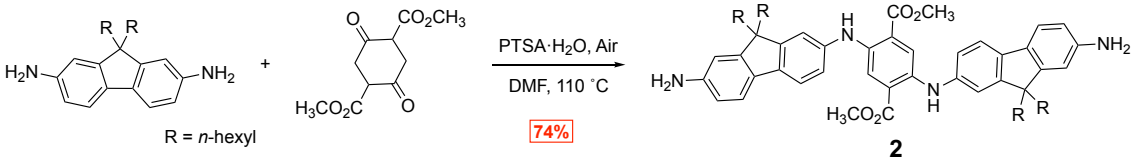

Compound **2**: 2,7-Diamino-9,9-hexyl-fluorene (0.65 g, 1.78 mmol), DMSS (0.16 g, 0.70 mmol), and PTSA·H_2O (30 mg, 0.14 mmol) was dissolved in DMF (10 mL). The mixture was heat to 110 ˚C under N_2 for 4 h and exposed to air for 8 h. After cooling down, the mixture was poured into water and extracted with ethyl acetate (3 × 10 mL). The combined organic layer was washed with water and brine. After removing the solvent under reduced pressure, the crude product was purified by flash column chromatography (SiO_2, hexane/ethyl acetate: v/v = 6/1). The pure product was isolated as a dark red powder (0.60 g, 74%). ^{1}H NMR (500 MHz, $CDCl_3$, 298 K, ppm): δ = 0.72 (m, 8H), 0.75-0.85 (t, 12H), 0.97-1.19 (m, 24H), 1.87 (t, 8H, *J* = 8.3 Hz), 3.73 (br, 4H), 3.85 (s, 6H), 6.61-6.71 (m, 4H), 7.06-7.14 (m, 4H), 7.42 (d, 2H, *J* = 8.3 Hz), 7.50 (d, 2H, *J* = 8.0 Hz), 8.01 (s, 2H), 8.86 (s, 2H). ^{13}C NMR (126 Hz, $CDCl_3$, 298 K, ppm): δ = 14.0, 22.7, 23.8, 29.9, 31.6, 40.8, 52.2, 54.8, 110.0, 113.9, 115.0, 117.9, 118.3, 119.0, 119.7, 132.5, 136.3, 138.2, 139.6, 145.2, 151.4, 152.2, 168.2. HRMS (+ESI): $C_{60}H_{78}N_4O_4$ $[M+H]^+$ calcd. *m/z* = 919.6096, found *m/z* = 919.6071.

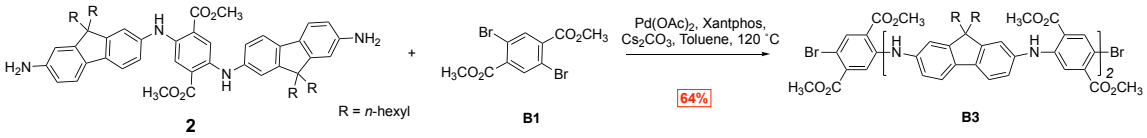

B3: Compound **2** (0.12 g, 0.13 mmol), dimethyl 2,5-dibromoterephthalate **B1** (0.18 g, 0.52 mmol), $Pd(OAc)_2$ (3 mg, 0.013 mmol), Xantphos (12 mg, 0.019 mmol), and Cs_2CO_3 (0.17 g, 0.52 mmol) were mixed in 5 mL of anhydrous toluene in a 50 mL Schlenk tube. After freeze-pump-thaw for 3 times, the reaction was heated to 110 ˚C under nitrogen protection and stirred for 12 h. After cooling down, the mixture was diluted with dichloromethane and filtered through a Celite pack and concentrated by a rotatory evaporator. It was further purified by flash column chromatography (SiO_2, hexane/ethyl acetate: v/v = 20/1 ~ 5/1). The pure product was isolated as a red powder (0.19 g, 64%). ^{1}H NMR (500 MHz, $CDCl_3$, 298 K, ppm): δ = 0.77 (m, 20H), 1.12 (m, 32H), 1.92 (t, 8H, J = 8.4 Hz), 3.86 (s, 6H), 3.88 (s, 6H), 3.96 (s, 6H), 7.17 (m, 8H), 7.56 (s, 2H), 7.61 (dd, 4H, J_1 = 7.9, J_2 = 3.3 Hz), 8.09 (s, 2H), 8.21 (s, 2H), 8.97 (s, 2H), 9.52 (s, 2H). ^{13}C NMR (126 Hz, $CDCl_3$, 298 K, ppm): δ =14.1, 22.7, 23.8, 24.0, 24.7, 29.9, 30.0, 31.6, 36.6, 40.6, 40.7, 52.3, 52.7, 54.9, 55.2, 105.4, 114.2, 116.2, 116.2, 117.9, 118.3, 118.6, 118.7, 119.8, 120.2, 121.9, 122.0, 135.1, 136.4, 136.5, 137.6, 137.9, 138.1, 140.9, 147.3, 152.1, 152.3, 166.5, 167.5, 168.1. HRMS (+ESI): $C_{80}H_{92}Br_2N_4O_{12}$ $[M+H]^+$ calcd. m/z = 1461.5153, found m/z = 1461.5086.

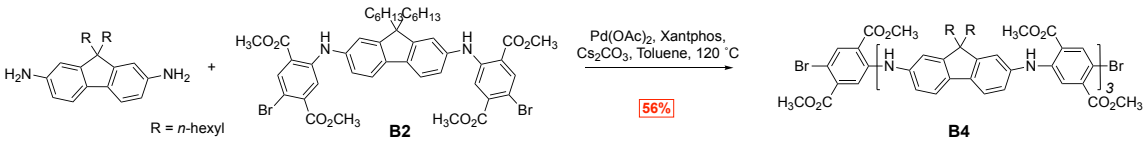

B4: 2,7-Diamino-9,9-dihexylfluorene (16 mg, 0.044 mmol), **B2** (0.16 g, 0.18 mmol), $Pd(OAc)_2$ (2.4 mg, 0.01 mmol), Xantphos (10 mg, 0.015 mmol), and Cs_2CO_3 (0.14 g, 0.42

mmol) were mixed in 5 mL of dry toluene in a 50 mL Schlenk tube. After freeze-pump-thaw for 3 times, the reaction was heated up to 130 ˚C under nitrogen and stirred for 12 h. After cooling down, the mixture was diluted in dichloromethane and filtered through a Celite pack. Followed by being concentrated by a rotatory evaporator, the crude product was further purified by flash column chromatography (SiO_2, hexane/ethyl acetate: v/v = 20/1 ~ 7/1). The pure product was isolated as a red powder (80 mg, 56%). ^{1}H NMR (500 MHz, $CDCl_3$, 298 K, ppm): δ = 0.72 (m, 12H), 0.78 (m, 18H), 0.99-1.20 (m, 36H), 1.92 (t, 12H, J = 8.4 Hz), 3.86 (s, 6H), 3.88 (s, 6H), 3.89 (s, 6H), 3.96 (s, 6H), 7.10-7.21 (m, 12H), 7.55 (s, 2H), 7.57-7.61 (m, 4H), 8.07 (s, 2H), 8.09 (s, 2H), 8.21 (s, 2H), 8.94 (s, 2H), 8.96 (s, 2H), 9.52 (s, 2H). ^{13}C NMR (126 MHz, $CDCl_3$, 298 K, ppm) δ = 168.1, 167.4, 166.5, 152.3, 152.1, 152.0, 147.3, 141.0, 140.2, 138.3, 138.1, 137.6, 137.3, 136.5, 135.8, 134.9, 121.9, 120.2, 119.7, 119.0, 118.8, 118.6, 118.3, 118.1, 117.9, 116.2, 114.8, 114.2, 105.4, 105.1, 55.2, 52.6, 52.3, 40.7, 31.7, 30.0, 29.7, 23.9, 22.7, 14.0. HRMS (+ESI): $C_{115}H_{134}Br_2N_6O_{16}$ $[M+H]^+$ calcd. m/z = 2016.8236, found m/z = 2016.9336.

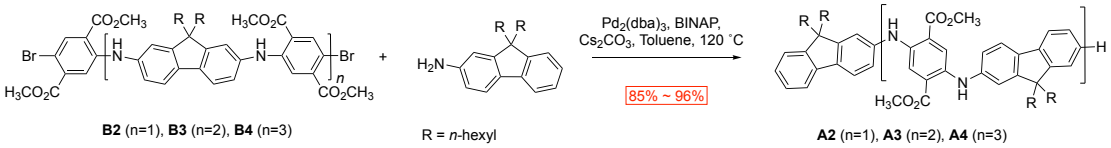

B2 (n=1), **B3** (n=2), **B4** (n=3)

A2 (n=1), **A3** (n=2), **A4** (n=3)

General Procedure to A2, A3, A4: Compound **Bn** (n=1, 2, 3) (*ca.* 0.1 mmol scale, 1 equiv.), 2-amino-9,9-dihexyl-fluorene (3 equiv.), $Pd_2(dba)_3$ (10 mol%), BINAP (30 mol%), and Cs_2CO_3 (4 equiv.) mixed dissolved in 5 mL dry toluene in a Schlenk flask. After freeze-pump-thaw for 3 times, the reaction was heat to 120 ˚C under nitrogen for 12 h. After cooling down to room temperature, the mixture was diluted by dichloromethane

and filtered through Celite. After removing the solvent, the crude product was recrystallized in methanol to give the pure product.

A2: Red solid (0.15 g, 85%). ^{1}H NMR (500 MHz, $CDCl_3$, 298 K, ppm): δ = 0.78 (m, 18H), 1.10 (m, 48H), 1.95 (m, 12H), 3.88 (d, 12H, J = 1.1Hz), 7.11-7.21 (m, 8H), 7.31 (ddd, 4H, J_1 = 7.1, J_2 = 6.2, J_3 = 1.4 Hz), 7.56-7.69 (m, 8H), 8.08 (dd, 4H, J_1 = 13.3, J_2 = 1.0 Hz), 8.94 (d, 4H, J = 10.5 Hz). ^{13}C NMR (125 Hz, $CDCl_3$, 298 K, ppm): δ = 14.01, 22.64, 23.81, 29.86, 31.56, 40.52, 52.28, 55.01, 114.23, 114.81, 118.07, 118.35, 118.57, 118.76, 118.98, 119.71, 120.47, 122.77, 126.03, 135.52, 135.75, 137.73, 138.27, 140.23, 141.13, 150.21, 152.02, 152.44, 168.10. HRMS (+ESI): $C_{95}H_{118}N_4O_8$ $[M+H]^+$ calcd. *m/z* = 1443.8983, found *m/z* = 1443.8986.

A3: Red solid (0.14 g, 95%). ^{1}H NMR (500 MHz, $CDCl_3$, 298 K, ppm): δ = 0.59-0.78(m, 40H), 0.99-1.31 (m, 48H), 1.94 (t, 16H, J = 8.4 Hz), 3.88 (d, 18H, J = 2.9 Hz), 7.12-7.20 (m, 12H), 7.29-7.34 (m, 4H), 7.59 (d, 4H, J = 8.0 Hz), 7.64 (m, 4H), 8.07 (d, 4H, J = 3.8 Hz), 8.09 (s, 2H), 8.95 (d, 6H, J = 10.2 Hz). ^{13}C NMR (126 MHz, $CDCl_3$, 298 K, ppm) δ = 168.32, 168.24, 152.61, 152.20, 150.42, 141.33, 141.21, 140.47, 140.39, 138.46, 138.25, 137.90, 135.94, 135.87, 135.70, 126.86, 126.19, 122.93, 120.62, 119.86, 119.18, 119.10, 119.01, 118.94, 118.76, 118.67, 118.51, 118.31, 118.23, 115.01, 114.93, 114.42, 77.40, 77.15, 76.89, 55.23, 55.17, 52.41, 40.81, 40.66, 31.80, 31.71, 30.15, 30.00, 29.85, 24.09, 23.97, 22.86, 22.78, 14.16, 14.14. HRMS (+ESI): $C_{130}H_{160}N_6O_{12}$ $[M+H]^+$ calcd. *m/z* = 1999.2201, found *m/z* = 1999.2889.

A4: Red solid (0.12 g, 96%). ^{1}H NMR (500 MHz, $CDCl_3$, 298 K, ppm): δ =0.60-0.83 (m, 50H), 0.95-1.22 (m, 60H), 1.81-2.03 (m, 40H), 3.81-3.91 (m, 24H), 7.12-7.20 (m, 16H),

7.31 (m, 6H), 7.58-7.66 (m, 10H), 8.00-8.11 (m, 8H), 8.86-8.99 (m, 8H). ^{13}C NMR (125 MHz, $CDCl_3$, 298 K, ppm) δ = 168.1, 152.5, 152.0, 150.2, 141.1, 140.3, 140.2, 138.3, 138.1, 137.7, 135.8, 135.7, 135.5, 126.7, 126.0, 122.8, 120.5, 119.7, 119.0, 118.9, 118.8, 118.6, 118.5, 118.4, 118.1, 114.8, 114.2, 55.1, 55.0, 52.3, 40.7, 40.5, 31.7, 31.6, 30.0, 29.9, 24.0, 23.8, 22.7, 14.0. HRMS (+MALDI-TOF): $C_{165}H_{202}N_8O_{16}$ $[M+H]^+$ calcd. *m/z* = 2552.5212, found *m/z* = 2552.5985.

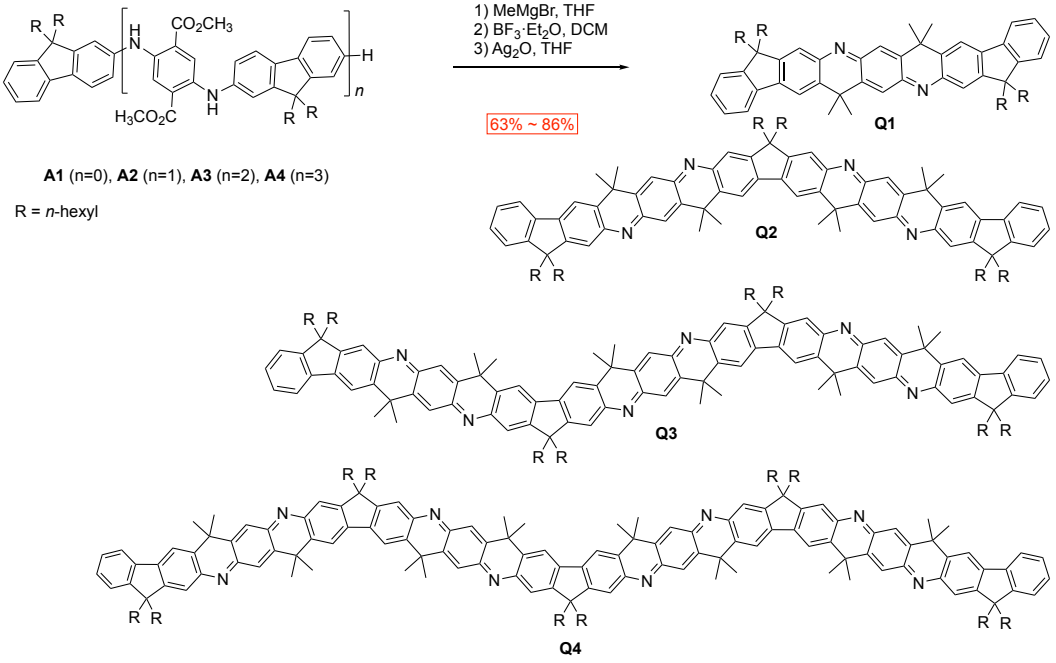

General Procedure to Q1, **Q2**, **Q3**, and **Q4**: To a solution of methylmagnesium bromide (3 M in diethyl ester) in dry THF (10n equiv.), a THF solution of **An** (n = 1, 2, 3, 4) (*ca.* 0.1 mmol, 1 equiv.) was added dropwise at 0 ˚C in 30 min. The reaction mixture was heat up to 35 ˚C for 12 h. After cooled to room temperature, the reaction was quenched with saturated aqueous ammonia chloride solution. Ethyl acetate was used to extract the mixture for 3 times. The combined organic layer was washed with brine. After dried with anhydrous sodium sulfonate, the solvent was removed and the residue was redissolved in

dry dichloromethane. Boron trifluoride diethyl etherate (1 M) (1 equiv.) was added into the solution. The reaction was run under nitrogen protection at room temperature for 12 h and quenched with NaOH aqueous solution (1 M). After extraction with ethyl acetate, the combined organic layer was washed with brine. After removing the solvent, the crude product was directly used in the following oxidation step. The crude product was redissolved in THF. Ag_2O (*ca.* 50 mg) was subsequently added into the solution and the mixture was stirred in air for 12 h. After filtered, the solution was concentrated under reduced pressure. **Q1** was purified with flash column chromatography (SiO_2, hexane/CH_2Cl_2: v/v = 3/1). **Q2**, **Q3**, and **Q4** were first purified by flash column chromatography (SiO_2, hexane/ethyl acetate), then further purified by preparation SEC with chloroform as the eluent.

Q1: Dark red solid (1.03 g, 63%). ^{1}H NMR (500 MHz, $CDCl_3$, 298 K, ppm): δ = 0.70 (m, 8H), 0.78 (t, 12H, J = 7.2 Hz), 0.94-1.19 (m, 24H), 1.70 (s, 12H), 2.01 (pd, 8H, J_1 = 13.2 Hz, J_2 = 5.0 Hz), 7.26 (s, 2H), 7.37 (m, H), 7.54 (s, 2H), 7.77 (d, 2H, J = 7.4 Hz), 7.80 (s, 2H). ^{13}C NMR (125 MHz, $CDCl_3$, 298 K, ppm) δ = 154.27, 151.83, 150.14, 142.84, 142.26, 142.03, 140.35, 136.36, 131.16, 127.63, 126.89, 124.41, 122.99, 119.93, 116.84, 54.90, 40.45, 37.05, 33.42, 31.55, 29.77, 23.88, 22.62, 13.99. HRMS (+ESI): $C_{62}H_{78}N_2$ $[M+H]^+$ calcd. *m/z* = 851.6238, found *m/z* = 851.6233.

Q2: Dark purple powder (0.12 g, 86%). ^{1}H NMR (500 MHz, $CDCl_3$, 298 K, ppm): δ = 0.58-0.73 (m, 12H), 0.77 (t, 18H, J = 7.2 Hz), 0.97-1.22 (m, 36H), 1.72 (s, 12H), 1.76 (s, 12H), 2.01 (m, 12H), 7.27 (s, 2H), 7.29 (s, 2H), 7.35 (m, 6H), 7.52 (s, 2H), 7.53 (s, 2H), 7.74 (m, 2H), 7.78 (s, 2H), 7.82 (s, 2H). ^{13}C NMR (125 MHz, $CDCl_3$, 298 K, ppm) δ =

154.50, 154.18, 151.84, 151.31, 150.17, 143.43, 142.85, 142.15, 142.09, 141.16, 140.30, 136.70, 136.40, 135.19, 131.32, 131.08, 127.69, 126.91, 125.00, 124.45, 122.99, 119.95, 117.19, 116.88, 54.89, 54.71, 40.54, 40.44, 37.08, 33.49, 33.42, 32.19, 31.61, 31.55, 29.82, 29.76, 26.38, 24.01, 23.87, 23.42, 22.67, 22.61, 13.99. HRMS (+ESI): $[M+H]^+$ calcd. *m/z* = 1368.9781, found *m/z* = 1368.9738.

Q3: Dark blue powder (20 mg, 72%). ^{1}H NMR (500 MHz, $CDCl_3$, 298 K, ppm): δ = 0.76 (m, 40H), 0.93-1.18 (m, 48H), 1.57 (s, 12H), 1.70 (s, 12H), 1.74 (s, 12H), 2.01 (m, 16H), 7.27 (s, 2H), 7.29 (s, 2H), 7.30 (s, 2H), 7.32-7.39 (m, 6H), 7.53 (s, 6H), 7.75 (d, 2H, *J* = 7.0 Hz), 7.78 (s, 2H), 7.82 (s, 4H). ^{13}C NMR (125 MHz, $CDCl_3$, 298 K, ppm) δ = 154.53, 154.43, 154.16, 153.30, 151.84, 151.34, 150.17, 144.40, 143.46, 142.84, 142.44, 142.17, 142.07, 141.39, 141.29, 141.12, 140.30, 136.75, 136.41, 131.35, 131.25, 131.07, 127.68, 126.93, 124.51, 124.44, 123.00, 119.96, 117.23, 116.89, 54.89, 54.71, 40.55, 40.45, 37.13, 33.50, 33.42, 31.62, 31.55, 29.72, 24.02, 23.87, 22.68, 22.62, 14.01. HRMS(+ESI): $C_{136}H_{166}N_6$ $[M+2H]^{2+}$ calcd. *m/z* = 943.6660, found *m/z* = 943.6690.

Q4: Dark blue powder (27 mg, 73%). ^{1}H NMR (500 MHz, $CDCl_3$, 298 K, ppm): δ 7.83 (m, 8H), 7.78 (d, *J* = 5.7 Hz, 2 H), 7.56 (m, 8H), 7.36 (m, 6H), 7.33-7.21 (m, 8H), 2.05 (m, 20H), 1.75 (m, 48H), 1.22-1.00 (m, 60H), 0.79 (m, 50H). ^{13}C NMR (126 MHz, d_8-THF, 298 K, ppm) δ = 155.07, 155.04, 155.03, 154.89, 152.21, 151.46, 151.43, 150.36, 144.76, 144.71, 144.30, 142.66, 142.60, 142.55, 142.54, 142.45, 142.16, 142.08, 141.56, 141.47, 137.40, 137.37, 137.09, 131.94, 131.82, 131.44, 131.08, 128.95, 128.13, 127.92, 127.52, 125.34, 123.46, 120.70, 118.21, 117.63, 55.44, 55.18, 41.08, 37.59, 33.39, 32.38,

32.32, 30.63, 30.53, 23.39, 23.31, 14.18. HRMS (+MALDI-TOF): $C_{173}H_{210}N_8$ $[M+H]^+$ calcd. *m/z* = 2401.6785, found m/z = 2401.4970.

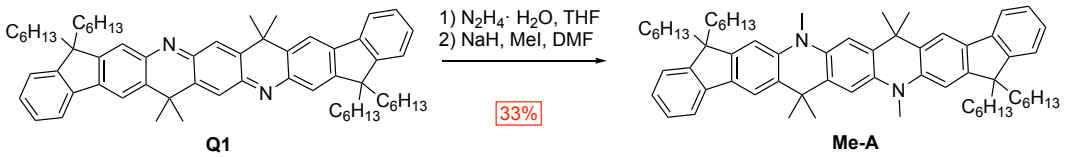

Me-A: **Q1** (0.45 g, 0.53 mmol) was dissolved in degassed THF under N_2 protection. $N_2H_4 \cdot H_2O$ (0.26 mL, 5.3 mmol) was added slowly and the mixture was stirred at 40 ˚C for 12 h. The solution turned from red to light yellow. It was then cooled to room temperature and the solvent and excess hydrazine was removed under reduced pressure. After dried under vacuum, the crude product was charged into the next step without further purification. It was redissolved in 10 mL anhydrous DMF and sodium hydride (88 mg, 60%, 2.2 mmol) was added. The mixture was heat to 60 ˚C and stirred for 1 h. After cooling to 35 ˚C, methyl iodide (0.23 mL, 4.1 mmol) was added slowly into the mixture. The reaction was stirred for 12 h before being quenched by water. The mixture was then extracted by dichloromethane for 3 times. The combined organic layer was washed by water. After dried against magnesium sulfonate, the crude product was purified using flash column (SiO_2, hexane/ethyl acetate: v/v = 9/1). The pure product was isolated as a white powder with purple fluorescence (0.13 g, 33%). ^{1}H NMR (500 MHz, $CDCl_3$, 298 K, ppm) δ = 7.70 (s, 2H), 7.64 (d, *J* = 7.5 Hz, 4H), 7.29 (m, 4H), 7.18 (t, *J* = 7.3 Hz, 2H), 7.09 (s, 2H), 6.83 (s, 2H), 3.57 (s, 6H), 1.93 (m, 8H), 1.65 (s, 12H), 1.17-0.94 (m, 24H), 0.75 (t, *J* = 7.1 Hz, 12H), 0.69-0.52 (m, 8H). ^{13}C NMR (125 MHz, $CDCl_3$, 298 K, ppm) δ = 150.35, 149.59, 142.96, 142.09, 136.95, 133.43, 131.60, 131.25, 126.67, 125.33, 122.75, 118.43,

114.90, 108.18, 106.43, 54.99, 40.82, 37.10, 34.11, 31.66, 29.96, 27.61, 23.87, 22.78, 14.16. HRMS(+ESI): $C_{64}H_{84}N_2$ $[M\cdot]^+$ calcd. *m/z* = 880.6629, found *m/z* = 880.6610.

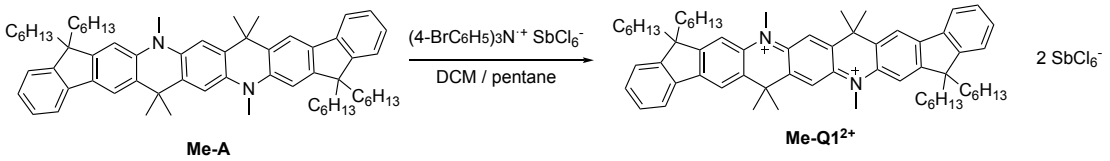

Me-Q1$^{2+}\cdot$**2SbCl$_6^-$** : **Me-A** (10.7 mg, 0.01 mmol) was dissolved in anhydrous dichloromethane (3 mL). Tris(4-bromophenyl)ammoniumyl hexachloroantimonate ("magic blue", 18.4 mg, 0.022 mmol) was added into the solution and the mixture was stirred in a nitrogen-filled glovebox for 10 min, turning the color from color-less into deep-blue. The solution was filtered through a syringe filter (PTFE, 0.45 μm) into a clean 20 mL vial and pentane was then layered above. The single crystal was obtained after diffusion for 2 days and collected by filtration.

3.7.3 Determination of Energy Levels of Frontier Molecular Orbitals

The redox properties of oligomers **Q1 ~ Q4** and **NLQ** and the corresponding energy levels of frontier orbitals were determined by CV and DPV carried out at room temperature under argon protection with a CHI720 voltammetric analyzer. $TBAPF_6$ in anhydrous dichloromethane (0.1 M) was used. A conventional 3-electrode configuration was used, including a 3-mm glassy carbon working electrode, a Pt wire auxiliary electrode, and an Ag wire pseudoreference electrode with electrolyte solution ($AgNO_3$ 10 mM in dichloromethane) freshly prepared in glovebox right before the measurement. Scan rate was 100 mV/s for CV test and 40 mV/s for DPV test. Ferrocene was used as an exterior reference for determination of potentials and energy levels. The onset potentials of CV

oxidation and reduction processes were used to determine the HOMO and LUMO levels, respectively.

In DFT calculation, the atomic structures of **Q2** ~ **Q4** were optimized at B3LYP/6-311G(d,p) level of theory. Molecular orbitals and energies were calculated based on single crystal structure of **Q1** and the optimized geometries of **Q2** ~ **Q4**. The alkyl chains are replaced with methyl groups for computational simplicity. Orbital pictures were generated with GaussView 5.08.

3.7.4 Protonation Study

To record the optical spectra of **NLQ** after protonation, **NLQ** was dissolved in THF and diluted into a solution of 1.1×10^{-5} M. UV-vis absorption of **NLQ** solution (2.5 mL) was measured in a 1-cm quartz cuvette. MSA was dissolved in THF (1.54 M) and added into the cuvette in portions of 2, 4, 6, 10, 20, 30, 50, 70, 110, 150, and 250 μL. For experiments with high acid concentrations, **NLQ** was dissolved in nitrogen-bubbled solutions of MSA/THF (0.15, 1.54, 3.08, 7.7, and 15.4 M) and measured.

During the first protonation stage of **Q1**, a solution of MSA/THF (0.5 M) was added into **Q1** solution (2.5 mL, 2.2×10^{-5} M) by 1.5, 2.5, 3.5, 4.5, 5.5, 6.5, 8.5, 25, and 45 μL. During the second protonation stage, **Q1** was dissolved in a mixed solvent of MSA in THF (1.5 M), affording a fully protonated **Q1** solution (2.2×10^{-5} M). This fully protonated solution was added into the neutral **Q1** solution (1 mL) of the same concentration in steps of 10, 30, 90, 150, 210, 290, 350, 450, 650, and 910 μL.

PTSA was used for solid-state acid-doping. The acid was first dissolved in THF. **Qn** was dissolved in the PTSA solutions of varies volumes. The resulting mixtures were drop-cast on glass slides and dried in a desiccator for over 12 h under reduced pressure before measuring the UV-vis-NIR absorption.

3.7.5 Degradation Study

The degradation study of **Qn** and **NLQ** was performed with UV-vis absorption measurement. Solutions (*ca.* 10^{-5} M) were prepared by dissolving **Qn** and **NLQ** in a solution of MSA/THF (0.8 M). UV-vis absorption was measured every 5 min at room temperature at ambient condition for 70 min.

The structural integrity of **Q1** after protonation was further confirmed by NMR spectroscopy. ^{1}H NMR spectrum of **Q1** in TFA/$CDCl_3$ (0.44 M) remained identical after 24 h. The basic form of **Q1** was subsequently regenerated by adding KOH into the solution, showing a ^{1}H NMR spectrum identical to that of **Q1** before the acid/base treatment. These results confirmed that protonated **Q1** did not undergo significant decomposition or redox transformation in ambient conditions in the time scale of hours.

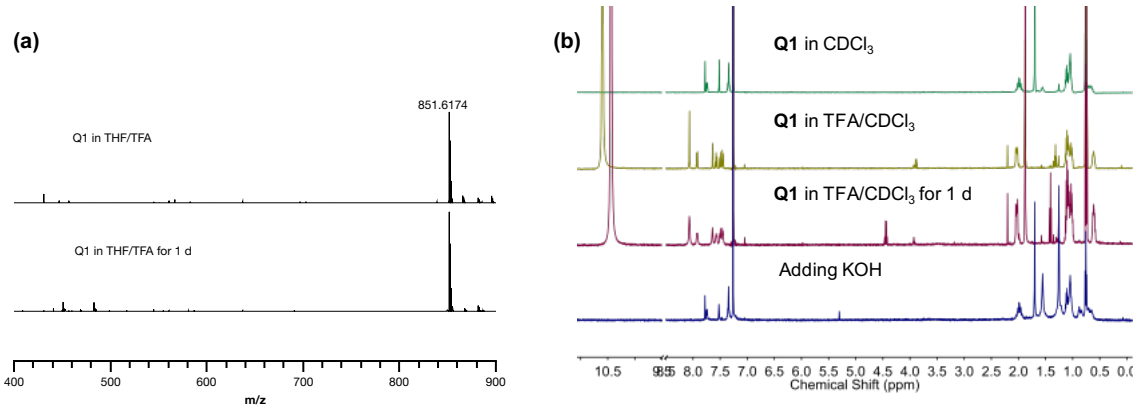

Figure 51. (a) HRMS of Q1 in TFA/THF (v/v = 1/10). (b)^{1}H NMR (500 MHz, 298 K) spectra of Q1 in $CDCl_3$, adding TFA (v/v = 1/1), after 1 day, and after adding KOH. Reprinted with permission from [134].

3.7.6 X-ray Crystallography

A Leica MZ 75 microscope was used to identify a representative sample of crystals of the same habit. The crystal mounted on a nylon loop was then placed in a cold nitrogen stream (Oxford) maintained at 100 K. A BRUKER Venture X-ray (kappa geometry) diffractometer was employed for crystal screening, unit cell determination, and data collection. The goniometer was controlled using the APEX3 software suite. The sample was optically centered with the aid of a video camera such that no translations were observed as the crystal was rotated through all positions. The X-ray radiation employed was generated from a Cu-Iμs X-ray tube (K_α = 1.5418Å with a potential of 50 kV and a current of 1.0mA). 45 data frames were taken at widths of 1°. These reflections were used to determine the unit cell. The unit cell was verified by examination of the *h k l* overlays on several frames of data. No super-cell or erroneous reflections were observed. After careful examination of the unit cell, an extended data collection procedure (30 sets) was initiated using omega and phi scans. Integrated intensity information for each reflection

was obtained by reduction of the data frames with the program APEX3. The integration method employed a three-dimensional profiling algorithm and all data were corrected for Lorentz and polarization factors, as well as for crystal decay effects. Finally, the data was merged and scaled to produce a suitable data set. The absorption correction program SADABS was employed to correct the data for absorption effects. A solution was obtained readily (Z=1; Z'=0.5) using XT/XS in APEX3. Hydrogen atoms were placed in idealized positions and were set riding on the respective parent atoms. All non-hydrogen atoms were refined with anisotropic thermal parameters. Appropriate restraints and constraints were used to keep the bond distances, angles and thermal ellipsoids meaningful. Absence of additional symmetry or void were confirmed using PLATON (ADDSYM). The structure was refined (weighted least squares refinement on F^2) to convergence. Olex2 was employed for the final data presentation and structure plots.

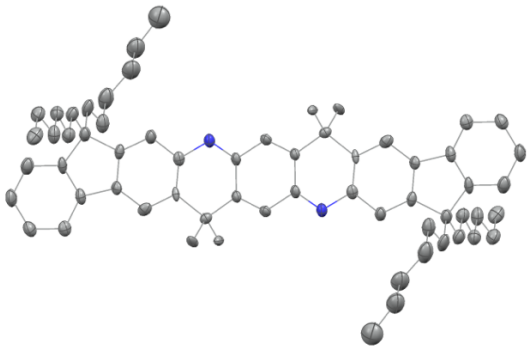

Figure 52. Single crystal structures of Q1. Hydrogen atoms and solvent molecules were omitted for the sake of clarity. Thermal ellipsoids are scaled to the 50% probability level. Reprinted with permission from [134].

3.8 Appendix

Table 4. Measured and calculated HOMO and LUMO levels of Q1 ~ Q4. Reprinted with permission from [134].

Compound	$HOMO_{exp}$ (eV)	$LUMO_{exp}$ (eV)	$HOMO_{DFT}$ (eV)	$LUMO_{DFT}$ (eV)
Q1	–5.56	–3.30	–5.19	–2.91
Q2	–5.08	–3.32	–4.78	–2.86
Q3	–5.24	–3.55	–4.98	–3.18
Q4	–4.98	–3.56	–4.95	–3.23

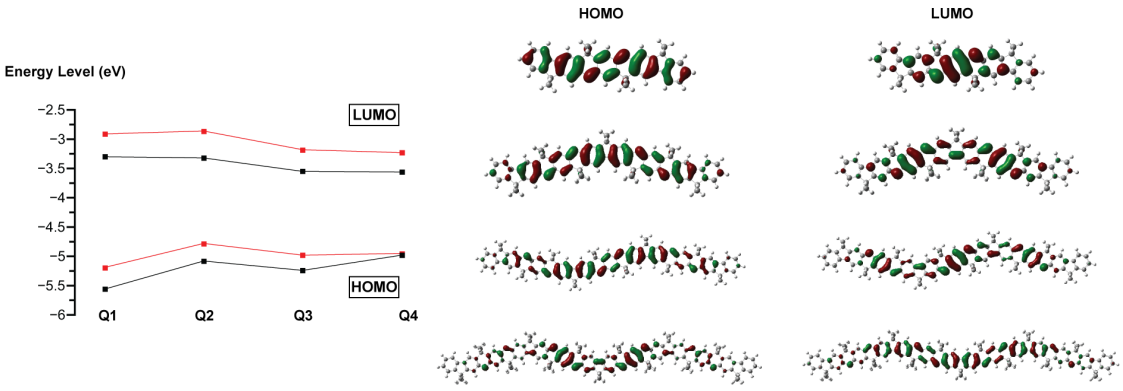

Figure 53. (left) Energy levels of frontier orbitals of Qn (n = 1 ~ 4) measured by CV (black) and calculated using DFT (red); (right) Diagrams of HOMOs and LUMOs of Qn (n = 1 ~ 4) generated by DFT calculation. Reprinted with permission from [134].

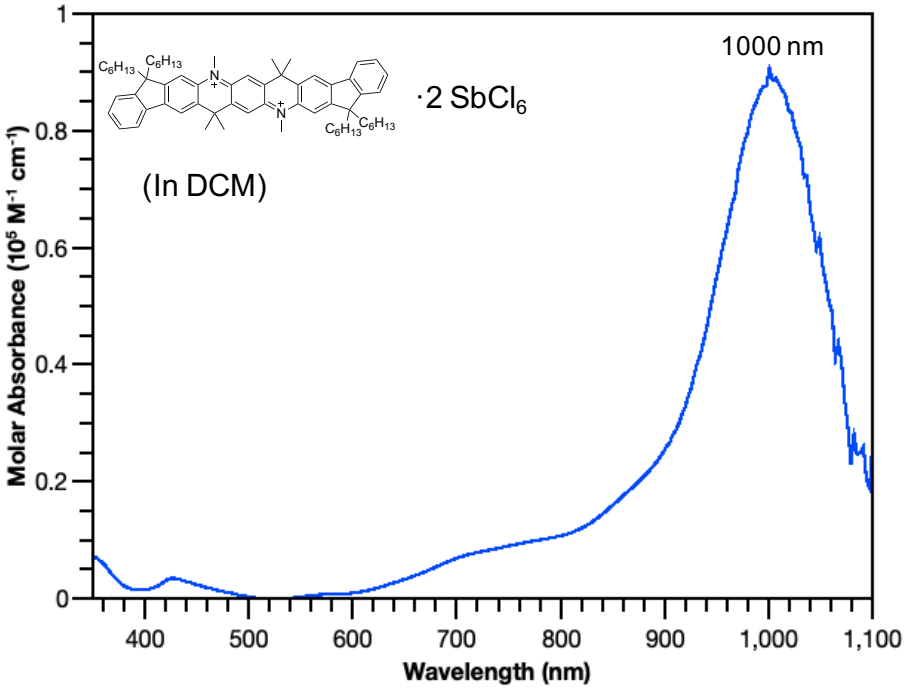

Figure 54. UV-vis-NIR absorption spectrum of Me-Q1^{2+}·2 SbCl^{6-} in dichloromethane. Reprinted with permission from [134].

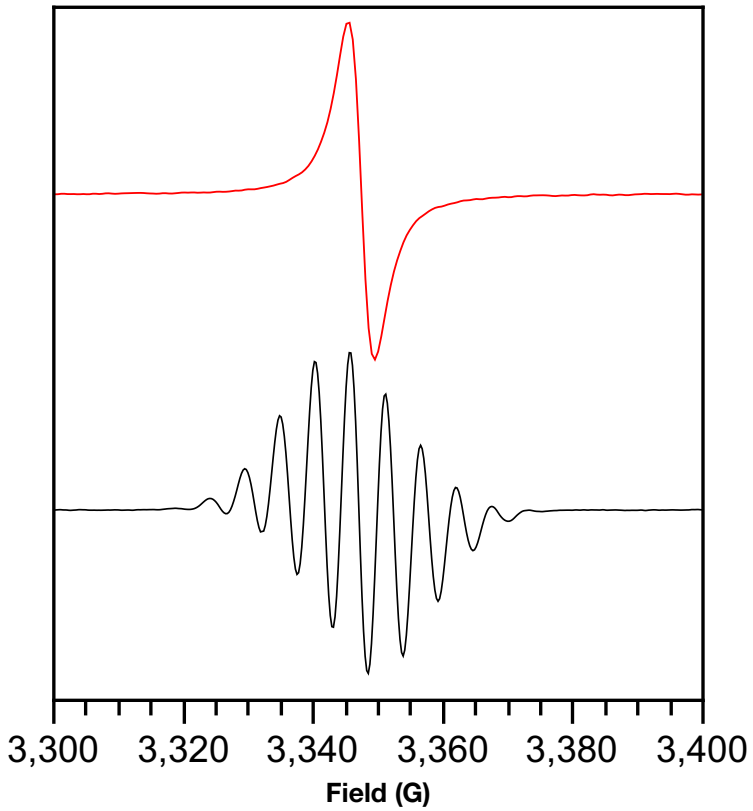

Figure 55. EPR spectra of Me-Q1^{2+}·2 SbCl^{6-} in solid state (red) and in dichloromethane solution (black) at room temperature. Reprinted with permission from [134].

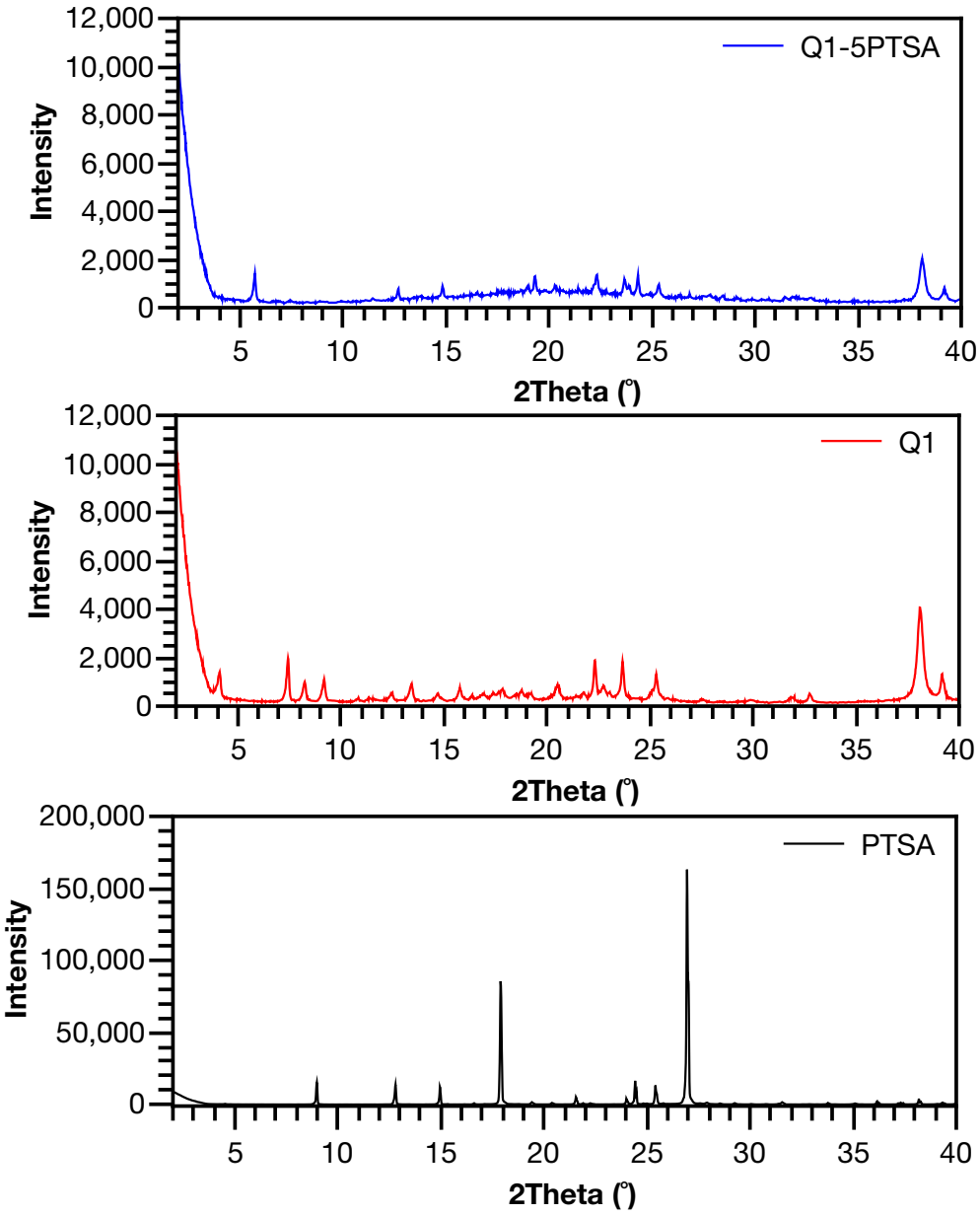

Figure 56. Powder X-ray diffraction spectra of Q1, PTSA, and Q1 mixed with 5 equiv. PTSA. Reprinted with permission from [134].

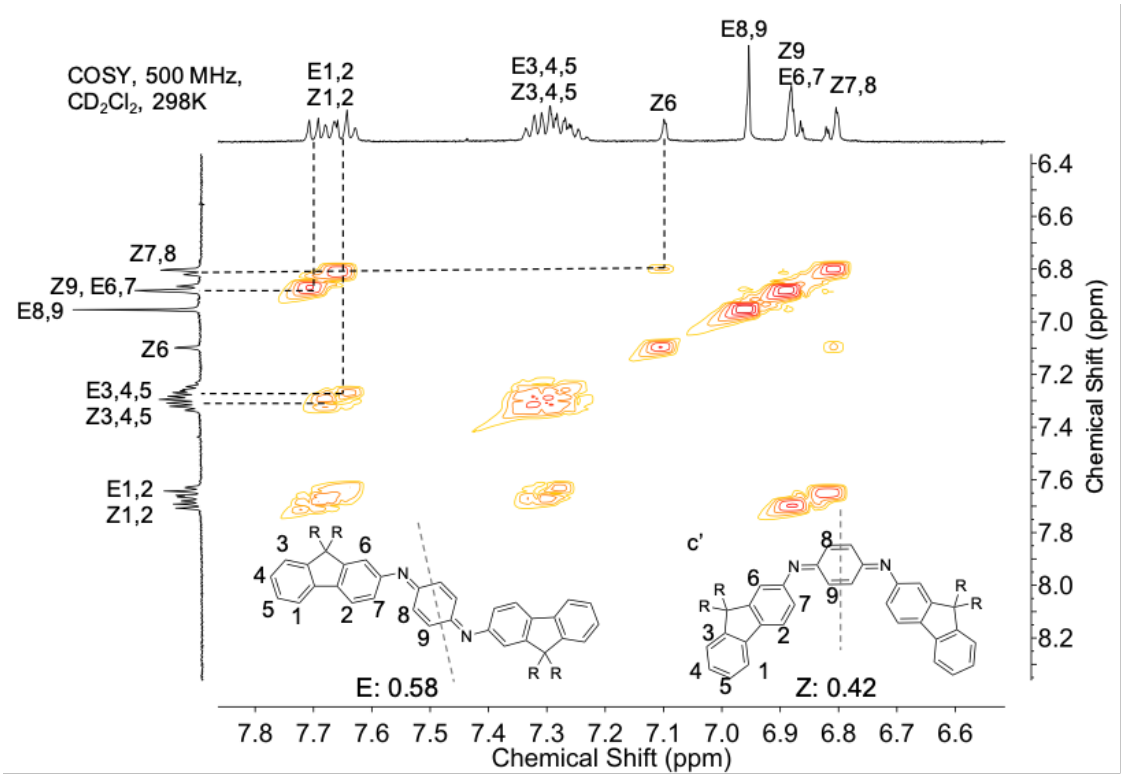

Peak	Integral (theoretical proton numbers)
E1,2 + Z1,2	2 *(2x+2y)*
E3,4,5 + Z3,4,5	3.2 *(3x+3y)*
Z6	0.42 *(y)*
E8,9	1.13 *(2x)*
E6,7 + Z9	1.60 *(2x+y)*
Z7,8	0.87 *(2y)*

Figure 57. ^{1}H-^{1}H COSY spectrum of NLQ in CD_2Cl_2 at room temperature and the peak assignments. The integral of peak (*E*1,2 + *Z*1,2) was set as 2 protons. The molar percentage of *E* and *Z* isomers were set to be *x* and *y*. Reprinted with permission from [134].

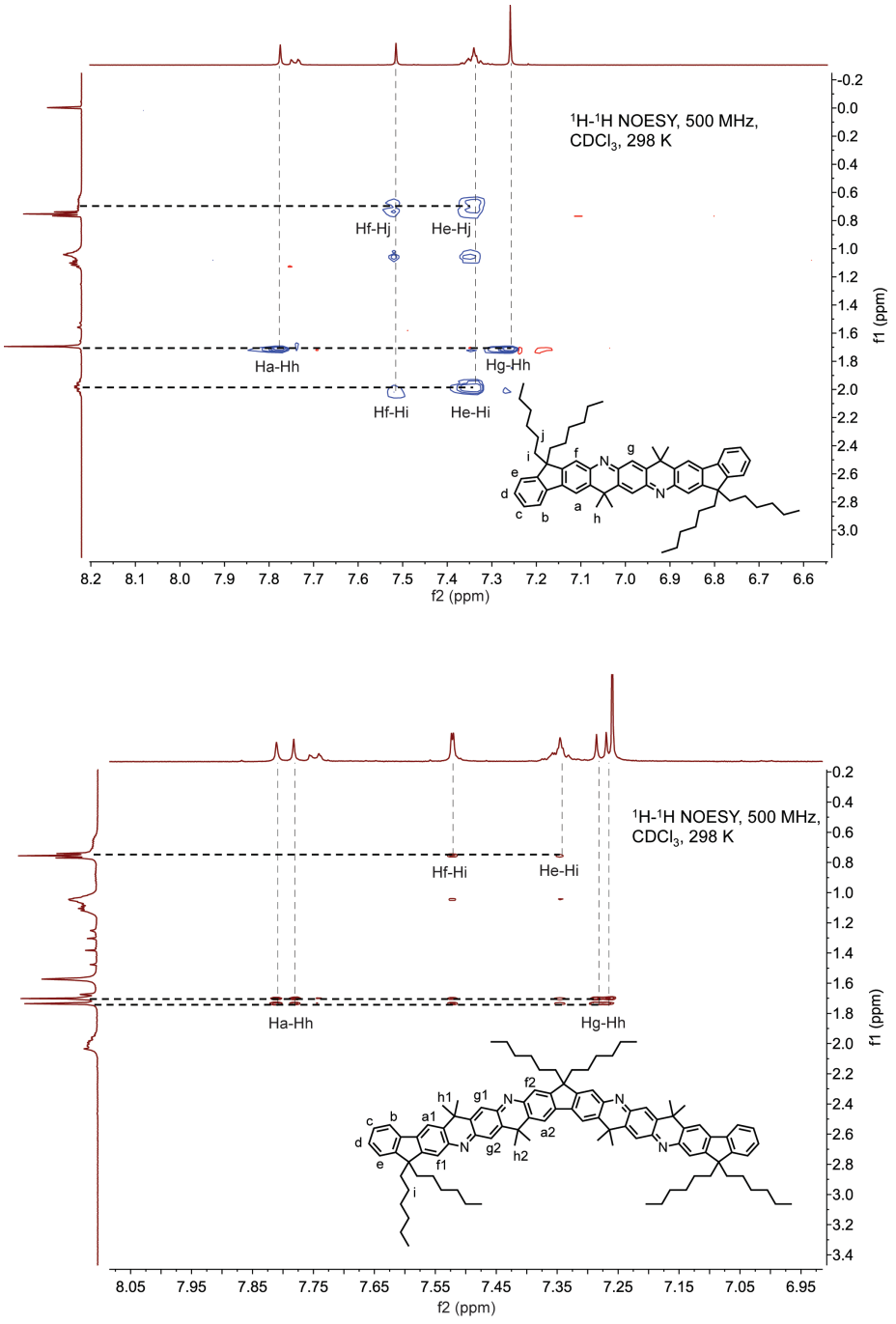

Figure 58. ^{1}H-^{1}H NOSEY NMR of Q1 and Q2 (500 MHz, $CDCl_3$, 298 K). Reprinted with permission from [134].

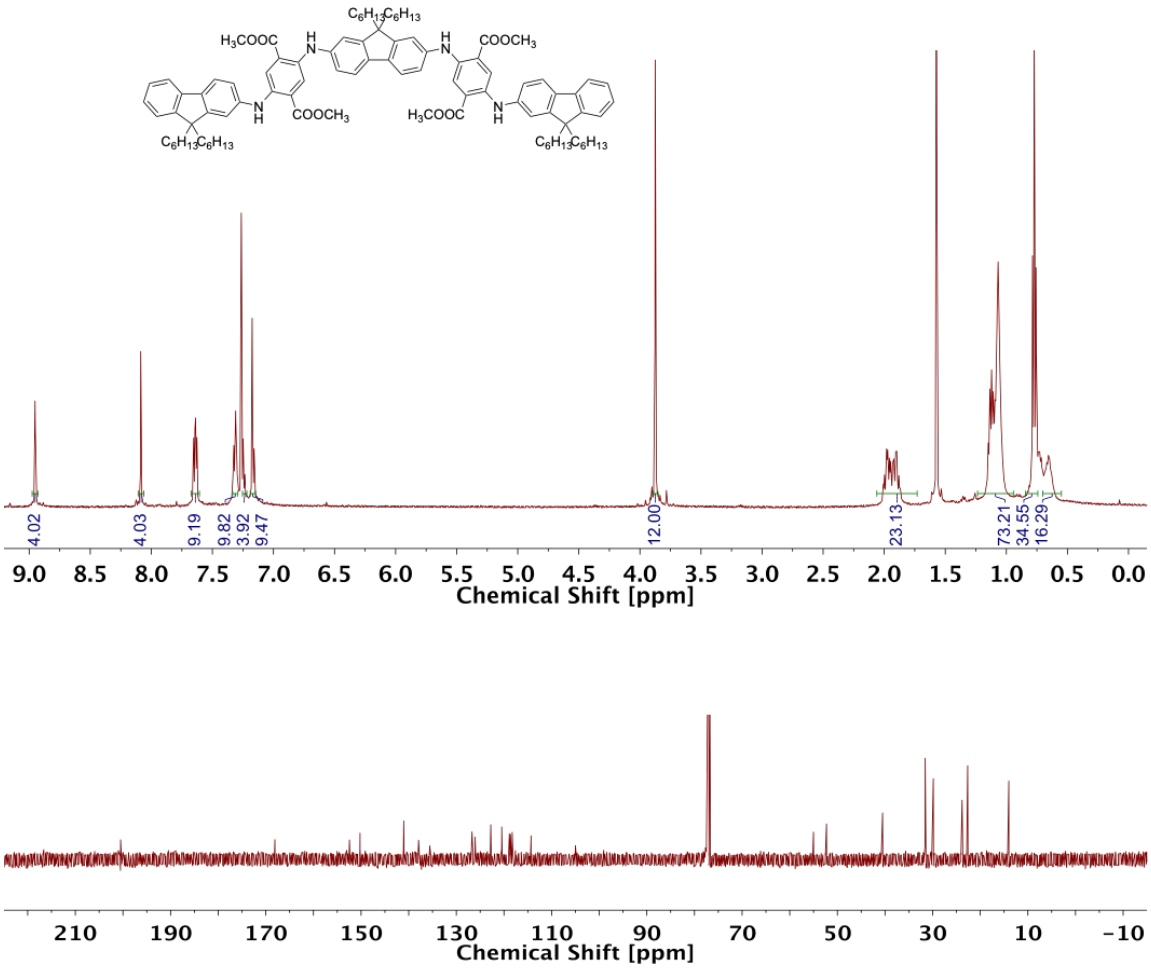

Figure 59. ^{1}H (500 MHz) and ^{13}C (125 MHz) NMR spectra of A2 in $CDCl_3$ at 298 K. Reprinted with permission from [134].

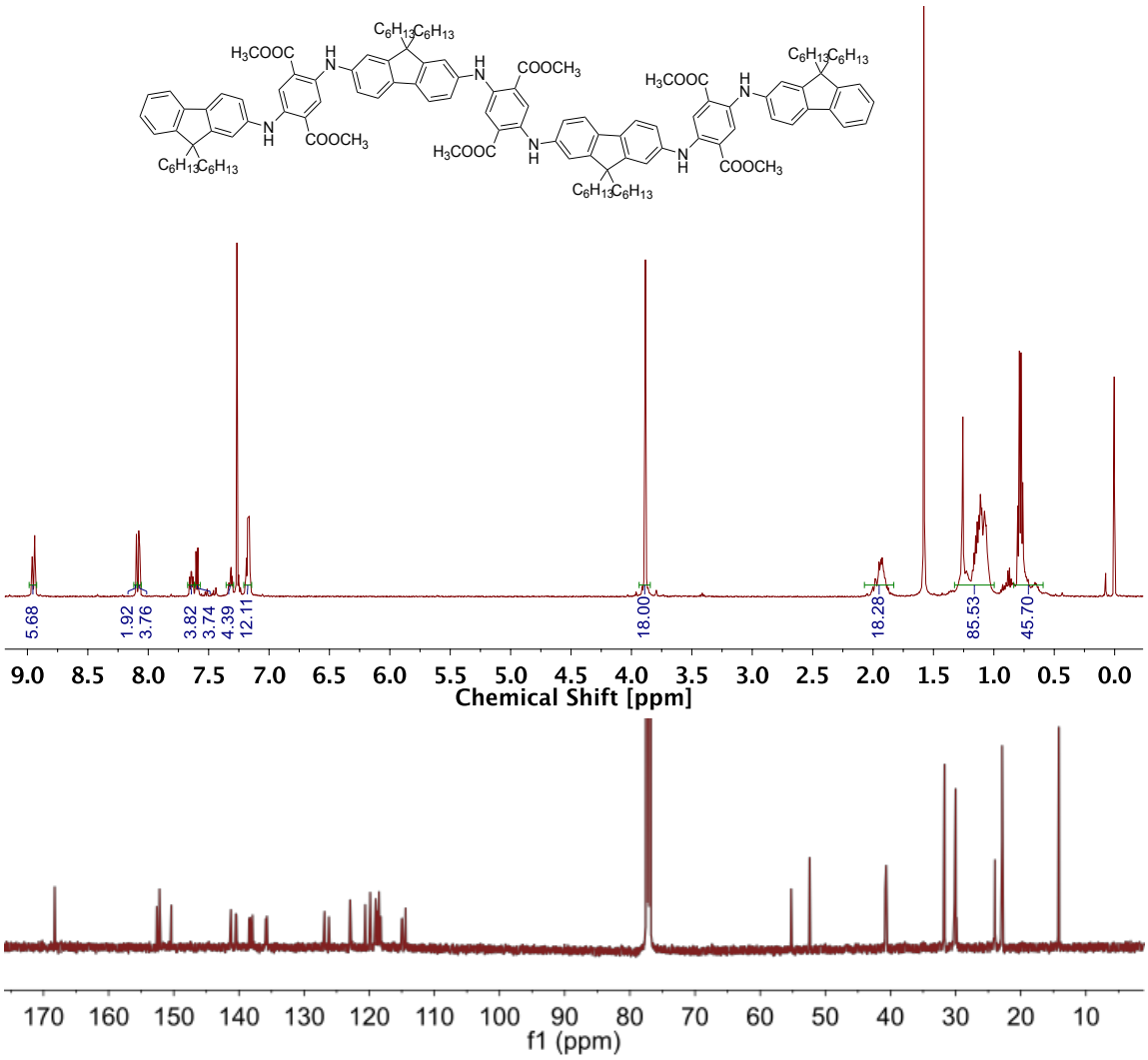

Figure 60. ^{1}H (500 MHz) and ^{13}C (125 MHz) NMR spectra of A3 in $CDCl_3$ at 298 K. Reprinted with permission from [134].

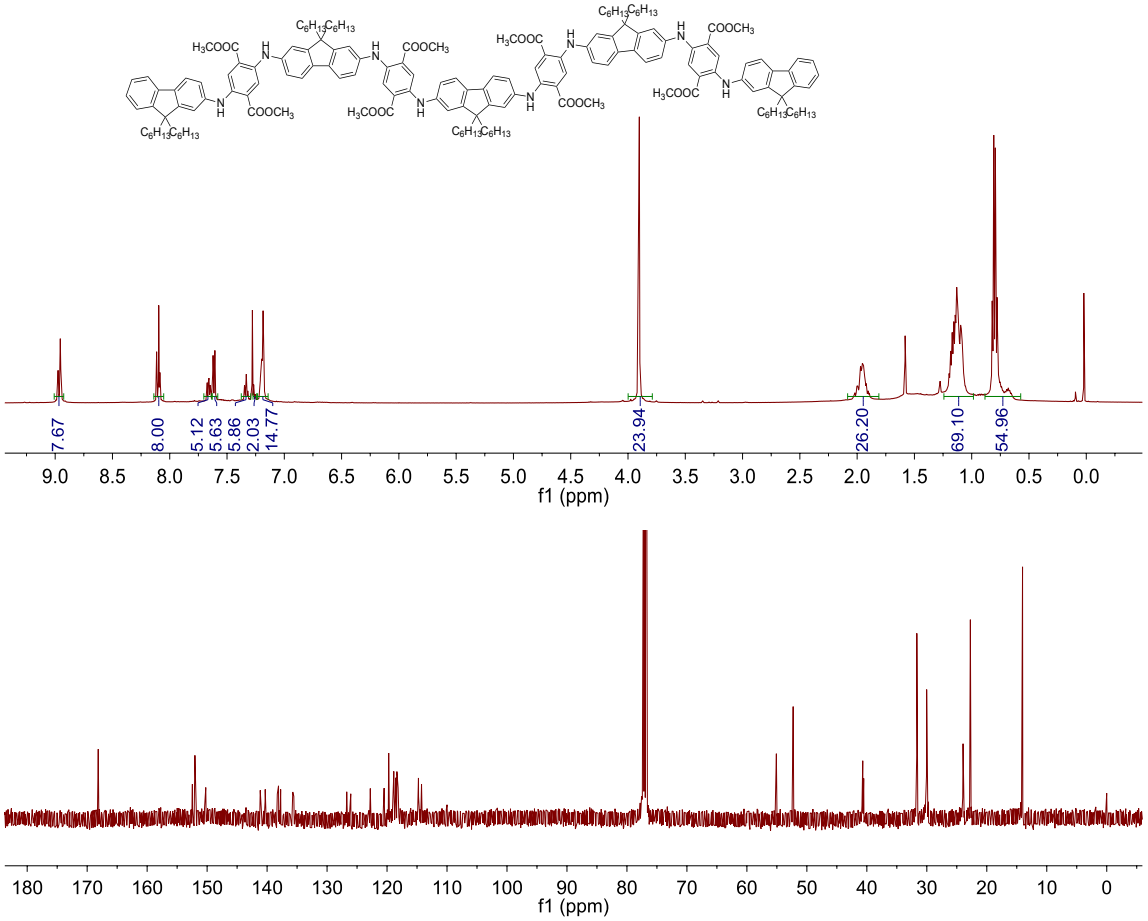

Figure 61. ^{1}H (500 MHz) and ^{13}C (125 MHz) NMR spectra of A4 in $CDCl_3$ at 298 K. Reprinted with permission from [134].

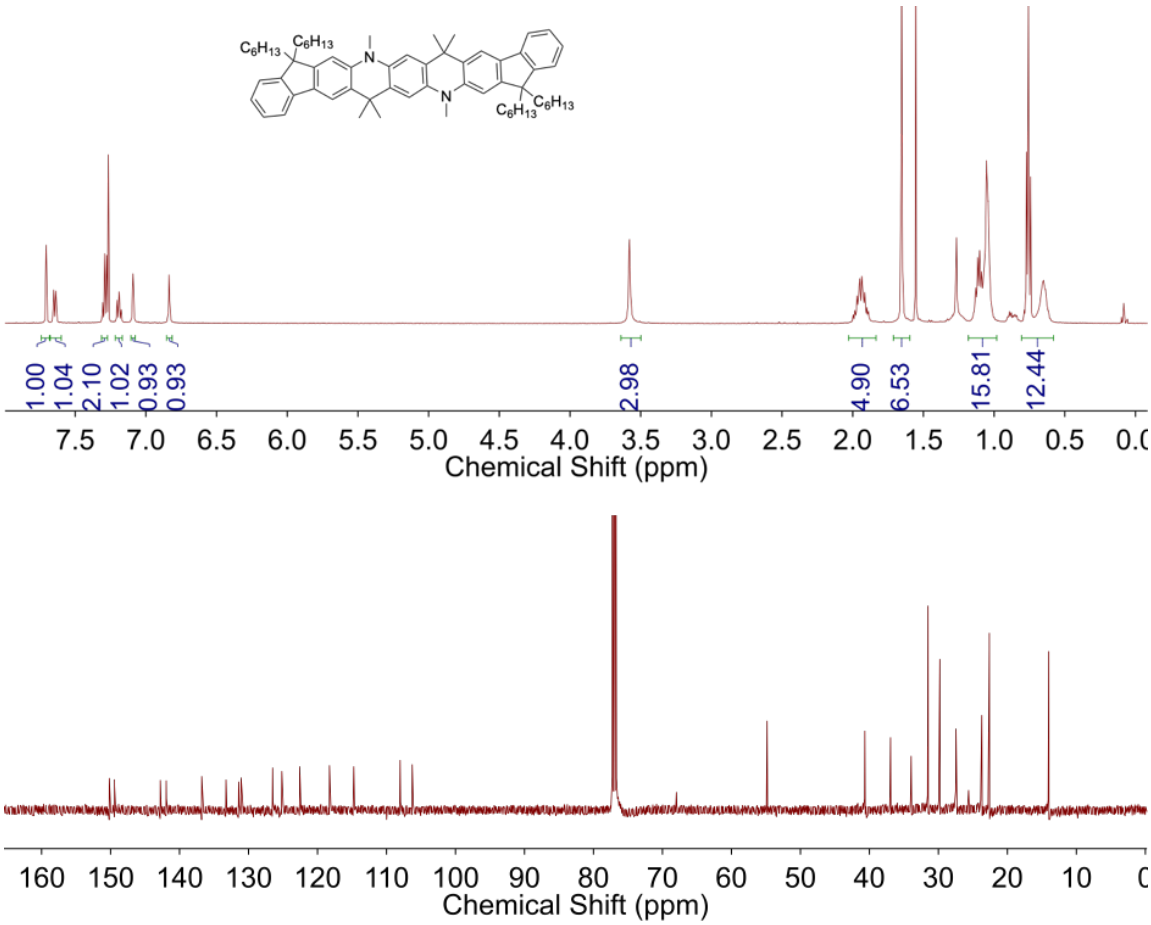

Figure 62. ^{1}H (500 MHz) and ^{13}C (125 MHz) NMR spectra of Me-A in $CDCl_3$ at 298 K. Reprinted with permission from [134].

CHAPTER IV

LADDER-TYPE POLYANILINE-ANALOGOUS POLYMERS*

4.1 Introduction

Polyaniline (PANI) derivatives, which represent one of the most extensively studied classes of conjugated polymers, are particularly intriguing for the incorporation of ladder-type constitution. PANI derivatives feature reversible redox transformation, high conductivity, feasible synthesis, and good processability,[106, 110, 137, 159-162] hence are widely employed in conductive protective coating,[100] electrochromism,[159] and energy storage.[102] However, PANI share some of the common drawbacks with other organic electronic materials, such as (1) low stability of molecular constitutions and degraded performance in devices over time, and (2) limited intrachain delocalization ranges of states or quasi-particles, such as polarons and excitons. One of the primary structural origins of these issues can be identified as the single-stranded and torsionally rotating bonds in the PANI polymer backbone, which gives rise to low barriers of bond scission and disordered chain conformation in the solid state. For example, the fundamental investigation and practical application of pernigraniline salt – the fully oxidized and protonated form of PANI – is severely limited due to its unstable nature. Iminium bond hydrolysis of pernigraniline salt takes place readily in acidic and oxidative conditions,[163, 164] leading to irreversible scission

---

*Reprinted (adapted) with permission from "Extraordinary electrochemical stability and extended polaron delocalization of ladder-type polyaniline-analogous polymers" Ji, X.; Leng, M.; Xie, H.; Wang, C.; Dunbar, K. R.; Zou, Y.; Fang, L. *Chem. Sci.* **2020**, DOI: 10.1039/D0SC03348K. Copyright 2020 Royal Society of Chemistry.

of the conjugated polymer chain and consequently loss in electrical conductivity, charge storage ability, and redox properties.[160, 165] Several engineering approaches have been developed to improve the apparent stability of devices fabricated from conventional PANI, such as introducing external protection,[117] applying limited voltage sweep windows and pretreatment at low voltages,[160] and compositing PANI with carbon or inorganic nanomaterials.[109, 160, 165] A few examples on the modification of the chemical constitution of PANI has also shown to be effective in enhancing the stability.[166-170] In these cases, however, the intrinsically labile iminium bonds still presented in the pernigraniline backbone, remaining as a potential weakness that impacts the wider application of these PANI derivatives, especially when harsh electrochemical conditions are involved.

In Chapter III, acid stability of pernigraniline salt-like structure is significantly improved in a series of ladder oligomers, in which the entropy-driven decomposition is inhibited by the ladder-type double stranded covalent bonds. In addition, unprecedented polaron delocalization in the solid state was observed. In this context, we envisioned that the implementation of ladder-type constitution in a polymeric PANI derivative could fundamentally address the unsolved issues of electrochemical stability and states delocalization of these polymers for their practical future applications. Herein, we reported the feasible synthesis of a series of PANI-derived ladder polymers, their extraordinary electrochemical stability under harsh conditions, and extensive polaron delocalization property. The intrinsic electrochemical stability and conductivity were further demonstrated by the excellent performance and cyclability of the polymer as the active material in NIR electrochromic device.

4.2 Polymer Design and Synthesis

The ladder-type PANI derivative (**LPANI**) in this study was synthesized (**Figure 63**) in a stepwise approach[171] from the non-ladder polymer precursor **P2** (M_n = 25.9 kg/mol, $Đ$ = 2.23), which could be synthesized using a scalable approach involving imine-condensation polymerization followed by *in situ* oxidation.[78, 172] To facilitate the next ring-annulation ladderization reaction, the ester groups in **P2** were converted into tertiary alcohol groups in **P4** by treating the polymer with *p*-tolyl Grignard reagent. Subsequently, Friedel-Crafts cyclization between the fluorene units and the tertiary alcohol group was promoted by boron trifluoride to afford the ladder polymer product **LLB**, which represents the fully reduced form of **LPANI**. This reaction was designed and optimized in a way that only the 3-position of the fluorene unit was activated for the cyclization, promoted by (1) the combined electronic effect of the fluorene moiety itself and the amino group on the 2-position, as well as (2) the steric effect of the two dodecyl groups that prevents the 1-position from reacting. In addition, the centrosymmetric positioning of the tertiary alcohol functional groups ensured a linear extension of the resulting rigid ladder polymer, instead of a helical extension if the repeating units are non-centrosymmetric.[173]

LLB can be considered as a ladder-type analogue of leucoemeraldine base – the fully reduced form of conventional PANI. Upon exposure to air, ~50% of the benzenoid phenylene-1,4-diamine units in **LLB** can be oxidized to quinonoid cyclohexadiene-1,4-diimine unit, to afford a green compound **LEB**, which is analogous to the emeraldine base form of conventional PANI. Complete oxidation of either **LLB** or **LEB** can be achieved quantitatively by treating the solution with *m*-chloroperoxybenzoic acid (mCPBA) to

afford a blue compound **LPB**, which is the ladder-type analogue of fully oxidized PANI, *i.e.* pernigraniline base. The reductive conversion from **LPB** through **LEB** to **LLB** was also clean and quantitative upon the treatment of reducing reagents, such as hydrazine or ascorbic acid. These well-defined, reversible oxidation and reduction processes indicated the highly robust nature of **LPANI**. In addition, **LPB** can be protonated on the cyclohexadiene-1,4-diimine units in in a strong acidic condition, such as 4.0 M MSA, to afford **LPS**, which is a ladder-type counterpart of the unstable, PANI-derived pernigraniline salt (**Figure 63d**). As expected, **LPS** exhibits much higher stability in acidic condition than conventional pernigraniline salt.

Thanks to the presence of *n*-dodecyl groups R^1 on the fluorene unit and the *p*-tolyl groups R^2 on the backbone, **LPANI** is well-soluble in common organic solvents such as THF and chloroform regardless the oxidation state, enabling comprehensive solution-phase characterization and processing. The molar mass values of all three forms of **LPANI** were measured by size exclusion chromatography (**Figure 63b**), showing similar dispersity values ($Đ$ = 1.67 ~ 1.95) and a slight increase in measured M_n from **LLB** (21.6 kg/mol) to **LPB** (25.5 kg/mol). Considering the higher rigidity of oxidized cyclohexadiene-1,4-diimine unit than that of the reduced phenylene-diamine unit, the higher apparent M_n of **LPB** and **LEB** than that of **LLB** is in a good agreement with the hypothesis that **LPB** has more rigid backbone and hence larger radius of gyration, according to Mark-Houwink equation.[174, 175] The decreased of measured M_n from **P1** to ladder polymers was attributed to the removal of unreacted or partially reacted intermediates.

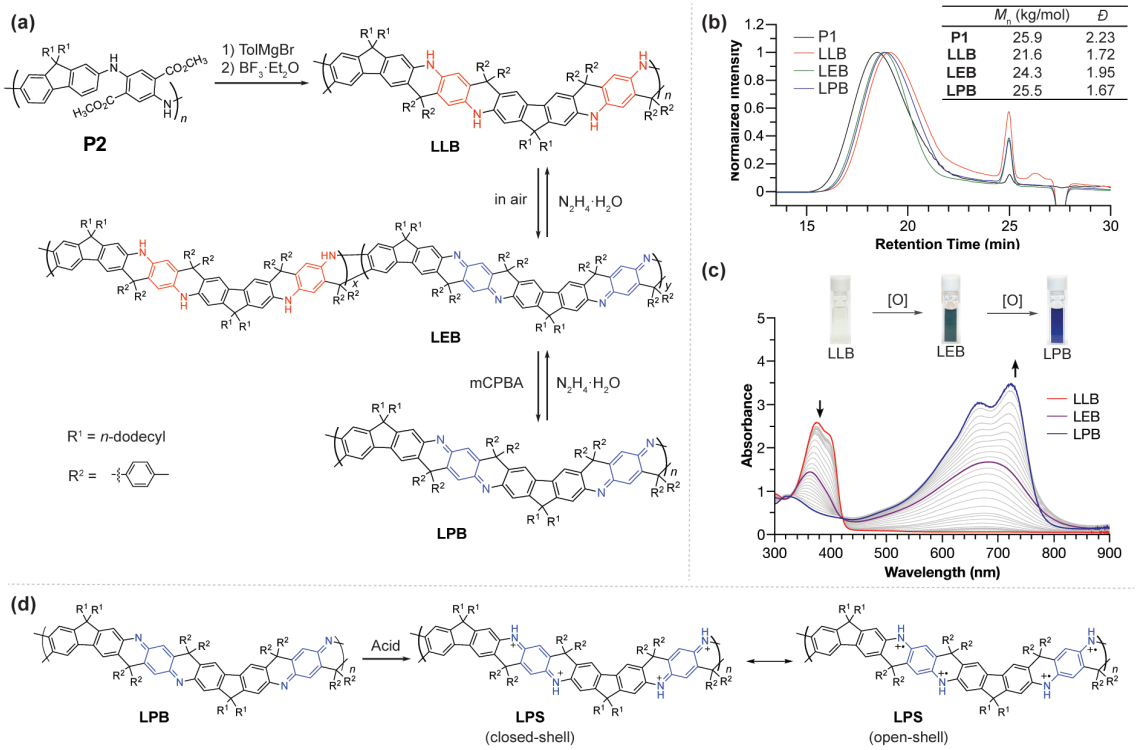

Figure 63. (a) Synthesis of LPANI from polymer precursor P2, and the redox interconversion of its LLB, LEB, and LPB forms. (b) Size exclusion chromatogram and calculated *M*n and dispersity (*Đ*) values. (c) UV-vis absorption spectra of oxidation process from LLB to LEB to LPB in THF; (inset) pictures of LLB, LEB and LPB solutions. (d) Protonation of LPB with MSA and structural formulas of the closed-shell and open-shell resonance forms of protonated LPS form. Reprinted with permission from [176].

The chemical oxidation conversion from **LLB** to **LPB** was monitored with UV-vis spectroscopy (**Figure 63c**). With an increasing amount of oxidant (mCPBA) added into **LLB**, the absorption peak of **LLB** at 375 nm decreased and a broad peak centered at 680 nm emerged as a result of the generation of conjugated cyclohexadiene-1,4-diimine unit moieties. The clear isosbestic point during the titration demonstrated the well-defined, clean transformation between these different redox states. In comparison, conventional PANI does not exhibit such a clear isosbestic point when transforming from

leucoemeraldine base to pernigraniline base, likely due to the presence of configurational isomers and poor solubility of pernigraniline base.[177] In addition, by comparing the spectra of **LEB** prepared by air oxidation with the titration plot, oxidation ratio of **LEB** was determined to be ~ 50% (**Figure 64**). The photo-absorption peak of **LPB** is narrow and exhibit a clear vibrational progression, indicating a well-defined configuration and a rigid conformation at room temperature. This result is in sharp contrast with the spectrum of conventional non-ladder pernigraniline base, which shows a broad absorption peak with no vibrational feature due to the fast *trans*-/*cis*- isomerization and torsional rotation.[118, 177, 178] These pronounced differences between **LPB** and conventional pernigraniline base suggest the important impacts of ladder-type constitution on extending orbital/states delocalization as well as inhibiting isomerization and conformational disorder.

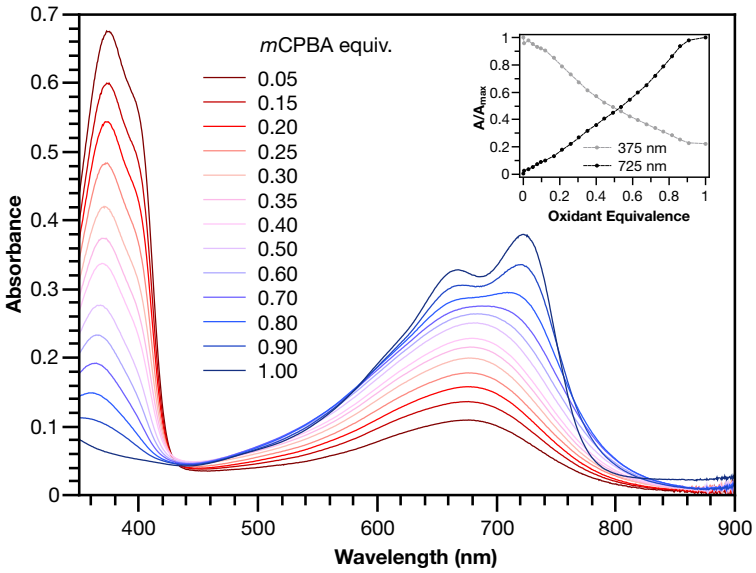

Figure 64. UV-vis spectra of a solution of LLB titrated with mCPBA in dichloromethane (concentration of repeating units = 8.3 μM). Reprinted with permission from [176].

In order to fully elucidate the constitutional structures of **LPANI**, two small molecular model compounds, **SLB** and **SPB**, were synthesized and characterized with ^{1}H, ^{13}C, HSQC, and HMBC NMR spectroscopy (**Figure 80 ~ 85**). The ^{13}C NMR peaks for **SLB** and **SPB** were fully assigned to their structures, so that they can be used as references to analyze the spectra of **LPANI**. ^{1}H and ^{13}C NMR spectra of **LLB**, **LEB**, and **LPB** were obtained in *d*8-THF at room temperature. Compared to the broad and heavily overlapping ^{1}H NMR signals (**Figure 86 ~ 88**), the ^{13}C NMR peaks of **LLB** and **LPB** are sharp and well-defined. They matched well with those of **SLB** and **SPB**, respectively, so that full assignments of these polymer peaks were accomplished (**Figure 65**). The clearly identified NMR signals of **LLB** indicated high efficiency and regioselectivity of the Friedel-Crafts cyclization reaction, and the absence of observable defects during the ladderization step. Comparing the ^{13}C NMR spectra of **LLB** and **LPB**, it is notable that the signals of the central ring (C5, C6, C9, C12) downfield shifted dramatically in the spectrum of **LPB** due to the more electron-deficient property of the oxidized cyclohexadiene-1,4-diimine units compared to the electron-rich form of phenylene-1,4-diamine in **LLB**. Less distinct shifts were observed for carbons on the fluorene units (C10, C11, C13) and the sp^3-C bridge (C14). Apart from the backbone, the *p*-tolyl side groups (C7 and C8) also showed distinguishable chemical shifts changes, serving as a good probe for identifying different oxidation states. **LEB** can be considered as a statistic copolymer of the phenylene-1,4-diamine- and the cyclohexadiene-1,4-diimine-containing repeating units. Not surprisingly its ^{13}C NMR spectrum exhibited clearly both sets of peaks found in those of **LLB** and **LPB**.

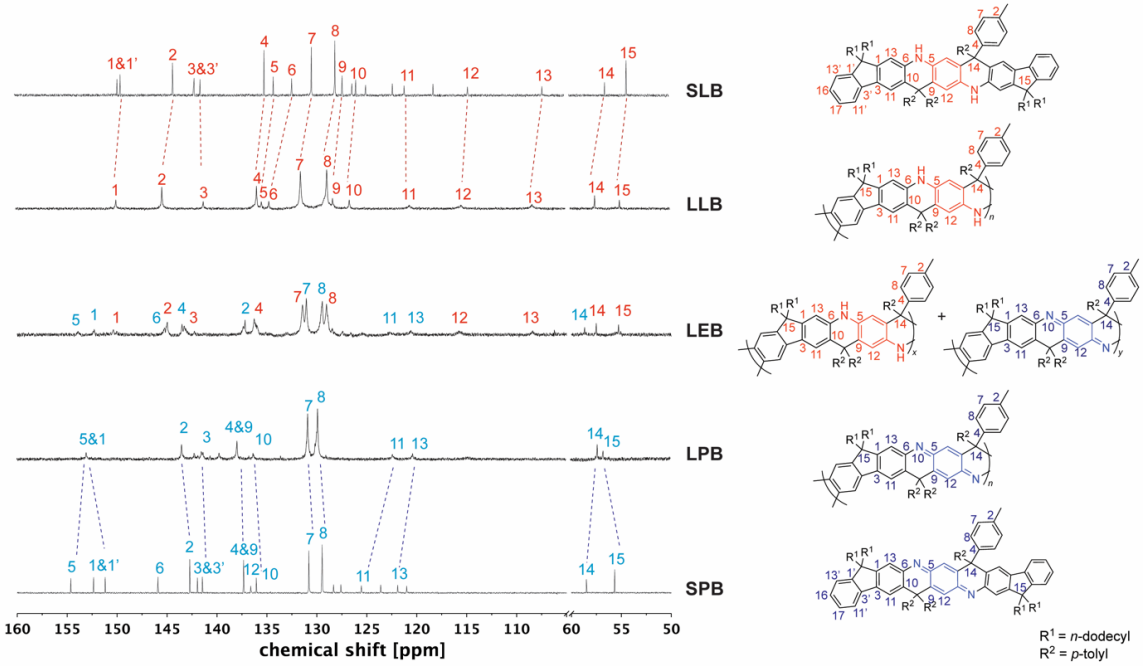

Figure 65. ^{13}C NMR spectra of small molecule model SLB and SPB, and varied oxidation states of LPANI (126 MHz, d_8-THF, 298 K). Reprinted with permission from [176].

The functional group transformation among these compounds is further confirmed by FT-IR spectra. The characteristic C=N (1681 cm^{-1}) and C=C (1604 cm^{-1}) stretching bands of cyclohexadiene-1,4-diimine units were observed in **LEB** and **LPB** while absent in **LLB** (**Figure 66**).

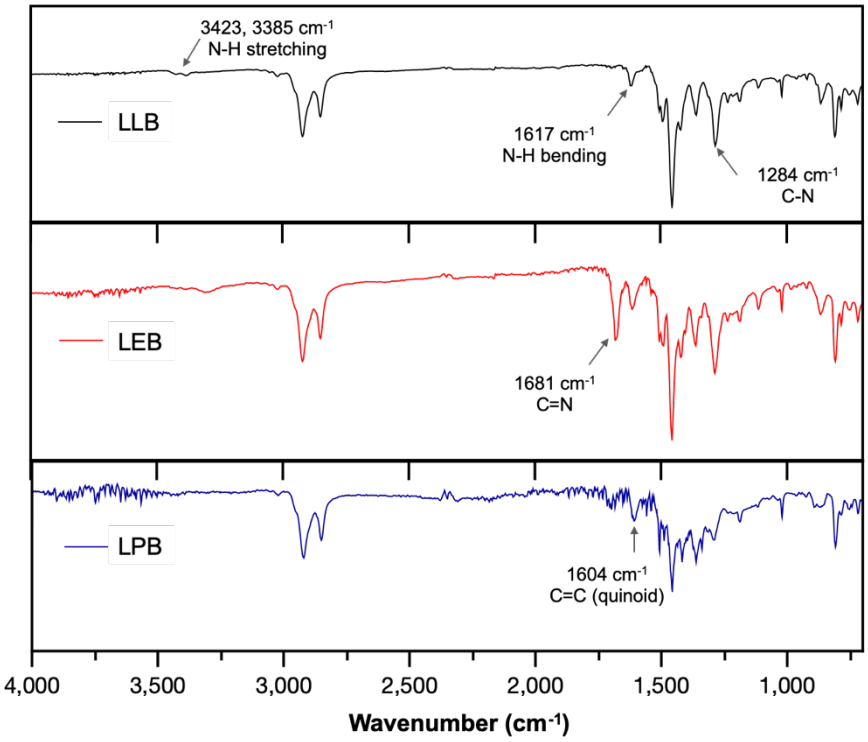

Figure 66. FT-IR spectra of LLB, LEB, and LPB. Reprinted with permission from [176].

4.3 Electrochemical Stability

The electrochemical interconversion of different oxidation states of **LPANI** was investigated in both solution phase and solid state by CV experiments. **LEB** was selected as the focus of the analysis as the polymer backbone contains both the phenylene-1,4-diamine unit (unit **A** in **Figure 67**), which can be oxidized, and the cyclohexadiene-1,4-diimine unit (unit **D** in **Figure 67**), which can be reduced (**Figure 67a**). Referred to the cyclic voltammograms of **SLB** and **SPB** (**Figure 73**), the step-wise oxidation and reduction processes of a thin film of **LEB** were identified. In an inert electrolyte ($TBAPF_6$) solution, these processes are electrochemically irreversible although the chemical redox

processes were confirmed to be reversible. The electrochemical irreversibility was attributed to the deprotonation of the fully oxidized form **C** into **C'** and protonation of the fully reduced form **F** into **A** shown in **Figure 67a**. Differently, with high concentration electrolytes of Brønsted acid or $LiClO_4$, reversible oxidation processes were observed among different oxidation states, because the oxidized unit **C** was kept protonated or lithiated upon oxidation (**Figure 67b**, **67c**). These results demonstrated the intrinsically reversible nature of the interconversion between **A** and **C**, which was important for the subsequent electrochromic device with Li^+ electrolyte. CV of **LLB** and **LPB** were also conducted, showing only the anticipated oxidation process of **A** and reduction process of **D**, respectively (**Figure 74**). The presence of multiple redox peaks in these cyclic voltammograms indicated good electronic coupling between neighboring units along the ladder-type polymer backbones, *i.e.,* the oxidation/reduction of one unit made it much more difficulty to oxidize/reduce the neighboring unit due to strong electronic coupling and molecular orbital delocalization. The fully reversible oxidation and reduction processes of **LPANI** in protonated or lithiated conditions demonstrated its excellent robustness within a wide potential range, and set the foundation for its electrochemical applications.

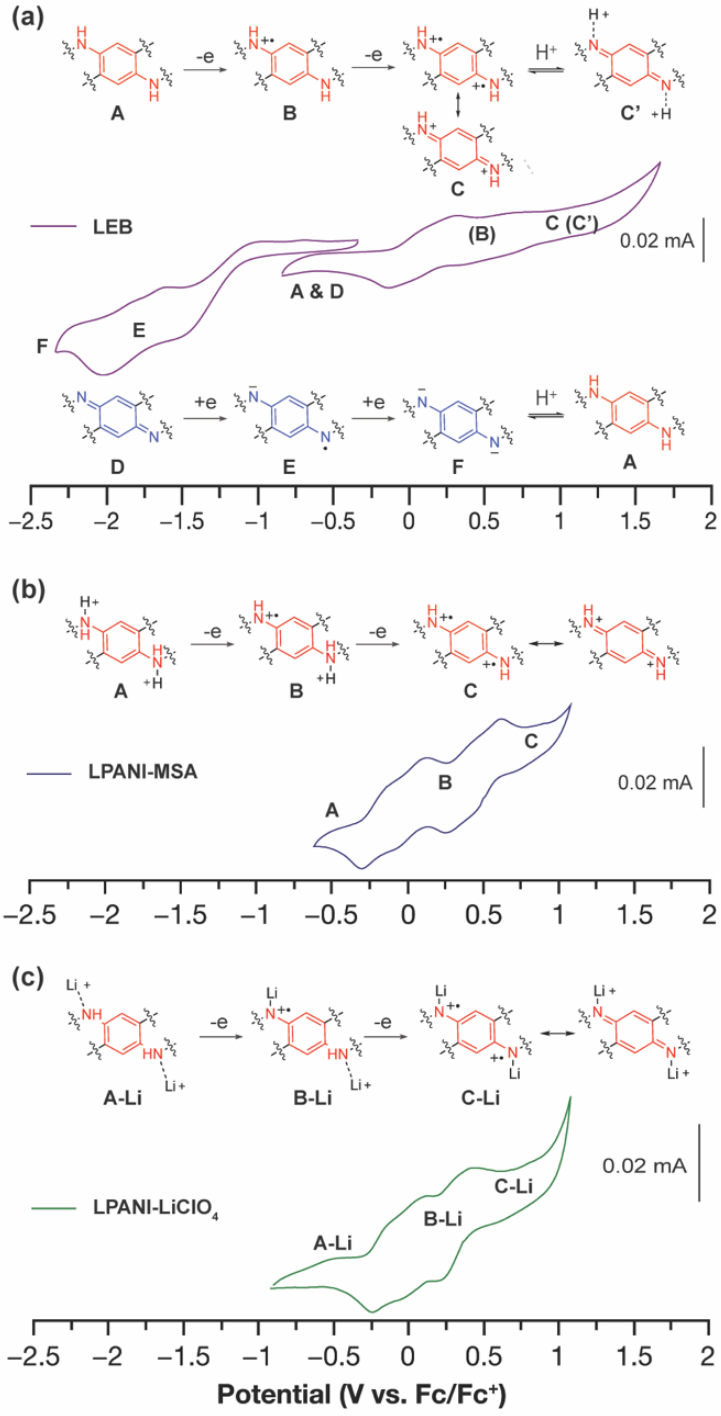

Figure 67. Cyclic voltammograms of (a) LEB film in acetonitrile with 0.1 M $TBAPF_6$. (b) LPANI solution in THF with 0.15 M MSA. (c) LPANI solution in THF with 1.2 M $LiClO_4$. In all cases, a Pt wire was used as the counter and Ag/AgCl was used as the reference electrode. Reprinted with permission from [176].

The electrochemical stability of **LPANI** was studied under highly acidic and oxidative conditions, which is of great importance for applications including energy storage and electrochromic devices.[123] It is well known that, in acidic conditions, electrochemically oxidized conventional PANI (in its pernigraniline salt form) readily degrades and leads to deterioration of the electrochemical cycles.[179, 180] In this work, conventional PANI and **LPANI** were both coated on carbon fabric cloth as the working electrodes for the test. In highly acidic acetonitrile solution with 0.5 M of sulfuric acid, a controlled potential at +1.0 V (vs. Ag/AgCl) was held on for variable time periods (0 ~ 60 min), during which polymers on the working electrode were fully oxidized and maintained in the form of pernigraniline salt at the oxidation potential. After each controlled-potential period, a CV experiment was performed and the peak current intensity was used to evaluate the relative amount of remaining electroactive species.[181, 182] A rapid decreasing on CV current intensity of conventional PANI was observed (**Figure 68a**), showing degradation by *ca.* 40 % in the first 10 min. The degradation process was also found to be accelerated with increased oxidative potentials (**Figure 75a**). In contrast, the cyclic voltammograms of **LPANI** maintained almost unchanged after applying controlled potential at +1.0 V in this harsh condition for up to 60 min (**Figure 68b**, **68c**). Although slight decomposition started to take place when the potential was increased to +2.0 V (**Figure 68d**), the much enhanced electrochemical and acidic stability of **LPANI** suggested that the long-standing issues of hydrolysis and redox side-reactions of PANI derivatives could be intrinsically inhibited by the fully ladder-type constitution.

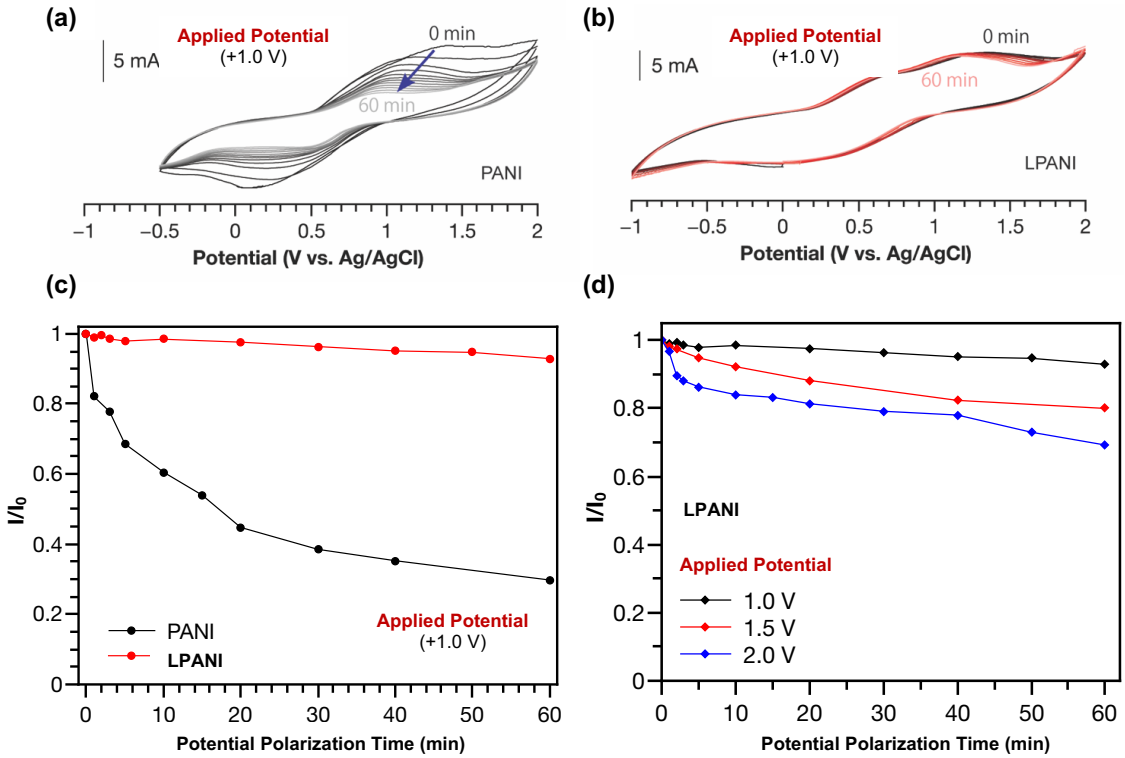

Figure 68. Cyclic voltammograms of (a) conventional PANI and (b) LPANI after applying +1.0 V potential for variable amount of time (0 ~ 60 min). (c) Plot of the current intensities in (a) and (b) vs the time of holding at +1.0 V. (d) Plots of current intensities of LPANI after applying various potentials for variable amount of time (0 ~ 60 min). Reprinted with permission from [176].

4.4 Characterization of Ladder-Type Pernigraniline Salt

The superior stability of **LPANI** at the **LPS** state sets the stage for comprehensive investigations of this acid-doped species with ensured structural integrity. The absorption spectrum of **LPS** exhibits a significant red-shift of the band compared to that of **LPB,** into the NIR region (λ_{max} ~1400 nm) (**Figure 69**, **70a**). Solid-state **LPS** was prepared by mixing **LPB** with an excess amount of non-volatile acid such as PTSA. A spin-casted thin film of **LPS**/PTSA mixture exhibits a further red-shift of the absorption peak to λ_{max} ~ 1650 nm, likely as a result of intermolecular electronic coupling between the ladder

polymer chains. Despite in highly acidic media, **LPS** is remarkably stable in either solution phase or solid state, with little change on the absorption spectra for over 48 hours in ambient conditions (**Figure 69**). Such an excellent stability in highly acidic condition is unprecedented among conventional non-ladder pernigraniline derivatives.

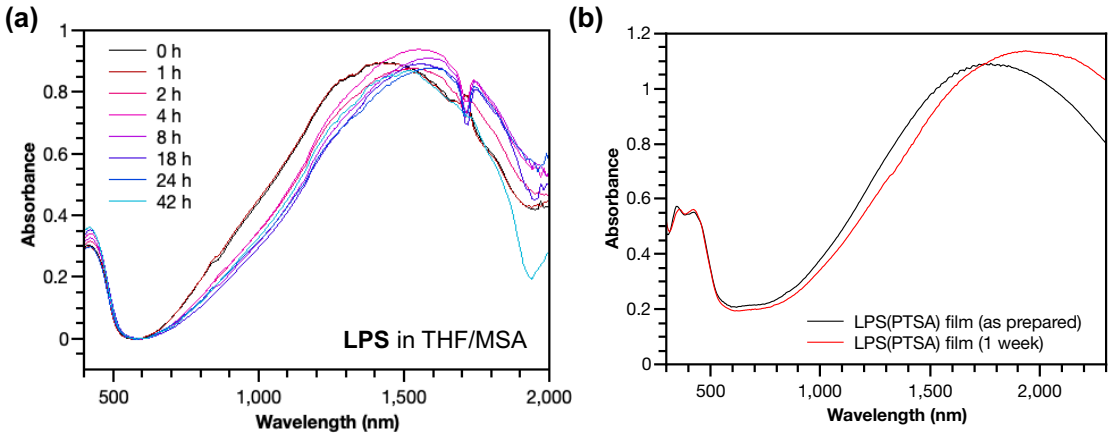

Figure 69. (a) Visible-NIR absorption spectra of LPS in THF with 4 M MSA over a period of 42 h; (b) vis-NIR absorption spectra of as prepared acidified LPS thin film in the presence of PTSA, and the sample after 1 week stored under ambient condition. Reprinted with permission from [176].

The electronic structures of the varied state of **LPANI** was elucidated experimentally. Based on the CV data and UV-vis-NIR absorption spectra, HOMO and LUMO energy levels of **LLB**, **LEB**, **LPB,** and **LPS** were determined (**Figure 70b**). The estimated bandgaps of **LLB**, **LEB**, and **LPB** are 3.10, 1.22, and 1.57 eV, respectively, which are all lower by 0.6 ~ 0.9 eV than those of corresponding conventional PANI derivatives.[183] The uniformly lower bandgaps indicate that the coplanar conformation of the ladder polymer backbone greatly extends the molecular orbital delocalization and π-conjugation. A drastically lower LUMO level of **LPS** than that of **LPB** is a result of acid-doping of the cyclohexa-1,4-diimine units.[184, 185] The small energy gap results into a better

admixture of HOMO and LUMO in the ground state, leading to significant natural orbital occupancies in the lowest unoccupied natural orbitals and therefore open-shell diradical character.[29, 186-189] As shown in the EPR spectra (**Figure 70c**), **LPS** possesses a much higher spin concentration compared to **LPB**, as a result of the acid-induced transition from the closed-shell to open-shell resonance. The acid-doping is also expected to lead to polaron delocalization, which is evidenced by DC conductivity of the solid pellet of acid-mixed **LPS** (**Figure 76**). Magnetic susceptibility measurement of **LPS** solid by SQUID revealed a dominant temperature-independent Pauli paramagnetism (χ_{Pauli}) at 0.015 emu per mole of repeating unit (**Figure 70d**), indicative of a delocalized nature of the radical cations (polarons) in the solid state. Compared to emeraldine salt of conventional PANI, which demonstrates both Pauli paramagnetism and Curie paramagnetism, **LPS** features one order of magnitude higher χ_{Pauli} value and absence of Curie paramagnetism, corresponding to a significantly enhanced polaron delocalization range and higher density of states of polarons at the Fermi level.[113] The χ_{Pauli} of **LPS** is also significantly higher than those measured on shorter oligomeric analogues,[134] suggesting that the longer ladder polymer chains allow for the extension of polaron delocalization.

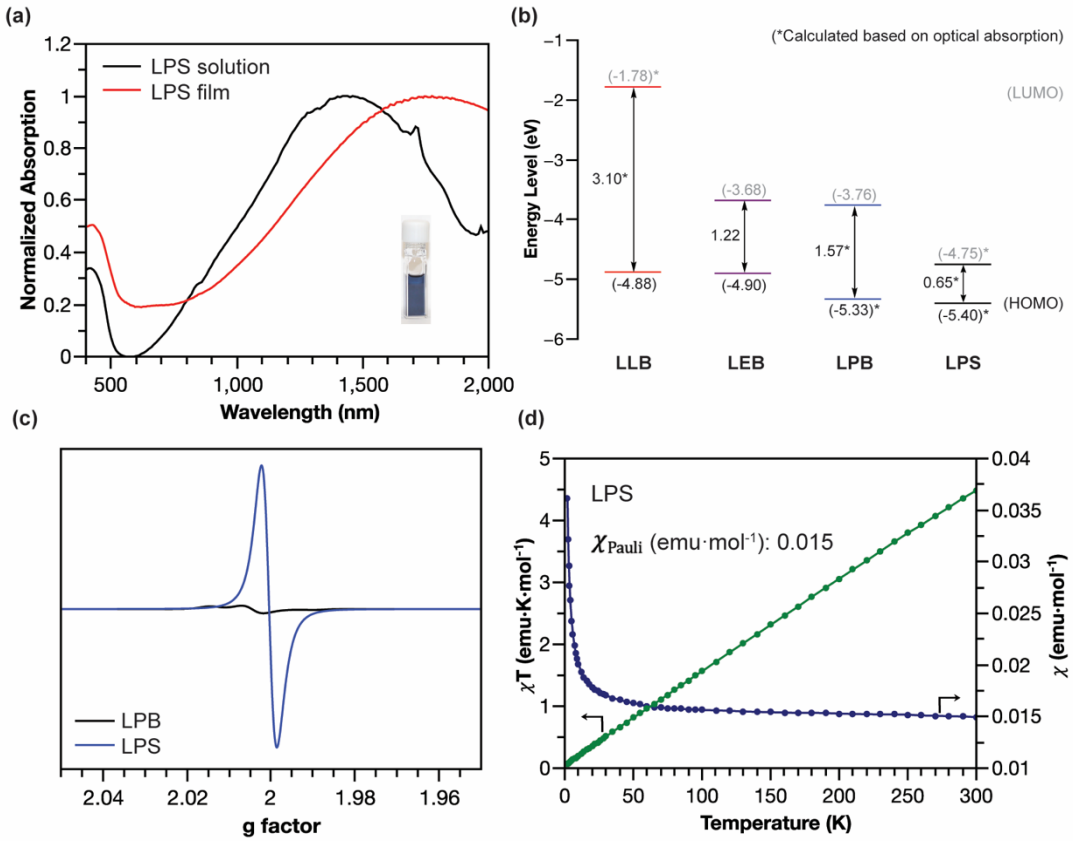

Figure 70. (a) Visible-NIR absorption spectra of LPS in solution and in thin film. (b) HOMO/LUMO energy level diagrams of LLB, LEB, LPB, and LPS. (c) EPR spectra of LPB and LPS solid. (d) Temperature-varied magnetic susceptibility of LPS solid. Reprinted with permission from [176].

The acid-doped salt of **LEB** (**LES**) was also characterized with EPR and SQUID (**Figure 71**). Dominant Pauli paramagnetism was observed with χ_{Pauli} at 0.0023 emu per mole of repeating unit, indicating the enhanced polaron delocalization in ladder-type structure compared to conventional PANI.

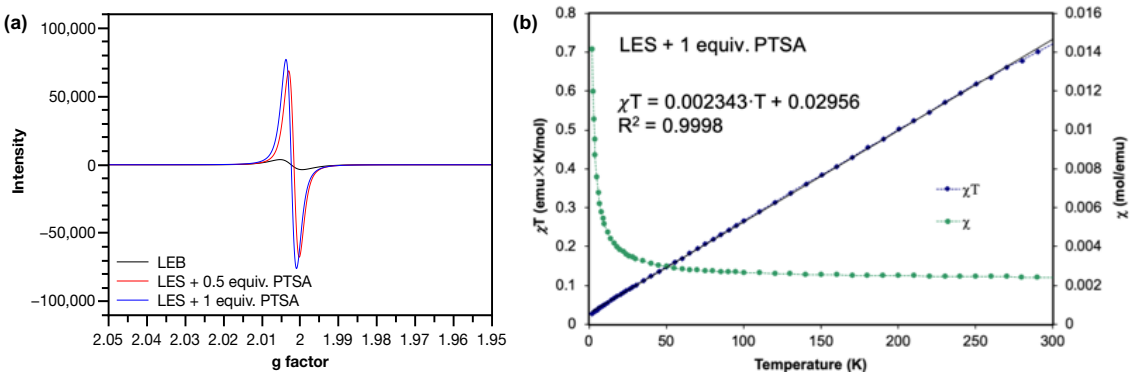

Figure 71. (a) EPR spectra of (b) LES solids doped with different molar equivalents of PTSA. Each sample contained 1.0 mmol of cyclohexadiene-1,4-diimine units. (b) Temperature-varied magnetic susceptibility of LES solid. Reprinted with permission from [176].

4.5 Electrochromic Application

The outstanding electrochemical stability, fully reversible redox transformation, and conductive nature enable the application of **LPANI** in highly robust electrochromic devices. Organic electrochromic materials possessing reversible optical changes upon electrochemical oxidation or reduction have attracted a great deal of interest in diverse applications.[190] Compared with inorganic materials, organic molecules, especially polymers, exhibit advantages in high coloration efficiency, excellent processability, and fast switching ability.[191] PANI represents an important class of organic electrochromic materials that can cover visible and NIR regions and has been applied in various fields, such as smart windows, displays, and camouflage.[192] The switching between the bleached and colored states of PANI corresponds to the interconversion between leucoemeraldine and half-oxidized emeraldine salt states. The rapid degradation of fully oxidized pernigraniline salt, however, limits the range of operational voltage, hence imposing an intractable challenge on the practical deployment of robust and recyclable devices based

on PANI.[123] In this study, **LPANI** was employed as the active material in a sandwiched electrochromic device, which was fabricated with two ITO-glass substrates, spin-casted **LPANI** thin film, and lithium gel electrolyte (PMMA/PC/$LiClO_4$) (**Figure 72a**). When −2.0 V voltage was applied on the **LPANI** layer, the device showed pale yellow color with an absorption peak at 378 nm, corresponding to the **LLB** state. As the voltage switched to +2.0 V, the device turned into deep blue color and a broad absorption peak evolved in NIR region (λ_{max} = 905 nm), corresponding to the lithiated **LPS** state (**Figure 72b**). The color-switching cyclability was studied by applying alternating working voltage at −2.0 V and +2.0 V for 30 s at each stage, leading to fully reversible transitions of the absorption between the **LLB** and **LPS** states, in agreement with the solid-state CV results (**Figure 66c**). No observable degradation of absorption intensity at 378 nm was observed over 200 cycles, while only less than 2% decay was observed for the absorption at 845 nm (**Figure 73c**). Such an excellent cyclability allows for a reliable kinetic analysis of the electrochromic processes based on data from multiple cycles (**Figure 77**). Both the oxidation and reduction processes fit in a pseudo-first-order model to give the apparent rate constants of 0.10 and 0.39 s^{-1}, respectively (**Figure 72d**). The lower oxidation rate is likely a result of the rate-determining lithiation process which requires a slow process of lithium diffusing to the oxidized cyclohexadiene-1,4,-diimine unit.[193] In contrast, during reduction, the phenylene-1,4-diamine unit state is recovered through the reductive charge transfer followed by a rapid protonation step so that a higher rate constant was observed. Overall, **LPANI** show unprecedented electrochromic cyclability among PANI-like polymers over a wide operation voltage window (spanning for 4 V), thanks to the highly-

reversible interconversion between **LLB** and **LPS** states and the extraordinary stability of **LPS** under highly oxidative conditions. This result further demonstrates the superior electrochromic properties endowed by the ladder type backbone constitution. It is anticipated that, with the understanding of the electrochromic mechanism and kinetics, further chemical and device optimization can lead to devices with desired electrochromic performance in terms of response rate and color contrast. The design principle of such robust electrochemical transition can also benefit the development of electrochemical energy storage application using conjugated polymers.

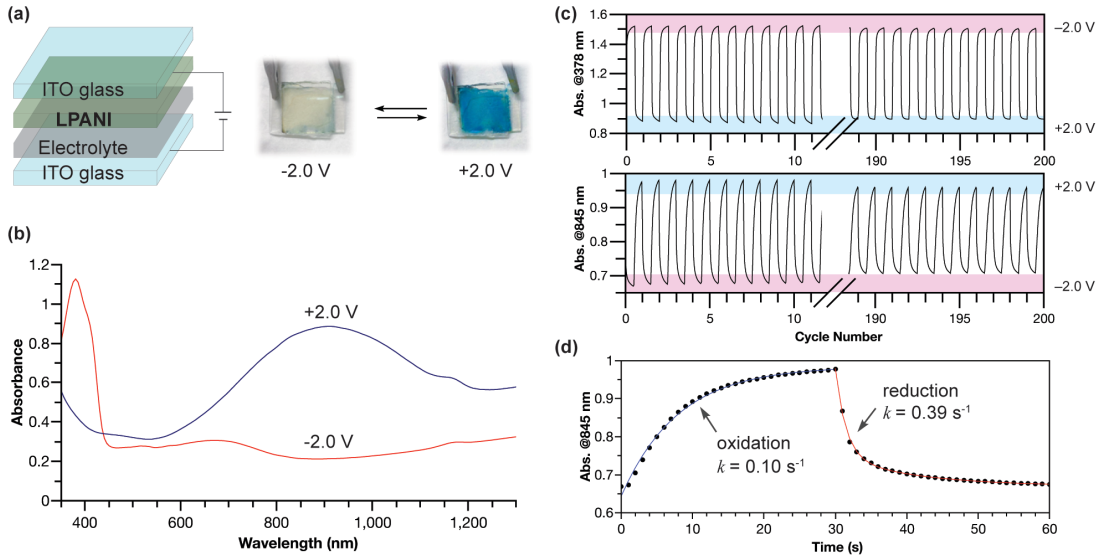

Figure 72. (a) Architecture and photographic images of the electrochromic device at –2.0 V and +2.0 V, respectively. (b) Absorption spectra of the electrochromic device when applying –2.0 V or +2.0 V for 60 s. (c) Absorbance at 378 nm and 845 nm with voltage swept between -2.0V and +2.0V for 200 cycles. (d) Time-dependent absorbance changes at 845 nm; dots: experimental data spots; lines: pseudo-first-order fitting. Reprinted with permission from [176].

4.6 Conclusion

In summary, this work demonstrates that ladder-type backbone constitution can be incorporated into polyaniline analogues through a feasible and scalable synthesis. A ladder-type polyaniline-analogous polymer with low defect level was obtained through the highly-efficient and regioselective cyclization. The ladder-type constitution imparts unprecedented stability and extensive states delocalization into the resulting **LPANI** derivatives. Specifically, **LPANI** derivatives exhibit significantly superior electrochemical stability compared to non-ladder PANI derivatives, evidenced by the highly reversible transformation among different oxidation states, and extraordinary robustness in harsh electrochemical conditions. The excellent stability also allows for the investigation and application of the strong NIR absorption and Pauli paramagnetism of the acidified and fully oxidized **LPS** form, revealing its low bandgap and the presence of extended polaron delocalization in the solid state. The unique combination of these functions enables the fabrication of a robust and highly recyclable NIR electrochromic device using **LPANI** as the active material. Taken together, this work establishes the principle of using ladder-type constitution to address the long-standing challenges of stability and states-delocalization seen in the field of organic electronic materials. This strategy should be formulated into the future design of electronically active polymers.

4.7 Experimental Details

4.7.1 General Methods

All reaction solvents were dried and purified by an Inert Technology pure solvent system (PureSolv-MD-5a). All starting materials were obtained from commercial suppliers and were used without further purification unless otherwise specified. ^{1}H, ^{13}C, ^{1}H-^{13}C HSQC and ^{1}H-^{13}C HMBC NMR spectra were recorded on a Varian Inova 500 MHz spectrometer at room temperature and processed by MestReNova. Chemical shifts are reported in ppm relative to the signals corresponding to the residual non-deuterated solvents (for ^{1}H NMR: d_8-THF $\delta = 3.58$ ppm; for ^{13}C NMR: d_8-THF $\delta = 67.21$ ppm). Flash column chromatography purifications were carried out using a Biotage® Isolera™ Prime with various sizes of SiO_2 Biotage SNAP® cartridges. SEC was performed on a TOSOH EcoSEC (HLC-8320GPC) chromatography at 40 ºC with UV detector at 254 nm and THF as the eluent. The molecular weights were calculated using a calibration curve based on the UV absorption signal of polystyrene standards. UV-Vis-NIR absorption spectra were recorded on a Hitachi U-4100 UV-Vis-NIR spectrophotometer. ESI-MS experiments were performed using a Thermo Scientific Q-Exactive Focus operated in full MS in positive mode. FT-IR spectra were recorded in attenuated total reflectance mode (with ZnSe) using a Shimadzu IRAffinity-1S spectrometer. CV and controlled potential experiments were performed with a Gamry Interface 1010 T potentiostat. EPR spectroscopy was conducted on a Bruker ELEXSYS II E500 with microwave frequency of ca. 9.38 GHz at 288 K. Elemental analysis was performed by Robertson Microlit Laboratories. Magnetic measurements were conducted on a Quantum Design MPMS XL SQUID magnetometer

from 2 to 300K. The diamagnetic contributions of the sample holders and the atoms were corrected with blank holders and the Pascal's constants. TGA was undertaken with a TA Q500 thermogravimetric analyzer. Nitrogen flow was set as 60 mL/min. Temperature ramping was from 40 ˚C to 900 ˚C with a rate of 10.00 ˚C/min.

4.7.2 Synthesis

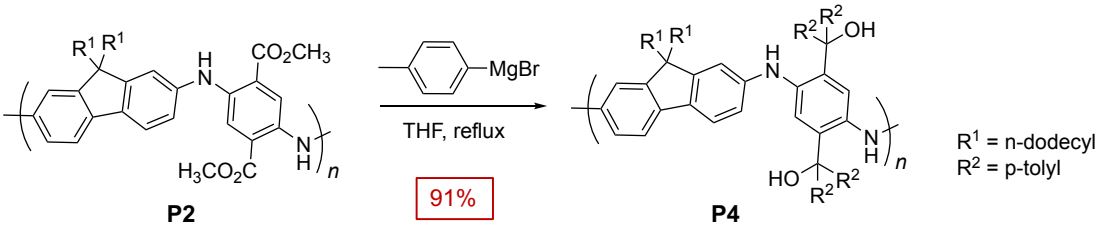

P4: **P2** ($M_{n,\ SEC}$ = 25.9 kg/mol, $Đ$ = 2.23) was synthesized according to a previously reported procedure.[78] To a solution of *p*-tolyl magnesium bromide in THF (1.5 mL, 1.0 M) under N_2 protection, **P2** solution (0.10 g) in THF (5 mL) was added dropwise. The reaction was heated to reflux for 12 h. After cooled to room temperature, the mixture was poured into saturated NH_4Cl aqueous solution. The solid precipitate was filtered and dried under vacuum, affording **P4** as a dark blue solid (0.13 g, 91%). ^{1}H NMR (500 MHz, d_8-THF, 298 K, ppm) δ = 7.25-6.86 (m, 16H), 6.67 (s, 2H), 6.40 (s, 4H), 6.23 (s, 2H), 2.90 (br, 2H), 2.19 (s, 12H), 1.70 (m, 4H), 1.35-0.94 (m, 36H), 0.87 (t, J = 6.9 Hz, 6H), 0.56 (m, 4H). ^{13}C NMR (126 MHz, d_8-THF, 298 K, ppm) δ = 151.44, 144.80, 143.45, 137.98, 136.54, 134.32, 128.77, 128.20, 125.70, 123.60, 118.65, 115.90, 112.14, 82.70, 54.87, 41.19, 34.91, 32.69, 31.27, 30.80, 30.49, 30.45, 30.13, 23.38, 21.07, 14.29. FT-IR (ATR) (cm^{-1}): 3544, 3379, 3028, 2923, 2854, 1608, 1504, 1460, 1392, 1264, 1020, 812. SEC: M_n = 20.7 kg/mol, $Đ$ = 2.54.

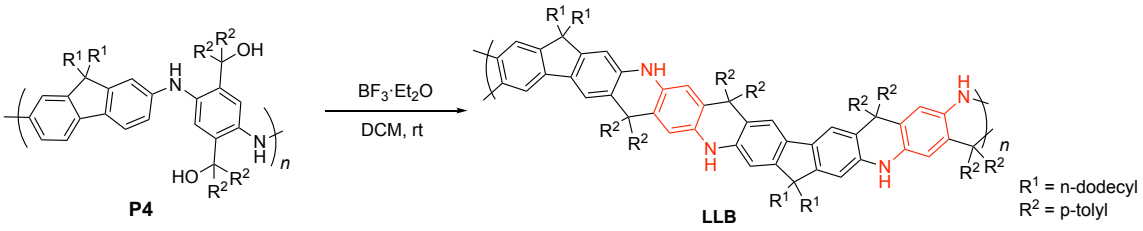

LLB: In a **P4** (0.13 g) solution in dichloromethane (10 mL), $BF_3{\cdot}Et_2O$ (0.25 mL, 0.3 M) was added and the mixture was stirred at room temperature under N_2 protection for 12 h. The reaction was quenched by adding into aqueous NaOH solution (1 M). The resulting precipitate was filtered, washed with acetone, and dried under vacuum, affording a brown solid as **LLB** (0.10 g, 84%). ^{1}H NMR (500 MHz, d_8-THF, 298 K, ppm) δ = 7.77 (br, 4H), 6.86 (AB_q, 32H), 6.62 (s, 4H), 6.51 (s, 4H), 6.37 (s, 4H), 2.29 (s, 24H), 1.35 – 0.95 (m, 80H), 0.86 (m, 20H). ^{13}C NMR (126 MHz, d_8-THF, 298 K, ppm) δ = 150.50, 150.20, 144.95, 142.78, 142.18, 135.78, 134.86, 133.03, 131.04, 128.70, 127.96, 126.98, 126.60, 125.61, 122.93, 121.76, 118.87, 115.42, 107.96, 57.18, 55.03, 41.45, 32.66, 30.93, 30.40, 30.17, 30.09, 23.37, 20.89, 14.28. FT-IR (ATR) (cm^{-1}): 3423, 3385, 2922, 2949, 1617, 1492, 1455, 1360, 1275, 811. Size exclusion chromatography: M_n = 21.6 kg/mol, $Đ$ = 1.72.

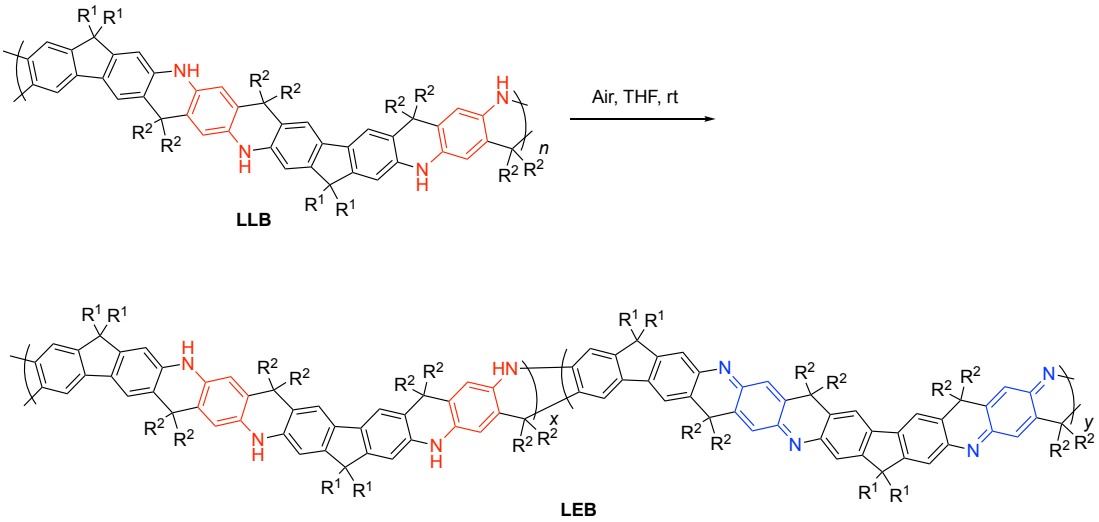

LEB: An **LLB** (0.10 g) solution in THF (10 mL) was gently stirred open in air for 12 h. The color turned from light yellow to dark green. After evaporating the solvent, the product **LEB** was collected as a black powder (0.1 g, quant.). ^{1}H NMR (500 MHz, d_8-THF, 298 K, ppm) δ = 7.17 – 6.14 (m, 16H), 1.72 (s, 6H), 1.42 – 0.96 (m, 40H), 0.86 (m, 10H). ^{13}C NMR (126 MHz, d_8-THF, 298 K, ppm) δ 153.46, 151.83, 149.89, 144.54, 143.01, 142.82, 136.75, 135.85, 130.93, 130.61, 128.99, 128.56, 127.97, 127.00, 126.13, 125.17, 122.28, 120.12, 115.32, 107.99, 105.76, 58.22, 57.07, 54.83, 41.31, 32.66, 30.95, 30.43, 30.10, 23.37, 20.87, 14.27. FT-IR (ATR) (cm^{-1}): 3305, 2931, 2947, 1679, 1616, 1500, 1463, 1368, 1284, 810. SEC: M_n = 24.3 kg/mol, $Đ$ = 1.95. Elemental analysis: C: 85.15%, H: 8.37%, N: 3.14%.

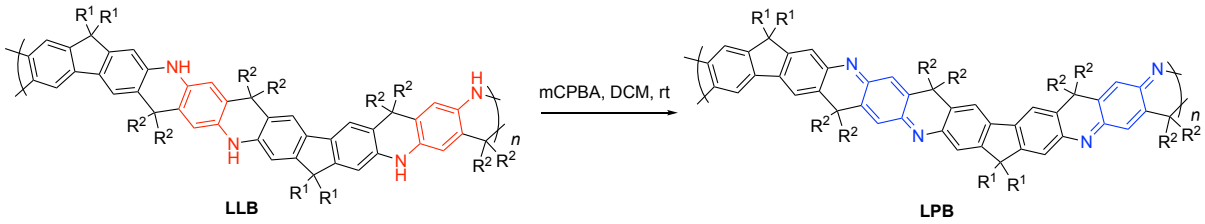

LPB: *m*CPBA (2 equiv.) was added into a solution of **LLB** (0.10 g) in CH_2Cl_2 (10 mL). The mixture was stirred at room temperature for 12 h. After washing with water (3 × 10 mL), the organic phase was dried over $MgSO_4$. After removing the solvent by rotatory evaporator, **LPB** product was isolated as a blackish powder (0.10 g, quant.). ^{1}H NMR (500 MHz, d_8-THF, 298 K, ppm) δ = 7.12-6.59 (m, 12H), 2.30 (s, 24H), 1.17 (m, 80H), 0.86 (m, 20H). ^{13}C NMR (126 MHz, d_8-THF, 298 K, ppm) δ = 152.59, 143.09, 141.73, 141.05, 140.86, 139.31, 137.56, 135.89, 130.40, 129.41, 121.91, 119.89, 56.86, 56.27, 32.64,

30.41, 30.35, 30.06, 23.34, 20.86, 14.24. FT-IR (ATR) (cm^{-1}): 2921, 2852, 1689, 1604, 1510, 1468, 1363, 1289, 815. SEC: M_n = 25.5 kg/mol, $Đ$ = 1.67.

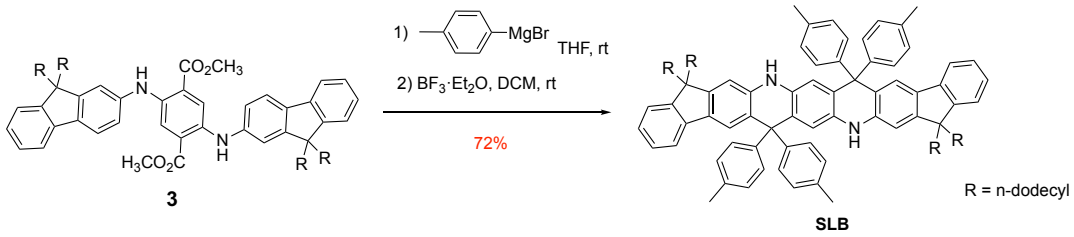

SLB: Compound **3** was synthesized according to a previously reported procedure.[79] *p*-Tolyl magnesium bromide (5 mL, 1.0 M in THF) was added into a dried flask under N_2 protection. Compound **3** (0.61 g, 0.50 mmol) was dissolved in THF (5 mL) and the solution was added into the mixture slowly. The mixture was stirred at reflux for overnight. After cooled to room temperature, the reaction was quenched with saturated NH_4Cl aqueous solution, and extracted with ethyl acetate for 3 times. The organic layers were combined and dried with $MgSO_4$. After removing solvent by rotatory evaporator, the crude product was dissolved in dry CH_2Cl_2 (10 mL). $BF_3·Et_2O$ (1 mL, 0.3 M) was added into the solution and the reaction was stirred at room temperature for 12 h in N_2 protection. The reaction was quenched with NaOH aqueous solution (1 M), and extracted with ethyl acetate. The combined organic layers were dried over $MgSO_4$ and purified with flash column chromatography (SiO_2, hexane/CH_2Cl_2: v/v = 3/1). The pure product was collected as a while solid (0.53 g, 72%). ^{1}H NMR (500 MHz, d_8-THF, 298 K, ppm) δ = 7.99 (s, 2H), 7.29-7.19 (m, 4H), 7.13-7.04 (m, 6H), 7.02 (abq, J = 8.2 Hz, 8H), 6.96-6.87 (abq, J = 8.2 Hz, 8H), 6.71 (s, 2H), 6.35 (s, 2H), 2.31 (s, 12H), 2.01-1.80 (m, 8H), 1.36-0.99 (m, 72H), 0.87 (t, J = 6.9 Hz, 12H), 0.72 (m, 4H). ^{13}C NMR (125 MHz, d_8-THF, 298

K, ppm) δ = 150.86, 150.56, 145.31, 143.14, 142.54, 136.14, 135.22, 133.39, 131.40, 129.06, 128.32, 127.34, 126.96, 125.97, 123.29, 122.12, 119.23, 115.78, 108.33, 57.54, 55.39, 41.81, 33.02, 31.28, 30.76, 30.53, 30.45, 24.97, 23.72, 21.25, 14.64. HRMS (+ESI): calcd. $[M+H]^+$ *m/z* = 1494.1402, found *m/z* = 1494.1334.

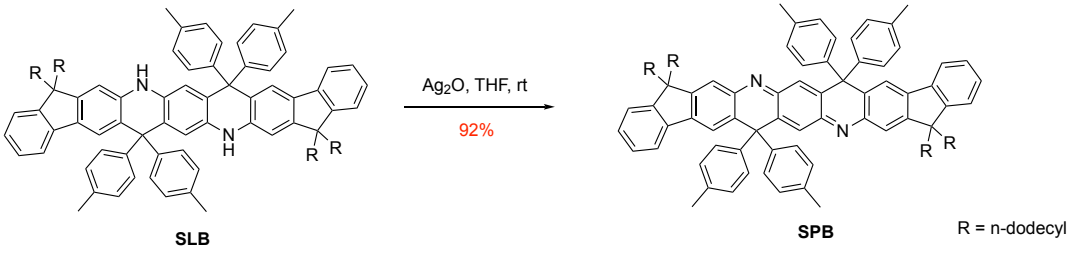

SPB: Ag_2O (0.10 g) was added into a solution of **SLB** (0.50 g, 0.33 mmol) in THF (20 mL). The mixture was stirred at room temperature for 12 h followed by filtration. The filtrate was collected and solvent was removed by rotatory evaporator. The crude product was further purified by flash column chromatography (SiO_2, hexane/CH_2Cl_2: v/v = 4/1). The product was collected as a dark red solid (0.46 g, 92%). ^{1}H NMR (500 MHz, d_8-THF, 298 K, ppm) δ = 7.51 (s, 2H), 7.48 (d, *J* = 7.4 Hz, 2H), 7.36 (m, 4H), 7.23 (m, 4H), 7.10 (abq, *J* = 8.0 Hz, 8H), 7.01 (abq, *J* = 8.0 Hz, 8H), 6.68 (s, 2H), 2.34 (s, 12H), 2.04 (m, 8H), 1.36-1.04 (m, 72H), 0.87 (t, *J* = 6.7 Hz, 12H), 0.74 (m, 8H). ^{13}C NMR (125 MHz, d_8-THF, 298 K, ppm) δ = 154.80, 152.52, 151.37, 146.08, 142.90, 142.87, 142.14, 141.64, 137.52, 136.79, 136.25, 130.98, 129.65, 128.50, 127.78, 125.72, 123.78, 122.09, 121.19, 58.68, 55.84, 41.30, 33.01, 31.18, 30.72, 30.44, 25.04, 23.73, 21.25, 14.67. HRMS (+ESI): calcd. $[M+H]^+$ *m/z* = 1493.1279, found *m/z* = 1493.1246.

4.7.3 Electrochemical Analysis

CV experiments were performed with Fc/Fc^+ as the external reference. $TBAPF_6$ solution in THF (0.1 M), MSA in THF (0.15 M), and $LiClO_4$ solution in THF (1.2 M) were used as electrolytes depending on the experimental setting. For solution-phase measurement, a 3-mm glass-carbon electrode was used as the working electrode. For thin-film measurement, ITO-coated glass with spin-coated polymer thin films were used as the working electrodes. **LPANI** samples were spin-coated on the ITO-coated glass as a thin film from their chlorobenzene solutions (20 mg/mL, 2000 rpm for 120 s) and annealed at 110 ˚C for 10 min in glovebox. The scan rate was set as 100 mV/s.

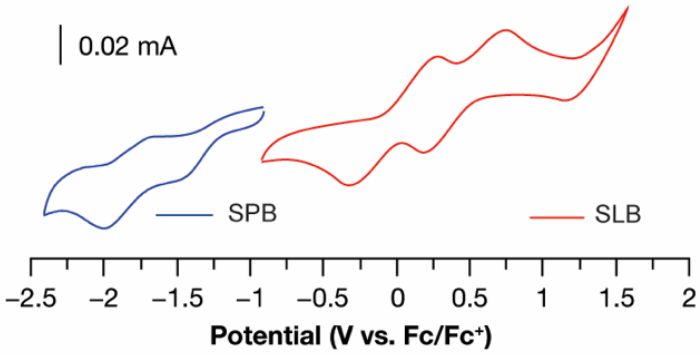

Figure 73. Cyclic voltammograms of SLB and SPB films in acetonitrile with $TBAPF_6$ (0.1 M). Reprinted with permission from [176].

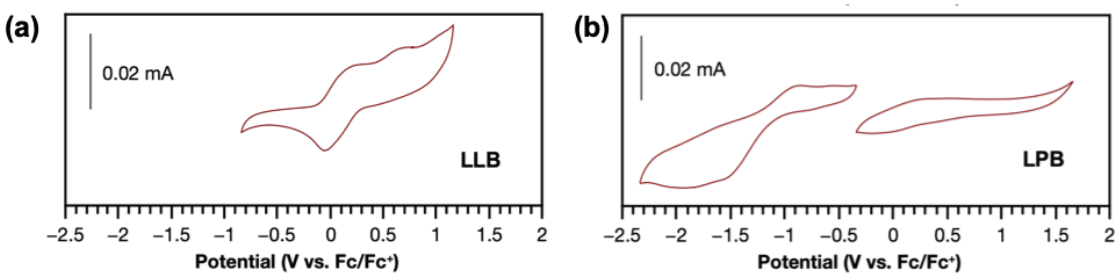

Figure 74. Cyclic voltammograms of (a) LLB and (b) LPB films in acetonitrile with $TBAPF_6$ (0.1 M). Reprinted with permission from [176].

The controlled potential experiments were performed using a three-electrode configuration. The working electrodes were held in the electrolyte containing 0.5 M of H_2SO_4 in acetonitrile, and controlled potentials of +1.0 V, +1.5 V, and +2.0 V (*vs* reference) were applied. A Pt wire was used as the counter and Ag/AgCl was used as the reference electrode. After definite time periods, CV were measured, and the anodic peak current obtained was used to evaluate the degradation percentage. PANI was deposit on the carbon fabric cloth electrode with electropolymerization in aqueous solution with aniline (0.03 M) and H_2SO_4 (0.5 M) by scanning from -0.9 V to +0.5 V for 50 cycles. The electrode was washed with deionized water and then acetonitrile before test.

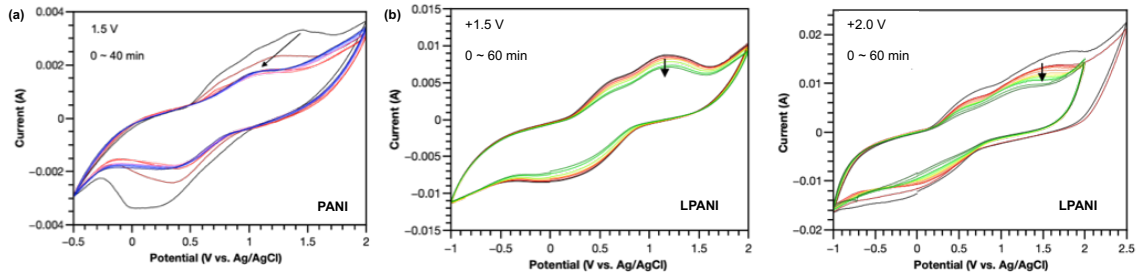

Figure 75. Cyclic voltammogram of (a) PANI and (b) LPANI on carbon fabric cloth in H_2SO_4 solution in acetonitrile (0.5 M). Oxidation potentials at +1.5 V and +2.0 V were applied on working electrodes. CV were measured after applying potential for 0, 1, 2, 3, 5, 10, 15, 20, 40, and 60 min. Reprinted with permission from [176].

4.7.4 DC Conductivity Measurement

DC conductivity was measured by a four-point probe method under vacuum. Pellet samples of **LPS** were prepared by compressing the powder materials (~ 0.1 g) in a mold with inner diameter of 25 mm at pressure of 20 kPa in air. The electrical resistance was measured with a Keithley 2450 SourceMeter. The thickness of the pellet was measured

using a profilometer as *ca.* 10^{-2} cm. The electrical conductivity was calculated based on the slope of the I-V plots.

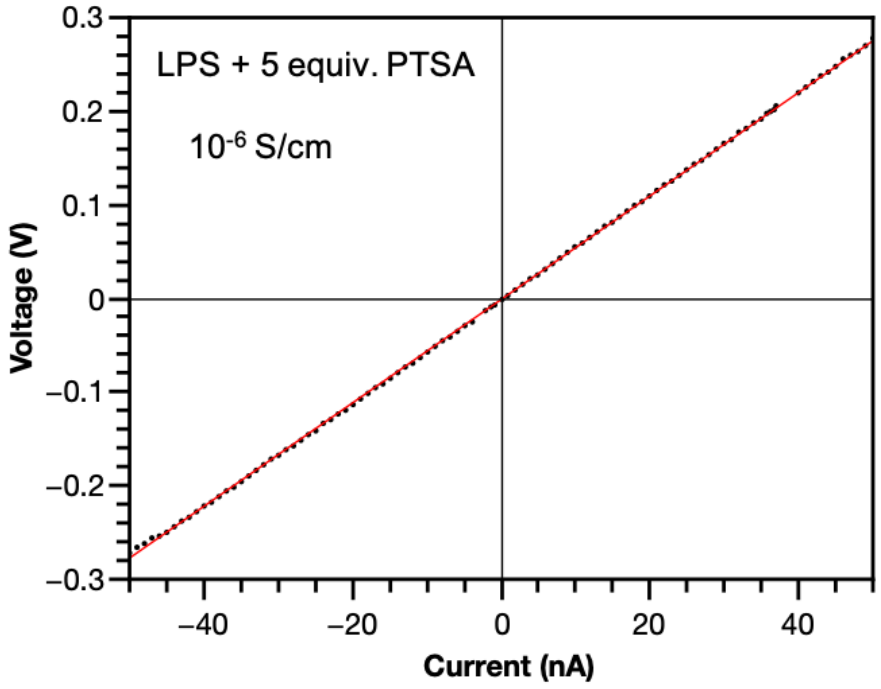

Figure 76. I-V plot of the LPS pellet mixed with PTSA using a four-probe method. Reprinted with permission from [176].

4.7.5 Electrochromic Device

Electrochromic devices were fabricated in a sandwich architecture. Gel electrolyte was prepared by mixing polymethyl methacrylate (12000 g/mol, 2 g), propylene carbonate (5 mL), and dry $LiClO_4$ (0.8 g) in acetonitrile (1 mL) at 50 ˚C for 72 h. The uniform gel was degassed under vacuum to remove the solvent. Then the gel electrolyte was drop-cast on a 1-mm-thick ITO-coated glass substrate. On another ITO-coated glass, **LEB** thin film was spin-cast (500 rpm for 30 s, then 2000 rpm for 120 s) from its chlorobenzene solution (10 mg/mL) and the sample was annealed in a glovebox at 120 ˚C for 10 min. These two

components were subsequently combined in a sandwich manner so that the gel layer and **LPANI** layer were in contact with each other. The resulting device was sealed with epoxy resin. The electrochromic response of the device was controlled with a potentiostat and recorded *in situ* with a UV-vis-NIR absorption spectrometer. Voltage on working electrode was programed to switch between –2.0 V and +2.0 V, 30 s at each stage. The visible-NIR spectra were recorded accordingly. The switching process was recycled for 200 times to test the recycling performance of the device.

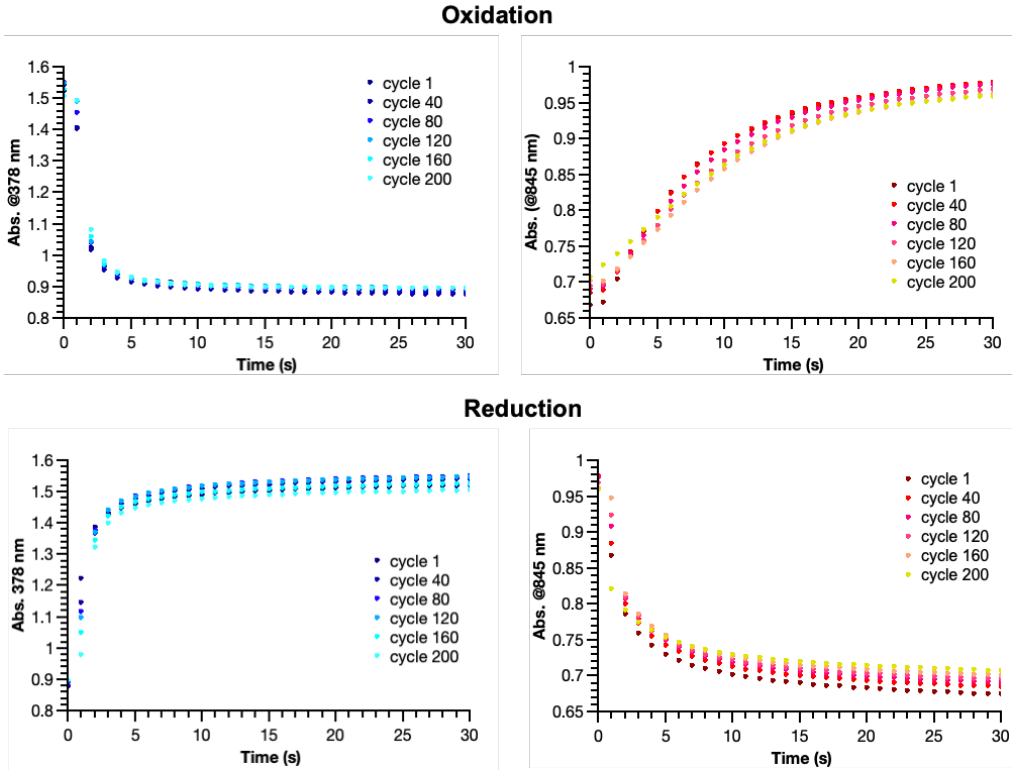

Figure 77. Time-dependent absorption of the electrochromic device at 378 nm and 845 nm at varied cycles. Reprinted with permission from [176].

The kinetics of oxidation and reduction processes were analyzed separately at both wavelengths. The time-dependent absorption plots of six cycles (**Figure 79**) were studied

and they were all fit in first-order exponential equations shown in **Table 5**. The averaged fitting parameters of six cycles and corresponding standard deviation (STD) values were obtained.

Table 5. Kinetics fitting equation and parameters of plots in Figure 80. Reprinted with permission from [176].

	378 nm	845 nm
$A = A_{oxi\_0} + A_{oxi\_1} \cdot e^{-k_{oxi}}$		
Avg. $A_{oxi,0}$	0.893	0.991
STD	0.005	0.003
Avg. $A_{oxi,1}$	0.696	-0.323
STD	0.015	0.015
Avg. k_{oxi} (s^{-1})	0.556	0.101
STD	0.029	0.016
R^2	0.927~0.954	0.993~0.997
$A = A_{red\_0} + A_{red\_1} \cdot e^{-k_{red}}$		
Avg. $A_{red,0}$	1.519	0.703
STD	0.015	0.010
Avg. $A_{red,1}$	-0.646	0.264
STD	0.013	0.020
Avg. k_{red} (s^{-1})	0.590	0.386
STD	0.077	0.042
R^2	0.955~0.989	0.942~0.980

4.7.6 Thermogravimetric Analysis

For **LPANI**, theoretical weight percentage values of backbone, alkyl chains, and tolyl groups are 29%, 34%, and 37%. On TGA plots of three **LPANI** samples, the first weight-loss stage could be identified as 280 ~ 460 ˚C, during which 25% ~ 36% weight loss was observed. This stage could be attributed to the cleavage of alkyl chains on the fluorene moieties. Above 500 ˚C, continuous weight loss was observed for all three

polymers. For **LEB** and **LPB**, this stage could be attributed to continuous cleavage of tolyl groups and the conversion of sp^3 carbon into more thermodynamically favorable sp^2 carbon. While for **LLB**, the backbone also underwent thermal degradation. Compared with the conventional polyaniline (emeraldine base), higher thermal stability was observed in ladder polymers up to 400 ˚C.

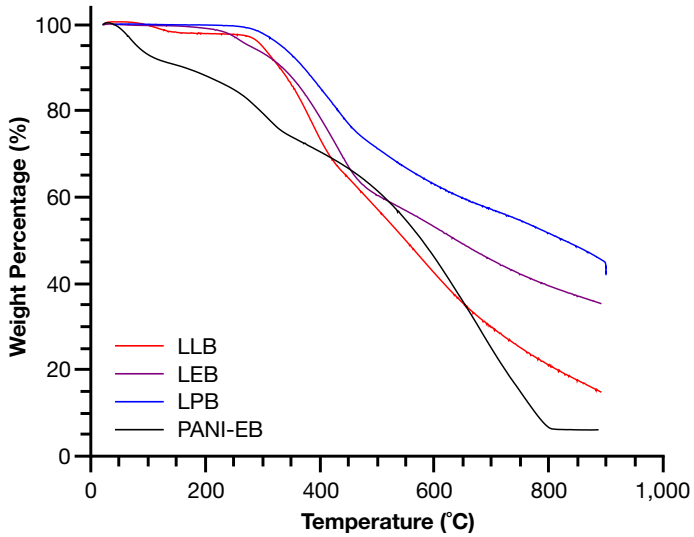

Figure 78. TGA plots of LLB, LEB, and LPB. Reprinted with permission from [176].

4.8 Appendix

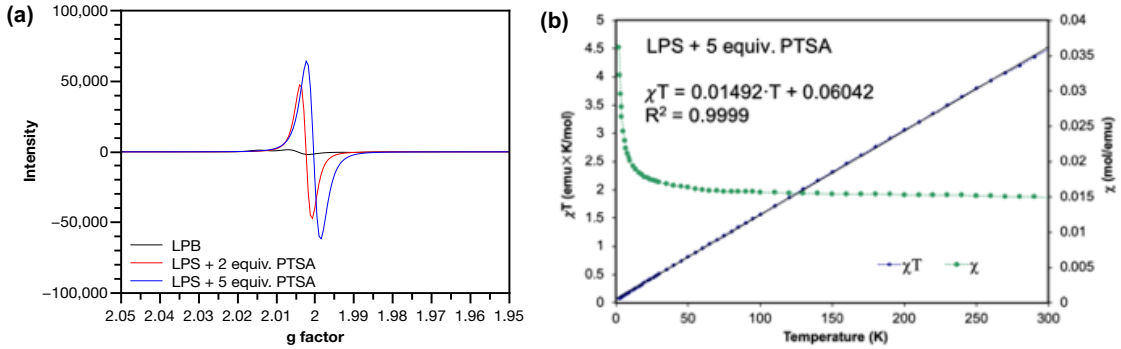

Figure 79. (a) EPR spectra of LPB and LPS with PTSA. (b) Varied-temperature paramagnetic susceptibility of LPS. Reprinted with permission from [176].

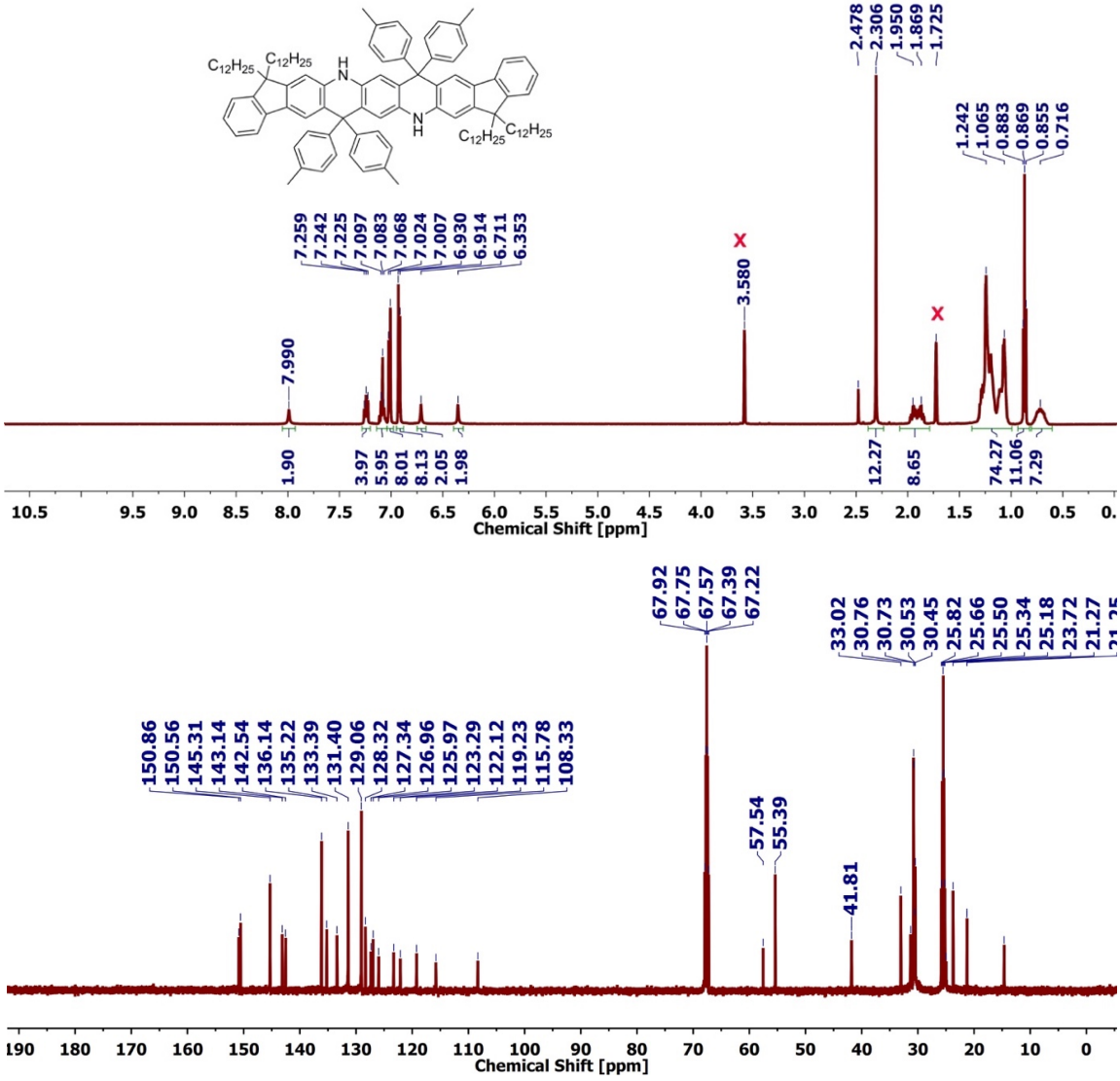

Figure 80. ^{1}H (500 MHz) and ^{13}C (125 MHz) NMR of SLB in d_8-THF at 298 K. Reprinted with permission from [176].

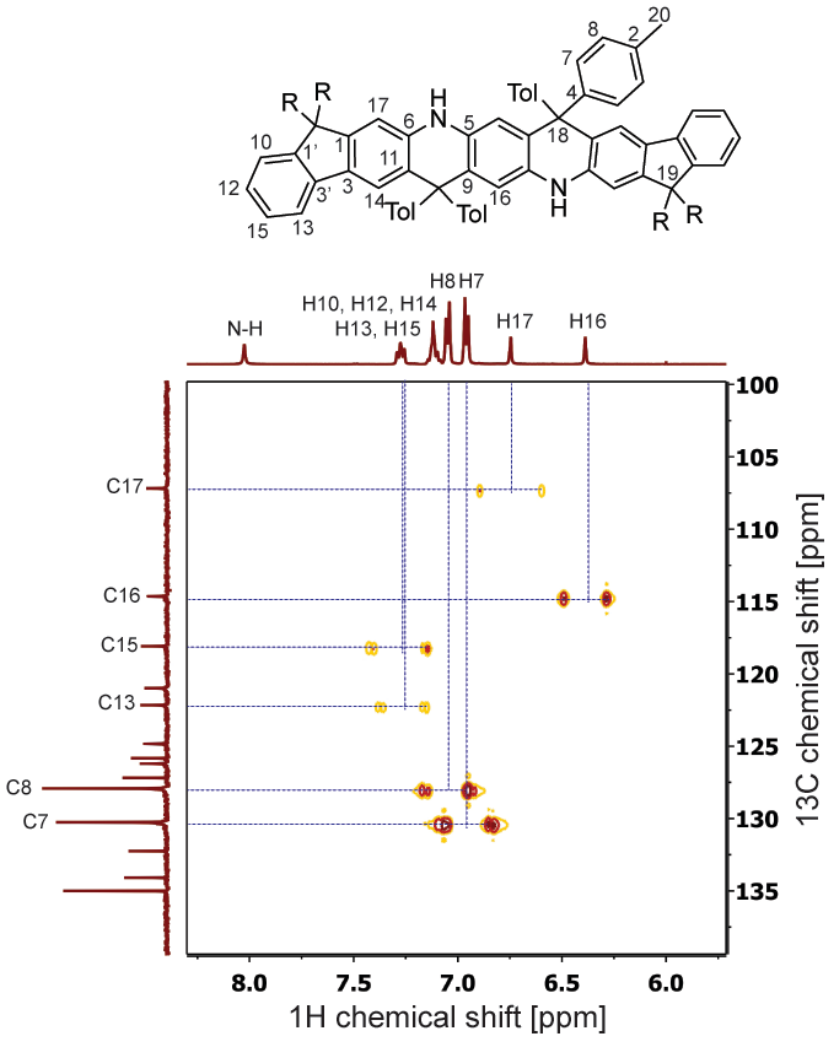

Figure 81. ^{1}H-^{13}C HSQC NMR spectrum of SLB in d_8-THF at 298 K. Reprinted with permission from [176].

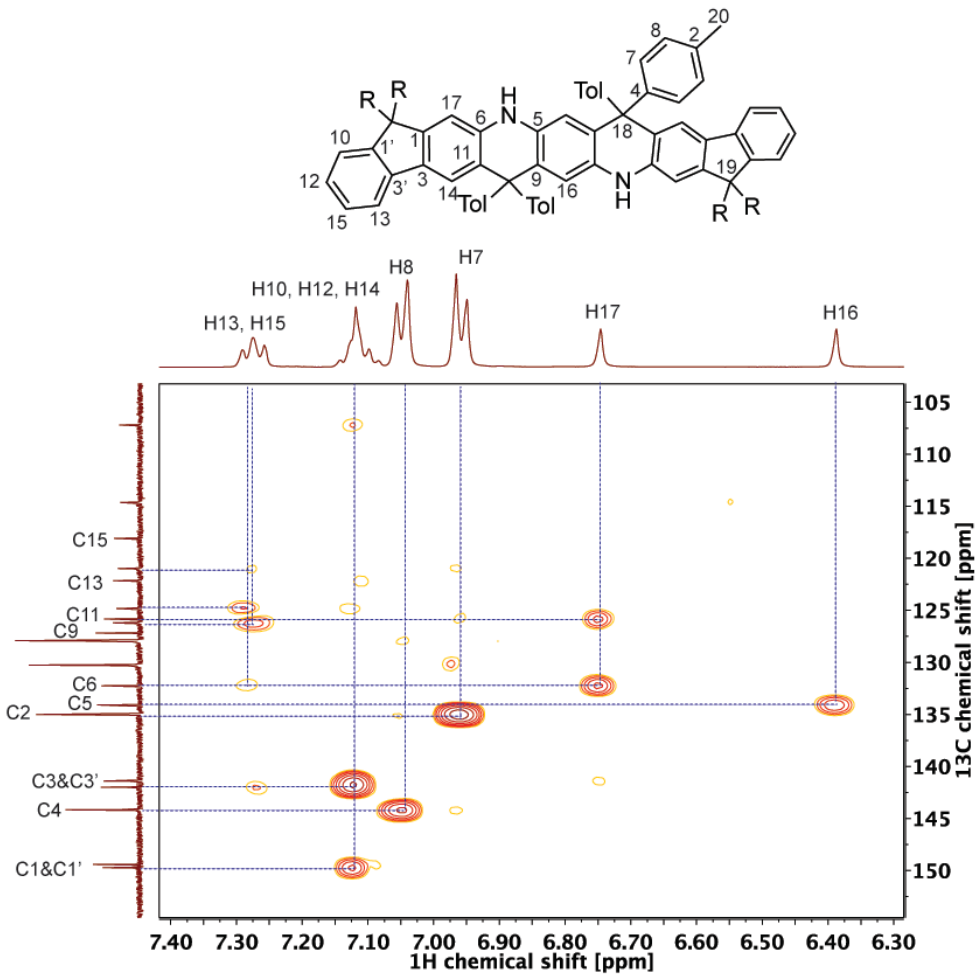

Figure 82. ^{1}H-^{13}C HMBC NMR spectrum of SLB in d_8-THF at 298 K. Reprinted with permission from [176].

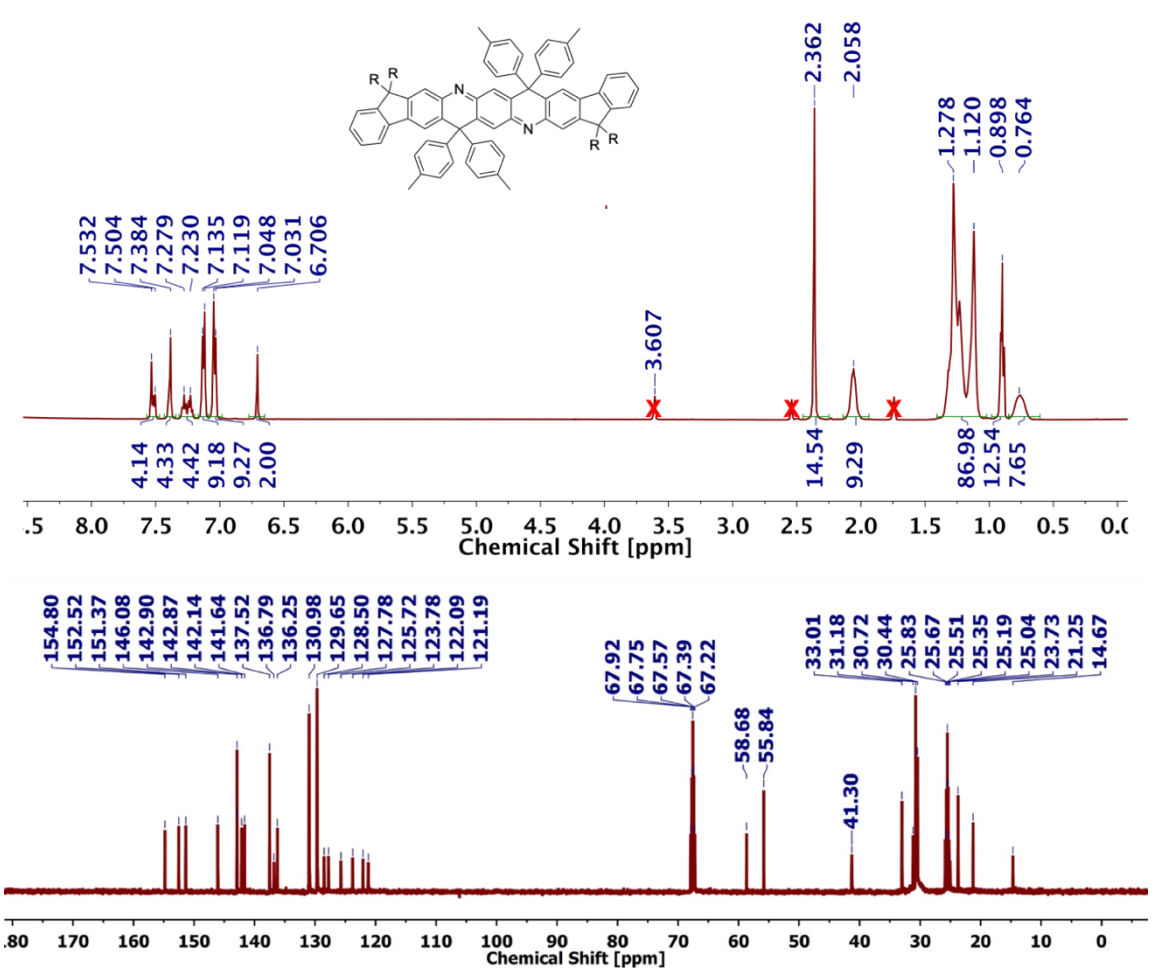

Figure 83. ^{1}H (500 MHz) and ^{13}C (125 MHz) NMR of SPB in d_8-THF at 298 K. Reprinted with permission from [176].

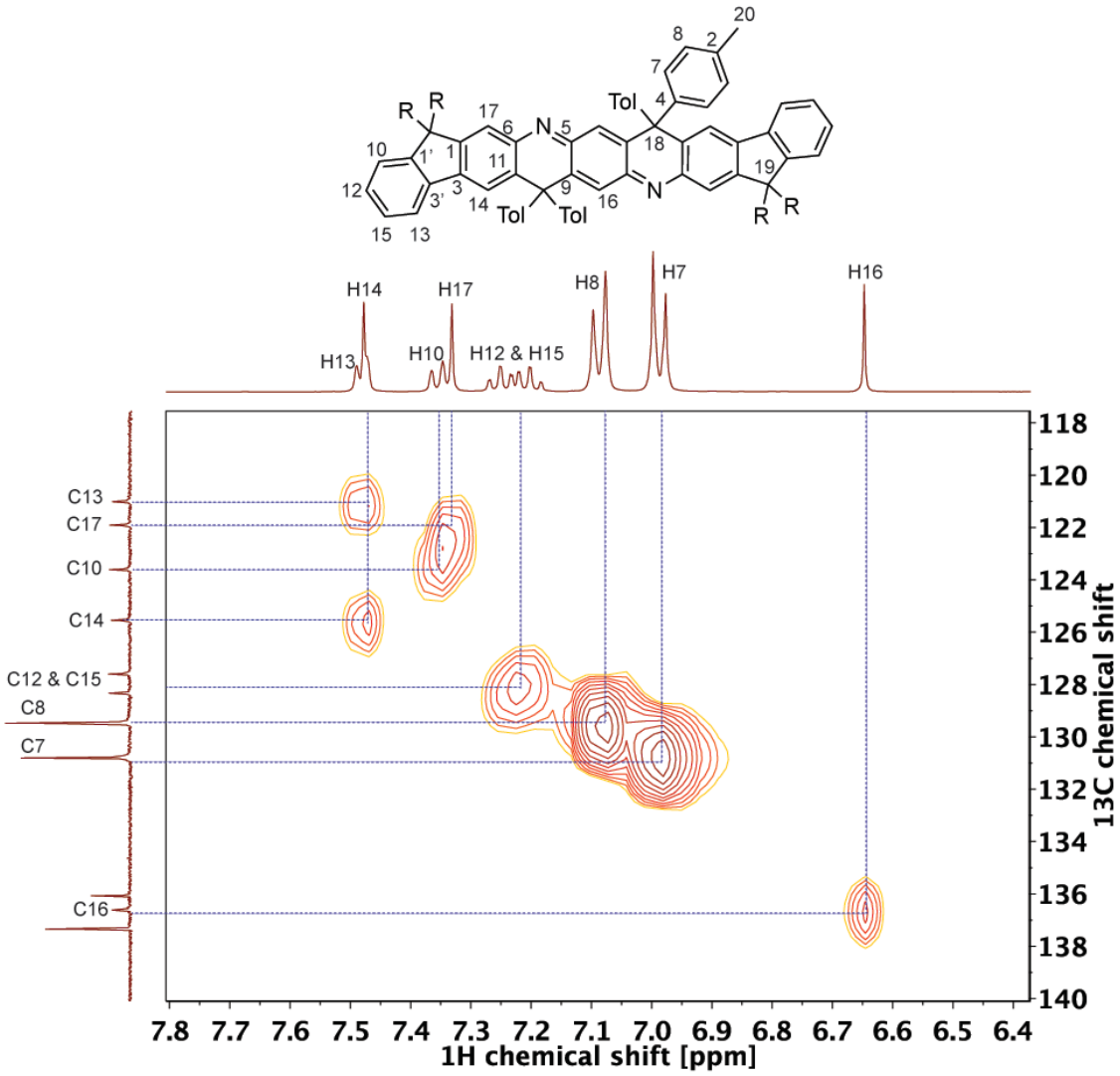

Figure 84. ^{1}H-^{13}C HSQC NMR spectrum of SPB in d_8-THF at 298 K. Reprinted with permission from [176].

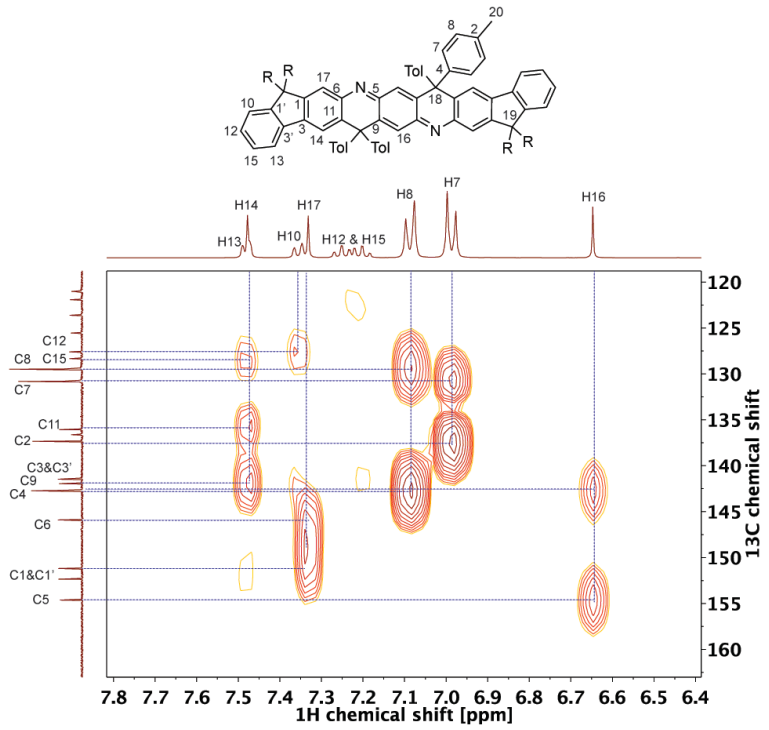

Figure 85. ^{1}H-^{13}C HMBC NMR spectrum of SPB in d_8-THF at 298 K. Reprinted with permission from [176].

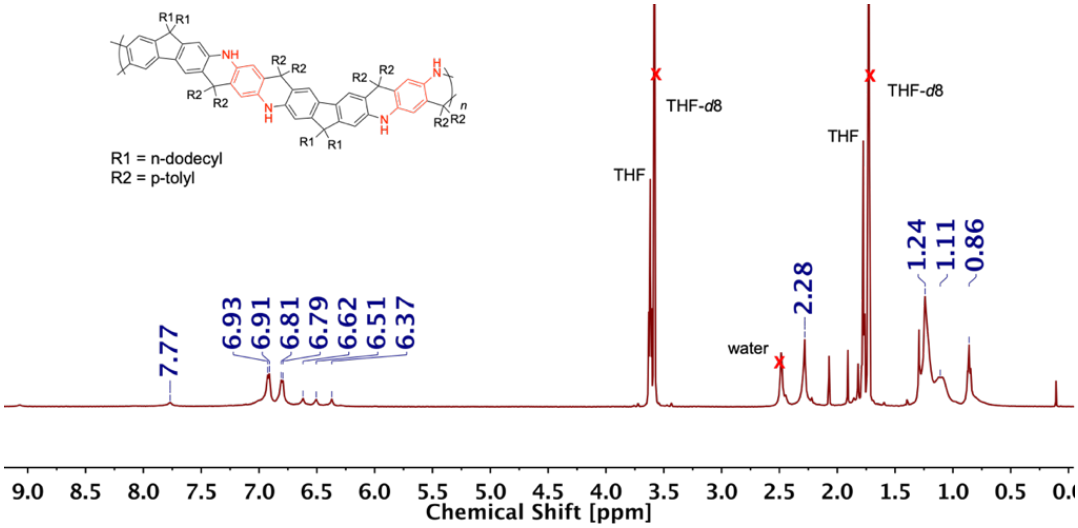

Figure 86. ^{1}H NMR (500 MHz) of LLB in d_8-THF at 298 K. Reprinted with permission from [176].

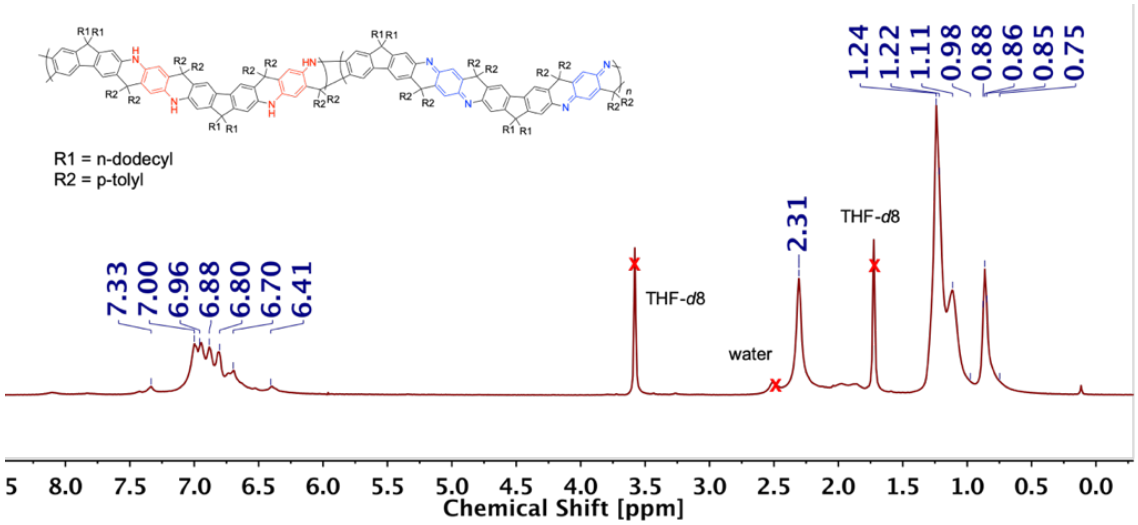

Figure 87. ^{1}H NMR (500 MHz) of LEB in d_8-THF at 298 K. Reprinted with permission from [176].

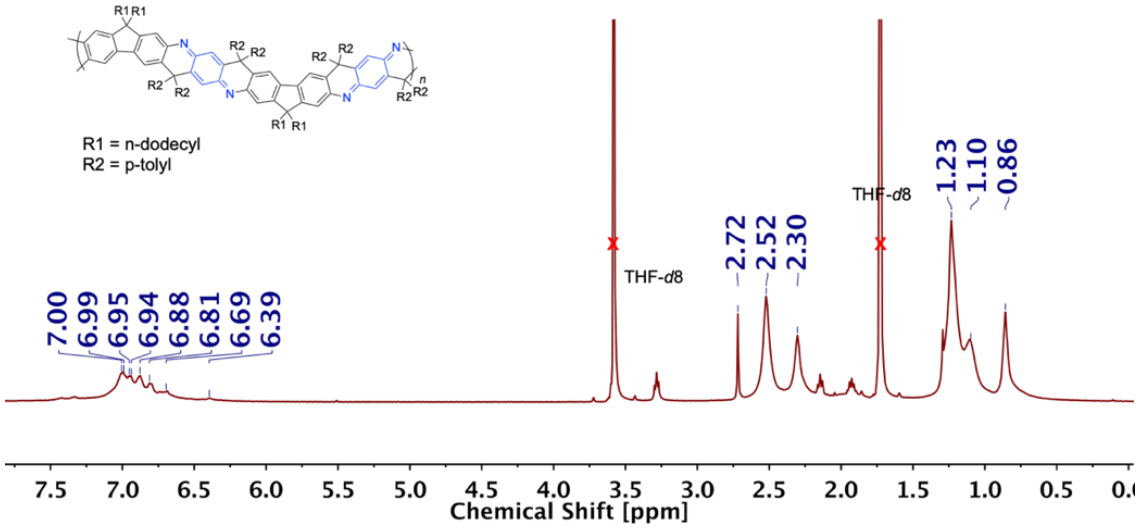

Figure 88. ^{1}H NMR (500 MHz) of LPB in d_8-THF at 298 K. Reprinted with permission from [176].

CHAPTER V

CONCLUSIONS

5.1 Aromatic Ladder Polymer Featuring Intermolecular Hydrogen-Bonds

5.1.1 Summary

Ladder-type conjugated molecules stand out as intriguing materials due to their extended intramolecular charge transfer, strong intermolecular interactions, and high stability, owing to the coplanar and rigid structure. However, challenges present in this field in twofold: difficulties in constructing low-defect ladder-type backbones, and the solubility issues in the synthesis, characterization and processing. In this research, we investigated polymer **PIQA** derived from quinacridone structure, with self-complementary H-bonds incorporated into ladder-type repeating units. A three-step gram-scale synthesis route was established with a high overall yield. A reversible post-functionalization strategy was applied to obtain good solubility which enabled both clear solution-phase characterization and solution-processing of this polymer. ^{13}C NMR spectroscopy characterization was achieved for structural elucidation, revealing the low-defect level of ladder-type backbones. Using a strategy of processing-followed-by-annealing approach, thin film casting of ladder polymer were achieved. This strategy is also promising to be applied in other processing techniques such as printing and electrospinning.

The features of backbone rigidity in ladder-type structure and intermolecular H-bonding interactions are integrated in **PIQA**, leading to its excellent thermal stability and chemical/solvent resistance in the solid state. High stability against aggressive solvents at

high temperature demonstrates the potential of the polymer to be used as protective coating materials for harsh environments.

Overall, this research achieved a ladder-type conjugated polymer with high rigidity and strong intermolecular interactions possessing unprecedented properties. The reversible post-functionalization strategy addressed the solubility challenge in ladder-type polymer research efficiently, opening up the possibility of designing and solution-phase processing of functional ladder polymers for various applications.

5.1.2 Perspectives

After annealing at 700 ˚C, **PIQA** shows graphitic character and becomes conductive, demonstrating its potential to be a precursor for functional carbon materials. The pre-ordered constitution combining polycyclic ladder-type backbone and *interchain* H-bonding is proposed to facilitate the carbonization process, affording a graphitic structure with a low defect-level. This process is also more energy-saving which requires lower annealing temperature.

The solubility challenge of ladder-type molecules can also be addressed by side-chain modification. As investigated in other conjugated polymers, side chains containing ionic moieties, such ammonium and sulfonate, can render aqueous or alcoholic solubility, promoting desired properties as polyelectrolytes for optoelectronic applications.[194-197] Ladder-type polyelectrolytes are also interesting materials considering the intrinsic coplanar and rigid structural features. While such polymers have not been well investigated due to the synthesis and characterization difficulties.[198] In an ongoing project, dimethylamine groups are installed on fluorene moieties and further incorporated into a

PIQA-like ladder polymer. Good water solubility is obtained when protonation process takes place. Interesting properties, including the pH-responsive aqueous solubility and strong fluorescence of the ladder polymer are under investigation.

5.2 Quinoidal Ladder-Type Pernigraniline Oligomers

5.2.1 Summary

In this project, a series of ladder-type pernigraniline salt-analogous oligomers with up to 27 fused ring constitution were obtained. The syntheses were achieved through iterative cross-coupling reactions followed by cyclization and oxidation. In contrast to their unstable non-ladder-type counterparts, these ladder-type pernigraniline-like molecules all adopt a well-defined all-trans configuration and demonstrate excellent chemical stability after protonation in ambient conditions, rendering possible to reveal the intrinsic electronic and magnetic properties. Open-shell spin character and a dominant temperature-independent Pauli paramagnetism were observed in the solid state, as indication of the delocalization nature of polarons in ladder-type pernigraniline salts.

The data and results obtained in this work offered a number of important principles for the design and development of next-generation functional organic materials. First, the employment of ladder-type constitution is demonstrated to be an efficient strategy to stabilize certain conventionally unstable organic materials, particularly those prone to undergo entropy-driven decomposition. Second, this strategy can also be used to lock the configuration and conformation of complex polymer backbones to afford desired

properties and to give a much clearer correlation between structural features and properties.

5.2.2 Perspectives

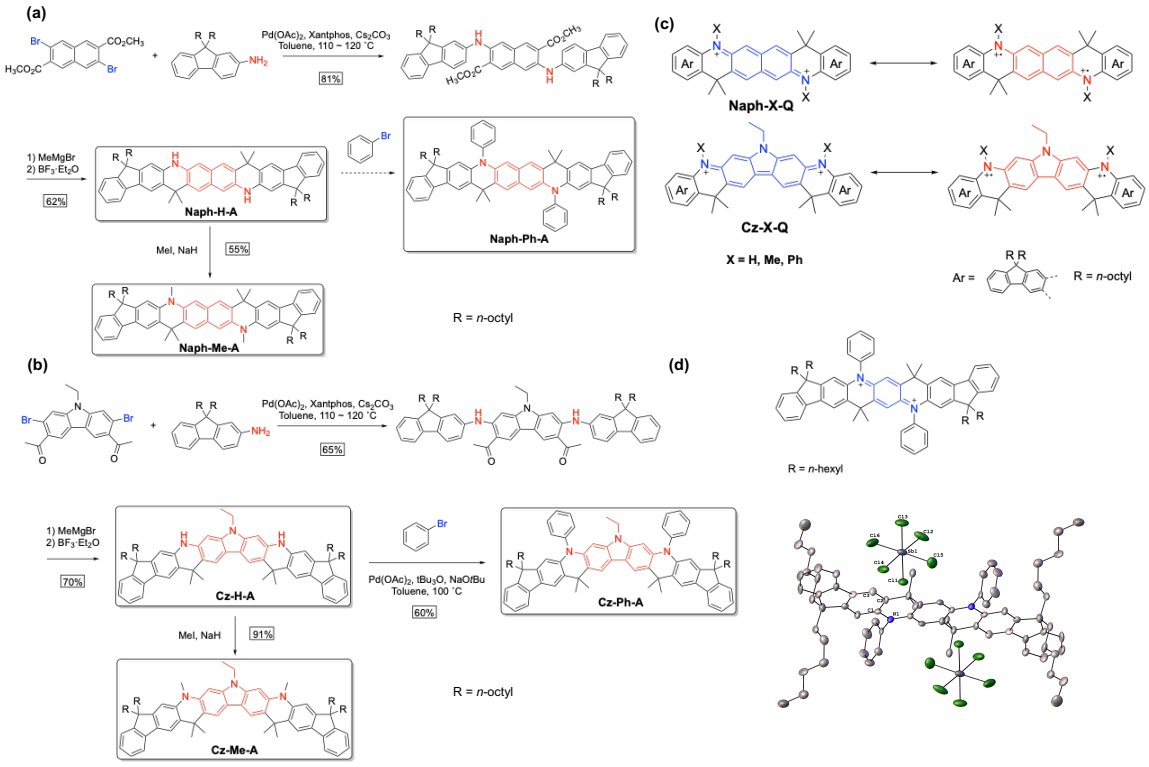

Figure 89. Synthesis routes of (a) naphthalene and (b) carbazole-derived ladder molecules; (c) resonance forms of proposed naphthalene and carbazole-derived ladder quinoidal molecules; (d) structure and single crystal structure of a phenyl-derived ladder quinoidal molecule.

Incorporation of ladder-type constitution into quinoidal molecules can drastically impact the electronic properties, including open-shell character and spin multiplicity. In this study, the comparison between **H_2-Q1^{2+}** and **Me-Q1^{2+}** revealed that side groups could tune the magnetic properties owing to the different intermolecular interactions. In an ongoing project, quinoidal molecules as derivatives of **H_2-Q1^{2+}** and **Me-Q1^{2+}** have been

designed and synthesized (**Figure 89a**, **b**, **d**). The structures, open-shell character (**Figure 89c**), paramagnetic properties, and stability of these molecules will be investigated systematically to study the impacts of different quinoidal constitutions and side groups. The structure-property correlation is expected to further our understanding of quinoidal conjugated systems.

5.3 Ladder-Type Polyaniline-Analogous Polymers

5.3.1 Summary

Electrochemical stability and states-delocalization critically impact the functions and practical applications of electronically active polymers. Incorporation of ladder-type constitution into conjugated polymers represents a promising strategy to enhance the aforementioned properties from a fundamental structural perspective. In this study, a series of ladder-type polyaniline-analogous polymers and designed and synthesized through a facile and scalable route. Chemical and electrochemical interconversions between the fully oxidized pernigraniline salt state and the fully reduced leucoemeraldine base state are both achieved in a highly reversible and robust manner. The protonated pernigraniline form of the ladder polymer exhibits unprecedented electrochemical stability in highly acidic and oxidative conditions. Such a stability enables the access of a near-infrared light-absorbing material with extended polaron delocalization in the solid state. An electrochromic device composed of this ladder polymer shows distinct switches between UV- and near-infrared-absorbing states with a remarkable cyclability, meanwhile tolerating a wide operating window of 4 volts. Taken together, this project demonstrates

the principle of employing ladder-type backbone constitution to endow superior electrochemical properties into electronically active polymers.

5.3.2 Perspectives

In the context of delocalized polarons found in these pernigraniline salt-derivatives, one can anticipate that the bulk conductivity of similar ladder-type analogues can be enhanced by orders of magnitudes once the insulating side-chains are shortened and the conjugated backbones are elongated. This goal can be achieved through a processing strategy involving *in situ* side-chain cleavage[78, 94] and backbone oxidation, from a soluble precursor functionalized with cleavable side-chains in its reduced state. Following design principle, monomers with short alkyl side-chains are designed to construct ladder-type polyanilines. Based on our experience in constructing oligomers and polymers, Buchwald-Hartwig cross-coupling reaction can be used to realize the polymerization process efficiently, which allows employment of a broader scope of monomers (**Figure 90a**). The reversible protection/deprotection strategy introduced in Chapter II will be used to increase the solubility and processability of the ladder polymer product (**Figure 90b**). After thermal annealing, oxidation, and doping process, the thin film will be measured to reveal the conductivity property. Future development along this direction can lead to a new class of highly conductive, metallic organic species.

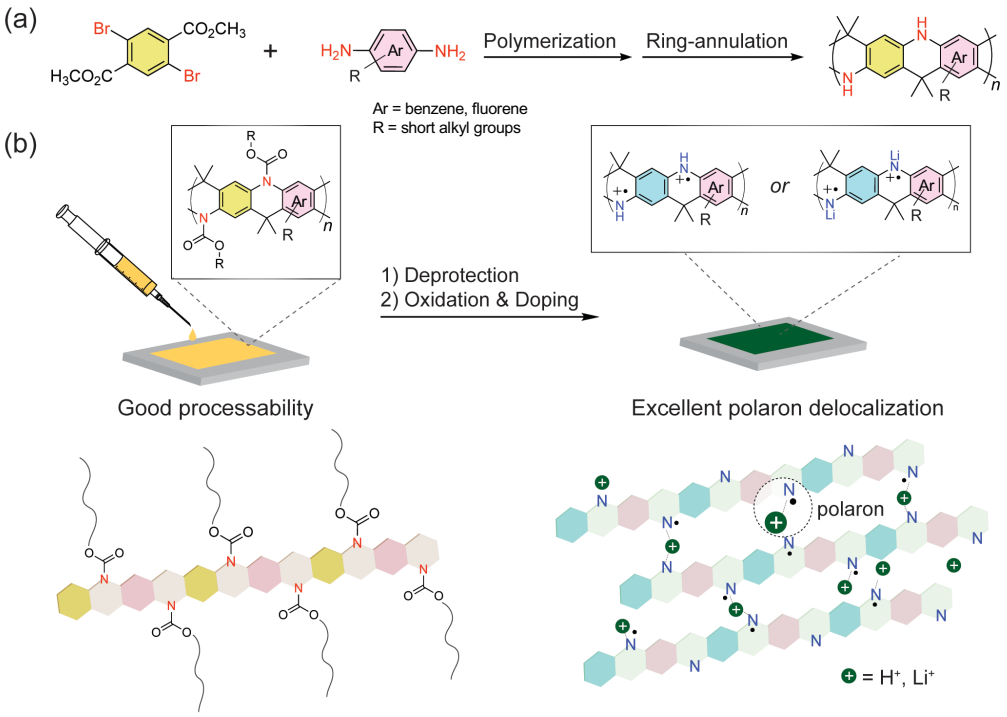

Figure 90. (a) Proposed synthesis route of ladder-type polyaniline with short alkyl side-chains. (b) Graphical illustration of the solution processing of ladder-type polyaniline thin films. After thermal annealing, oxidation and doping, delocalized polarons are expected to be generated.

REFERENCES

(1) *IUPAC. Compendium of Chemical Terminology, 2nd ed. (the "Gold Book")*. Blackwell Scientific Publications: Oxford, 1997.

(2) International Union of, P.; Applied, C., *Compendium of Polymer Terminology and Nomenclature - IUPAC Recommendations 2008*. Royal Society of Chemistry: 2009.

(3) Lee, J.; Kalin, A. J.; Yuan, T.; Al-Hashimi, M.; Fang, L., Fully conjugated ladder polymers. *Chem. Sci.* **2017**, *8*, 2503-2521.

(4) Schlüter, A. D., Ladder polymers: the new generation. *Adv. Mater.* **1991**, *3*, 282-291.

(5) Schluter, A. D.; Loffler, M.; Enkelmann, V., Synthesis of a Fully Unsaturated All-Carbon Ladder Polymer. *Nature* **1994**, *368*, 831-834.

(6) Zhu, C.; Fang, L., Locking the Coplanar Conformation of π-Conjugated Molecules and Macromolecules Using Dynamic Noncovalent Bonds. *Macromol. Rapid Commun.* **2018**, *39*, 1700241.

(7) Wu, Y.; Zhang, J.; Fei, Z.; Bo, Z., Spiro-bridged ladder-type poly (p-phenylene) s: towards structurally perfect light-emitting materials. *J. Am. Chem. Soc.* **2008**, *130*, 7192-7193.

(8) Wang, Y.; Guo, H.; Harbuzaru, A.; Uddin, M. A.; Arrechea-Marcos, I.; Ling, S.; Yu, J.; Tang, Y.; Sun, H.; López Navarrete, J. T.; Ortiz, R. P.; Woo, H. Y.; Guo, X., (Semi) ladder-Type Bithiophene Imide-Based All-Acceptor Semiconductors: Synthesis, Structure–Property Correlations, and Unipolar n-Type Transistor Performance. *J. Am. Chem. Soc.* **2018**, *140*, 6095-6108.

(9) Zhang, W.; Han, Y.; Zhu, X.; Fei, Z.; Feng, Y.; Treat, N. D.; Faber, H.; Stingelin, N.; McCulloch, I.; Anthopoulos, T. D.; Heeny, M., A Novel Alkylated Indacenodithieno [3, 2-b] thiophene-Based Polymer for High-Performance Field-Effect Transistors. *Adv. Mater.* **2016**, *28*, 3922-3927.

(10) Cai, Z.; Awais, M. A.; Zhang, N.; Yu, L., Exploration of syntheses and functions of higher ladder-type π-conjugated heteroacenes. *Chem* **2018**, *4*, 2538-2570.

(11) Qiu, N.; Zhang, H.; Wan, X.; Li, C.; Ke, X.; Feng, H.; Kan, B.; Zhang, H.; Zhang, Q.; Lu, Y.; Chen, Y., A New Nonfullerene Electron Acceptor with a Ladder Type Backbone for High-Performance Organic Solar Cells. *Adv. Mater.* **2017**, *29*, 1604964.

(12) Hou, J.; Inganäs, O.; Friend, R. H.; Gao, F., Organic solar cells based on non-fullerene

acceptors. *Nat. Mater.* **2018**, *17*, 119.

(13) Wang, S.; Sun, H.; Ail, U.; Vagin, M.; Persson, P. O.; Andreasen, J. W.; Thiel, W.; Berggren, M.; Crispin, X.; Fazzi, D., Thermoelectric Properties of Solution-Processed n-Doped Ladder-Type Conducting Polymers. *Adv. Mater.* **2016**, *28*, 10764-10771.

(14) Babel, A.; Jenekhe, S. A., High electron mobility in ladder polymer field-effect transistors. *J. Am. Chem. Soc.* **2003**, *125*, 13656-13657.

(15) Lee, J.; Rajeeva, B. B.; Yuan, T.; Guo, Z.-H.; Lin, Y.-H.; Al-Hashimi, M.; Zheng, Y.; Fang, L., Thermodynamic synthesis of solution processable ladder polymers. *Chem. Sci.* **2016**, *7*, 881-889.

(16) Kalin, A. J.; Lee, J.; Fang, L., Annulation reactions for conjugated ladder-type oligomers. *Synlett* **2018**, *29*, 993-998.

(17) Teo, Y. C.; Lai, H. W.; Xia, Y., Synthesis of Ladder Polymers: Developments, Challenges, and Opportunities. *Chem. Eur. J.* **2017**, *23*, 14101-14112.

(18) Chen, J.; Yang, K.; Zhou, X.; Guo, X., Ladder-Type Heteroarene-Based Organic Semiconductors. *Chem. Asia. J.* **2018**, *13*, 2587-2600.

(19) Kertesz, M.; Choi, C. H.; Yang, S., Conjugated polymers and aromaticity. *Chem. Rev.* **2005**, *105*, 3448-3481.

(20) Brédas, J. L.; Thémans, B.; Fripiat, J.; André, J.-M.; Chance, R., Highly conducting polyparaphenylene, polypyrrole, and polythiophene chains: An ab initio study of the geometry and electronic-structure modifications upon doping. *Phys. Rev. B* **1984**, *29*, 6761.

(21) Brédas, J.; Thémans, B.; André, J., Electronic structure of highly conducting poly-(p-phenylene) chains: An ab initio Hartree-Fock study. *Phys. Rev. B* **1982**, *26*, 6000.

(22) Brédas, J. E.; Chance, R. R.; Silbey, R., Theoretical studies of charged defect states in doped polyacetylene and polyparaphenylene. *Mol. Cryst. Liq. Cryst.* **1981**, *77*, 319-332.

(23) Burrezo, P. M.; Zafra, J. L.; López Navarrete, J. T.; Casado, J., Quinoidal/Aromatic Transformations in π-Conjugated Oligomers: Vibrational Raman studies on the Limits of Rupture for π-Bonds. *Angew. Chem., Int. Ed.* **2017**, *56*, 2250-2259.

(24) Roncali, J., Synthetic principles for bandgap control in linear π-conjugated systems. *Chem. Rev.* **1997**, *97*, 173-206.

(25) Krygowski, T. M.; Cyrański, M. K., Structural aspects of aromaticity. *Chem. Rev.* **2001**, *101*, 1385-1420.

(26) Brédas, J. L., Relationship between band gap and bond length alternation in organic conjugated polymers. *J. Chem. Phys.* **1985**, *82*, 3808-3811.

(27) Brédas, J. L.; Thémans, B.; André, J. M., Electronic structure of highly conducting poly-(p-phenylene) chains: An ab initio Hartree-Fock study. *Phys. Rev. B* **1982**, *26*, 6000.

(28) Casado, J.; Ortiz, R. P.; Navarrete, J. T. L., Quinoidal oligothiophenes: new properties behind an unconventional electronic structure. *Chem. Soc. Rev.* **2012**, *41*, 5672-5686.

(29) Gopalakrishna, T. Y.; Zeng, W.; Lu, X.; Wu, J., From open-shell singlet diradicaloids to polyradicaloids. *Chem. Comm.* **2018**, *54*, 2186-2199.

(30) Dressler, J. J.; Teraoka, M.; Espejo, G. L.; Kishi, R.; Takamuku, S.; Gómez-García, C. J.; Zakharov, L. N.; Nakano, M.; Casado, J.; Haley, M. M., Thiophene and its sulfur inhibit indenoindenodibenzothiophene diradicals from low-energy lying thermal triplets. *Nat. Chem.* **2018**, *10*, 1134-1140.

(31) Zeng, Z.; Shi, X.; Chi, C.; Navarrete, J. T. L.; Casado, J.; Wu, J., Pro-aromatic and anti-aromatic π-conjugated molecules: an irresistible wish to be diradicals. *Chem. Soc. Rev.* **2015**, *44*, 6578-6596.

(32) Zeng, W.; Phan, H.; Herng, T. S.; Gopalakrishna, T. Y.; Aratani, N.; Zeng, Z.; Yamada, H.; Ding, J.; Wu, J., Rylene ribbons with unusual diradical character. *Chem* **2017**, *2*, 81-92.

(33) Salem, L.; Rowland, C., The electronic properties of diradicals. *Angew. Chem., Int. Ed. Engl.* **1972**, *11*, 92-111.

(34) Sun, Z.; Huang, K.-W.; Wu, J., Soluble and stable heptazethrenebis (dicarboximide) with a singlet open-shell ground state. *J. Am. Chem. Soc.* **2011**, *133*, 11896-11899.

(35) Rudebusch, G. E.; Zafra, J. L.; Jorner, K.; Fukuda, K.; Marshall, J. L.; Arrechea-Marcos, I.; Espejo, G. L.; Ortiz, R. P.; Gómez-García, C. J.; Zakharov, L. N.; Makano, M.; Ottosson, H.; Casado, J.; Haley, M. M., Diindeno-fusion of an anthracene as a design strategy for stable organic biradicals. *Nat. Chem.* **2016**, *8*, 753-759.

(36) Hu, P.; Lee, S.; Herng, T. S.; Aratani, N.; Gonçalves, T. P.; Qi, Q.; Shi, X.; Yamada, H.; Huang, K.-W.; Ding, J.; Kim, D.; Wu, J., Toward tetraradicaloid: the effect of fusion mode on radical character and chemical reactivity. *J. Am. Chem. Soc.* **2016**, *138*, 1065-1077.

(37) Chow, C. H. E.; Han, Y.; Phan, H.; Wu, J., Nitrogen-doped heptazethrene and octazethrene diradicaloids. *Chem. Comm.* **2019**, *55*, 9100-9103.

(38) London, A. E.; Chen, H.; Sabuj, M. A.; Tropp, J.; Saghayezhian, M.; Eedugurala, N.;

Zhang, B.; Liu, Y.; Gu, X.; Wong, B.; Rai, N.; Bowman, M. K.; Azoulay, J. D., A high-spin ground-state donor-acceptor conjugated polymer. *Sci. Adv.* **2019**, *5*, eaav2336.

(39) Hu, X.; Wang, W.; Wang, D.; Zheng, Y., The electronic applications of stable diradicaloids: present and future. *J. Mater. Chem. C* **2018**, *6*, 11232-11242.

(40) Brédas, J. L.; Heeger, A. J.; Wudl, F., Towards organic polymers with very small intrinsic band gaps. I. Electronic structure of polyisothianaphthene and derivatives. *J. Chem. Phys.* **1986**, *85*, 4673-4678.

(41) Moliton, A.; Hiorns, R. C., Review of electronic and optical properties of semiconducting π-conjugated polymers: applications in optoelectronics. *Polym. Int.* **2004**, *53*, 1397-1412.

(42) Brédas, J. L.; Street, G. B., Polarons, bipolarons, and solitons in conducting polymers. *Acc. Chem. Res.* **1985**, *18*, 309-315.

(43) Yuan, D.; Huang, D.; Rivero, S. M.; Carreras, A.; Zhang, C.; Zou, Y.; Jiao, X.; McNeill, C. R.; Zhu, X.; Di, C.-a.; Zhu, D.; Casanova, D.; Casado, J., Cholesteric aggregation at the quinoidal-to-diradical border enabled stable n-doped conductor. *Chem* **2019**, *5*, 964-976.

(44) Yamamoto, J.; Furukawa, Y., Electronic and vibrational spectra of positive polarons and bipolarons in regioregular poly (3-hexylthiophene) doped with ferric chloride. *J. Phys. Chem. B* **2015**, *119*, 4788-4794.

(45) Yuan, B.; Li, C.; Zhao, Y.; Gröening, O.; Zhou, X.; Zhang, P.; Guan, D.; Li, Y.; Zheng, H.; Liu, C.; Mai, Y.; Liu, P.; Ji, W.; Jia, J.; Wang, S., Resolving quinoid structure in poly-para-phenylene chains. *J. Am. Chem. Soc.* **2020**, *142*, 10034-10041.

(46) Tam, T. L.; Wu, G.; Chien, S. W.; Lim, S. F. V.; Yang, S.-W.; Xu, J., High Spin Pro-Quinoid Benzo [1, 2-c; 4, 5-c'] bisthiadiazole Conjugated Polymers for High Performance Solution-Processable Polymer Thermoelectrics. *ACS Mater. Lett.* **2020**, *2*, 147-152.

(47) Huang, L.; Eedugurala, N.; Benasco, A.; Zhang, S.; Mayer, K. S.; Adams, D. J.; Fowler, B.; Lockart, M. M.; Saghayezhian, M.; Tahir, H.; King, E. R.; Morgan, S.; Bowman, M. K.; Gu, X.; Azoulay, J. D., Open-Shell Donor–Acceptor Conjugated Polymers with High Electrical Conductivity. *Adv. Funt. Mater.* **2020**, *30*, 1909805.

(48) Tam, T. L.; Ng, C. K.; Lim, S. L.; Yildirim, E.; Ko, J.; Leong, W. L.; Yang, S.-W.; Xu, J., Proquinoidal-Conjugated Polymer as an Effective Strategy for the Enhancement of Electrical Conductivity and Thermoelectric Properties. *Chem. Mater.* **2019**, *31*, 8543-8550.

(49) Yuan, D.; Liu, L.; Jiao, X.; Zou, Y.; McNeill, C. R.; Xu, W.; Zhu, X.; Zhu, D., Quinoid-Resonant Conducting Polymers Achieve High Electrical Conductivity over 4000

S cm− 1 for Thermoelectrics. *Adv. Sci.* **2018**, *5*, 1800947.

(50) Kleinhenz, N.; Yang, L.; Zhou, H.; Price, S. C.; You, W., Low-band-gap polymers that utilize quinoid resonance structure stabilization by thienothiophene: Fine-tuning of HOMO level. *Macromolecules* **2011**, *44*, 872-877.

(51) Yao, Y.; Dong, H.; Hu, W., Ordering of Conjugated Polymer Molecules: Recent Advances and Perspectives. *Polym. Chem.* **2013**, *4*, 5197-5205.

(52) Dou, J.-H.; Zheng, Y.-Q.; Lei, T.; Zhang, S.-D.; Wang, Z.; Zhang, W.-B.; Wang, J.-Y.; Pei, J., Systematic Investigation of Side-Chain Branching Position Effect on Electron Carrier Mobility in Conjugated Polymers. *Adv. Funt. Mater.* **2014**, *24*, 6270-6278.

(53) Olivier, Y.; Niedzialek, D.; Lemaur, V.; Pisula, W.; Mullen, K.; Koldemir, U.; Reynolds, J. R.; Lazzaroni, R.; Cornil, J.; Beljonne, D., 25th Anniversary Article: High-Mobility Hole and Electron Transport Conjugated Polymers: How Structure Defines Function. *Adv. Mater.* **2014**, *26*, 2119-36.

(54) Diao, Y.; Zhou, Y.; Kurosawa, T.; Shaw, L.; Wang, C.; Park, S.; Guo, Y.; Reinspach, J. A.; Gu, K.; Gu, X.; Tee, B. C.; Pang, C.; Yan, H.; Zhao, D.; Toney, M. F.; Mannsfeld, S. C.; Bao, Z., Flow-Enhanced Solution Printing of All-Polymer Solar Cells. *Nat Commun* **2015**, *6*, 7955.

(55) Thomas, S. W.; Long, T. M.; Pate, B. D.; Kline, S. R.; Thomas, E. L.; Swager, T. M., Perpendicular Organization of Macromolecules: Synthesis and Alignment Studies of a Soluble Poly(iptycene). *J. Am. Chem. Soc.* **2005**, *127*, 17976-17977.

(56) Shacklette, L. W., Dipole and Hydrogen-Bonding Interactions in Polyaniline: A Mechanism for Conductivity Enhancement. *Synth. Met.* **1994**, *65*, 123-130.

(57) Dudek, S. P.; Pouderoijen, M.; Abbel, R.; Schenning, A. P. H. J.; Meijer, E. W., Synthesis and Energy-Transfer Properties of Hydrogen-Bonded Oligofluorenes. *J. Am. Chem. Soc.* **2005**, *127*, 11763-11768.

(58) Abbel, R.; Grenier, C.; Pouderoijen, M. J.; Stouwdam, J. W.; Leclère, P. E. L. G.; Sijbesma, R. P.; Meijer, E. W.; Schenning, A. P. H. J., White-Light Emitting Hydrogen-Bonded Supramolecular Copolymers Based on π-Conjugated Oligomers. *J. Am. Chem. Soc.* **2008**, *131*, 833-843.

(59) González-Rodríguez, D.; Schenning, A. P. H. J., Hydrogen-bonded Supramolecular π-Functional Materials†. *Chem. Mater.* **2010**, *23*, 310-325.

(60) Daniel Głowacki, E.; Leonat, L.; Irimia-Vladu, M.; Schwödiauer, R.; Ullah, M.; Sitter, H.; Bauer, S.; Serdar Sariciftci, N., Intermolecular Hydrogen-Bonded Organic Semiconductors—Quinacridone versus Pentacene. *Applied Physics Letters* **2012**, *101*,

023305.

(61) Black, H. T.; Perepichka, D. F., Crystal Engineering of Dual Channel p/n Organic Semiconductors by Complementary Hydrogen Bonding. *Angew. Chem., Int. Ed. Engl.* **2014**, *53*, 2138-42.

(62) Ley, D.; Guzman, C. X.; Adolfsson, K. H.; Scott, A. M.; Braunschweig, A. B., Cooperatively Assembling Donor-Acceptor Superstructures Direct Energy into an Emergent Charge Separated State. *J. Am. Chem. Soc.* **2014**, *136*, 7809-12.

(63) Huang, J.; Peng, B. G.; Wang, W. N.; Ji, H. X.; Li, L. L.; Xi, K.; Lai, W. Y.; Zhang, X. W.; Jia, X. D., Architecture of Conjugated Donor-Acceptor (D-A)-Type Polymer Films with Cross-Linked Structures. *Adv. Funt. Mater.* **2016**, *26*, 1646-1655.

(64) Kimura, S., Preparation of polyquinolones. *Macromol. Chem. Phys.* **1968**, *117*, 203-209.

(65) Liu, Z. P.; Lin, Y. B.; Wen, X. H.; Su, Q., Preparation and Electrorheological Properties of Polyquin(2,3-b)acridine-12,14(5,7)dione-Based Suspensions. *Colloid Surface A* **2005**, *264*, 55-60.

(66) Wu, J.; Rui, X.; Long, G.; Chen, W.; Yan, Q.; Zhang, Q., Pushing Up Lithium Storage through Nanostructured Polyazaacene Analogues as Anode. *Angew. Chem., Int. Ed.* **2015**, *54*, 7354-7358.

(67) Labana, S. S.; Labana, L. L., Quinacridones. *Chem. Rev.* **1967**, *67*, 1-18.

(68) Osaka, I.; Akita, M.; Koganezawa, T.; Takimiya, K., Quinacridone-Based Semiconducting Polymers: Implication of Electronic Structure and Orientational Order for Charge Transport Property. *Chem. Mater.* **2012**, *24*, 1235-1243.

(69) Song, H.-J.; Kim, D.-H.; Lee, E.-J.; Moon, D.-K., Conjugated Polymers Consisting of Quinacridone and Quinoxaline as Donor Materials for Organic Photovoltaics: Orientation and Charge Transfer Properties of Polymers Formed by Phenyl Structures with a Quinoxaline Derivative. *J. Mater. Chem. A* **2013**, *1*, 6010-6020.

(70) Song, H.-J.; Kim, D.-H.; Choi, M.-H.; Heo, S.-W.; Lee, J.-Y.; Lee, J.-Y.; Moon, D.-K., Self-Organization Polymer Consisting of Quinacridone and Quaterthiophene Units: Coplanar Structure Between Benzene and Thiophene Linkage. *Sol. Energy Mater. Sol. Cells* **2013**, *117*, 285-292.

(71) Gsanger, M.; Bialas, D.; Huang, L.; Stolte, M.; Wurthner, F., Organic Semiconductors based on Dyes and Color Pigments. *Adv. Mater.* **2016**, *28*, 3615-45.

(72) De Feyter, S.; Gesquière, A.; De Schryver, F. C.; Keller, U.; Müllen, K., Aggregation

Properties of Soluble Quinacridones in Two and Three Dimensions. *Chem. Mater.* **2001**, *14*, 989-997.

(73) Paulus, E. F.; Leusen, F. J. J.; Schmidt, M. U., Crystal structures of quinacridones. *CrystEngComm* **2007**, *9*, 131-143.

(74) Fukunaga, H.; Fedorov, D. G.; Chiba, M.; Nii, K.; Kitaura, K., Theoretical Analysis of the Intermolecular Interaction Effects on the Excitation Energy of Organic Pigments: Solid State Quinacridone. *J. Phys. Chem. A* **2008**, *112*, 10887-10894.

(75) Lincke, G., A Review of Thirty Years of Research on Quinacridones. X-ray Crystallography and Crystal Engineering. *Dyes Pigm.* **2000**, *44*, 101-122.

(76) Głowacki, E. D.; Irimia-Vladu, M.; Kaltenbrunner, M.; Gsiorowski, J.; White, M. S.; Monkowius, U.; Romanazzi, G.; Suranna, G. P.; Mastrorilli, P.; Sekitani, T.; Bauer, S.; Someya, T.; Torsi, L.; Sariciftci, N. S., Hydrogen-Bonded Semiconducting Pigments for Air-Stable Field-Effect Transistors. *Adv. Mater.* **2013**, *25*, 1563-1569.

(77) Enengl, C.; Enengl, S.; Havlicek, M.; Stadler, P.; Glowacki, E. D.; Scharber, M. C.; White, M.; Hingerl, K.; Ehrenfreund, E.; Neugebauer, H.; Sariciftci, N. S., The Role of Heteroatoms Leading to Hydrogen Bonds in View of Extended Chemical Stability of Organic Semiconductors. *Adv. Funt. Mater.* **2015**, *25*, 6679-6688.

(78) Zou, Y.; Ji, X.; Cai, J.; Yuan, T.; Stanton, D. J.; Lin, Y.-H.; Naraghi, M.; Fang, L., Synthesis and Solution Processing of a Hydrogen-Bonded Ladder Polymer. *Chem* **2017**, *2*, 139-152.

(79) Zou, Y.; Yuan, T.; Yao, H.; Frazier, D. J.; Stanton, D. J.; Sue, H.-J.; Fang, L., Solution-processable core-extended quinacridone derivatives with intact hydrogen bonds. *Org. Lett.* **2015**, *17*, 3146-3149.

(80) Kitahara, K.; Yanagimoto, H.; Nakajima, N.; Nishi, H., Synthesis of Soluble Quinacridones. *J. Heterocycl. Chem.* **1992**, *29*, 167-169.

(81) Wang, C.; Chen, D.; Chen, W.; Chen, S.; Ye, K.; Zhang, H.; Zhang, J.; Wang, Y., Polymorph, assembly, luminescence and semiconductor properties of a quinacridone derivative with extended [small pi]-conjugated framework. *J. Mater. Chem. C* **2013**, *1*, 5548-5556.

(82) Wudl, F.; Angus, R. O.; Lu, F. L.; Allemand, P. M.; Vachon, D.; Nowak, M.; Liu, Z. X.; Schaffer, H.; Heeger, A. J., Poly(*p*-phenyleneamineimine): Synthesis and Comparison to Polyaniline. *J. Am. Chem. Soc.* **1987**, *109*, 3677-3684.

(83) Keller, U.; Müllen, K.; De Feyter, S.; De Schryver, F. C., Hydrogen-Bonding and Phase-Forming Behavior of a Soluble Quinacridone. *Adv. Mater.* **1996**, *8*, 490-493.

(84) Xia, C.; Advincula, R. C., Ladder-Type Oligo(p-phenylene)s Tethered to a Poly(alkylene) Main Chain: The Orthogonal Approach to Functional Light-Emitting Polymers. *Macromolecules* **2001**, *34*, 6922-6928.

(85) Cocherel, N.; Poriel, C.; Rault-Berthelot, J.; Barrière, F.; Audebrand, N.; Slawin, A. M. Z.; Vignau, L., New 3π-2Spiro Ladder-Type Phenylene Materials: Synthesis, Physicochemical Properties and Applications in OLEDs. *Chem. Eur. J.* **2008**, *14*, 11328-11342.

(86) Wu, Y.; Hao, X.; Wu, J.; Jin, J.; Ba, X., Pure Blue-Light-Emitting Materials: Hyperbranched Ladder-Type Poly(p-phenylene)s Containing Truxene Units. *Macromolecules* **2010**, *43*, 731-738.

(87) Yang, J.-S.; Huang, H.-H.; Liu, Y.-H.; Peng, S.-M., Synthesis and Electronic Properties of Isotruxene-Derived Star-Shaped Ladder-Type Oligophenylenes: Bandgap Tuning with Two-Dimensional Conjugation. *Org. Lett.* **2009**, *11*, 4942-4945.

(88) Huang, H.-H.; Prabhakar, C.; Tang, K.-C.; Chou, P.-T.; Huang, G.-J.; Yang, J.-S., Ortho-Branched Ladder-Type Oligophenylenes with Two-Dimensionally π-Conjugated Electronic Properties. *J. Am. Chem. Soc.* **2011**, *133*, 8028-8039.

(89) Qiu, S.; Lu, P.; Liu, X.; Shen, F. Z.; Liu, L. L.; Ma, Y. G.; Shen, J. C., New Ladder-Type Poly(p-phenylene)s Containing Fluorene Unit Exhibiting High Efficient Electroluminescence. *Macromolecules* **2003**, *36*, 9823-9829.

(90) Jacob, J.; Sax, S.; Gaal, M.; List, E. J. W.; Grimsdale, A. C.; Müllen, K., A Fully Aryl-Substituted Poly(ladder-type pentaphenylene): A Remarkably Stable Blue-Light-Emitting Polymer. *Macromolecules* **2005**, *38*, 9933-9938.

(91) D. Gernon, M.; Wu, M.; Buszta, T.; Janney, P., Environmental Benefits of Methanesulfonic Acid . Comparative Properties and Advantages. *Green Chem.* **1999**, *1*, 127-140.

(92) Liu, S.; Jin, Z.; Teo, Y. C.; Xia, Y., Efficient Synthesis of Rigid Ladder Polymers via Palladium Catalyzed Annulation. *J. Am. Chem. Soc.* **2014**, *136*, 17434-17437.

(93) Kass, K.-J.; Forster, M.; Scherf, U., Incorporating an Alternating Donor–Acceptor Structure into a Ladder Polymer Backbone. *Angew. Chem., Int. Ed.* **2016**, DOI: 10.1002/anie.201600580.

(94) Guo, Z.-H.; Ai, N.; McBroom, C. R.; Yuan, T.; Lin, Y.-H.; Roders, M.; Zhu, C.; Ayzner, A. L.; Pei, J.; Fang, L., A side-chain engineering approach to solvent-resistant semiconducting polymer thin films. *Poly. Chem.* **2016**, *7*, 648-655.

(95) Wang, S.; Chen, Z.-H.; Ma, W.-J.; Ma, Q.-S., Influence of Heat Treatment on

Physical–Chemical Properties of PAN-Based Carbon Fiber. *Ceram. Int.* **2006**, *32*, 291-295.

(96) Liu, C.; Dong, S.; Cai, P.; Liu, P.; Liu, S.; Chen, J.; Liu, F.; Ying, L.; Russell, T. P.; Huang, F.; Cao, Y., Donor–Acceptor Copolymers Based on Thermally Cleavable Indigo, Isoindigo, and DPP Units: Synthesis, Field Effect Transistors, and Polymer Solar Cells. *ACS Appl. Mater. Interfaces* **2015**, *7*, 9038-9051.

(97) Bahl, O. P.; Manocha, L. M., Characterization of Oxidised PAN Fibres. *Carbon* **1974**, *12*, 417-423.

(98) Wangxi, Z.; Jie, L.; Gang, W., Evolution of Structure and Properties of PAN Precursors during Their Conversion to Carbon Fibers. *Carbon* **2003**, *41*, 2805-2812.

(99) Rostami, A.; Wei, C. J.; Guérin, G.; Taylor, M. S., Anion Detection by a Fluorescent Poly(squaramide): Self-Assembly of Anion-Binding Sites by Polymer Aggregation. *Angew. Chem., Int. Ed.* **2011**, *50*, 2059-2062.

(100) Mirmohseni, A.; Oladegaragoze, A., Anti-corrosive properties of polyaniline coating on iron. *Synth. Met.* **2000**, *114*, 105-108.

(101) Gupta, V.; Miura, N., High performance electrochemical supercapacitor from electrochemically synthesized nanostructured polyaniline. *Mater. Lett.* **2006**, *60*, 1466-1469.

(102) MacDiarmid, A.; Yang, L.; Huang, W.; Humphrey, B., Polyaniline: Electrochemistry and application to rechargeable batteries. *Synth. Met.* **1987**, *18*, 393-398.

(103) Jiménez, P.; Levillain, E.; Alévêque, O.; Guyomard, D.; Lestriez, B.; Gaubicher, J., Lithium n-Doped Polyaniline as a High-Performance Electroactive Material for Rechargeable Batteries. *Angew. Chem., Int. Ed.* **2017**, *56*, 1553-1556.

(104) Zhao, L.; Zhao, L.; Xu, Y.; Qiu, T.; Zhi, L.; Shi, G., Polyaniline electrochromic devices with transparent graphene electrodes. *Electrochim. acta* **2009**, *55*, 491-497.

(105) Akhtar, M.; Weakliem, H.; Paiste, R.; Gaughan, K., Polyaniline thin film electrochromic devices. *Synth. Met.* **1988**, *26*, 203-208.

(106) MacDiarmid, A. G., "Synthetic metals": A novel role for organic polymers (Nobel lecture). *Angew. Chem., Int. Ed.* **2001**, *40*, 2581-2590.

(107) Javadi, H. H. S.; Treat, S. P.; Ginder, J. M.; Wolf, J. F.; Epstein, A. J., Aniline tetramers: Comparison with aniline octamer and polyaniline. *J. Phys. Chem. Solids* **1990**, *51*, 107-112.

(108) Wei, Z.; Faul, C. F., Aniline oligomers–architecture, function and new opportunities for nanostructured materials. *Macromol. Rapid Commun.* **2008**, *29*, 280-292.

(109) Ćirić-Marjanović, G., Recent advances in polyaniline research: Polymerization mechanisms, structural aspects, properties and applications. *Synth. Met.* **2013**, *177*, 1-47.

(110) Genies, E.; Boyle, A.; Lapkowski, M.; Tsintavis, C., Polyaniline: A historical survey. *Synth. Met.* **1990**, *36*, 139-182.

(111) MacDiarmid, A. G.; Zhou, Y.; Feng, J., Oligomers and isomers: new horizons in poly-anilines. *Synth. Met.* **1999**, *100*, 131-140.

(112) Lin, C.-W.; Li, R. L.; Robbennolt, S.; Yeung, M. T.; Akopov, G.; Kaner, R. B., Furthering Our Understanding of the Doping Mechanism in Conjugated Polymers Using Tetraaniline. *Macromolecules* **2017**, *50*, 5892-5897.

(113) Krinichnyi, V.; Konkin, A.; Monkman, A., Electron paramagnetic resonance study of spin centers related to charge transport in metallic polyaniline. *Synth. Met.* **2012**, *162*, 1147-1155.

(114) Cao, Y., Spectroscopic studies of acceptor and donor doping of polyaniline in the emeraldine base and pernigraniline forms. *Synth. Met.* **1990**, *35*, 319-332.

(115) Cao, Y.; Smith, P.; Heeger, A., Spectroscopic studies of polyaniline in solution and in spin-cast films. *Synth. Met.* **1989**, *32*, 263-281.

(116) D'Aprano, G.; Leclerc, M.; Zotti, G., Stabilization and characterization of pernigraniline salt: the" acid-doped" form of fully oxidized polyanilines. *Macromolecules* **1992**, *25*, 2145-2150.

(117) Bazito, F. F.; Silveira, L. T.; Torresi, R. M.; de Torresi, S. I. C., On the stabilization of conducting pernigraniline salt by the synthesis and oxidation of polyaniline in hydrophobic ionic liquids. *Phys. Chem. Chem. Phys.* **2008**, *10*, 1457-1462.

(118) MacDiarmid, A. G.; Manohar, S. K.; Masters, J. G.; Sun, Y.; Weiss, H.; Epstein, A. J., Polyaniline: Synthesis and properties of pernigraniline base. *Synth. Met.* **1991**, *41*, 621-626.

(119) Chandrakanthi, N.; Careem, M., Preparation and characterization of fully oxidized form of polyaniline. *Polym. Bull.* **2000**, *45*, 113-120.

(120) Chen, L.; Yu, Y.; Mao, H.; Lu, X.; Zhang, W.; Wei, Y., Synthesis of phenyl-capped aniline heptamer and its UV–vis spectral study. *Synth. Met.* **2005**, *149*, 129-134.

(121) Bogomolova, O. E.; Sergeyev, V. G., Acid Doping of Phenyl-Capped Aniline Dimer:

Intermolecular Polaron Formation Mechanism and Its Applicability to Polyaniline. *J. Phys. Chem. A* **2018**, *122*, 461-469.

(122) Cao, Y.; Heeger, A., Charged solitons in pernigraniline. *Synth. Met.* **1990**, *39*, 205-214.

(123) Mažeikien, R.; Malinauskas, A., Electrochemical stability of polyaniline. *Eur. Polym. J.* **2002**, *38*, 1947-1952.

(124) Simoes, F.; Pocrifka, L.; Marchesi, L.; Pereira, E., Investigation of electrochemical degradation process in polyaniline/polystyrene sulfonated self-assembly films by impedance spectroscopy. *J. Phys. Chem. B* **2011**, *115*, 11092-11097.

(125) Stejskal, J.; Bober, P.; Trchová, M.; Horský, J.; Pilař, J.; Walterová, Z., The oxidation of aniline with p-benzoquinone and its impact on the preparation of the conducting polymer, polyaniline. *Synth. Met.* **2014**, *192*, 66-73.

(126) Jeon, J.-W.; Ma, Y.; Mike, J. F.; Shao, L.; Balbuena, P. B.; Lutkenhaus, J. L., Oxidatively stable polyaniline: polyacid electrodes for electrochemical energy storage. *Phys. Chem. Chem. Phys.* **2013**, *15*, 9654-9662.

(127) Jeon, J.-W.; O'Neal, J.; Shao, L.; Lutkenhaus, J. L., Charge storage in polymer acid-doped polyaniline-based layer-by-layer electrodes. *ACS Appl. Mater. Interfaces* **2013**, *5*, 10127-10136.

(128) Sandberg, M.; Hjertberg, T., E/Z isomerism in polyaniline, a model study. *Synth. Met.* **1989**, *29*, 257-264.

(129) Wakim, S.; Bouchard, J.; Blouin, N.; Michaud, A.; Leclerc, M., Synthesis of diindolocarbazoles by Ullmann reaction: a rapid route to ladder oligo (p-aniline) s. *Org. Lett.* **2004**, *6*, 3413-3416.

(130) Zheng, T.; Cai, Z.; Ho-Wu, R.; Yau, S. H.; Shaparov, V.; Goodson III, T.; Yu, L., Synthesis of Ladder-Type Thienoacenes and Their Electronic and Optical Properties. *J. Am. Chem. Soc.* **2016**, *138*, 868-875.

(131) Lee, J.; Li, H.; Kalin, A. J.; Yuan, T.; Wang, C.; Olson, T.; Li, H.; Fang, L., Extended Ladder-Type Benzo [k] tetraphene-Derived Oligomers. *Angew. Chem., Int. Ed.* **2017**, *56*, 13727-13731.

(132) Wang, Y.; Guo, H.; Ling, S.; Arrechea-Marcos, I.; Wang, Y.; López Navarrete, J. T.; Ortiz, R. P.; Guo, X., Ladder-type Heteroarenes: Up to 15 Rings with Five Imide Groups. *Angew. Chem.* **2017**, *129*, 10056-10061.

(133) Wang, Z.; Gu, P.; Liu, G.; Yao, H.; Wu, Y.; Li, Y.; Rakesh, G.; Zhu, J.; Fu, H.; Zhang,

Q., A large pyrene-fused N-heteroacene: fifteen aromatic six-membered rings annulated in one row. *Chem. Comm.* **2017**, *53*, 7772-7775.

(134) Ji, X.; Xie, H.; Zhu, C.; Zou, Y.; Mu, A. U.; Al-Hashimi, M.; Dunbar, K. R.; Fang, L., Pauli Paramagnetism of Stable Analogues of Pernigraniline Salt Featuring Ladder-Type Constitution. *J. Am. Chem. Soc.* **2020**, *142*, 641-648.

(135) Scherf, U.; Müllen, K., Polyarylenes and poly (arylenevinylenes), 7. A soluble ladder polymer via bridging of functionalized poly (p-phenylene)-precursors. *Makromol. Chem. Rapid Comm.* **1991**, *12*, 489-497.

(136) Zhang, X.-X.; Sadighi, J. P.; Mackewitz, T. W.; Buchwald, S. L., Efficient synthesis of well-defined, high molecular weight, and processible polyanilines under mild conditions via palladium-catalyzed amination. *J. Am. Chem. Soc.* **2000**, *122*, 7606-7607.

(137) Pullen, A. E.; Swager, T. M., Regiospecific copolyanilines from substituted oligoanilines: Electrochemical comparisons with random copolyanilines. *Macromolecules* **2001**, *34*, 812-816.

(138) Mills, B. M.; Fey, N.; Marszalek, T.; Pisula, W.; Rannou, P.; Faul, C. F., Exploring Redox States, Doping and Ordering of Electroactive Star-Shaped Oligo (aniline)s. *Chemistry-A European Journal* **2016**, *22*, 16950-16956.

(139) Sariciftci, N.; Kolbert, A.; Cao, Y.; Heeger, A.; Pines, A., Magnetic resonance evidence for metallic state in highly conducting polyaniline. *Synth. Met.* **1995**, *69*, 243-244.

(140) Huber, R. C.; Ferreira, A. S.; Thompson, R.; Kilbride, D.; Knutson, N. S.; Devi, L. S.; Toso, D. B.; Challa, J. R.; Zhou, Z. H.; Rubin, Y., Long-lived photoinduced polaron formation in conjugated polyelectrolyte-fullerene assemblies. *Science* **2015**, *348*, 1340-1343.

(141) Beldjoudi, Y.; Osorio-Román, I.; Nascimento, M. A.; Rawson, J. M., A fluorescent dithiadiazolyl radical: structure and optical properties of phenanthrenyl dithiadiazolyl in solution and polymer composites. *J. Mater. Chem. C* **2017**, *5*, 2794-2799.

(142) Earney, J.; Finn, C.; Najafabadi, B., Van Vleck temperature independent paramagnetism in some rare earth double nitrates. *J. Phys. C: Solid State Phys.* **1971**, *4*, 1013.

(143) Carrington, A., The temperature-independent paramagnetism of permanganate and related complexes. *Mol. Phys.* **1960**, *3*, 271-275.

(144) Goldberg, I.; Crowe, H.; Newman, P.; Heeger, A.; MacDiarmid, A., Electron spin resonance of polyacetylene and AsF5-doped polyacetylene. *J. Chem. Phys.* **1979**, *70*,

1132-1136.

(145) Kang, K.; Watanabe, S.; Broch, K.; Sepe, A.; Brown, A.; Nasrallah, I.; Nikolka, M.; Fei, Z.; Heeney, M.; Matsumoto, D., 2D coherent charge transport in highly ordered conducting polymers doped by solid state diffusion. *Nat. Mater.* **2016**, *15*, 896-902.

(146) Tanaka, H.; Hirate, M.; Watanabe, S.; Kuroda, S. i., Microscopic signature of metallic state in semicrystalline conjugated polymers doped with fluoroalkylsilane molecules. *Adv. Mater.* **2014**, *26*, 2376-2383.

(147) Rajca, A., Organic Diradicals and Polyradicals - from Spin Coupling to Magnetism. *Chem. Rev.* **1994**, *94*, 871-893.

(148) Beck, M.; Stiel, H.; Leupold, D.; Winter, B.; Pop, D.; Vogt, U.; Spitz, C., Evaluation of the energetic position of the lowest excited singlet state of beta-carotene by NEXAFS and photoemission spectroscopy. *Bba-Bioenergetics* **2001**, *1506*, 260-267.

(149) Sandberg, M. O.; Nagao, O.; Wu, Z. K.; Matsushita, M. N.; Sugawara, T., Generation of a triplet diradical from a donor-acceptor cross conjugate upon acid-induced electron transfer. *Chem. Comm.* **2008**, 3738-3740.

(150) Huggins, R. A., Simple method to determine electronic and ionic components of the conductivity in mixed conductors a review. *Ionics* **2002**, *8*, 300-313.

(151) Hui, D.; Alexandrescu, R.; Chipara, M.; Morjan, I.; Aldica, G.; Chipara, M.; Lau, K., Impedance spectroscopy studies on doped polyanilines. *J. Optoelectron. Adv. Mater.* **2004**, *6*, 817-824.

(152) Babu, V. J.; Vempati, S.; Ramakrishna, S., Conducting polyaniline-electrical charge transportation. *Mater. Sci. Appl.* **2013**, *4*, 1.

(153) Zheng, Y.; Miao, M. s.; Dantelle, G.; Eisenmenger, N. D.; Wu, G.; Yavuz, I.; Chabinyc, M. L.; Houk, K. N.; Wudl, F., A Solid-State Effect Responsible for an Organic Quintet State at Room Temperature and Ambient Pressure. *Adv. Mater.* **2015**, *27*, 1718-1723.

(154) Angelopoulos, M.; Dipietro, R.; Zheng, W.; MacDiarmid, A.; Epstem, A., Effect of selected processing parameters on solution properties and morphology of polyaniline and impact on conductivity. *Synth. Met.* **1997**, *84*, 35-39.

(155) Zeng, Z.; Shi, X.; Chi, C.; Lopez Navarrete, J. T.; Casado, J.; Wu, J., Pro-aromatic and anti-aromatic pi-conjugated molecules: an irresistible wish to be diradicals. *Chem Soc Rev* **2015**, *44*, 6578-96.

(156) Wang, L.; Zhang, L.; Fang, Y.; Zhao, Y.; Tan, G.; Wang, X., Orthogonal Oriented

Bisanthrancene-Bridged Bis (Triarylamine) Diradical Dications: Isolation, Characterizations and Crystal Structures. *Chem. Asia. J.* **2019**, *14*, 1708-1711.

(157) Hu, X.; Chen, H.; Zhao, L.; Miao, M.; Han, J.; Wang, J.; Guo, J.; Hu, Y.; Zheng, Y., Nitrogen analogues of Chichibabin's and Müller's hydrocarbons with small singlet–triplet energy gaps. *Chem. Comm.* **2019**, *55*, 7812-7815.

(158) Lungerich, D.; Papaianina, O.; Feofanov, M.; Liu, J.; Devarajulu, M.; Troyanov, S. I.; Maier, S.; Amsharov, K., Dehydrative π-extension to nanographenes with zig-zag edges. *Nat. Comm.* **2018**, *9*, 4756.

(159) Mortimer, R. J., Electrochromic materials. *Chem. Soc. Rev.* **1997**, *26*, 147-156.

(160) Fong, K. D.; Wang, T.; Smoukov, S. K., Multidimensional performance optimization of conducting polymer-based supercapacitor electrodes. *Sustainable Energy Fuels* **2017**, *1*, 1857-1874.

(161) MacDiarmid, A. G., Polyaniline and polypyrrole: where are we headed? *Synth. Met.* **1997**, *84*, 27-34.

(162) Virji, S.; Huang, J.; Kaner, R. B.; Weiller, B. H., Polyaniline nanofiber gas sensors: examination of response mechanisms. *Nano Lett.* **2004**, *4*, 491-496.

(163) Pud, A., Stability and degradation of conducting polymers in electrochemical systems. *Synth. Met.* **1994**, *66*, 1-18.

(164) Malinauskas, A.; Holze, R., In situ UV–vis spectroelectrochemical study of polyaniline degradation. *J. Appl. Polym. Sci.* **1999**, *73*, 287-294.

(165) Santino, L. M.; Lu, Y.; Acharya, S.; Bloom, L.; Cotton, D.; Wayne, A.; D'Arcy, J. M., Enhancing cycling stability of aqueous polyaniline electrochemical capacitors. *ACS appl. Mater. Interfaces* **2016**, *8*, 29452-29460.

(166) Yen, H.-J.; Lin, H.-Y.; Liou, G.-S., Novel starburst triarylamine-containing electroactive aramids with highly stable electrochromism in near-infrared and visible light regions. *Chem. Mater.* **2011**, *23*, 1874-1882.

(167) Sun, N.; Meng, S.; Chao, D.; Zhou, Z.; Du, Y.; Wang, D.; Zhao, X.; Zhou, H.; Chen, C., Highly stable electrochromic and electrofluorescent dual-switching polyamide containing bis (diphenylamino)-fluorene moieties. *Polym. Chem.* **2016**, *7*, 6055-6063.

(168) Yen, H.-J.; Liou, G.-S., Solution-processable novel near-infrared electrochromic aromatic polyamides based on electroactive tetraphenyl-p-phenylenediamine moieties. *Chem. Mater.* **2009**, *21*, 4062-4070.

(169) Nobrega, M. M.; Silva, C. H.; Constantino, V. R.; Temperini, M. L., Spectroscopic study on the structural differences of thermally induced cross-linking segments in emeraldine salt and base forms of polyaniline. *J. Phys. Chem. B* **2012**, *116*, 14191-14200.

(170) Xiong, S.; Li, S.; Zhang, X.; Wang, R.; Zhang, R.; Wang, X.; Wu, B.; Gong, M.; Chu, J., Synthesis and performance of highly stable star-shaped polyaniline electrochromic materials with triphenylamine core. *J. Electron. Mater.* **2018**, *47*, 1167-1175.

(171) Zhu, C.; Kalin, A. J.; Fang, L., Covalent and Noncovalent Approaches to Rigid Coplanar π-Conjugated Molecules and Macromolecules. *Acc. Chem. Res.* **2019**, *52*, 1089-1100.

(172) Li, F.; Zou, Y.; Wang, S.; Fang, L.; Lutkenhaus, J. L., Scalable Synthesis and Multi-Electron Transfer of Aniline/Fluorene Copolymer for Solution-Processable Battery Cathodes. *Macromol. Rapid Commun.* **2017**, *38*, 1700067.

(173) Daigle, M.; Morin, J.-F. o., Helical conjugated ladder polymers: tuning the conformation and properties through edge design. *Macromolecules* **2017**, *50*, 9257-9264.

(174) Su, W.-F., *Polymer Size and Polymer Solutions. In: Principles of Polymer Design and Synthesis*. Springer: Berlin, Heidelberg, 2013; Vol. 82.

(175) Lai, H. W.; Liu, S.; Xia, Y., Norbornyl benzocyclobutene ladder polymers: conformation and microporosity. *J. Polym. Sci., Part A: Polym. Chem.* **2017**, *55*, 3075-3081.

(176) Ji, X.; Leng, M.; Xie, H.; Wang, C.; Dunbar, K. R.; Zou, Y.; Fang, L., Extraodinary Electrochemical Stability and Extended Polaron Delocalization of Ladder-Type Polyaniline-Analogous Polymers. *Chem. Sci.* **2020**.

(177) De Albuquerque, J.; Mattoso, L.; Faria, R.; Masters, J.; MacDiarmid, A., Study of the interconversion of polyaniline oxidation states by optical absorption spectroscopy. *Synth. Met.* **2004**, *146*, 1-10.

(178) Albuquerque, J.; Mattoso, L.; Balogh, D. T.; Faria, R. M.; Masters, J.; MacDiarmid, A., A simple method to estimate the oxidation state of polyanilines. *Synth. Met.* **2000**, *113*, 19-22.

(179) Watanabe, A.; Mori, K.; Iwasaki, Y.; Nakamura, Y.; Niizuma, S., Electrochromism of polyaniline film prepared by electrochemical polymerization. *Macromolecules* **1987**, *20*, 1793-1796.

(180) Tang, H.; Ding, Y.; Zang, C.; Gu, J.; Shen, Q.; Kan, J., Effect of temperature on electrochemical degradation of polyaniline. *Int. J. Electrochem. Sci* **2014**, *9*, 7239-7252.

(181) Zhang, A.; Cui, C.; Lee, J. Y., Electrochemical degradation of polyaniline in HClO4 and H2SO4. *Synth. Met.* **1995**, *72*, 217-223.

(182) Cui, C.; Su, X.; Lee, J. Y., Measurement and evaluation of polyaniline degradation. *Polym. Degrad. Stab.* **1993**, *41*, 69-76.

(183) Huang, W.; MacDiarmid, A., Optical properties of polyaniline. *Polymer* **1993**, *34*, 1833-1845.

(184) Varela-Álvarez, A.; Sordo, J. A.; Scuseria, G. E., Doping of polyaniline by acid− base chemistry: density functional calculations with periodic boundary conditions. *J. Am. Chem. Soc.* **2005**, *127*, 11318-11327.

(185) Wang, R.-X.; Huang, L.-F.; Tian, X.-Y., Understanding the protonation of polyaniline and polyaniline–graphene interaction. *J. Phys. Chem. C* **2012**, *116*, 13120-13126.

(186) Barker, J. E.; Dressler, J. J.; Cárdenas Valdivia, A.; Kishi, R.; Strand, E. T.; Zakharov, L. N.; MacMillan, S. N.; Gómez-García, C. J.; Nakano, M.; Casado, J., Molecule Isomerism Modulates the Diradical Properties of Stable Singlet Diradicaloids. *J. Am. Chem. Soc.* **2019**.

(187) Tan, G.; Wang, X., Isolable bis (triarylamine) dications: analogues of Thiele's, Chichibabin's, and Muller's hydrocarbons. *Acc. Chem. Res.* **2017**, *50*, 1997-2006.

(188) Hu, X.; Chen, H.; Zhao, L.; Miao, M.; Han, J.; Wang, J.; Guo, J.; Hu, Y.; Zheng, Y., Nitrogen analogues of Chichibabin's and Müller's hydrocarbons with small singlet–triplet energy gaps. *Chem. Comm.* **2019**, *55*, 7812-7815.

(189) Yang, K.; Zhang, X.; Harbuzaru, A.; Wang, L.; Wang, Y.; Koh, C.; Guo, H.; Shi, Y.; Chen, J.; Sun, H., Stable Organic Diradicals Based on Fused Quinoidal Oligothiophene Imides with High Electrical Conductivity. *J. Am. Chem. Soc.* **2020**, *142*, 4329-4340.

(190) Wang, S.; Todd, E. K.; Birau, M.; Zhang, J.; Wan, X.; Wang, Z. Y., Near-infrared electrochromism in electroactive pentacenediquinone-containing poly (aryl ether) s. *Chem. Mater.* **2005**, *17*, 6388-6394.

(191) Beaujuge, P. M.; Reynolds, J. R., Color control in π-conjugated organic polymers for use in electrochromic devices. *Chem. Rev.* **2010**, *110*, 268-320.

(192) Tarver, J.; Yoo, J. E.; Loo, Y.-L., Polyaniline exhibiting stable and reversible switching in the visible extending into the near-IR in aqueous media. *Chem. Mater.* **2010**, *22*, 2333-2340.

(193) Ge, D.; Yang, L.; Tong, Z.; Ding, Y.; Xin, W.; Zhao, J.; Li, Y., Ion diffusion and

optical switching performance of 3D ordered nanostructured polyaniline films for advanced electrochemical/electrochromic devices. *Electrochim. acta* **2013**, *104*, 191-197.

(194) Duan, C.; Zhang, K.; Zhong, C.; Huang, F.; Cao, Y., Recent advances in water/alcohol-soluble π-conjugated materials: new materials and growing applications in solar cells. *Chem. Soc. Rev.* **2013**, *42*, 9071-9104.

(195) Duarte, A.; Pu, K.-Y.; Liu, B.; Bazan, G. C., Recent advances in conjugated polyelectrolytes for emerging optoelectronic applications. *Chem. Mater.* **2011**, *23*, 501-515.

(196) Liu, B.; Wang, S.; Bazan, G. C.; Mikhailovsky, A., Shape-adaptable water-soluble conjugated polymers. *J. Am. Chem. Soc.* **2003**, *125*, 13306-13307.

(197) Stolz, S.; Petzoldt, M.; Kotadiya, N.; Rödlmeier, T.; Eckstein, R.; Freudenberg, J.; Bunz, U. H.; Lemmer, U.; Mankel, E.; Hamburger, M., One-step additive crosslinking of conjugated polyelectrolyte interlayers: improved lifetime and performance of solution-processed OLEDs. *J. Mater. Chem. C* **2016**, *4*, 11150-11156.

(198) Trilling, F.; Ausländer, M.-K.; Scherf, U., Ladder-Type Polymers and Ladder-Type Polyelectrolytes with On-Chain Dibenz [a, h] anthracene Chromophores. *Macromolecules* **2019**, *52*, 3115-3122.